SNOW COVER AS A SOURCE OF CLIMATE PREDICTABILITY:

MECHANISMS OF SNOW-ATMOSPHERE COUPLING

by

Li Xu

A Dissertation
Submitted to the
Graduate Faculty
of
George Mason University
in Partial Fulfillment of
The Requirements for the Degree
of
Doctor of Philosophy
Climate Dynamics

Committee:

_____ Dr. Paul Dirmeyer, Dissertation Director

_____ Dr. Jagadish Shukla, Committee Chair & Advisor

_____ Dr. Bohua Huang, Committee Member

_____ Dr. John Qu, Committee Member

_____ Dr. David Straus, Department Chairperson

_____ Dr. Richard Diecchio, Associate
Dean for Academic and Student
Affairs, College of Science

_____ Dr. Vikas Chandhoke, Dean,
College of Science

Date: _____Spring Semester 2011
George Mason University
Fairfax, VA

Snow cover as a source of climate predictability: Mechanisms of snow-atmosphere coupling

A dissertation submitted in partial fulfillment of the requirements for the degree of Doctor of Philosophy at George Mason University

By

Li Xu
Master of Science
University of Utah, 2007

Dissertation Director: Dr. Paul Dirmeyer, Scienist
Center for Ocean-Land-Atmosphere studies

Spring Semester 2011
George Mason University
Fairfax, VA

ACKNOWLEDGEMENTS

Firstly, I especially thank my advisors Prof. J Shukla and Dr. Paul Dirmeyer, for giving me valuable guidance and counsel. They always encouraged me to think independently and develop my research skills. Their comments are always extremely perceptive, helpful and appropriate.

I would also like to thank the rest of my dissertation committee, Prof. Bohua Huang and Prof. John Qu, for their invaluable advice and support during my doctoral work. I would also like to thank the scientists and staff at the Center for Ocean-Land-Atmosphere Studies (COLA), Dr. Zhichang Guo, Dr. Jiangfeng Wei and Prof. David Straus, for their suggestions and technical support. I would also like to thank Dr. David Lawrence at NCAR for providing the GLACE-I codes for implementing prescribed snow in the CLM model. I also thank Dr. Randal Koster at NASA/GSFC for insightful discussion about GLACE-type experiments.

Finally, I would like to thank my wife Hua Liu. Without her love and encouragement, I would never have made it this far.

This work was supported by the George Mason University Presidential Scholarship and NASA Earth and Space Sciences Fellowship Program.

TABLE OF CONTENTS

Page

LIST OF TABLES

LIST OF FIGURES

ABSTRACT

SNOW COVER AS A SOURCE OF CLIMATE PREDICTABILITY: MECHANISMS OF SNOW-ATMOSPHERE COUPLING

Li Xu, PhD

George Mason University, 2011

Dissertation Director: Dr. Paul Dirmeyer

This study investigates the role of snow cover as a source of predictability at seasonal time scales over the Northern Hemisphere. A global climate model is used, consisting of the fully-coupled land and atmosphere components of the Community Climate System Model. Ensembles of boreal spring-summer climate simulations are made with specified climatological sea surface temperatures. Following the methodology of the Global Land-Atmosphere Coupling Experiment (GLACE), a control ensemble is created with perturbed initial atmospheric states and realistic land surface initialization. In the test cases, snow cover fraction and snow water equivalent are specified in all ensemble members based on model simulated snow information or realistic snow data from remote sensing and an operational land surface analysis. The snow-atmosphere coupling strength is quantified as in GLACE

as the degree to which identically constrained snow boundary conditions reduce the ensemble spread of key meteorological variables like precipitation and near-surface air temperature. The snow albedo effect, snow hydrological effect or mixed effects are estimated by different experiments and snow stages. Metrics of potential predictability and feedback are also investigated.

From spring to early summer, the snow-covered regions demonstrate significant coupling to the atmosphere over large portions of the Northern Hemisphere. The local coupling between snow state and atmosphere is found to have three distinct stages: the stable-snow period before snowmelt when interactions are through radiative processes controlled by albedo; the period after snowmelt when interactions are through the delayed hydrologic effect of soil moisture anomalies resulting from snow anomalies; and the intervening period during snowmelt when both radiative and hydrologic effects are important. The coupling strength is strongest during the snowmelt period along the transient zone between snow-covered and snow-free areas, and migrates northward with the retreating snow line. The coupling strength due to the hydrological effect (soil moisture impact) after snowmelt is generally stronger than the coupling strength due to the albedo effect (radiative impact) before snowmelt. The Tibetan Plateau is a special snow-atmosphere coupling region due to its high incident solar radiation caused by its high altitude and relatively low latitude. The potential predictably from accurate knowledge of snow distribution is highly correlated with the snow-

atmosphere coupling strength. Conceptual models are proposed to explain the mechanisms behind the timing and spatial distribution of snow-atmosphere coupling.

CHAPTER 1. MOTIVATION

The cryosphere plays an important role in the earth climate system. In particular, snow cover is a key component of the cryosphere, with high reflectivity of sunlight, high infrared emissivity and low thermal conductivity compared to other natural land units. It imposes a significant impact on the surface radiation budget, turbulent energy fluxes and local hydrological fluxes to the atmosphere [*Cohen and Rind*, 1991], and can further influence climate locally and downstream [*Clark and Serreze*, 2000]. In addition, the positive snow-albedo feedback [*Dickinson*, 1983] can further amplify this impact as a strong forcing to the lower boundary of the atmosphere. Furthermore, snow melt in the spring may impact local soil moisture variability and further influence the local precipitation-soil moisture feedback in the following summer [*Cohen and Rind*, 1991].

Due to the significant effects of the continental snowpack, accurate snow simulation in a Land Surface Model (LSM) is critical to seasonal-interannual climate prediction and retrospective climate studies. However, inhomogeneous characteristics of continental snowpack on low resolution grids (roughly 100-200 km) makes it among the most difficult quantities to be modeled, especially during

accumulation and melt periods [*Zaitchik and Rodell*, 2008]. Inaccurate representation of snow within a LSM could lead to substantial errors in the atmospheric state in coupled simulations.

On the other hand, the degree to which the atmosphere responds to anomalies in snowpack in a consistent manner, particularly at daily to monthly time scales, can be referred to as the "snow-atmosphere coupling strength". This coupling phenomenon is a composite result of complicated interactions between numerous land and atmospheric processes and feedbacks, such as snow hydrology, surface albedo, snow sublimation and compaction, energy and water balance as well as atmospheric boundary layer development and moisture convection.

How are the snow cover and atmosphere coupled? To what degree does the atmosphere respond to anomalies in the snow cover, particularity at daily and seasonal time scales? How much would this coupling strength contribute to climate predictability? Quantifying and documenting the coupling strength of snow cover with climate is also important to seasonal climate prediction. An objective quantification and documentation of the coupling strength across the globe would be valuable to our knowledge of snow-climate interaction.

Inspired by the Global Land-Atmosphere Coupling Experiment (GLACE) [*Koster et al.*, 2006], we propose to utilize climate model and observation-based realistic snow information to study the snow-atmosphere coupling strength and its potential application to short range climate prediction. A series of experiments, the

Global Snow Atmosphere Coupling Experiment (SACE), aims to show the extent to which coupling strength varies between seasons, and more importantly, to characterize different regions as having relatively strong, intermediate, or weak coupling. The climate predictability due to improved representation of snow coupling will also be investigated for the later application in climate prediction.

CHAPTER 2. BACKGROUND

2.1 Snow in the climate system

As a key component of the cryosphere, snow cover modifies the thermal characteristics of land surfaces to modulate energy and moisture exchange with the atmosphere above it [*Cohen and Rind*, 1991]. Because of their strong thermal forcing to the lower atmosphere, snow cover anomalies potentially play an important role in climate fluctuations and predictability. In general, snow cover's influence on the local atmosphere can be separated into two categories: direct impact and indirect impact.

The direct impact includes:

- High reflectivity: Snow surface albedo ranges from 0.60 in wet and melting snow to greater than 0.85 for fresh new snow. Snow cover sharply increases the net surface albedo by 30-60%. The high albedo of snow cover dramatically reduces absorbed and net surface shortwave radiation.

- High emissivity: Snow also has a higher thermal emissivity than most other natural surfaces; it tends to increase the loss of longwave radiation over snow surface.
- Low thermal conductivity: Because a large fraction of the snow layer is filled with pockets of air, snow cover has an extremely low thermal conductivity. Snow cover acts as an excellent thermal insulator between the atmosphere and the ground surface to prevent the flux of heat out of the ground.
- Large latent heat sink: snow sublimation and melting require large amounts of latent heat (L_s=2.8337x10^6J/kg and L_m= 3.337x10^5J/kg respectively), acting as a large heat sink during the ablation season.

The first item is the most important, and is known as the snow albedo effect. It dramatically impacts the land surface energy budget and then influences air temperature, density, pressure, etc. Walsh et al. [1982] demonstrated that the presence of snow cover is associated with near-surface cooling of 5-10 K in the lower troposphere.

The indirect impact, also known as the snow hydrological effect, is a result of anomalous soil moisture from snowmelt that will later impact the atmosphere through land-climate interactions. However, very few studies have investigated this issue, partially due to the complicated snowmelt and runoff processes and the unavailability of accurate snow water content datasets. Quiring and Kluver [2009]

found the maximum snow depth during the previous winter shows a good correlation with soil moisture anomalies in the following summer, based on snowfall observations. Positive (negative) snowfall anomalies are associated with wetter (drier) than normal soil conditions during the summer (JJA) in the northern Great Plains. However, the strength of the relationship between winter/spring snowfall and summer soil moisture varies significantly over space and time, which limits its utility for seasonal forecasting.

Besides the direct and indirect snow effects, positive and negative snow-atmosphere feedbacks will further amplify or ameliorate anomalies. The feedback refers to the modification of a process or state by changes resulting from the process itself. Positive feedback will accelerate or amplify the process, while negative feedback will slow it down to reach equilibrium.

The most important positive feedback is the snow albedo feedback shown in Figure 2.1.a. Snow has the highest albedo in nature. This causes the land surface to reflect more of the incoming solar radiation. With warmer temperatures, the area of snow-cover decreases and land surfaces absorb an increasing fraction of solar radiation. This increase of total absorbed solar radiation contributes to continued and accelerated melting and warming. On the other hand, a colder climate will keep more snow cover and sustain lower air temperatures [*Wiscombe and Warren*, 1980].

Another important but less known negative (self-regulating) feedback is the snowfall-stability feedback, first suggested by Walland and Simmonds [1996]. With

the sudden increase in snow cover after a snow storm, the air temperature in the lower troposphere decreases and static stability of the atmosphere increases; this reduces the probability of subsequent snowfall; reducing snowfall further results in decreasing snow cover by snow sublimation and blowing snow event; decreasing snow cover at the land surface increases the sensible heating to the atmosphere and decreases the static stability, increasing the probability of snowstorms (figure 2.1.b). This negative feedback keeps the snow cover relatively stable over high latitudes in the winter.

2.2 Snow observation and monitoring

Accurate observations or monitoring of the snow cover across the globe has great potential applications to weather, climate and hydrology. Systematic measurements of snow depth at meteorological observation stations have been collected for over a century. At these stations, only the presence or absence of snow along with snow depth is measured on a daily basis by a snow stick or stake. Due to the sparseness of measuring stations, it is difficult to adequately capture the spatial variability of snow cover on a global scale. Furthermore, most of these observations are limited to snow depth, which is not suitable for snow modeling due to rapid gravity compaction. In other words, density can vary greatly, making it difficult to estimate the mass of water in the snow pack. Until the development of automatic stations like SNOTEL (**SNO**w **TEL**emetry) in recent decades, accurate real-time measurement of snow water equivalent (SWE) was not available. However, the

point measurements at stations can only give a potentially representative status in the given locality. Also, the snow extent or snow cover fraction (SCF) cannot be measured easily in-situ.

With developments in remote sensing, satellite-derived snow information has become an important alternative data source. Weekly snow mapping of the Northern Hemisphere using National Oceanographic and Atmospheric Administration (NOAA) National Environmental Satellite, Data and Information Service (NESDIS) data began in 1966 [*Robinson et al.*, 1993]. However, the coarse spatial resolution (1° over Northern Hemisphere) in the NESDIS data cannot well represent the patchy and shallow snow cover at middle-latitudes. In recent decades, the NOAA Interactive Multi-sensor Snow and Ice Mapping System (IMS) increased spatial resolution of snow maps to 24km [*Ramsay*, 1998]. Besides visible images, passive microwave SSMR-SMM/I [*Chang et al.*, 1987] and AMSR-E [*Chang and Rango*, 2000] also provide snow water estimation over the globe at low resolution, although the accuracy still cannot reach the requirements for many modeling applications.

With improvements in polar-orbiting satellites, the National Aeronautics and Space Administration (NASA) Earth Observing System (EOS) Terra satellite was launched on December 18, 1999 with a complement of five instruments, one of which is Moderate Resolution Imaging Spectroradiometer (MODIS). Besides the comprehensive observations of cloud, ocean, and earth surface characteristics

available from the Terra MODIS, a snow-cover product has been available since February 2000. With substantially improved spatial resolution (500m globally), high temporal frequency (daily), enhanced capability to separate snow and clouds [*Hall et al.*, 2001; *Hall et al.*, 2002b] due to more spectral bands (particularly in the short-wave infrared), as well as a consistently applied, automated snow-mapping algorithm [*Riggs and Hall*, 2002], MODIS provides quantitative monitoring of global snow extent, even in inaccessible regions such as the Tibetan Plateau (TP) and the Himalayas. In particular, the single satellite platform provides excellent consistency with MODIS snow data that are hard to obtain in previous satellite datasets.

It is still difficult to obtain a complete, accurate global SWE dataset only based on in-situ observations, due to limited observational stations with SWE measurements, as described earlier. Data assimilation incorporated with land surface models has proved to provide the best estimation of SWE by optimally merging observation and model information to minimize potential errors [*Pan et al.*, 2003; *Rodell et al.*, 2004].

2.3 Observational studies

Observational studies have demonstrated that regional scale snow cover anomalies are strongly linked with many large scale general circulation anomalies, such as summer monsoon onset and intensity [*Bamzai and Shukla*, 1999], lagged changes in the northern annual mode [*Thompson et al.*, 2000], typhoons over the

western Pacific [*Xie et al.*, 2005] and the outbreak of cold waves at middle-latitudes [*Vavrus*, 2007].

Over one hundred years ago, Blanford [1884] first suggested that the variability of continental snow cover might exert a thermal forcing on the land surface and consequently influence the Asian summer monsoon and its rainfall. Based on Blanford's Hypothesis, Walker [1910] found a negative correlation between Himalayan snow depth at the end of May and the amount of summer rainfall over India. Hahn and Shukla [1976] first used modern observations to confirm an apparent relationship between the Eurasian snow cover and Indian monsoon rainfall based on NOAA/NESDIS snow mappings derived from satellite visible imagery. There have been many empirical studies focused on this relationship between winter/spring snow cover and the Indian summer monsoon rainfall [*Hahn and Shukla*, 1976; *Dey and Kumar*, 1983; *Dickson*, 1984; *Parthasarathy and Yang*, 1995; *Sankar-Rao et al.*, 1996; *Yang*, 1996; *Bamzai and Shukla*, 1999; *Kripalani and Kulkarni*, 1999].

In particular, the snow cover over the Tibetan Plateau (TP) is believed to exert a significant influence on the summer rainfall over East Asia (EA). As EA is located in the downstream region of the TP, the snow cover anomalies over the TP could exert a stronger thermal forcing on the East Asian Summer Monsoon (EASM). Chen and Yan [1979; 1981] first found that positive snow depth anomalies over the Tibetan Plateau in boreal winter-spring are accompanied by above normal May-June

rainfall in southern China. Other observational studies [*Chen et al.*, 2000; *Wu and Qian*, 2003b], however, suggested a negative correlation between Tibetan winter snow depth and subsequent summer precipitation over southern China, but indicated a positive correlation over the Yangtze River Basin (YRB). Chen and Wu [2000] obtained positive correlations over the Yangtze River region but negative correlations in South China for JJA. It has also been found that the correlation of rainfall with the Tibetan Plateau winter snow depth has a pronounced change from July to August and the correlation for JJA rainfall differs from that for May-June [*Chen and Wu*, 2000]. Although the snow cover connection with EASM is not very robust, snow cover is applied as one of four key predictors besides ENSO, subtropical high, and blocking for short range climate prediction at National Climate Center of China [*Zhao*, 1999; *Xu and Li*, 2010].

Aside from the monsoon, other linkages between snow cover and atmospheric circulation have been discovered by numerous observation studies. Studies show that excessive summer-autumn snow coverage over Eurasia favors unusually cold winters over Europe and US, due to forcing of the negative phase of Arctic Oscillation [*Cohen and Entekhabi*, 1999]. Subsequent studies confirmed the physical mechanism of this relationship [*Saito et al.*, 2001; *Gong et al.*, 2002; *Cohen and Saito*, 2003; *Gong et al.*, 2004a]: early-season snow cover anomalies trigger vertically propagating planetary waves that quickly alter the stratospheric polar vortex. These observational linkages between snow cover and atmospheric

circulation have motivated efforts for seasonal climate forecasts based on snow anomalies.

In addition to being a climate predictor, snow cover also has profound ecological and societal impact on the hydrosphere since snowpack strongly affects the underlying soil temperature and local river runoff. Groisman et al. [1994] found a retreat of North American springtime snow associated with strong warming. The extent of boreal snow during spring was significant lower during the 1990s than at any time in the previous century [*IPCC*, 2007]. Barnett et al. [2005] concluded future water supplies may be hindered in a warmer climate with less snowfall and earlier melting. In the background of global warming, how the snow cover will change is a challenging scientific question.

2.4 Numerical simulations

Atmospheric general circulation models (AGCMs) coupled with various LSMs are popular tools for examining the snow-atmosphere interaction studies, largely because the numerical model can be easy manipulated via deliberate changes to physics processes or parameterizations in controlled experiments. Numerical simulations also provide a method to explore the climate system with some extreme snow situations that could not happen in nature.

Various GCM modeling studies [*Barnett et al.*, 1988; *Vernekar et al.*, 1995; *Dong and Valdes*, 1998; *Bamzai and Marx*, 2000; *Dash et al.*, 2005] have been conducted to support the snow-monsoon inverse relationship first suggested by

Blanford [1884]. These studies indicate the GCMs are able to reproduce an inverse snow-monsoon relationship and snow cover and snow mass impact on climate on a seasonal time-scale. Ferranti and Molteni [1999] investigated the effect of springtime snow conditions over Eurasia on the monsoon circulation by using ensemble simulations. The results suggested Eurasian snow depth is probabilistically predictable, and that it does influence the seasonal-mean monsoon independently of the ENSO phase. As a result, proper observations and simulations of the Eurasian snowfield can provide an additional and independent contribution to monsoon prediction.

Several prior studies have attempted to quantify the snow role in the cold region climate [*Walsh et al.*, 1985; *Watanabe and Nitta*, 1998; *Gong et al.*, 2004b; *Vavrus*, 2007]. However, those earlier works have been limited in spatial and temporal extent. Prescribed excessive or deficient snow over a specific region, such as Eurasia, Siberia etc., has been investigated based on the observed fluctuation over monthly to seasonal time scales.

Due to the limitation and imperfections of snow schemes in land surface models, some simulation studies get conflicting results, even with the same model. For example, Zhang and Tao [2001] created a conceptual model to explain the possible mechanism on the impact of the in-phase change of snow cover over the TP with the EASM and summer rainfall over Yangtze River Basin. They further verified their conclusion by model simulations with excessive/deficient snow depth in the

winter. However, with the same IAP-9L AGCM model and the updated snow data, Li and Chen [2006] obtained an opposite result.

2.5 Global land atmosphere coupling experiment

Koster et al. [2002] designed a prototype of a numerical experiment to examine and quantify the strength of the coupling between the land and atmosphere; specifically, the degree to which precipitation-induced soil moisture anomalies affect the overlying atmosphere. This experiment essentially consists of one control ensemble experiment with initialized land surface anomalies compared with another ensemble experiment where the land state is specified identically in each ensemble member. The differences in atmospheric behavior between the two experiments indicate the degree to which the state of the land surface controls atmospheric processes. Based on this prototype, 12 weather and climate models participated in the Global Land Atmosphere Coupling Experiment (GLACE) to investigate land-atmosphere coupling characteristics [*Guo et al.*, 2006; *Koster et al.*, 2006]. Despite notable differences among the 12 models, some common features, "hot spots" of land-atmosphere coupling, were identified. The GLACE experiment provides an approach for testing land-atmosphere coupling strength that cannot be directly investigated by observational studies. The principles underlying the GLACE experiment could also extend to other coupling phenomena, such as snow atmosphere coupling.

2.6 Summary

In summary, snow cover is an integral component of the earth climate system. Observational studies have demonstrated strong snow impacts and interaction with local weather and climate through both radiative and hydrological effects. The numerical simulations provide a "virtual lab" to study snow-climate interaction. Pervious numerical experiments illustrated some key aspects of snow–atmosphere-coupling behavior even though these couplings and interactions are difficult to investigate by only observation-based studies. However, some fundamental questions about snow-atmosphere coupling are still unanswered. Inspired by GLACE [*Koster et al.*, 2006], we expand the GLACE-type experimental framework to investigate snow-atmosphere coupling strength and its potential application to short range climate prediction.

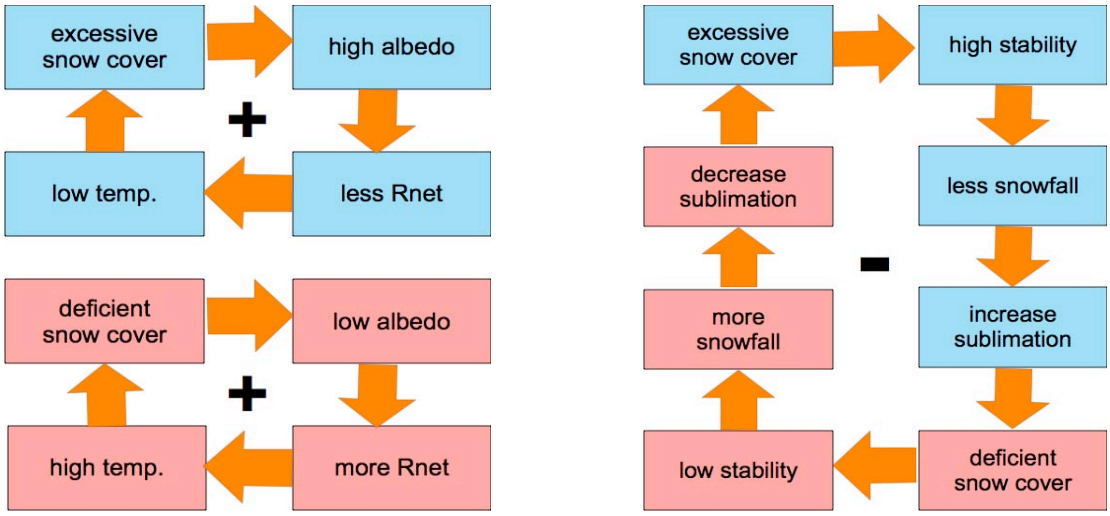

a. Positive feedback b. Negative feedback

Figure 2.1 A schematic for snow albedo effect (left) and snowfall-stability feedback (right).

CHAPTER 3. SNOW ATMOSPHERE COUPLING EXPERIMENTS

3.1. Key questions

3.1.1 snow-atmosphere coupling and predictability

Although previous studies have demonstrated strong snow impact and interaction with local and even remote climate, some key scientific questions remain:

- **How strong is the snow-atmosphere coupling?**
- **To what degree does the atmosphere respond to anomalies in the snow cover?**
- **Where and when does the atmosphere respond most strongly to snow anomalies?**
- **What is the relative importance of the snow direct impact (albedo effect) and indirect impact (hydrological effect)?**

Quantifying and documenting the coupling strength of snow cover with climate is also important to seasonal climate prediction.

- **How do snow cover anomalies affect local and remote weather and climate?**
- **How much would snow-albedo feedback and the hydrological effect contribute to climate predictability?**

An objective quantification and documentation of the coupling strength across the globe would be valuable to our knowledge of snow-climate interaction. Determining how snow anomalies contribute to seasonal forecast skill will improve our understanding of climate predictability.

3.1.2 Snow Water Equivalent vs. Snow Cover Fraction

Snow Water Equivalent (SWE) is the equivalent water volume per unit area, or depth of standing water, that snow cover would produce if melted immediately. The Snow Depth (SD) is the thickness of the snow cover sitting on the ground. SD is an alternate variable to SWE in some LSMs, equal to the SWE divided by the snow density. Snow Cover Fraction (SCF) is defined as the fractional area of a region covered by snow of any depth. In an LSM, the region is defined as each grid cell.

The limited meteorological observational stations provide SD or SWE measurements four times daily across the globe for weather and climate services. However, it is still difficult to obtain a complete, accurate global SWE dataset only based on in-situ observations, due to the limited number of observation sites and the inhomogeneous characteristics of snow distribution. In addition, difficulties in obtaining representative SCF information by in-situ measurement have also been

intensively discussed [*Robinson et al.*, 1993; *Brown*, 2000]. However, SWE and SCF are two key variables in any snow scheme or model.

Generally, SWE or SD is a prognostic variable in any LSM, which is explicitly calculated by the snow water balance equation at each grid:

$$\frac{dW}{dt} = P + E - M \qquad \text{EQ. 1.}$$

where *dW/dt* is the snowpack water mass change rate (positive for accumulation); *P* is the snowfall rate and *M* is snow melting rate; *E* is the sum of sublimation and evaporation rate at the snow surface, which may contribute either positively or negatively to the snow mass balance. In the snow ablation phase, generally from later winter to spring, snowmelt will generate soil moisture anomalies.

Snow cover fraction, however, is always a diagnostic variable that is obtained only by parameterization. SCF parameterizations usually are a function of SWE or SD, and can vary from model to model. In the default snow scheme of CLM 3.0, the relationship between snow cover fraction and snow depth in each grid is:

$$f_{snow} = \frac{Z_{snow}}{10Z_{om,g} + Z_{snow}} \qquad \text{EQ. 2.}$$

where f_{snow} and Z_{snow} are the snow cover fraction (%) and the snow depth (m) and $Z_{om.g}$=0.01 is the momentum roughness length for bare soil (Dai et al. 2004, section 7.2).

Figure 3.1 shows the snow cover fraction observed from MODIS with respect to in-situ snow observations over the Tibetan plateau, where the snow anomalies are believed to exert an important forcing to the Asian monsoon (Wu et al. 1997; Wu et al 2003). The blue error bars show the observational range of snow cover fraction (%) for different depths of snow. The green dotted line indicates the computational result from the parameterization of CLM 3.0. Due to the high elevation of this largest plateau in the world, even shallow snowpack can persist for relatively long periods. The parameterization from CLM 3.0 seriously underestimates snow cover fraction over the Tibetan Plateau. Furthermore, observed snow cover fraction varies greatly even for the same snow depth. In shallow snow pack, the SCF ranges from near 30 to 100 percent. The range of the variability of SCF generally decreases with increasing SD until the snow depth reaches 15cm, where almost all land is buried by snow.

A new improved SCF parameterization has been developed for CLM 3.5 by Niu and Yang (2007), which uses the snowpack density to account for the large-scale depletion pattern and its temporal variability:

$$SCF = \tanh\{\frac{h_{sno}}{2.5 * Z_0(\rho_{sno} / \rho_{new})^{\alpha}}\} \qquad \text{EQ. 3.}$$

where h_{sno} and Z_0 are the spatially averaged snow depth (rewritten to be a function of SWE and snow density) and the ground roughness length, respectively. ρ_{new} is a prescribed fresh snow density with adjustable values depending on local conditions. ρ_{sno} is the model calculated snow density. The curve shape parameter α is tunable

and assumed to be controlled by several factors including scale and, hypothetically, grid-specific geographic properties such as vegetation and orographic variability. The value 2.5 in this equation is a tunable parameter, but it is usually assumed to be a constant for simplicity. This new parameterization depends on fresh snow density that is highly variable in different regions and needs to be calibrated on the basis of field measurements.

The left panel in Figure 3.2 shows the curves of snow cover fraction with snow depth from the parameterization of CLM 3.5 [*Niu and Yang*, 2007] with different fresh snow densities from 100 kg/m^3 to 400 kg/m^3. Compared with the default CLM 3.0 parameterization, the new formula greatly reduces the underestimation of SCF, especially when the snow depth is above 20 cm. The change of snow cover fraction with the snow depth (*df/dh*) is an important parameter for indicating the variability of the snow albedo effect since the albedo of a grid box is a linear function of snow cover fraction within all land surface models. The sensitivity of SCF to SD is most serious for shallow snow and generally becomes insensitive at large snow depth. This sensitivity also strongly depends on the snow density (Figure 3.2.b). As the snow ages, the snow density increases and sensitivity decreases for the same snow depth.

Both parameterizations could only represent the monotonic relationship between the snow depth and snow cover fraction. In reality, however, the snow cover fraction variability is large for most snow depths. The SCF depends on

numerous factors, including elevation, slope and aspect, wind, sunshine, etc. However, the small inaccuracies in this parameterization could trigger huge errors in SCF that quickly cascade into larger inaccuracies in albedo, net radiation, energy exchange and finally on atmospheric conditions. Consequently, these errors can lead to serious uncertainty in seasonal to inter-annual climate prediction.

Finally, the ground albedo is linear function of snow cover fraction:

$$\alpha_g = f_s * \alpha_s + (1 - f_s) * \alpha_{bg} \qquad \text{EQ. 4.}$$
$$= f_s(\alpha_s - \alpha_{bg}) + \alpha_{bg}$$

Where α_g is net surface albedo for the ground; f_s is the SCF; the α_s and α_{bg} are albedos for snow and the snow-free background land surface respectively. The snow albedo effect is strongly controlled by the SCF.

In this study, we pioneer the utilization of observed SCF information to replace the SD-SCF parameterization and to study the separate impacts of prescribed SWE and SCF on the atmosphere, based on observations or reanalysis data. Under the assumption that the snow hydrological effect is initiated by the snowmelt in spring and the snow albedo effect is linear function of SCF, the snow albedo effect and hydrological effect could be careful separated in the experiment design.

3.2 Model setup

The recent stable version of the NCAR Community Atmospheric Model (CAM) v 3.6.48 coupled with Community Land Model (CLM) is chosen as the main study model. The land component, CLM 3.5 (Oleson et al. 2008), is a so-called "third generation" land surface model that explicitly represents the role of carbon and nitrogen in photosynthesis, unlike "the second generation" models that are built only with the explicit description of soil and vegetation processes involved in the surface energy and water budgets. CLM 3.5 employs 10 soil layers to resolve soil moisture and temperature dynamics and uses plant functional types (PFTs) to represent sub-grid vegetation heterogeneity.

The CLM model has up to 5 layers of snow depending on total SD, and accounts for processes such as liquid water retention, diurnal cycling of thawing-freezing, snow-melting, surface frost and sublimation. This multilayer approach is found to significantly enhance the simulation quality, correcting the previously underestimated snow mass and early time of melting that was obtained in a single layer model [*Dai et al.*, 2003]. Heat and water are transported between adjacent snow layers, also between the top layer and the overlying canopy and/or the atmosphere. CLM applies a two-stream approximation for radiative transfer calculations over the snow surface. Snow albedo is based separately on the diffuse and the direct radiation and also on snow age [*Oleson et al.*, 2004a]. Snow layers may be combined or divided every time step to ensure a realistic representation of

snow physics and numerical stability. The CLM also explicitly incorporates densification processes (e.g., destructive or equi-temperature metamorphism, compaction by snow overburden, and melt metamorphism). The vegetation effect is accounted for in snow accumulation, melt, interception, through-fall and canopy drip. CLM calculates the water transfer between snow layers, infiltration, runoff, and subsurface drainage, although water vapor transport within the snowpack is neglected.

The model is set up as shown at Figure 3.3. The atmosphere is fully coupled with the land surface component. The energy, mass and momentum fluxes are exchanged between land and atmosphere at each time step. The ocean and sea ice components are prescribed by the climatological cycle or from an observed dataset. The dynamic vegetation parameterization is turned off in the LSM for these experiments.

In this study, we choose the finite-volume dynamical core (FV dycore) version of CAM that was originally developed during the 1990's at the NASA Goddard Space Flight Center [*Lin and Rood*, 1997]. FV dycore shows some benefits for numerical simulation compared with traditional finite difference or spectral methods. FV dycore is also more convenient to scale with parallel computation. The pure spectral approach, due to its costly transforms, is known not to scale well with horizontal resolution. The finite-volume approach completely conserves dry air mass and the mass of transported atmospheric constituents such as water vapor,

which is particularly important for climate simulations due to their long integration times, and imperative for accurate representation of chemical interactions in climate/chemistry simulations. In addition, the FV dycore greatly improves the simulation of sharp gradients, which usually cannot be handled well in the finite difference and spectral methods.

3.3 Global snow data

In spite of snow cover being important to climate modeling, in-situ snow observations are very limited over the world, mainly restricted to snow depth at weather and hydrological stations. High-quality continental-scale SWE data sets are not available, although they would be so important for climate research and water resources management. In addition, snow cover fraction cannot be measured easily in-situ, only estimated by remote sensing.

Since neither observations nor LSMs alone are capable of providing adequate information about the temporal-spatial variability of continental snow pack, it becomes necessary to combine their information through Data Assimilation (DA) algorithms, such as ensemble Kalman filters [*Evensen and van Leeuwen*, 1996]. Data assimilation algorithms use the information from discontinuous observations by integrating them into a numerical model. The physics-based LSMs provide a continuous quantity to monitor the evolution of modeled variables. The observation system provides reliable, independent information on a variable that the model simulates imperfectly, preventing model drift and improving the accuracy of the

simulation. Such assimilation can effectively reduce uncertainties in estimation through optimally combining the information from both LSMs and observations.

In this study, we pioneer utilization of the most recent advancements in snow remote sensing technology and the Global Land Data Assimilation System (GLDAS) to study the snow-atmosphere coupling and predictability. Detailed information is provided below:

3.3.1 MODIS SCF

NASA's Earth Observing System (EOS) Moderate Resolution Imaging Spectroradiometer (MODIS) instrument provides the capability to observe snowpack based on a Normalized Difference Snow Index (NDSI), along with threshold tests, to provide global, automated binary maps of snow cover. This method takes advantage of the spectral differences of snow versus other features in short-wave infrared and visible spectral bands to identify the area of snow cover. In addition, the cloud-distinguishing algorithm in MODIS greatly reduces the cloud-snow confusion that could not be eliminated in previous NOAA satellite snow maps. In the most recent advance in MODIS snow monitoring, a new algorithm can estimate the fraction of snow within a 500m MODIS pixel and thereby enhance the monitoring of fractional snow cover (Salomonson and Appel, 2003). The evaluation of MODIS snow maps against in-situ observations indicate robust accuracy globally (Hall et al. 2001; Hall et al. 2002), and even relatively high accuracy over the Tibetan

Plateau, where traditional observations are almost impossible to obtain due to the harsh environment (Pu et al 2007).

With MODIS 500m pixel monitoring, MOD10C2-v4 products derived SCF at 0.05° climate modeling grids (CMG). Three parameters are provided in each CMG grid, including snow cover fraction, cloud fraction and confidence index (CI).

The snow cover fraction (SCF) or snow percent in each CMG grid is defined as

$$f_{snow} = \frac{n_{snow}}{n} * 100 \qquad \text{EQ. 5.}$$

where n is the total number of pixels in this CMG grid:

$$n = n_{snow} + n_{clear\_land} + n_{cloud\_obscured} + n_{unknown} \qquad \text{EQ. 6.}$$

n_{snow} is the total number of pixels identified as snow in this grid, n_{clear_land} for snow-free land, $n_{cloud\_obscured}$ for cloud and $n_{unknown}$ for other types of land.

The fraction of the CMG grid obscured by cloud is

$$f_{cloud} = \frac{n_{cloud\_obscured}}{n} * 100 \qquad \text{EQ. 7.}$$

The Confidence Index (CI) is defined as the fraction of all pixels determined to be cloud-free land

$$CI = \frac{n_{snow} + n_{clear\_land}}{n} * 100 \qquad \text{EQ. 8.}$$

which is an index to express the confidence of information based on the number of valid observations available in this CMG grid.

The cloud mask in MODIS is a "double-edged sword". It has greatly enhanced the ability of MODIS to distinguish cloud from snow and significantly reduced error. However, it also increases the cloud obscuration count, which cannot provide any snow information below the cloud. In the daily snow map, a large portion of the globe is obscured by cloud (cloud fraction range from 0-50% depending on the season). To minimize loss of data due to cloud obscuration, 8-days composited snow maps (MOD10C2) are used this study.

The expected value of SCF under cloud obscuration [*Brubaker et al.*, 2005] is

$$E(SCF) = \frac{1}{3}(f_{snow} + \frac{f_{snow}}{CI} + f_{snow} + f_{cloud}) \qquad \text{EQ. 9.}$$

and the standard deviation:

$$Var(SCF) = \frac{1}{18}[f_{snow}^2 + (\frac{f_{snow}}{CI})^2 + (f_{snow} + f_{cloud})^2 - f_{snow}\frac{f_{snow}}{CI} - \frac{f_{snow}}{CI}(f_{snow} + f_{cloud}) - (f_{snow} + f_{cloud})f_{snow}]$$

EQ. 10.

We aggregate daily 0.25° MODIS snow cover fraction into the FV 1.9x2.5 grid by box averaging.

3.3.2 GLDAS SWE

Observationally based global snow water equivalent maps are still unavailable. SWE retrieved by microwave scattering signatures over snowpack from the NASA Advanced Microwave Scanning Radiometer (AMSR-E) may provide useful information about snowpack. However, sensitivity to weather conditions (such as atmospheric water vapor) and snow evolution (mainly grain size growth and

densification) make passive microwave retrievals still unable to satisfy the accuracy required for land surface models or hydrological models (Zhang et al. 2005).

With advancements in remote sensing, land surface modeling and data assimilation in recent years, NASA Global Land Data Assimilation System (GLDAS) [*Rodell et al.*, 2004] provides a potentially useful estimation of SWE over the globe. The goal of the GLDAS is to generate optimal fields of land surface states and fluxes by using advanced land surface models and data assimilation techniques with satellite and ground based observational data. GLDAS has reanalyzed key land surface states and fluxes using several different land surface models by constraining them with all available observational data from 1979 to present, emphasizing the satellite retrievals from NASA.

Compared to offline simulations, such as the Second Global Soil Wetness Project (GSWP-2) [*Dirmeyer et al.*, 2006] data set, GLDAS applied two constraints to optimally merge model and observation data to obtain the best estimates. First, by forcing the land surface models with observationally based meteorological fields, bias on the atmospheric model-based forcing can be avoided. Second, by employing data assimilation techniques, observations of land surface states can be used to curb unrealistic model state. It has a longer period than the GSWP-2 data set, which only covers 1986–1995.

In this study, 1x1 degree, 3-hourly output from a 1979-present run of the same CLM model driven by GLDAS forcings is used. The usefulness of the GLDAS

data set has been demonstrated in weather and sub-seasonal forecasts [*Koster et al.*, 2004; *de Goncalves et al.*, 2006]. Although the quality and accuracy of SWE information from GLDAS has only been validated at few sites, the observationally based atmospheric forcing and available remote sensing snow information make the GLDAS output useful for providing global SWE information at daily time scales [*Zaitchik and Rodell*, 2008] .

3.4 The experiment design

Inspired by the GLACE-I project [*Koster et al.*, 2006], this global Snow Atmosphere Coupling Experiment (SACE) aims to show the extent to which coupling strength varies between seasons, and more importantly, to characterize different regions as having relatively strong, intermediate, or weak coupling, for later application in climate prediction.

We have designed a series of experiments to quantify and document the coupling strength of global snow cover variation and atmospheric conditions. In a climate model, the degree to which the atmosphere responds to anomalies in snowpack (the "coupling strength") is a composite result of complex interactions between numerous snow processes, such as snow persistence, surface albedo, sublimation and compaction, as well as boundary layer development and moisture convection. We will also utilize MODIS SCF retrievals and GLDAS SWE estimates to study the albedo effect and hydrological effect separately and investigate their maximum potential contribution to the short-range climate predictability.

3.4.1 Experiments

In this series of ensemble experiments, each ensemble run will include ten 6-month simulations from March 1st to August 31st (figure 3.4). Since snow cover in the NH is generally at a maximum in March and gradually depletes through May and June, the snow albedo effect is mainly concentrated during spring and the snowmelt hydrological effect contributes mostly after snow depletion. To concentrate only on the snow-atmosphere coupling and eliminate the possible noise from ocean, all ensemble experiments are forced by the same climatological SST cycle from Hadley Centre SST data set [*Rayner et al.*, 2006] .

The first ensemble experiment, called **Control** (the same as the ensemble **W** in GLACE-I), is a typical climate simulation where sea surface temperatures are prescribed at all time steps to climatological annual cycle (to eliminate possible ENSO effects). The 10 different atmosphere and land initializations are obtained from model restart files at March 1st from 2000 to 2009 from an Atmospheric Model Inter-comparison Project (AMIP, [*Hurrell et al.*, 2008]) style simulation (detailed information about land and atmospheric initial conditions is described in the following section). In each simulation, the LSM is fully coupled with the AGCM without any constraints. The global grids of the prognostic variable SWE and diagnostic SCF are recorded into a special data file (**S**_state) at every model time step (Figure 3.5 Part 1). Because of the chaos in the climate system, the snow states

in the different simulations in this **Control** experiment will evolve differently to reflect the potentially broad range of snow states that are consistent with system.

In the remaining ensemble experiments (**ModBoth**, **RealSCF**, **RealSWE**, **RealBoth** and **RealClim**), all atmosphere initial and SST boundary conditions are the same as the first **Control** experiment. However, the original snow states (SCF and SWE) in the model are replaced. Initial soil moisture is unified to the model climatological mean values in the **ModBoth**, **RealSCF**, **RealSWE** and **RealBoth** experiments to isolate the snow hydrological effect (details see sect. 3.4.2).

In the second ensemble experiment, named **ModBoth** (Model Both, similar to ensemble **R** of the GLACE experiment), all member simulations are forced to maintain precisely the same time series of key snow states (the S1_state SWE and SCF) taken from one randomly chosen ensemble member in the **Control** experiment (Figure 3.5 Part 2). To achieve this, the snow states in each simulation are read from the previously recorded S1_state file. Koster et al. [2002] demonstrate that the choice of the ensemble member used to write S1_state is not important (at least for the one model examined); for the global average, any ensemble member should produce approximately the same results in the later months of the experiment. Since all ensemble members in **ModBoth** are forced to have identical model-generated SWE and SCF, the atmospheric variability contributed by atmosphere internal chaos versus snow state can be well quantified.

The third experiment, **RealSCF** (realistic snow cover fraction) is similar to the experiment **ModBoth** except the SCF in the ten ensemble members are read from gridded observed MODIS SCF from 2000-2009 (Figure 3.5 Part 3). Each ensemble member takes specified realistic surface SCF that is prescribed by the remote sensing retrieval from MODIS. In the meantime, the SWE at each time step is still read from the same S1_state data file written by one of member **Control**. The main purpose of **RealSCF** is to investigate how the simulation is improved by using realistic SFC without parameterization. Since ground albedo is a linear function of SCF and all ensemble members are forced by same SWE, the **RealSCF** experiment could precisely quantify the atmospheric variability contributed only by snow albedo effect. Opposite to **RealSCF**, all members in experiment **RealSWE** (realistic Snow Water Equivalent) are prescribed to have the realistic SWE obtained from NASA Global Land Data Assimilation System (GLDAS) from 2000-2009 but with same SCF read from S1_state (Figure 3.5 Part 4). Since the initial soil moisture of each ensemble member is set to the climatological mean (for details, see next section) and SCF are forced to same S1_state, the snow melt contribution to soil moisture anomalies can emerge and the atmosphere variability via the snow hydrological effect can be separately investigated.

Note that the SCF and SWE could be inconsistent at some locations and times in experiments **RealSCF** and **RealSWE**, especially where S1_state disagrees with MODIS or GLDAS about the presence of snow. Although these kinds of

inconsistencies happen, the model will self adjust the snow state and converge toward the observed value by continuous insertion of realistic snow information. Inconsistencies like this would happen most in middle-latitude regions where snow is unstable and not well simulated by model. Based on the comparison of independent SCF from MODIS and SWE from GLDAS, there are only 2% of grid points across the globe where SWE is equal to zero but the SCF is larger than zero, or vice versa, during the ten-year period from 2000 to 2009. There are no serious impacts on the high latitude regions where snow is stable and well simulated by CLM model.

In the fifth ensemble experiment **RealBoth** (realistic Both), each ensemble member has imposed both realistic SCF and SWE (Figure 3.5 Part 5). This experiment examines the impact of realistic snow on the atmospheric variability by well representing both the snow albedo effect and the hydrological effect.

In the last experiment named as **RealClim** (realistic climatology), the SCF and SWE are replaced by the climatology values at each time step, based on MODIS SCF and GLDAS SWE during 2000-2009. The model configuration, initial field (both atmosphere and land) and SST forcing are same as **RealBoth**. This will effectively remove the inter-annual variability of snow boundary forcing. In other words, the atmosphere is uncoupled with snow boundary.

In these experiments, we ignore the small amount of snow intercepted by the canopy although the CLM 3.5 has a greatly improved snow scheme with respect to

vegetation. Snow through-fall can easily submerge below vegetation, greatly changing the albedo and roughness of the surface. Moreover, intercepted snow on a forest canopy has a large exposed surface area for sublimation, moistening and cooling the air, whereas snow on the ground below the canopy is sheltered. We don't know how much would be the impact on model results by ignoring snow within canopy.

3.4.2 Model run specifications

The criterion for the initial conditions of the ensembles is to sample the possible range of snow (or land) and atmosphere states. The snow initializations are not allowed to be artificially similar. The CAM model is run in multi-decadal AMIP style simulations (forced by observed SST) from 1991 onward to extract 10 different restart initial fields of land and atmosphere states at 1 March for 2000 to 2009. Land initial fields obtained from this multi-decadal run should be spun-up as they are nine or more years from the start of the integration.

Since we try to isolate the snow hydrological effect, soil moisture in each land initial field is unified in all ensemble members to the model climatological mean values (based on 2000-2009) in the **ModBoth**, **RealSCF**, **RealSWE** and **RealBoth** experiments. Snowmelt in spring will suddenly increase the water infiltrating into soil until the underlying soil become saturated. Until the top layer soil thaws and becomes permeable, the melt water will form surface runoff and discharge directly into the rivers. The SWE before melt is critical for the hydrological modeling of

snowmelt. The soil moisture anomalies in these experiments will be initially triggered by the snowmelt, then feedback to the atmosphere forming a positive moisture-evaporation-precipitation feedback. If we define the snow hydrological effect to include all composite climate effects due to snowmelt infiltration into soil and then consequent soil moisture-evaporation-precipitation feedbacks, the **RealSWE** experiment can well isolate the climate impact due to hydrological effect by excluding the impact of albedo.

Note that given this design of the experiments, the initialization of snow states for **ModBoth**, **RealSCF**, **RealSWE** and **RealBoth** is actually irrelevant because these snow states will be replaced after first step during model integration. Note also that in all the cases, the atmosphere may feel a "shock" at the beginning of simulations because initially it is not in equilibrium with the prescribed surface state [*Koster et al.*, 2006].

One other problem may occur in the prescribed snow experiment (Such as **RealSCF**, **RealSWE** and **RealBoth**): a relatively warm initial model surface temperature may encounter a prescribed realistic observed snow that will cause rapid snowmelt and dramatically increase the runoff. To eliminate this phenomenon, when snow is present in the initial field we prescribe the soil temperature at the top soil layer to be below the freezing point. With integration of the model, the soil temperature profile will quickly adjust to reach equilibrium.

In the **ModBoth**, **RealSCF**, **RealSWE** and **RealBoth** experiments, it is not necessarily to maintain a strict energy and water balance below the snow interface. However, the energy and water fluxes that cross the coupled interface to and from the atmosphere are still exactly conserved; only the land reservoir is not conserving. Since we focus on the sensitivity of the atmosphere response to the anomalous snow states, the un-conserved land energy and water balance is acceptable.

3.5 Key diagnostics and analyses

We focus mainly on air temperature and precipitation in this study, using subscripts T and P to indicate those variables accordingly. To examine the mechanism of snow-atmosphere coupling, we also analyzed evaporation, sublimation, boundary layer height, surface pressure etc. in the some experiments. In the simulations, the model captures diurnal variations since we forced it at each time step. In the computation and analysis, however, we only use daily mean time series and focused on the daily to monthly time scales of snow-atmosphere coupling. The key diagnostics and analysis are listed here.

3.5.1 Ω Index

For key atmospheric variables, the "level of agreement" across ensemble members of the time series can be determined. The comparison of these levels of agreement obtained from different ensembles will allow the snow's impact on the atmosphere (SCF, SWE or both) to be directly and objectively quantified. A

diagnostic index Ω derived by Koster et al. [2006] will be used to quantify the coupling strength by the phase and shape similarity of a forecast ensemble.

For one variable's ensemble simulation time series $X_{i,j}$ (where i=1,2,…,m is ensemble member, j=1,2,…,n is time , following the notation from [*Yamada et al.*, 2007]), the ensemble mean b_j at time *j*:

$$b_j = \frac{1}{m}\sum_{i=1}^{m} X_{i,j} \qquad \text{EQ. 11.}$$

and the full ensemble mean over time:

$$\bar{x} = \frac{1}{n}\sum_{j=1}^{n} b_j \qquad \text{EQ. 12.}$$

can be computed accordingly. Ω is defined as:

$$\Omega = \frac{m\sigma_b^2 - \sigma^2}{(m-1)\sigma^2} \qquad \text{EQ. 13.}$$

where σ^2 and σ_b^2 are the full-sample variance and temporal variance of the ensemble mean respectively

$$\sigma_b^2 = \frac{1}{n}\sum_{j=1}^{n}(b_j - \bar{x})^2 \qquad \text{EQ. 14.}$$

$$\sigma^2 = \frac{1}{mn}\sum_{i=1}^{m}\sum_{j=1}^{n}(x_{i,j} - \bar{x})^2 \qquad \text{EQ. 15.}$$

Theoretically, if all the ensemble members have identical time series, σ_b^2 will be equal to σ^2 and Ω will be 1. On the other extreme, if the ensemble time series are

completely uncorrelated, σ_b^2 will equal to σ^2/m and Ω will be 0. Without sample error, the index Ω varies from 0 to 1, with larger values indicating a greater degree of similarity.

Under the assumption that both boundary forcings and atmospheric chaos contribute to the value of a meteorological variable at a given time step, Ω is equivalent to the square of the correlation coefficient between the variable and the forcing [*Yamada et al.*, 2007]. On the other hand, Ω, mathematically, is associated with two quantities: the average value of the anomaly cross correlation coefficient (ACCC) and the average value of the variance ratio (AVR). The statistical characteristics of Ω reflect both phase similarity (correlation) and shape similarity (mean value and amplitude).

Figure 3.6 shows an idealized time series of atmospheric states for different ensemble members under four situations: (a) low temporal variability σ and low similarity Ω ,(b) low variability σ and high similarity Ω,(c) high variability σ and low similarity Ω and (d) high variability σ and high similarity Ω. Clearly, in the high Ω cases, the atmosphere would show "robust" responses to the snow boundary forcing across the ensemble members. On the other hand, when the atmosphere is insensitive to snow, the time series of meteorological variables are different as shown in the low Ω cases.

To study air temperature coupling with snow cover in March, for example, we could compute the Ω_T(Control) and Ω_T(ModBoth) for daily mean temperature at

2m height from March 1st to 31st (the subscripts T indicates Temperature). The Ω_T(Control) represents the fraction of temperature variance across ensemble members that is "explained" (forced) by both initial and boundary (SST) conditions. Since the snow and atmosphere are freely coupled without any constraint in each ensemble member, Ω_T(Control) should be relatively low compared to other experiments. Due to forcing each ensemble member to the same SWE and SCF, however, Ω_T(ModBoth) should show relative larger values indicating that the air temperature shows a more "robust" response to the prescribed snow boundary conditions. The difference Ω_T(Control)-Ω_T(ModBoth) shows the suppression of temperature variance by eliminating the free snow-atmosphere coupling, indicating regions where the snow-atmosphere coupling is strong.

Similarly, Ω_T(RealSCF)-Ω_T(ModBoth) will indicate the snow-atmosphere coupling strength due to the snow albedo effect, since both experiments are forced to the same SWE. On the other hand, Ω_T(RealSWE)-Ω_T(ModBoth) indicate the snow-atmosphere coupling strength due to the snow hydrological effect since both experiments are forced to the same SCF.

3.5.2 Signal-to-Total Ratio (STR)

Based on the ensemble simulation, Signal-to-Total Ratio (STR) will be used to diagnose the predictability associated with the coupling strength. Let the same ensemble matrix be X_{nk}, where k is time and n is the ensemble member (following the notation from [*DelSole and Tippett*, 2008]). Then the forecast mean is:

$$\tilde{\mu}_f(k) = \frac{1}{N}\sum_{n=1}^{N} X_{nk} \qquad \text{EQ.16.}$$

The Grand or Climatological mean is:

$$\tilde{\mu}_c = \frac{1}{NK}\sum_{k=1}^{K}\sum_{n=1}^{N} X_{nk} \qquad \text{EQ.17.}$$

The difference between the ensemble mean and climatological mean is the estimated signal. The estimated signal variance is:

$$\left\langle (\tilde{\mu}_f - \tilde{\mu}_c)^2 \right\rangle = \frac{1}{K}\sum_{k} (\tilde{\mu}_f(k) - \tilde{\mu}_c)^2 \qquad \text{EQ. 18.}$$

The difference between an individual member and its corresponding ensemble mean is called the noise. The estimated noise variance is:

$$\left\langle (\hat{\sigma}_f{}^2) \right\rangle = \frac{1}{NK}\sum_{n}\sum_{k} (X_{kn} - \tilde{\mu}_f(k))^2 \qquad \text{EQ. 19.}$$

It follows that the estimated signal-to-noise ratio is:

$$SNR = \frac{N\sum_{k} (\tilde{\mu}_f(k) - \tilde{\mu}_c)^2}{\sum_{n}\sum_{k} (X_{nk} - \tilde{\mu}_f(k))^2} \qquad \text{EQ. 20.}$$

The f-statistic under the null hypothesis of no prediction information has the following distribution [*DelSole and Tippett*, 2008]

$$SNR\frac{K(N-1)}{K-1} \sim F_{K-1,K(N-1)} \qquad \text{EQ. 21.}$$

However, SNR ranges from 0 to infinity. The Signal-to-Total Ratio (STR)

$$STR = \frac{<(\tilde{\mu}_f - \tilde{\mu}_c)^2>}{<\sigma_f^2> + <(\tilde{\mu}_f - \tilde{\mu}_c)^2>} \quad \text{EQ. 22.}$$

$$STR = \frac{SNR}{SNR + 1} \quad \text{EQ. 23.}$$

is a better measurement of potential predictability. STR always range from 0 to 1 with higher values indicate the larger potential predictability.

Signal-to-Total Ratio (STR) is a good quantitative measurement the potential predictability associated within ensemble simulation. Comparing the STR between the designed experiments will isolate the predictability contributed by snow boundary information, such as snow albedo effect, snow hydrological effect or both. For example, STR_T(ModBoth)- STR_T(Control) will provide a insight on the how much temperature predictability is enhanced by perfect snow boundary information (the subscript T indicates Temperature). This enhancement in the predictability is due to the atmosphere's "robust" response to snow boundary information.

3.5.3 Gain index

On the other hand, the temporal variability of a time series provides another way to measure the land-atmosphere interaction and feedback. As discussed in the background review, there are two feedbacks involved in the snow-atmosphere coupling, one positive temperature-albedo feedback to amplify it and another negative stability-snowfall feedback to stabilize it. An important question regarding snow coupling is whether the feedbacks lead to a net damping or amplification of climate variability. For example, the low temporal variability σ cases (a and b cases

in Figure 3.7) show relative small variability (amplitude) due to prescribe snow boundary forcing. However, high σ cases (c and d) demonstrate strong snow–atmosphere coupling and interaction. We can define a Gain index *G* as the ratio of mean temporal standard deviations of freely coupled ensemble and fixed snow boundary ensemble experiments, as an indicator of the coupling feedback factor.

$$G = \frac{\overline{\sigma_{coupled}}}{\overline{\sigma_{fixed}}} \qquad \text{EQ. 24.}$$

where σ is temporal standard deviations of one ensemble member, the bar indicate the mean over all ensemble members. *G* measures the gain (amplification factor) of mean temporal variability of the simulated time series due to free snow-atmosphere coupling and feedback compared with prescribing the snow boundary. The index G varies from 0 to infinity, with larger values indicating a greater degree of coupling feedback factor. When *G* is larger than 1, it indicates that the coupling will amplify the interaction (positive feedback). Otherwise, the coupling feedback will stabilize the coupled system (negative feedback).

For instance, G_T(Control, ModBoth) measures the amplification factor of the temporal variability of air temperature comparing freely coupled snow-atmosphere experiment (**Control**) with the fixed SCF and SWE experiment (**ModBoth**). Similarly, the G_T(**RealSCF**,**ModBoth**) and G_T(**RealSWE**, **ModBoth**) will measure feedback factor of snow albedo effect and hydrological effect separately.

3.6 Evaluations

Besides coupling strength, we can also evaluate the effect of the realistic snow information on climate prediction in the **RealSCF**, **RealSWE**, **RealBoth** experiments. This will be the case even though these experiments do not utilize any special initial information. Since realistic snow information is directly inserted into these three experiments, we can regard them as representing hypothetically "perfect" snow conditions. In addition, forced with the same SST climatological cycle, these runs will isolate the possible snow impact from the robust ENSO impacts. These evaluations can provide an insight how "perfect" snow boundary information, in term of albedo effect, hydrological effect or both, contribute to climate prediction without initial information and ENSO effect.

Four statistical parameters will be used to evaluate the predictive performance of the model with prescribed snow boundary information. These statistical indicators are: root mean square error (RMSE), the coefficient of determination (squared correlation coefficient R^2), percent of bias (PBIAS) and Nash-Sutcliffe Coefficient of Efficiency (NSE: [*Nash and Sutcliffe*, 1970]). The equations are given below:

$$RMSE = \sqrt{\frac{\sum (O - P)^2}{n}} \qquad \text{EQ. 25.}$$

$$R^2 = \left[\frac{\sum (O_i - \overline{O})(P_i - \overline{P})}{\sqrt{\sum (O_i - \overline{O})^2} \sqrt{\sum (P_i - \overline{P})^2}} \right]^2 \qquad \text{EQ. 26.}$$

$$PBIAS = \frac{\sum(O-P)}{\sum O} \times 100 \quad \text{EQ. 27.}$$

$$NSE = 1 - \frac{\sum(O-P)^2}{\sum(O-\bar{O})^2} \quad \text{EQ. 28.}$$

where O indicates the observed values, P is the predicted values, the bar indicates the mean of value and n is the number of data records. The RMSE measures the total magnitude of error between observed and predicted values. The R^2 is a statistical measure of how well the simulated values correlate in time or space with the observed data points. A value of 1 in R^2 represents a strong linear relationship between the observed and predicted value while a value of 0 indicates no linear relationship between observed and simulated values. The PBIAS valued indicate whether the model is over-predicting or under-predicting the observed values. Optimal value for PBIAS is 0; with negative values indicate over-prediction and positive values indicate under-prediction.

Since the correlation coefficient is based on an assumed linear regression, Nash and Suctliffe [1970] proposed an alternative index for goodness-of-fit, which is often referred to as Nash-Sutcliffe Coefficient of Efficiency (NSE) and widely used as a parameter to evaluate model performance. The NSE value ranges from -∞ to 1. An NSE value of 1 indicates a perfect agreement between the observed and predicted values; a value of 0 means that the model is good predictor only for the mean climatology; a negative value indicates that the climatology mean forecast is better than the model.

In the evaluation, we validated the model simulations with observation-based dataset. The National Centers for Environmental Prediction (NCEP)-National Center for Atmospheric Research (NCAR) reanalysis 1 data [R-1; *Kalnay et al.*, 1996] were used for the evaluation of temperature. Although NCEP-Department of Energy (DOE) reanalysis 2 products [R-2;*Kanamitsu et al.*, 2002] are updates of this widely used R-1 data set, we still chose to use the R-1 data set because of the relatively longer period of R-1 and for easy comparison with previous studies. For precipitation validation, the Global Precipitation Climatology Project one-degree daily (GPCP 1DD) precipitation dataset provides daily, global one-degree gridded data for precipitation (available online at http://precip.gsfc.nasa.gov/ gpcp_daily_comb.html). This precipitation dataset is a combined observation-only dataset based on satellite estimates of rainfall and is scaled to match the monthly accumulation provided by the GPCP satellite–gauge (SG) product, which combines monthly satellite and gauge observations [*Huffman et al.*, 1997]. To match the CAM model 1.9°X2.5°, the R1 reanalysis and GPCP 1DD data are interpolated to the CAM grid by bi-linear interpolation.

3.7 Summary

All experiments in the SACE are summarized in Table 3.1. The key diagnostics are also described in the table. Ω(Control) represents the fraction of variance across ensemble members that is "explained" (forced) by both boundary and initial conditions, including snow cover. The difference Ω(ModBoth)-Ω(Control)

is the enhancement of explained variance by prescribed snow boundary conditions, and indicates the snow-atmosphere coupling strength. Similarly, the difference in signal-to-total ratios STR(ModBoth)-STR(Control) measures the predictability enhanced by prescribed snow boundary condition. The Gain index, G(Control,ModBoth), represents the variability amplified by snow-atmosphere interaction and feedback.

By importing realistic snow information such as MODIS SCF and GLDAS SWE, we pioneer the investigation of the realistic snow albedo effect and hydrological effect on atmosphere predictability. Since the surface albedo is a linear function of snow cover fraction, the snow albedo effect is largely determined by the SCF. Because the soil moisture anomalies are triggered by snowmelt, which are correlated with maximum snow depth in winter, the snow hydrological effect in this designed experiment can be isolated.

Ω(ModBoth)-Ω(RealSCF) measures the fraction of variance explained by prescribed realistic SCF information (snow albedo effects). Similarly, STR(ModBoth)-STR(RealSCF) will measure the enhancement of predictability due to prescribed realistic snow albedo effects. On the other hand, Ω(ModBoth)-Ω(RealSWE) will quantify the fraction of variance explained by prescribed realistic SWE information (snow hydrological effects). STR(ModBoth)-STR(RealSWE) will quantify the predictability enhanced by the prescribed realistic snow hydrological effect.

In the last experiment, Both SCF and SWE information are prescribed. The Ω(RealBoth)-Ω(ModBoth) represent the fraction of variance explained by prescribed realistic snow information from both SWE and SCF. STR(RealBoth)-STR(ModBoth) represents the predictability enhanced by realistic snow modeling. In addition, Ω(RealBoth)-Ω(RealSCF) provide another way to separate the variance contributed by snow hydrological effect. Similarly, Ω(RealBoth)-Ω(RealSWE) gives another estimation of the snow albedo effect. Also, STR(RealBoth)-STR(RealSCF) and STR(RealBoth)-STR(RealSWE) measure the predictability enhancement due to snow hydrological effect and snow albedo effect accordingly.

Finally, based on the **RealSCF**, **RealSWE**, **RealBoth** experiments, an evaluation can be conducted to validate the "perfect" snow boundary information contribution to the climate predictability. Four statistical indicators will be used to evaluate the value of "perfect" snow simulation to climate prediction.

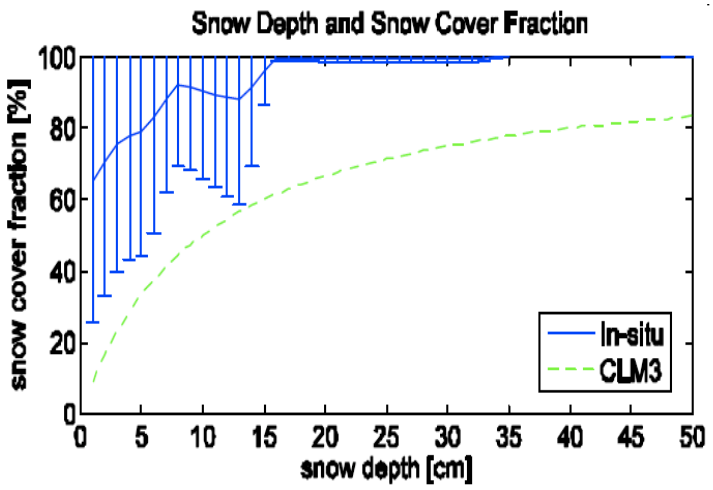

Figure 3. 1 In situ snow depth and snow cover fraction relationship over the Tibetan Plateau. The error bars show the observational range of snow cover fraction (%) at the different depth of snow. The green dotted line indicates the computation result from the parameterization in the CLM 3.0 model.

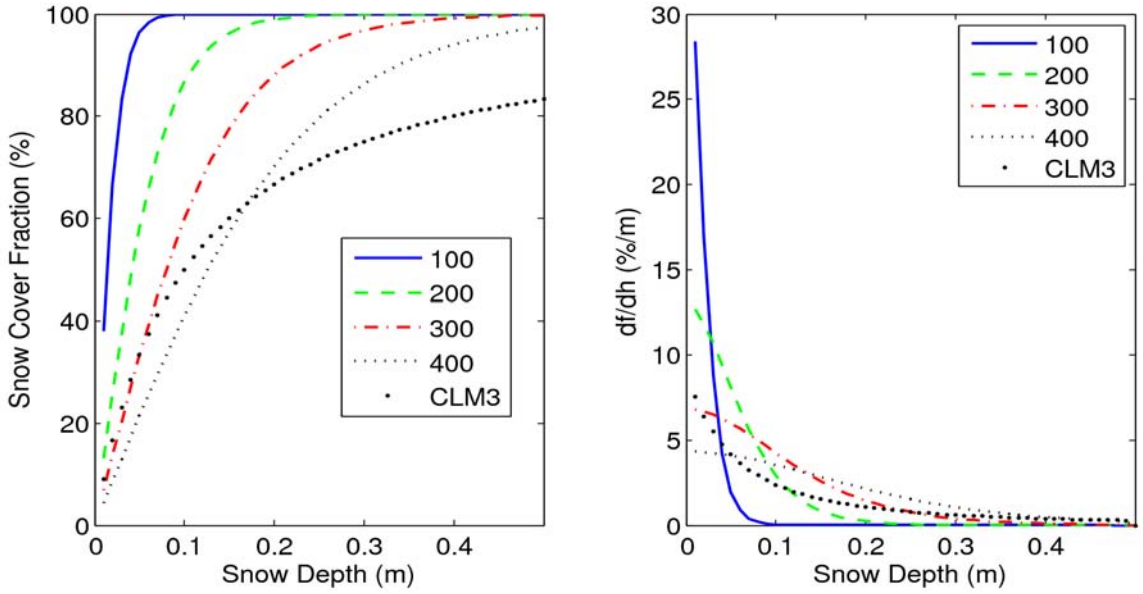

Figure 3. 2 The SCF parameterization of snow depth by CLM 3.5 with different snow densities from fresh new snow 100 kg/m^3 to 400 kg/m^3 compared to the default CLM 3.0 parameterization (left panel) and SCF change with snow depth (df_s/dh_s) at different snow densities (right panel).

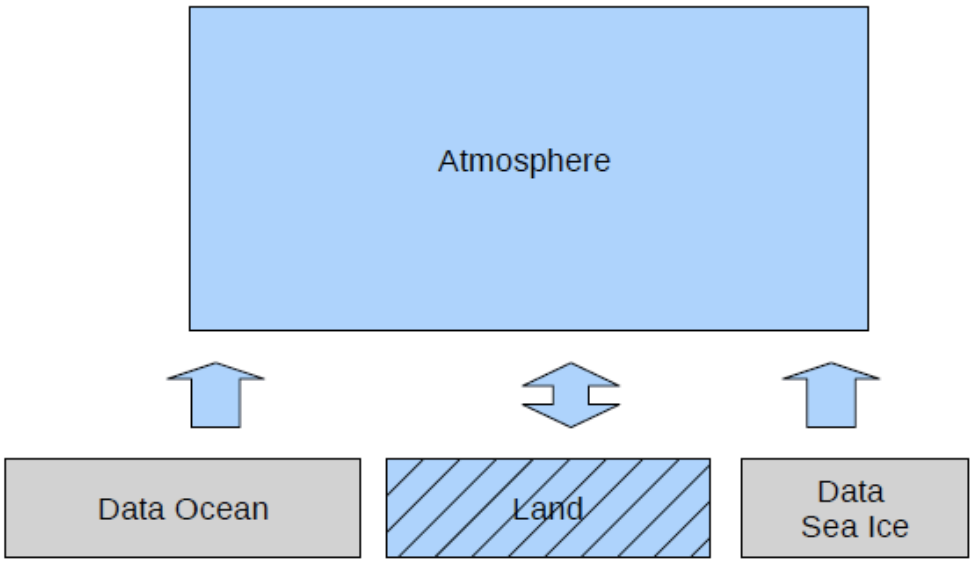

Figure 3. 3 The depiction of model setup for ocean, land and sea ice components.

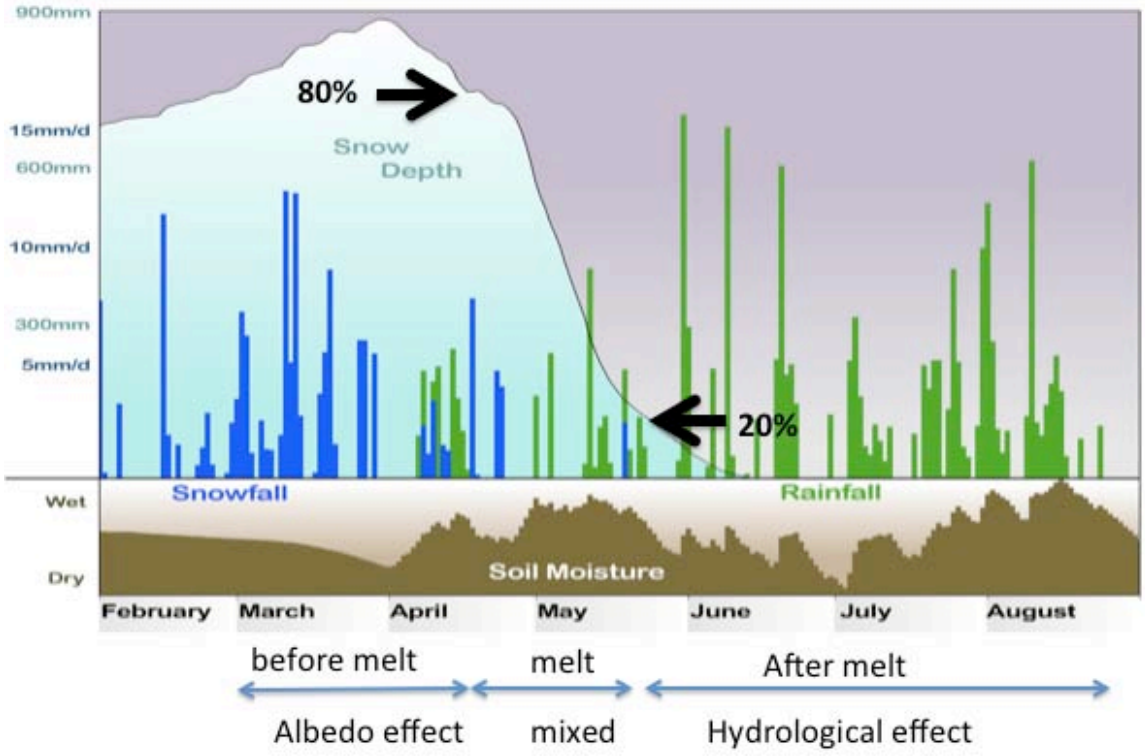

Figure 3. 4 A depiction of the model integration scheme. The background chart is a typical snow evolution with snowfall, rainfall and soil moisture from winter to summer obtained from the GSWP 2 dataset at a grid box in central Canada.

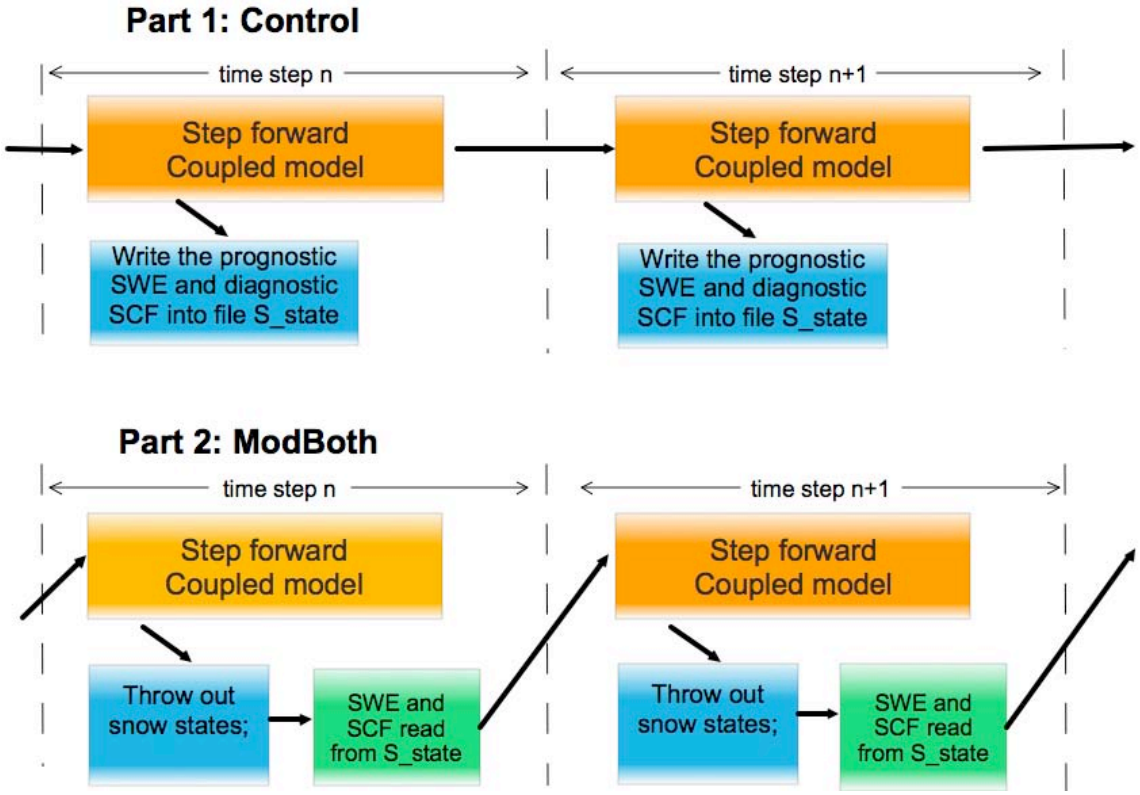

Figure 3.5 The demonstration of the Snow-Atmosphere Coupling Experiment (SACE).

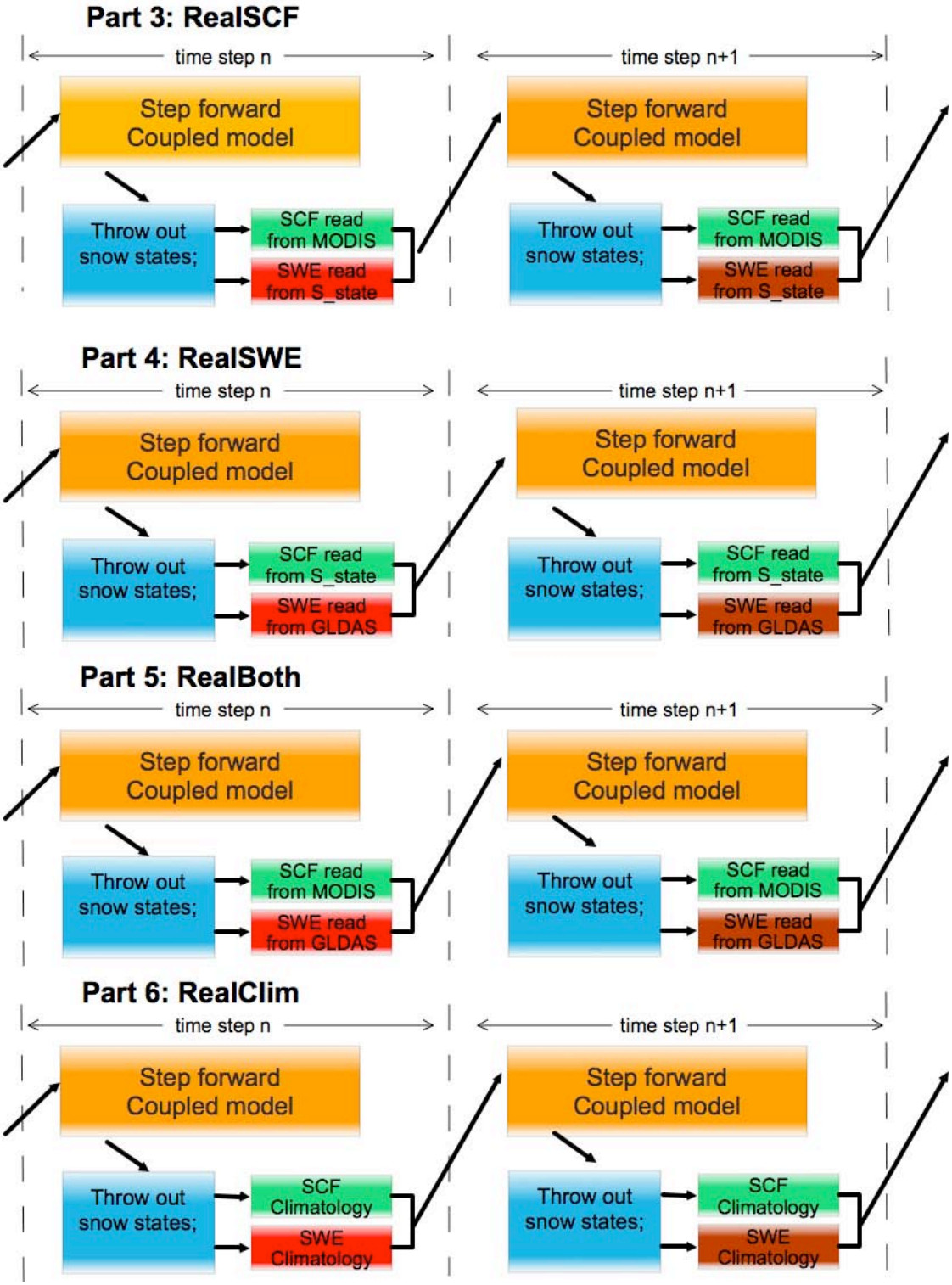

Figure 3.6 continued.

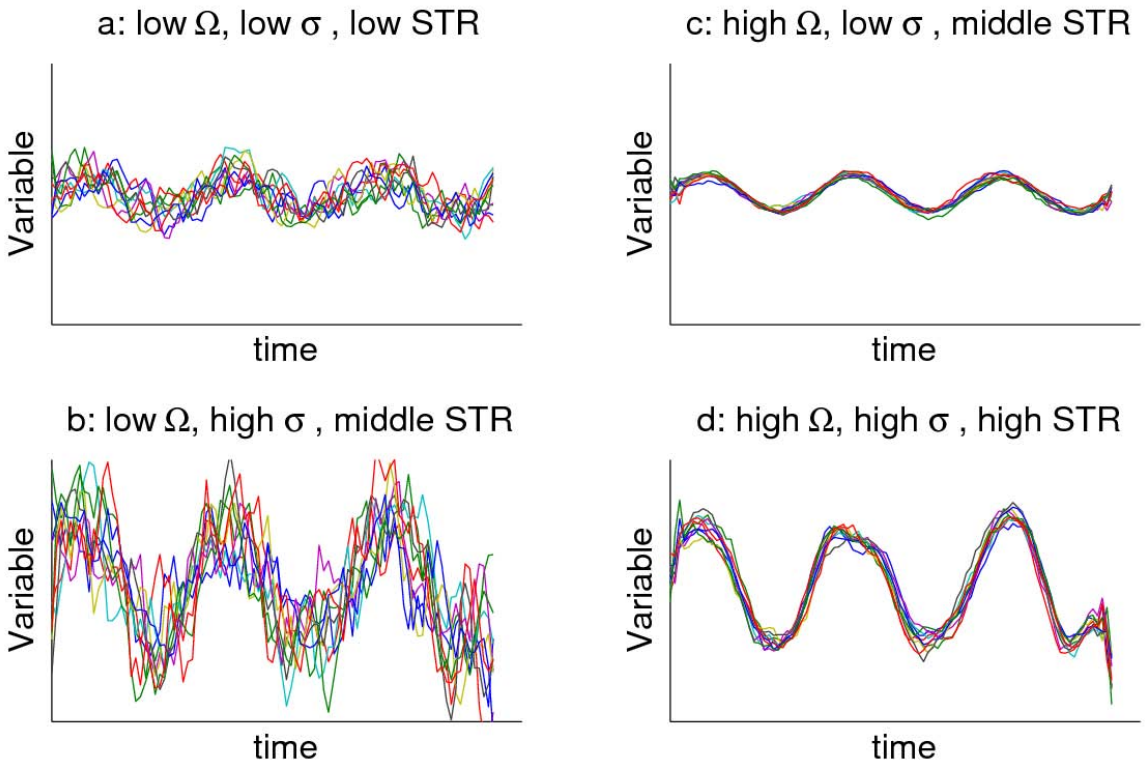

Figure 3.7 Idealized time series of the atmospheric state for different ensemble members under four situations: (a) low variability σ, low similarity Ω and low STR, (b) high variability σ, low similarity Ω and middle STR, (c) low variability σ, high similarity Ω and middle STR and (d) high variability σ, high similarity Ω and high STR.

Table 3. 1 summary of the SACE experiments

Identifier	Description	Key diagnostics
Control	Standard AGCM simulation with fully interactive LSM	Ω(Control): fraction of variance "explained" by all boundary and initial conditions
ModBoth	The same as **Control**, except the snow states are replaced by recorded data file from one random selected **Control** simulation.	Ω(ModBoth)-Ω(Control): coupling strength by model-simulated snow information STR(ModBoth)-STR(Control): Predictability enhanced by prescribed snow boundary Gain(Control,ModBoth): amplification by snow-atmosphere interaction
RealSCF	The same as **ModBoth**, except the SCF are prescribed by realistic yearly observations.	Ω(RealSCF)-Ω(ModBoth): coupling strength contributed snow albedo effects STR(RealSCF)-STR(ModBoth) : Predictability enhanced by snow albedo effect Gain(RealSCF,ModBoth): amplification factor by snow albedo effect
RealSWE	The same as **ModBoth**, except the SWE are prescribed by realistic yearly observations	Ω(RealSWE)-Ω(ModBoth): coupling strength by snow hydrological effects STR(RealSWE)-STR(ModBoth): Predictability enhanced by snow hydrological effect Gain(RealSCF,ModBoth): amplification factor by snow hydrological effect
RealClim	The same as **ModBoth**, except both SCF and SWE are prescribed by realistic observed climatology	Gain(Control,RealClim): amplification by snow-atmosphere interaction Gain(RealBoth,RealClim): amplification by snow-atmosphere interaction
RealBoth	The same as **ModBoth**, except both SCF and SWE are prescribed by realistic yearly observations.	Ω(RealBoth)-Ω(ModBoth): coupling strength by realistic SWE and SCF info Ω(RealBoth)-Ω(RealSCF): coupling strength by snow hydrological effects Ω(RealBoth)-Ω(RealSWE): coupling strength by snow albedo effects STR(RealBoth)-STR(ModBoth): Predictability enhanced by realistic snow info STR(RealBoth)-STR(RealSCF): Predictability enhanced by snow hydrological effects STR(RealBoth)-STR(RealSWE): Predictability enhanced by snow albedo effects

CHAPTER 4. SNOW SIMULATION IN THE NCAR CLM MODEL COMPARED WITH OBSERVATIONS

In this chapter, we compare the land snow variability simulated by the NCAR CLM 3.5 model at AMIP-style run (monthly mean) and **Control** experiment (daily time series) to realistic snow information obtained from MODIS and GLDAS accordingly. The main propose is to evaluate how well the current CLM model simulates global-scale snow variability.

4.1 Monthly mean climatology of SWE and SCF

Figures 4.1 and 4.2 show the monthly mean climatology of snow cover fraction and snow water equivalent in the CLM model based on the multi-decadal AMIP-style simulation during 2000-2009. From September to February, snows accumulate in high-latitude Polar Regions and then gradually extend to the south. The Tibetan Plateau, although located in the middle-latitudes (roughly 25-45°N), begins to build up shallow snow cover in October due to its high elevation. During the snow maximum (the end of February), more than half of the North American continent and a large portion of Eurasia are covered by snow (SCF larger than 90%).

The transition zone of the snow line (edge) reaches approximately 50°N. Tibet and the Rocky Mountains are two noteworthy snow regions in the middle-latitudes. From March to August, the snow cover gradually depletes toward the North Pole due to the increase in solar energy. The moving of the snowline is generally parallel with the latitude lines, except in mountainous regions where there exists some patchy scattered snow at high elevations.

4.2 Annual Cycle

Figures 4.3 and 4.4 show the annual cycle of snow cover fraction (SCF) and snow water equivalent (SWE) for the CLM model simulation compared with MODIS satellite retrievals and GLDAS data assimilation products for four regions: 1) Northern Hemisphere land, north of 20°N; 2) Eurasia, north of 20°N; 3) North America, north of 20°N; and 4) all middle-latitude land between 40°N and 60°N. Greenland is excluded from all four regions since there are very only small variations of snow there. The error bars show the inter-annual variability represented by standard deviation from 2000-2009.

Generally speaking, CLM overestimates the mean value of SWE and SCF in the four regions, but underestimates the inter-annual variability of SWE and SCF. The biases in the diagnostic variable SCF (through SD-SCF parameterization) are more significant than for the prognostic variable SWE.

In the SCF, the MODIS satellite retrieval and CLM simulation show significant differences. According to Hall et al. [2002a], the MODIS snow map estimated error,

annually averaged for the Northern Hemisphere, is approximately 8% in the absence of forest and clouds. Due to cloud (almost all have been removed by using 8-day composited maps) and forest obscuration, the MODIS data have a slight underestimate of the snow fraction in nature (less than 5% usually). Compared with MODIS, the snow fraction parameterization in CLM shows serious overestimates of the snow cover fraction. Direct insertion of SCF obtained from MODIS to the CLM may cause serious bias in the temperature simulation. For the **RealSCF** experiment, we should use a bias-removal technique, such as CDF-matching [*Reichle and Koster*, 2004], to reduce the potential bias in the simulation.

On the other hand, the underestimation of inter-annual variability of SWE and SCF in CLM could cause weak snow-atmosphere coupling in the simulation. Prescribing realistic SWE and SCF variability into the model in ensembles **RealSWE** and **RealSCF** will be key to quantify the coupling strength and the contribution to predictability.

In general, the snow simulation over the North American continent is much better than over Eurasia, probably because the snow fraction parameterization was constructed mainly based on available North American data. In addition, note that the AGCM shows a slower accumulation process from October to December than GLDAS reanalysis. This feature may be due to the snowfall parameterization in CAM that produces weaker snowfall in early winter.

Figures 4.5 and 4.6 show detailed maps of monthly mean differences of model simulated SWE and SCF with GLDAS and MODIS during the snow depletion period from March to June. The biases are not evenly distributed globally, but gradually reduce as snow disappears.

4.3 Grid-point scale inter-comparison

Figure 4.7 and 4.8 show daily SWE and SCF evolution of the **Control** simulation comparing with GLDAS reanalysis and MODIS snow retrievals at three typical snow points: 1) Canada (87.5°W, 55.98°N); 2) Tibetan Plateau (90°E, 36.95°N); 3) Central Siberia (90°E, 71.05°N). The detailed information about the three grid-points is shown in Table 4.1. In each panel, the ten lines represent ten different year's snow evolution during 2000-2009. The x-axis runs from March 1st to August 31st in Julian days.

Table 4. 1 Detailed information about 3 selected typical snow grid-points

Site	Longitude	Latitude	Grid coordinate (1.9x2.5 FV grid)	Dominated land type (units)	Summary
P1	87.5W	55.89N	(78,110)	Vegetated	Stable middle-latitude snowpack in Canada
P2	90.0E	36.94N	(68,37)	Vegetated	Topographic unstable snowpack at middle-latitude Tibetan Plateau
P3	90.0E	71.05N	(86,37)	Vegetated	Stable high-latitude snowpack at central Siberia

The CLM well represents the SWE depletion curve during March to August in Canada and central Siberia, but not in the Tibetan Plateau (TP). GLDAS shows a relatively large volume of snow during spring to summer in the TP, but the CLM

model seriously underestimates this. Ma et al. [2008] pointed out that the Tibetan Plateau, the roof of the world, is a challenge for land surface modeling not only due to the highly complex terrain, vegetation, and land classification but also due to the complicated permafrost over this region. However, the stronger incident solar radiation due to its low latitude will cause the snow albedo effect to be more sensitive to the snow cover variation.

Snow cover fractions computed by snow-depth parameterizations [*Niu and Yang*, 2007] show relatively large disagreement with MODIS data. Due to quick gravity compaction after fresh snowfall, the model snow depth shows a rapid collapse in the first few days after snowfall, and then leads to substantial collapse in the snow cover fraction beyond the first few days after new snowfall. These sudden collapses in the SCF are not realistic in nature, partially due the problem that the snow cover parameterization is based on snow depth that is over-compacted by gravity. Using SWE to instead snow depth in this parameterization may eliminate the problem.

4.4 Inter-annual variability of snow

Figure 4.9 shows the SWE variability represented by the monthly mean of standard deviations of the daily SWE from the **Control** experiment. During the boreal snow maximum period (March), there is considerable inter-annual variability over the snow-buried regions (Figure 4.9.a). The snow over the Tibetan plateau, Eastern Europe and the Far East show relatively larger values of inter-annual

variability. When snow coverage shrinks from March to June, only limited high-latitude regions and the margins of Greenland retain much inter-annual variability. Note that there is still some SWE variability over the Tibetan plateau due to its high elevation. Similarly, Figure 4.10 shows the snow cover fraction variability from the **Control** experiment. During March, the snow fraction strongly varies at middle-latitudes due to high sensitivity of SCF to the shallow snow (df/dh). The regions of high variability of the SCF move northward with the edge of the snowpack from March to June. There are still considerable variations at high-latitude regions during June.

4.5 Snow anomaly memory

Due to positive snow-albedo feedback, snow anomalies can persist a relatively longer period. We call this snow anomaly memory. This memory is considerably longer than most atmospheric processes and impacts on local and downstream weather and climate from weekly to seasonal time scales. To measure the snow anomaly memory, a lagged autocorrelation coefficient is calculated at each grid point, where the time series of SWE or SCF are correlated with themselves but lagged at different time intervals. Based on the first order Markov framework, the *e*-folding time scale τ provides a single parameter of measurement of the snow memory:

$$r(t) = \exp(-t / \tau) \qquad \text{EQ. 29.}$$

where r(t) is the autocorrelation at lagged time t.

Figure 4.11 shows the spatial mean lagged correlation *r* as a function of lagged days *t* in different latitude zones. The top panel is for snow cover fraction from GLDAS and bottom panel is for snow cover fraction from the **Control** experiment. We used daily mean snow values and a 30-day window for computing correlation. The thick dotted line indicates the *e*-folding time scale of the lagged autocorrelation.

From the MODIS observed SCF (upper panel), the snow anomaly memories persist through summer in the high latitude regions (lat > 80° and 80°>lat> 70°). The positive or negative anomalies in these regions can also persist for relatively long times in the regions between 60° and 70°, although the lagged autocorrelation quickly decreases to 0.6 by summer. In contrast, the lagged autocorrelations decease rapidly with lag in the middle-latitudes (40°<lat<60°). The *e*-folding time scale of snow memory is only about 30 days in the middle latitudes.

Compared with the SCF simulation obtained from the CLM model **Control** experiment ensemble (bottom panel), the snow anomaly memories in the high-latitude regions are not well simulated. The lagged autocorrelation quickly decreases below the *e*-folding scale within 30 days. The snow anomaly persistence is simulated better at middle-latitude regions in the CLM model.

Figure 4.12 is similar to Figure 4.11, but for the SWE. Based on the GLDAS estimated SWE (upper panel), the snow anomaly memories are strong at high-latitude regions and slowly decrease with the lagged days. The *e*-folding time scale τ

is roughly 120 days for the region between 60° to 70°, 80 days for the region between 50° and 60° and 30 days for the region between 40° and 50° accordingly. The CLM well simulates these features (bottom panel), although the *e*-folding time scale in the region between 50° and 60° is significantly shorter than observed.

The longer snow anomaly memories in the observed data also imply the CLM may simulate weak snow-atmosphere coupling and interaction. Importing the realistic snow data into the model may provide more accurate estimations of actual snow-atmosphere coupling strength.

4.6 Summary

CLM 3.5 shows improvement over version 3.0 in the global snow simulation, especially in the monthly climatology, in simple AMIP-style stimulations given the absence of direct snow observations. However, there are still significant deficiencies in the snow simulation made by CLM 3.5, including:

1. Overestimation of the monthly mean climatology with especially large systemic bias in the SCF in the Eurasian continent. Bias removal is necessary for importing satellite snow information in the prescribed observed snow experiments (direct insertion), such as **RealSCF**.
2. Underestimation of the inter-annual variability of snow in the CLM model, which may cause weaker snow-atmosphere coupling and interaction in the ideal experiment **ModBoth**. Realistic snow information in **RealBoth** needs to be implemented to quantify better the coupling strength.

3. Shorter snow anomaly memory (persistence) in the model simulation compared with realistic observations will also weaken the snow-atmosphere coupling and interaction compared to reality. Importing realistic snow variability into CLM becomes necessary and important for using the AGCM to estimate actual snow-atmosphere coupling strength.

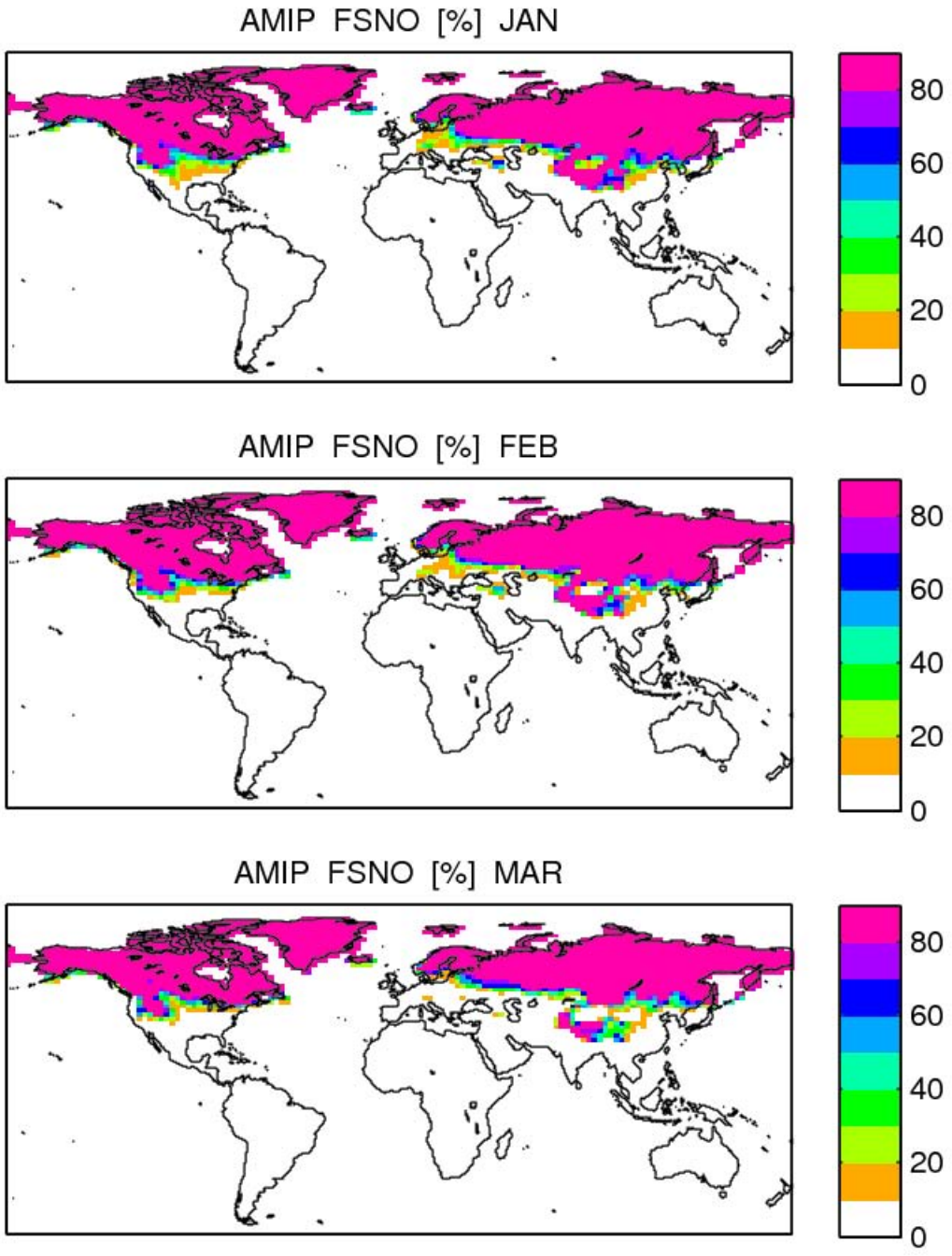

Figure 4.1 The monthly climatology of Snow Cover Frication (FSNO) in the CLM model based on the AMIP style simulation

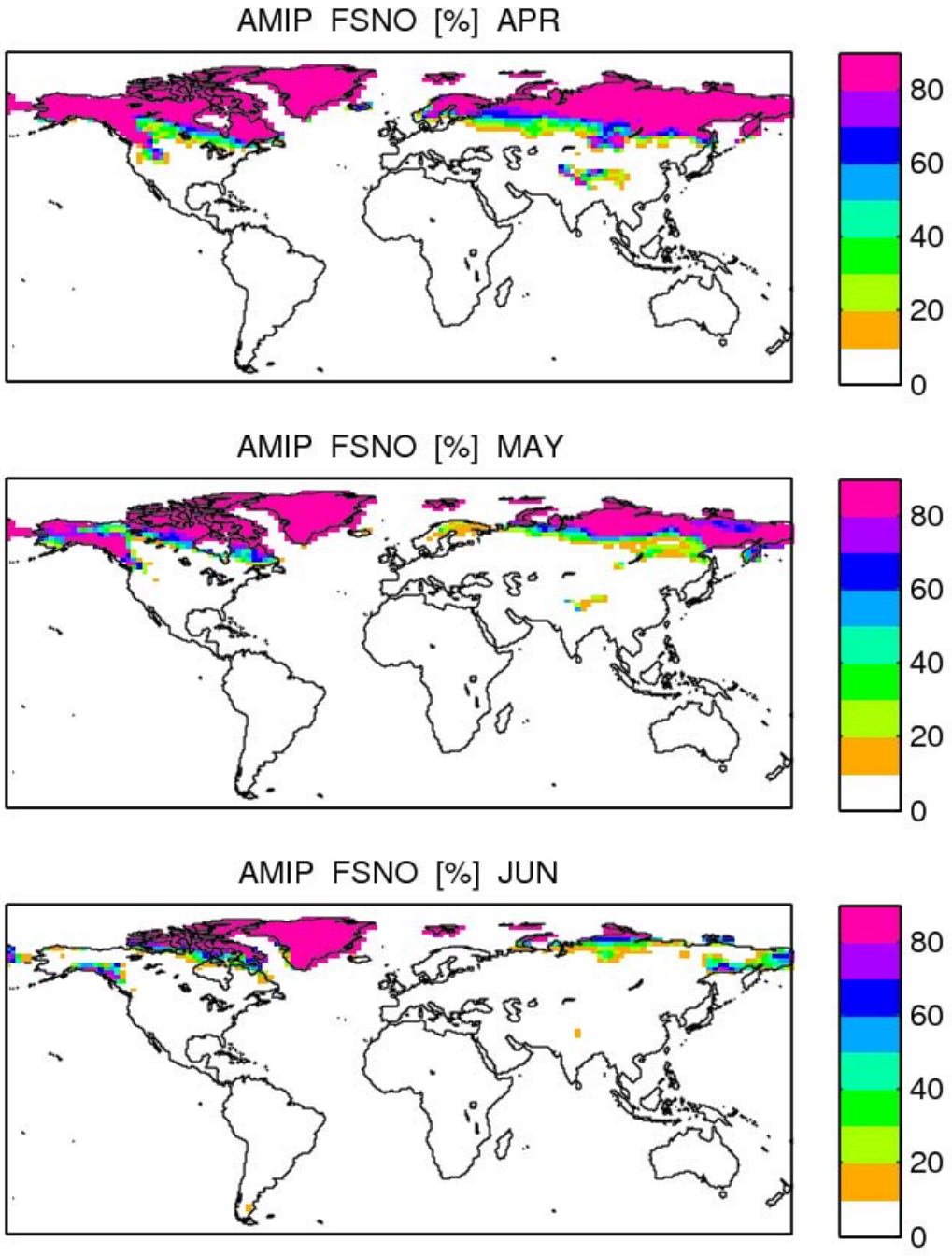

Figure 4.1 continued.

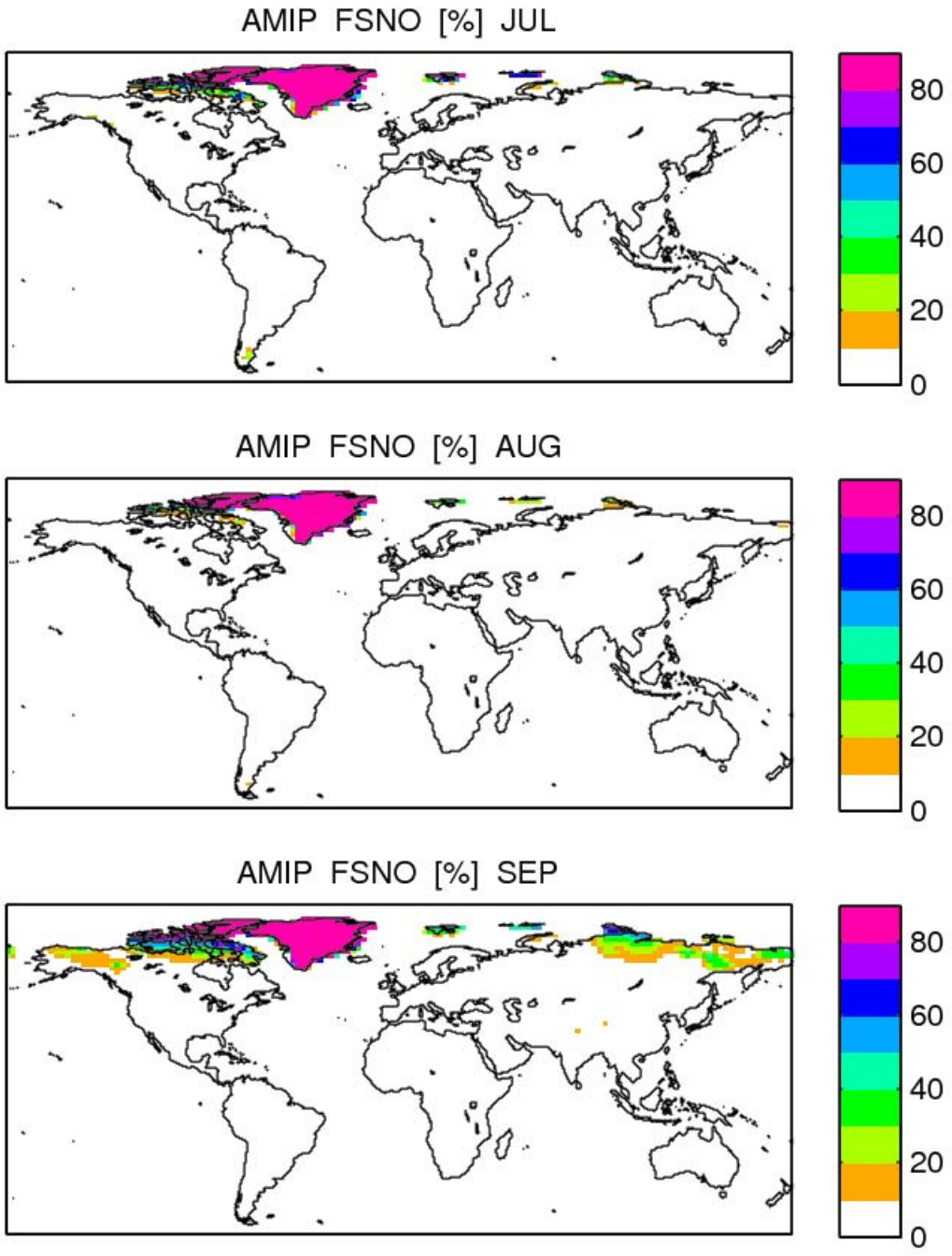

Figure 4.1 continued.

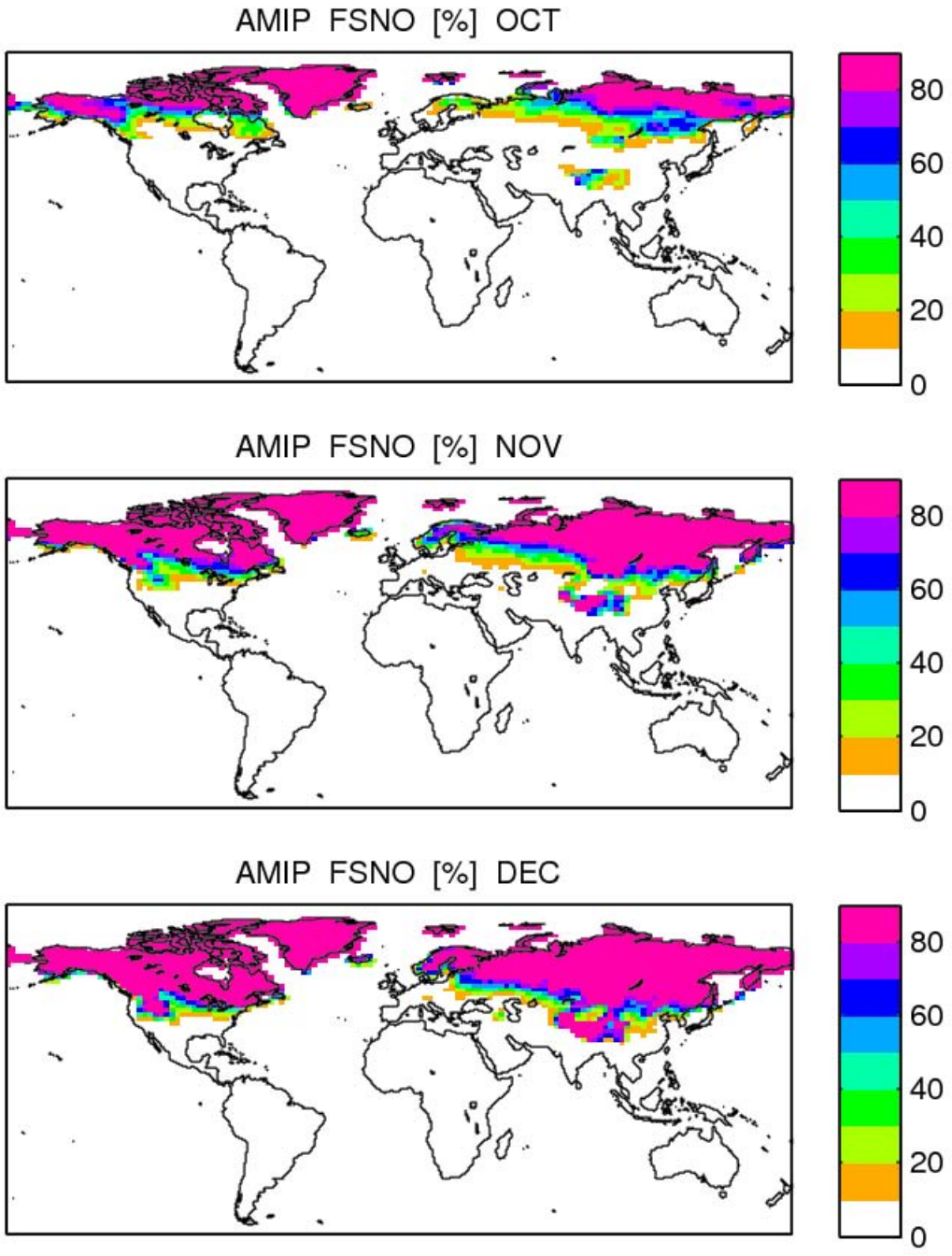

Figure 4.1 continued.

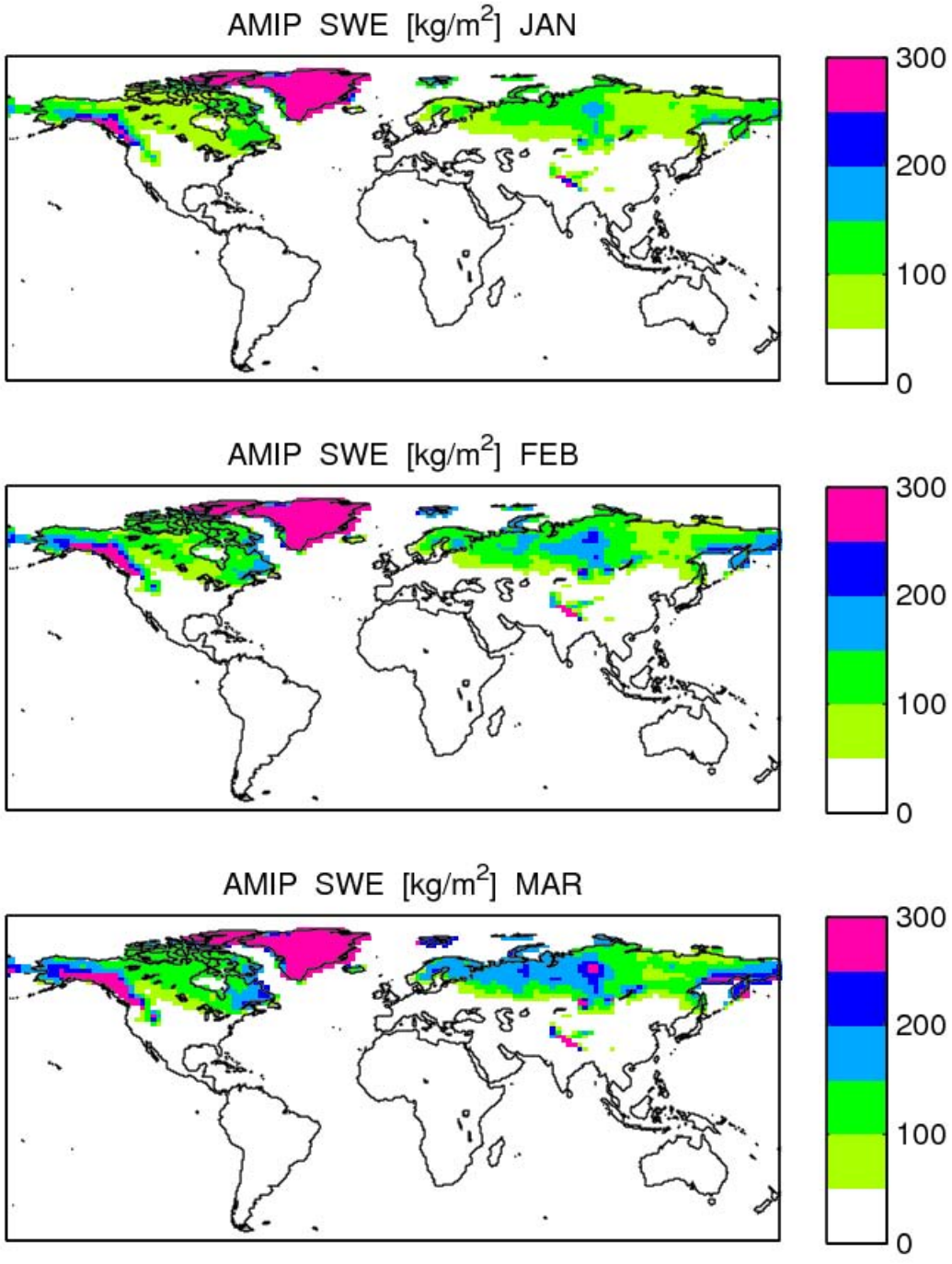

Figure 4.2 The monthly climatology of Snow Water Equivalent (SWE) in the CLM model based on the AMIP style simulation.

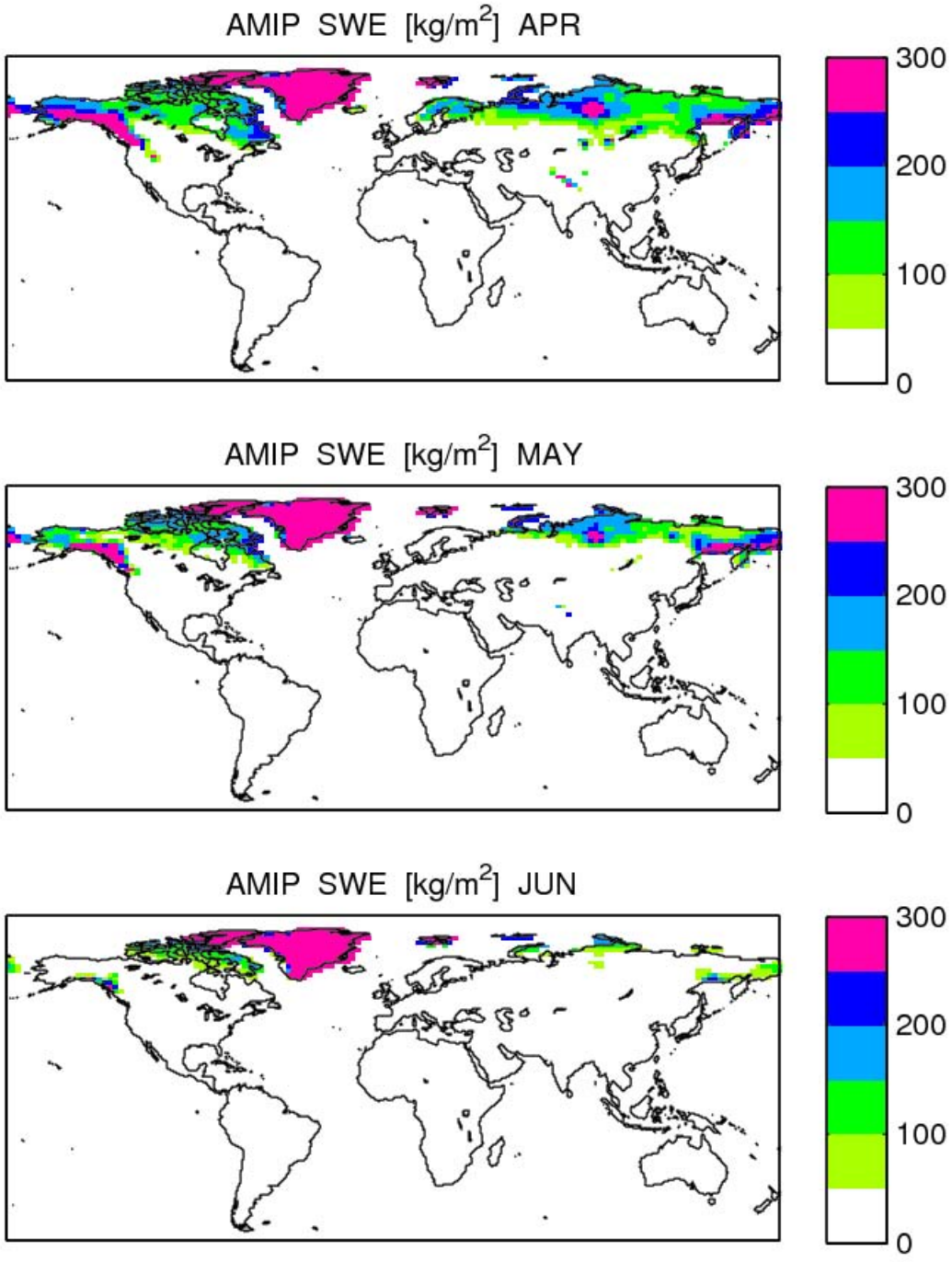

Figure 4.2 continued.

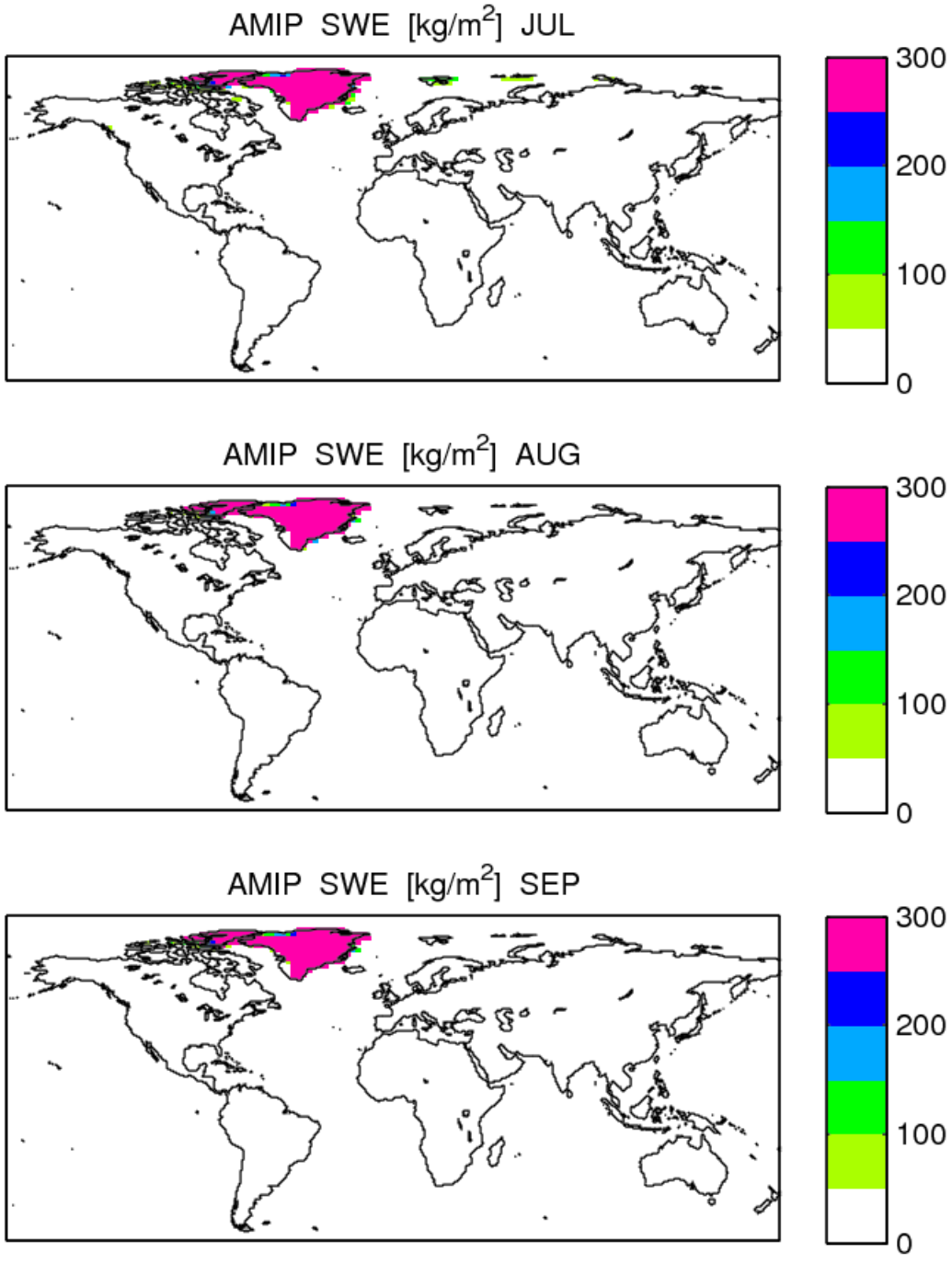

Figure 4.2 continued.

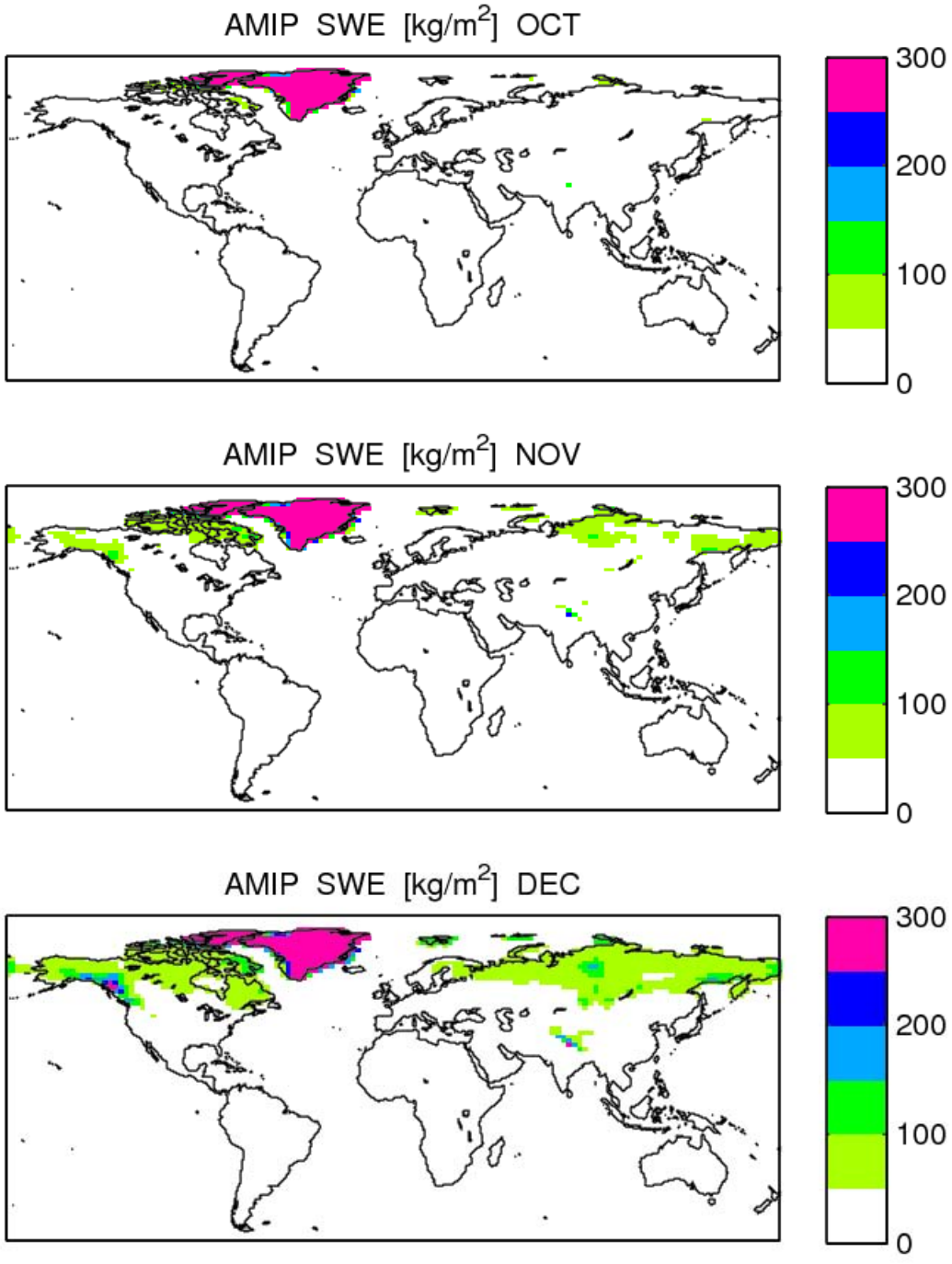

Figure 4.2 continued.

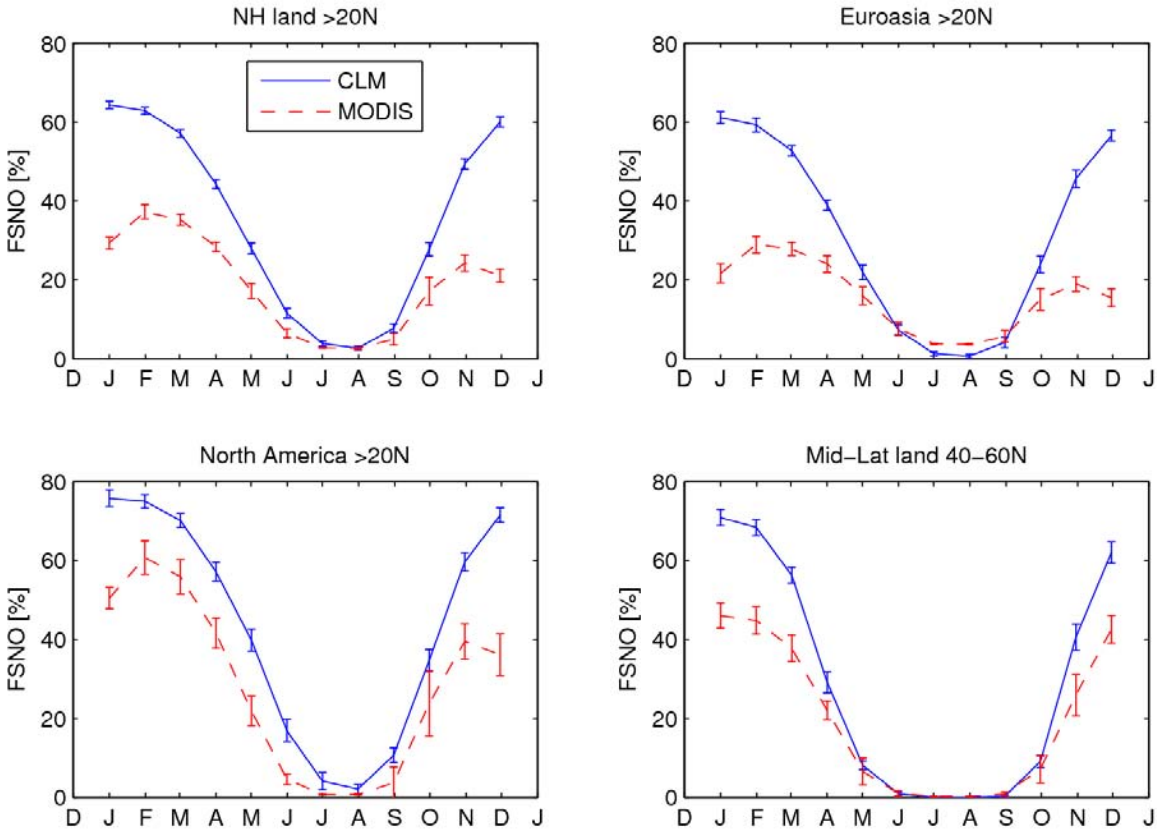

Figure 4.3 Monthly mean snow cover fraction (FSNO) for the CLM model simulation and MODIS satellite retrieval for the 1) Northern Hemisphere land; 2) Eurasia, north of 20°N; 3) North America, north of 20°N; and 4) middle-latitude land between 40 °N and 60°N. The error bars show the inter-annual variability represented by standard deviation from 2000-2009.

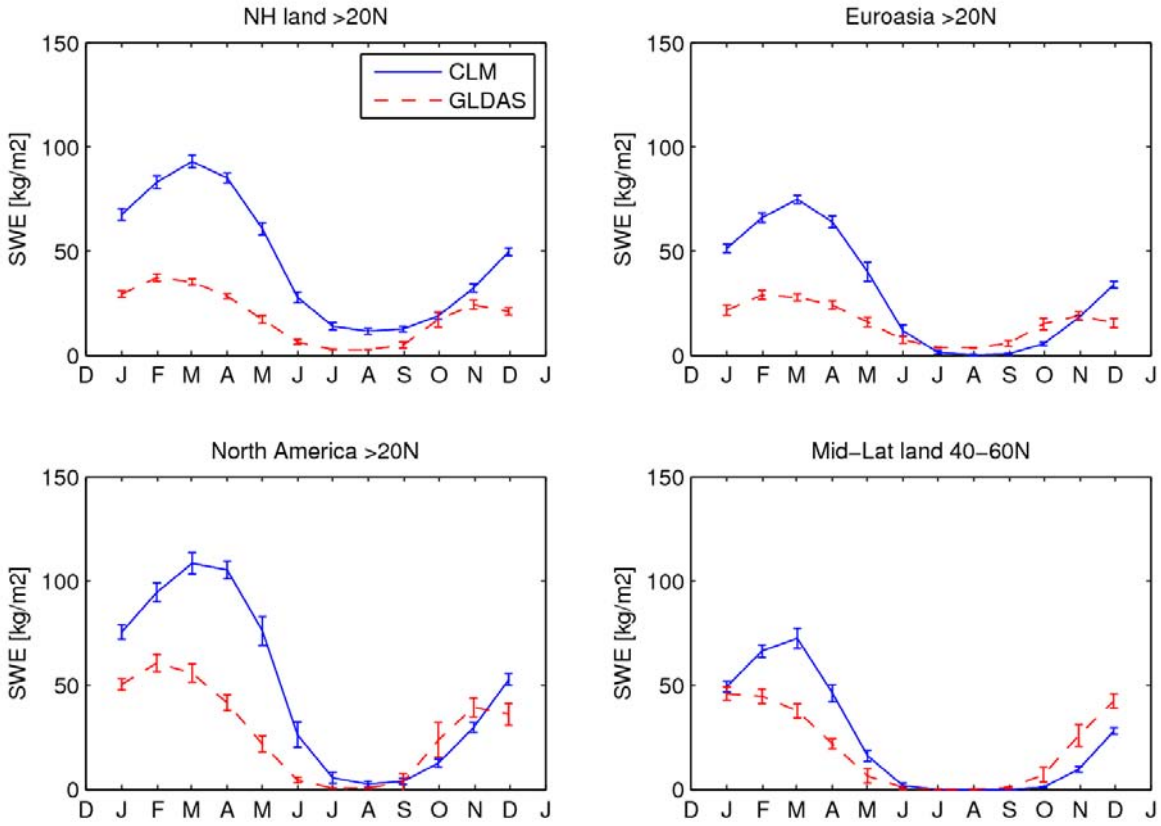

Figure 4.4 The same as Figure 4.3, but for Snow Water Equivalent (SWE).

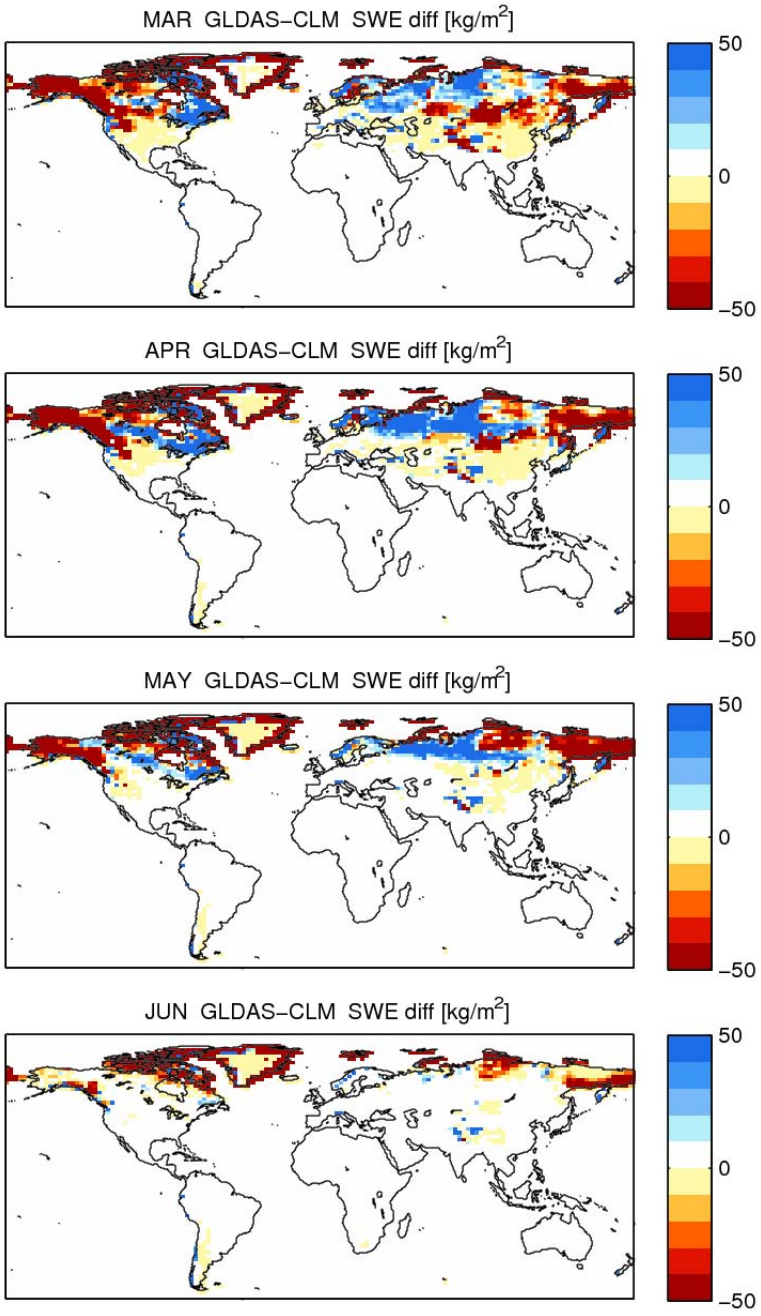

Figure 4.5 The monthly mean SWE difference between GLDAS and CLM simulation from March to June.

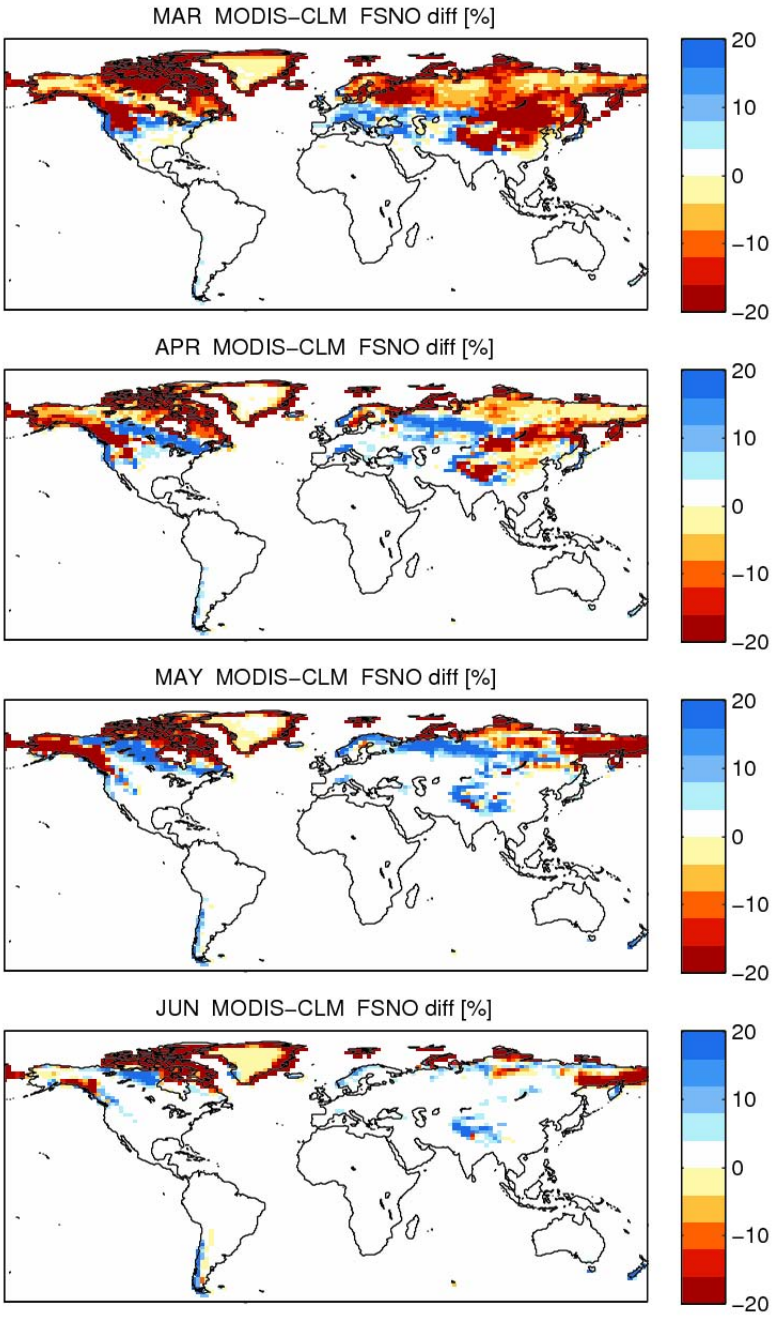

Figure 4.6 The monthly mean snow cover fraction difference between MODIS and CLM simulation from March to June.

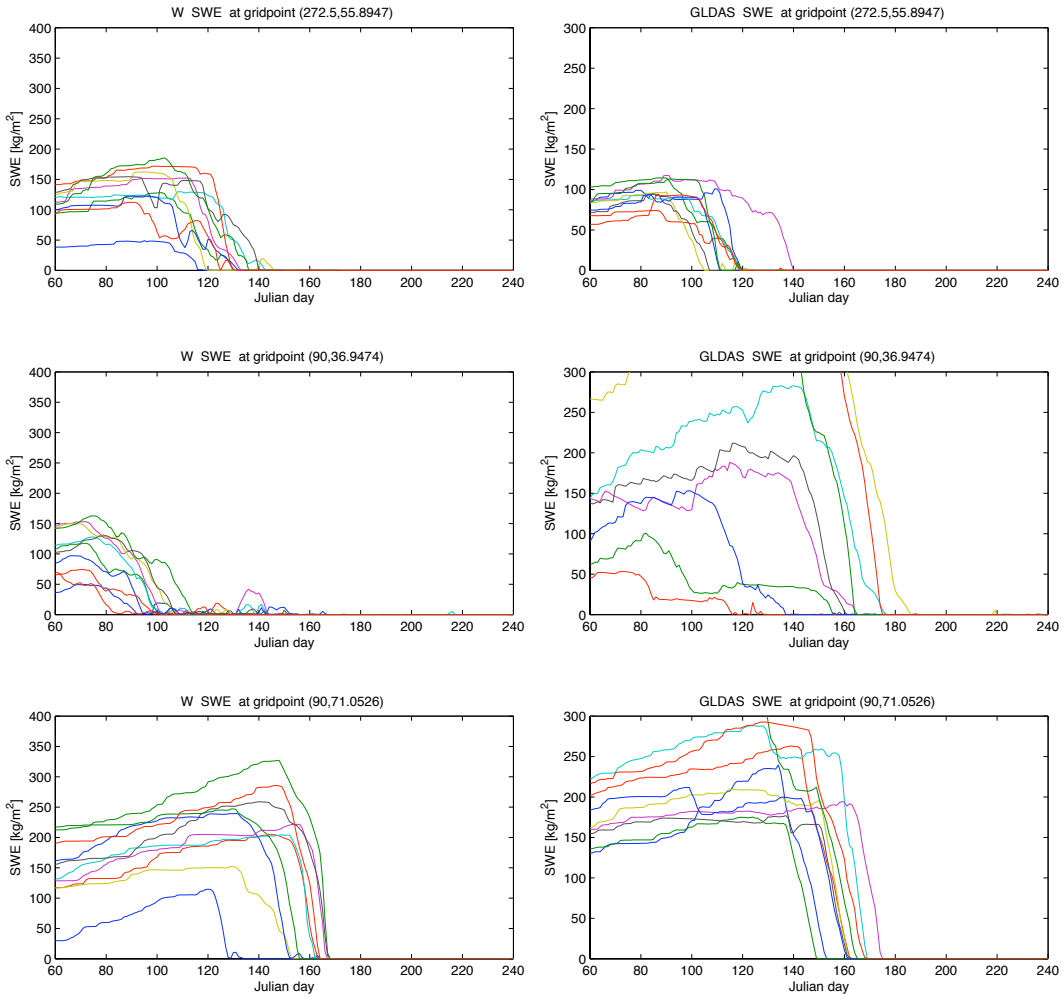

Figure 4.7 The daily SWE evolution of the Control simulation and GLDAS reanalysis at three typical snow grid-points: 1) Canada (87.5°W, 55.98°N); 2) Tibetan Plateau (90°E, 36.95°N); 3) Central Siberia (90°E, 71.05°N). The ten lines represent ten different year's snow evolution during 2000-2009. The x-axis spans March 1st to August 31st in Julian days.

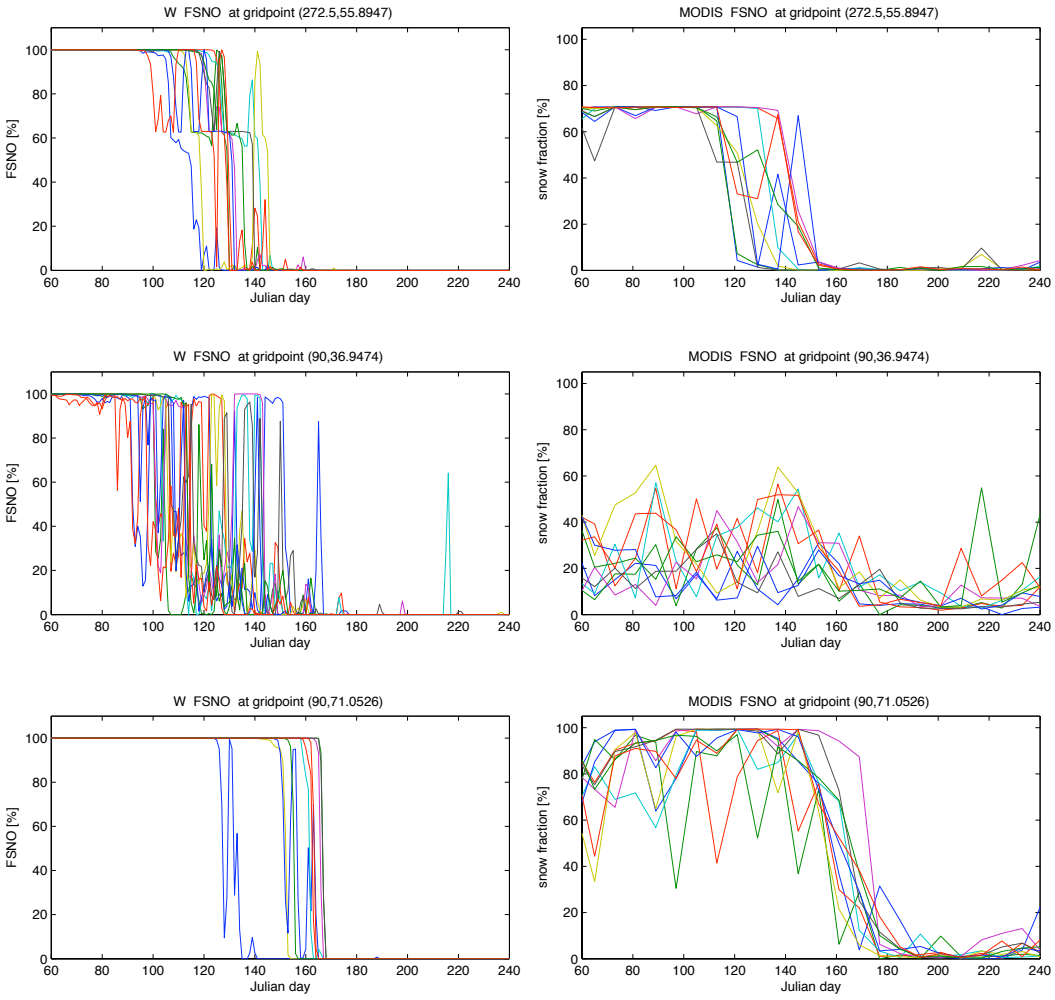

Figure 4.8 The same as Figure 4.7, but for daily snow cover fraction evolution of the Control simulation and GLDAS reanalysis at three typical snow grid-points.

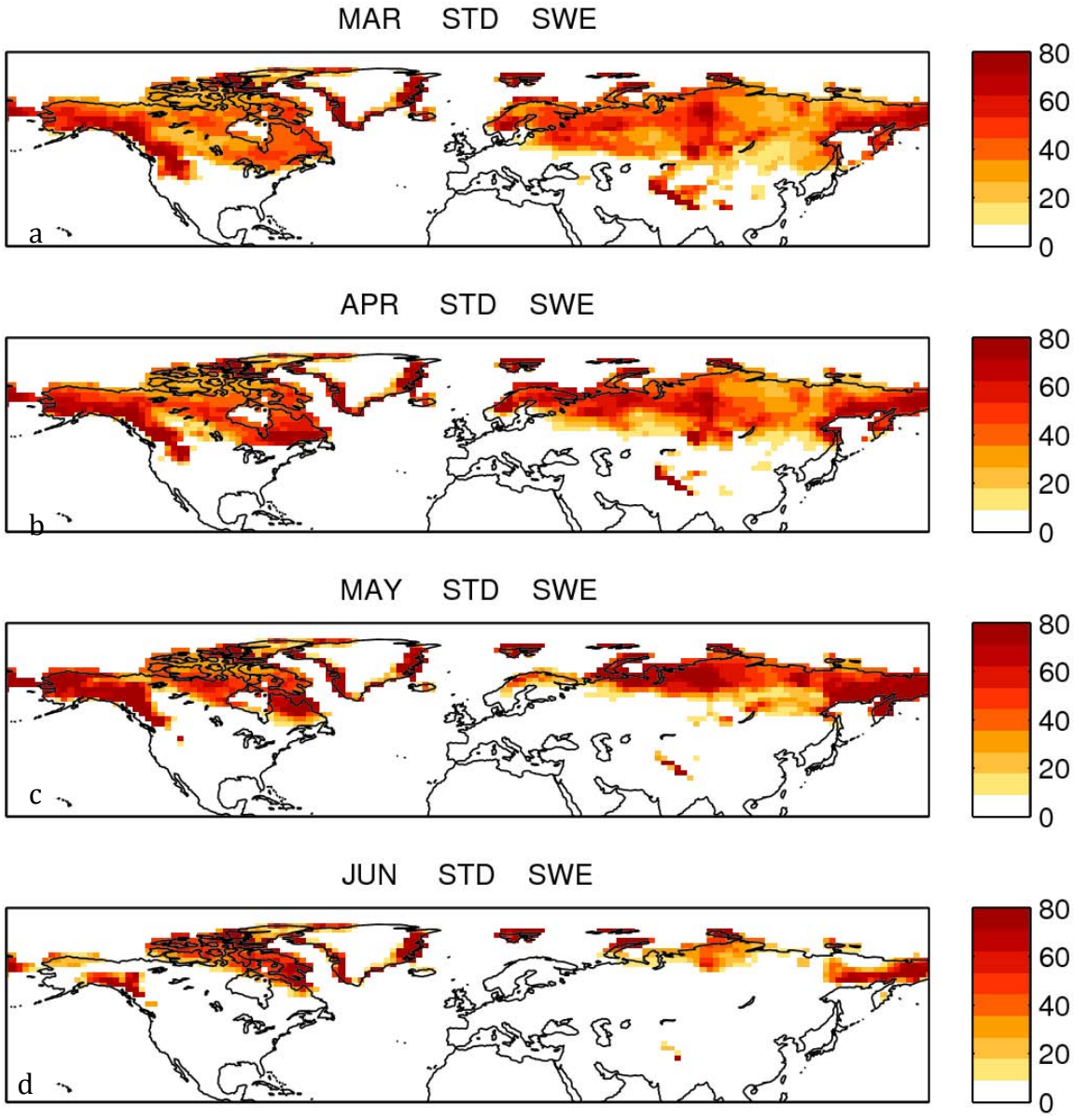

Figure 4.9 The monthly mean of the standard deviations of the daily snow water equivalent (Kg/m2) from the Control experiment: a) March b) April c) May and d) June.

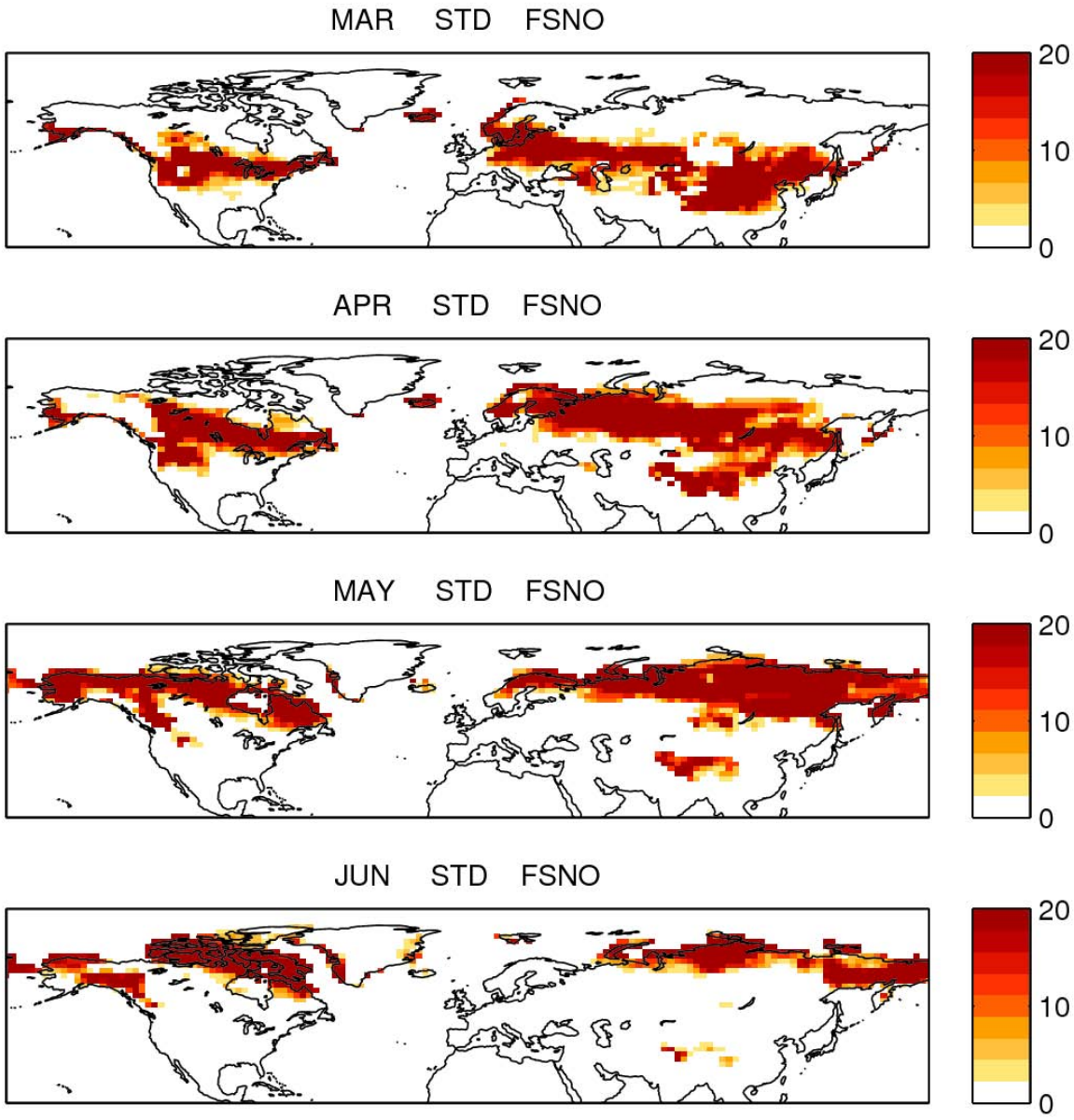

Figure 4.10 The monthly mean of the standard deviations of the daily snow cover fraction (%) from the Control experiment: a) March b) April c) May and d) June.

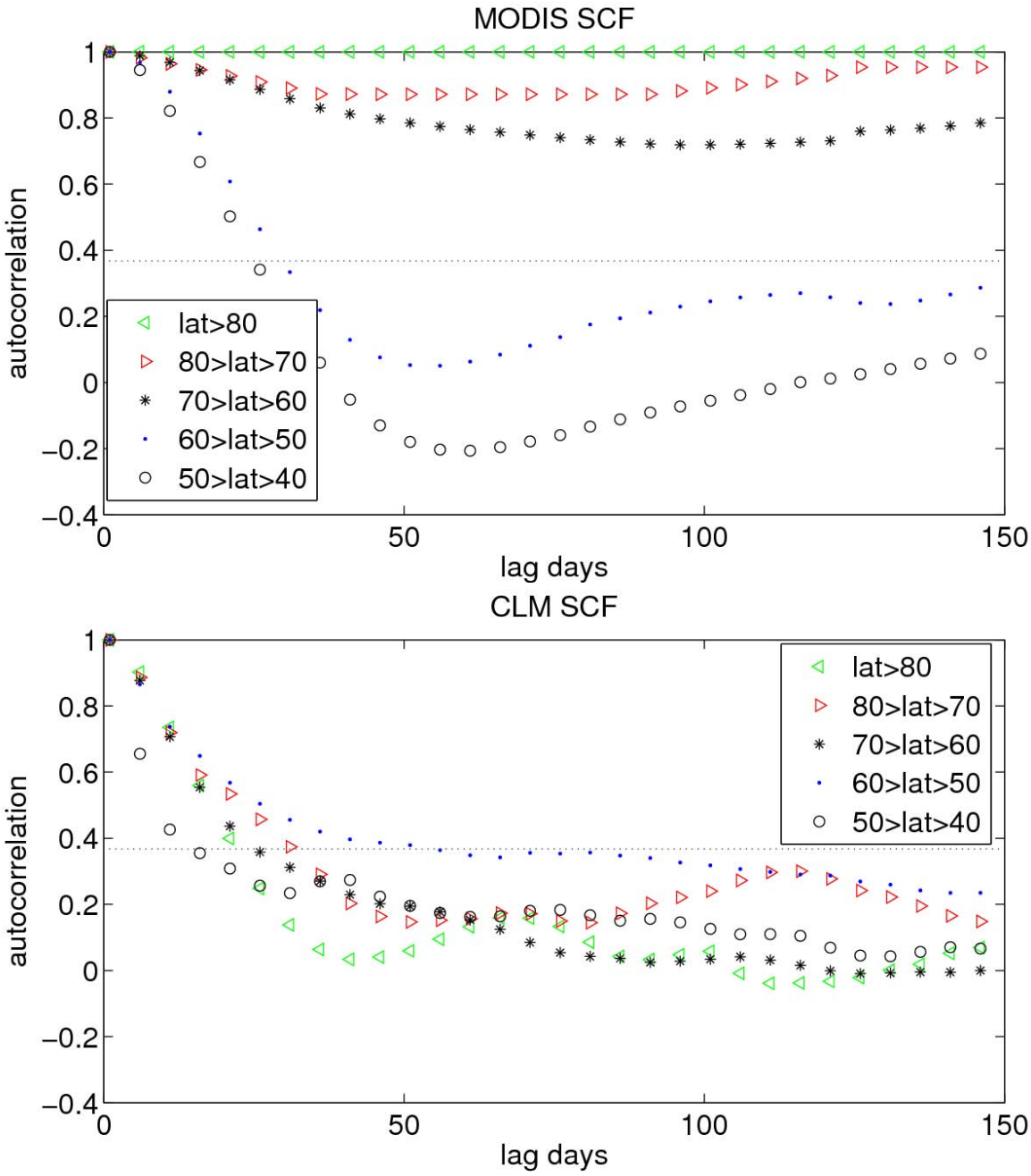

Figure 4.11 The mean lagged correlation r(t) in difference latitude bands: a) the snow cover fraction from GLDAS; b) snow cover fraction from the CLM Control run. The thick dotted line indicates the e-folding time scale of the lagged autocorrelation. The x-axis extends from March 1st to August 31st. The autocorrelations are computation over a 30-day window.

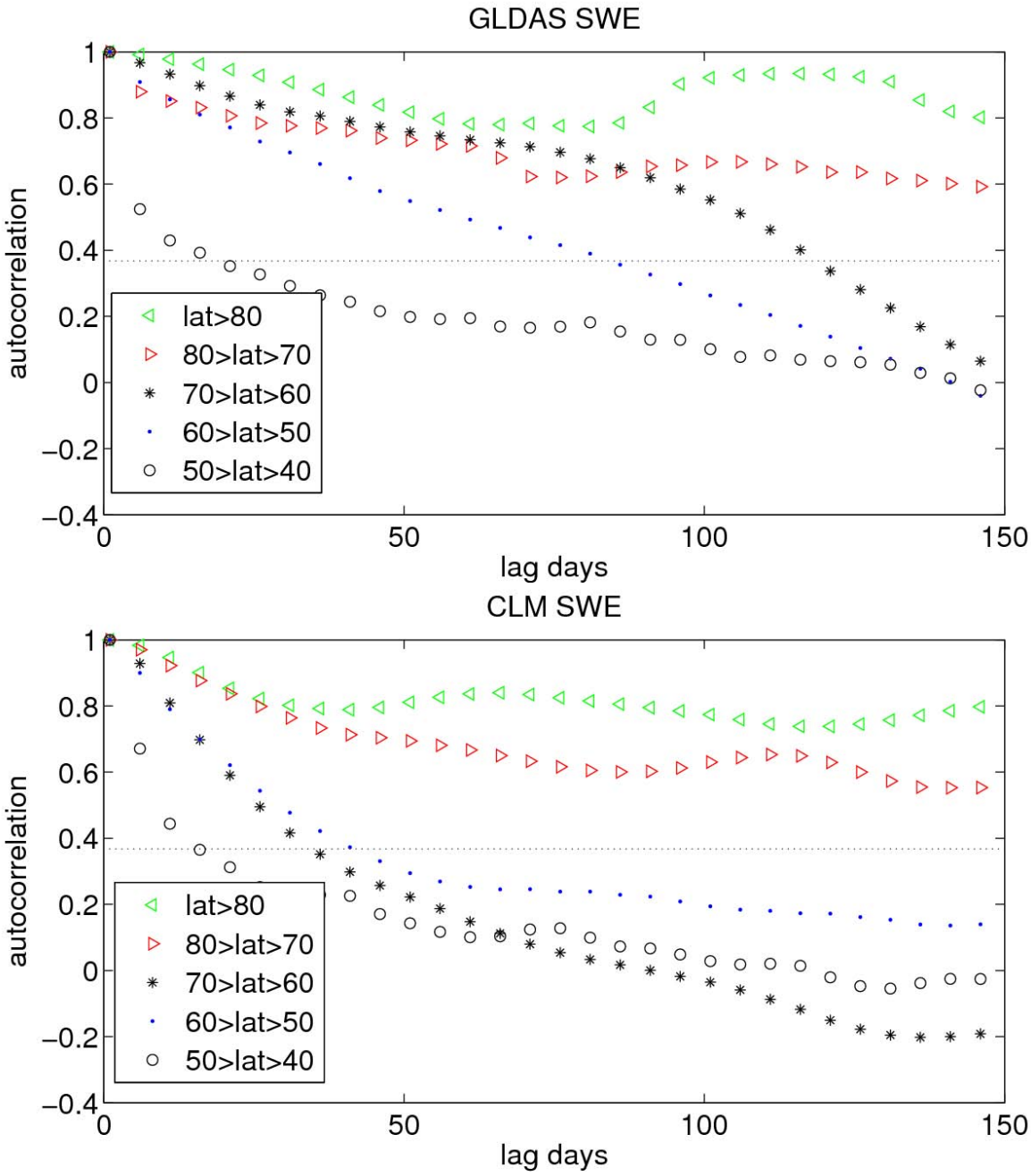

Figure 4.12 The same as Figure 4.11, but for SWE lagged correlation r(t) in different latitude bands: i) the SWE from GLDAS; ii) SWE from the CLM Control run.

CHAPTER 5. COUPLING STRENGTH AND PREDICTABILITY BY MODELLED SNOW EVOLUTION

5.1 Control and ModBoth experiment

In the ideal simulation **Control**, the land surface model is freely coupled with the AGCM without any constraint in each ensemble member, including the prognostic variable SWE and diagnostic variable SCF. The possible ENSO impacts are also removed by forcing with the same climatological SST annual cycle. Because of the chaos in the climate system, the snow states in the different ensemble members in **Control** will evolve differently to reflect the potentially broad range of snow values that are consistent with system.

In the second ensemble experiment **ModBoth**, all members are forced to maintain precisely the same time series of key snow states (SWE and SCF) that were generated by one randomly chosen ensemble member of the **Control** experiment. All initial and boundary conditions in **ModBoth**, including atmosphere and SST forcing, are the same as the **Control**, except that the original snow states (SCF and

SWE) in the model are replaced. Thus, the coupling strength due to the snow forcing can be investigated.

To quantify the coupling strength, Koster et al. [2002] illustrated that the similarity of atmospheric states (such as temperature or precipitation) between the ensemble members, marked as Ω(**ModBoth**), has two distinct sources. In this experiment they are: (a) the prescribed snow boundary forcing and (b) background seasonal behavior that is measured by Ω(**Control**). Therefore, subtracting Ω(**ModBoth**) from Ω(**Control**) should isolate the impact of the prescribed snow boundary variables on the atmosphere variability. The difference Ω(**ModBoth**)-Ω(**Control**) is a good estimate of snow-atmosphere coupling strength. Similarly, the difference of the Signal-Total-Ratio, STR(**ModBoth**)-STR(**Control**), represents the increase of potential predictability due to snow-atmosphere coupling.

5.2 Temperature and precipitation coupling with snow

We focus mainly on temperature and precipitation in this study. The subscripts T and P represent air temperature and precipitation accordingly. We use daily mean time series and focus on the daily to monthly time scales of snow-atmosphere coupling.

Figure 5.1 shows the Northern Hemisphere Ω_T(**Control**) (the similarity among time-series of daily air temperature from the members of the **Control** ensemble) from March to June. In the **Control** experiment, the snow states are not

prescribed. Therefore, the temperature variation reflects the extent of variability as induced by the time variation of imposed boundary conditions or forcings (such as snow and soil moisture etc.). The larger Ω_T(**Control**), the stronger the similarity among the temperature time series. The largest values tend to cluster in eastern Asia, India and the center of North America. The eastern European and Tibetan regions show relative small values of Ω_T(**Control**), indicating the larger disagreement in the temperature evolution.

The change of temperature similarity from **Control** to **ModBoth**, Ω_T(**ModBoth**)-Ω_T(**Control**), should isolate the impact of prescribed snow states on the synoptic scale temperature variance. To quantify snow-atmosphere coupling strength, we use this change in similarity.

Figure 5.2 shows the snow-atmosphere coupling strength over the NH. During March (Figure 5.2.a), relative high values of Ω_T(**ModBoth**)-Ω_T(**Control**) concentrate in Eastern Europe, the Tibetan Plateau and the middle latitudes of North America. In contrast, the snow coupling strength in high-latitude regions is weak. From March to April (Figure 5.2.b), the coupling strength is suddenly weakened over most of the middle-latitudes. The possible reason for weaker coupling strength is the rapid snowmelt that dramatic diminishes the albedo effect while the lagged hydrological effect is still on the way. From May to June (Figure 5.2.c and 5.2.d), the coupling strengths generally move northward to the Polar Regions.

There are some slightly negative values of Ω_T(**ModBoth**)- Ω_T(**Control**) which mainly cluster in the low-latitude regions. Spurious negative values may occur due to the small ensemble size based on the random analysis. Koster et al. [2006] estimated that less than 1% of grid cells may have negative values in consecutive 6-day periods, based on a Monte Carlo method with 16-member ensembles. With ten members, those odds increase.

According to Koster et al. [2006], Ω can be interpreted as the fraction of the total variance that is "explained" by the imposed boundary condition. The highest values of Ω_T(**ModBoth**)-Ω_T(**Control**) are roughly 0.4, implying that snow cover perturbations could explain as much as 40% of the synoptic scale temperature variability in those regions.

Figure 5.3 shows the same quantity for precipitation Ω_P(**ModBoth**)-Ω_P(**Control**). Comparing this figure with the previous figure reveals two features: First and foremost, the snow cover's control on precipitation is weaker in general than its control on surface air temperature. This is no surprise, given that the snow albedo effect has a much stronger impact on the air temperature than the snowfall-stability feedback has on the precipitation. Secondly, the horizontal scale of snow coupling on precipitation is much smaller than it is on temperature. The distributions of Ω_P(**ModBoth**)-Ω_P(**Control**) are much more "spotty" than temperature. In the early spring (Figure 5.3.a and 5.3b), the snow's control on precipitation is mainly based on the snowfall-stability feedback. Beginning in May

(Figure 5.3.c and 5.3.d), the snow hydrological effect becomes the main impact on the precipitation.

Note that the response of precipitation to snow conditions is more complex than temperature. Although the surface energy and water fluxes are responsible for communicating these snow states to the boundary layer, the precipitation will also involve other processes, such as atmosphere stability, convective initialization and transient weather systems.

5.3 Vertical propagation of the coupling strength

5.3.1 Coupling strength in the vertical dimension

Is this strong snow-temperature coupling strength as shown in the previous section only limited to the surface layer? Could this coupling strength propagate in the vertical to reach the middle-levels of the atmosphere?

The snow coupling strength of air temperature at 850 hPa, 700 hPa , 500 hPa, and of surface pressure (PS) and planetary boundary layer height (PBLH) in March are shown in Figure 5.4. The patterns of Ω_T(**ModBoth**)-Ω_T(**Control**) at different pressure levels are similar to the pattern at the surface (Figure 5.2.a) although the magnitude generally decreases with height. There are still significant coupling strengths over the middle latitudes of Eurasia at 500 hPa (Figure 5.4.c). Although it is not very obvious, the pattern of strong coupling has a slight shift to the east from

lower to middle levels, indicating slight downstream advection by the prevailing westerlies. The boundary layer height also shows significant coupling strength with snow depth, especially near the Tibetan Plateau (Figure 5.4.e). However, the surface pressure (PS) shows relative weaker coupling strength (Figure 5.4.d).

5.3.2 Significance testing

Is this coupling strength at 500 hPa statistically significant? To answer this question, we implemented a simple re-sampling method to estimate the mean and variance of Ω, and then performed Student's t-test significance testing.

Using a form of the bootstrapping technique called Jackknifing, we estimate the precision of a sample statistic (medians, variances, percentiles) by constructing a number of re-samples of the existing dataset, each of which is obtained by randomly removing a subset of data from the original dataset. The advantage of jackknifing is its great simplicity - it is straightforward to apply the bootstrap method to derive estimates of standard errors and confidence intervals for complex estimators of complex parameters of the distribution, such as Ω. Disadvantages of bootstrapping are that while (under some conditions) it is asymptotically consistent, it does not provide general finite-sample guarantees, it assumes the sample well represents the population, and it has a tendency to be overly optimistic.

For Student's t-test, μ_x and μ_y are the n_x and n_y years average of a specific variable from any two cases, and S_x and S_y are the inter-annual variance of the variables. Then the optimal Student's t-test is given as

$$t = \frac{\mu_x - \mu_y}{\sqrt{\frac{S_x^2}{n_x} + \frac{S_y^2}{n_y}}} \qquad \text{EQ. 30.}$$

with n-1 degrees of freedom. This hypothesis test examines the significance of two variable mean differences relative to their own variances.

Figure 5.5.a shows the significant test for the difference of the Ω between **ModBoth** and **Control** experiments. The color shadings show the difference of the Ω of 500 hPa temperature from Fig 5.4c. The dots indicate that the difference of Ω is significant based on the jackknifing estimation. Generally speaking, if the difference of Ω is larger than 0.1, the difference is significant since the variance of **ModBoth** is far smaller than for **Control**. Most regions with higher values in difference are significant even in 500 hPa temperature. This significance test supports the conjecture that signals from snow-atmosphere coupling could propagate to the middle levels of the atmosphere.

5.3.3 Mechanism

By what mechanism is this coupling phenomenon propagated to the middle levels of the atmosphere? The thermodynamic or heat budget equation in the middle-lower levels of the atmosphere involves:

$$\frac{\partial T}{\partial t} = -U_h \bullet \nabla_h T - \omega(\frac{\partial T}{\partial z} + \frac{g}{Cp}) - \frac{1}{\rho Cp}\frac{\partial}{\partial z}(F^+ - F^-) + \frac{1}{\rho Cp}(\rho K_h \frac{\partial \theta}{\partial z}) + \dot{Q} \quad \text{EQ. 31.}$$

where the terms on the right hand side are advection by the horizontal wind $-U_h \bullet \nabla_h T$, subsidence due to vertical velocity $-\omega(\frac{\partial T}{\partial z} + \frac{g}{Cp})$, the divergence of the net radiative flux $-\frac{1}{\rho Cp}\frac{\partial}{\partial z}(F^+ - F^-)$ (both shortwave and longwave), thermal eddy diffusion $\cdot \frac{1}{\rho Cp}(\rho K_h \frac{\partial \theta}{\partial z}) \cdot$ and condensation heating $\cdot \dot{Q}$. Generally, radiation and turbulence are dominant processes in the boundary layer. The horizontal advection is often significant above the boundary layer.

Figure 5.5.b shows the profile of each term in the heat budget equation at the middle-lower level of atmosphere during typical deficient and excessive snow cover situations at middle latitudes in March obtained from the **Control** experiment. The deficient snow years were composited by the two lowest mean snow depth cases during March within the 10 ensemble members. Similarly, the excessive snow years are composed of the two largest mean snow depth cases in March. The temperature tendencies due to eddy diffusion, both at vertical and horizontal direction, are very close during deficient snow cases and excessive snow cases. The shortwave heating rates have a clear difference but the magnitudes are relatively small (less than 0.05 K/day). In contrast, the longwave heating and condensation heating terms show large differences. During excessive snow cases, the stability increases due to the stable boundary layer, leading to less condensation heating at the lower levels of atmosphere. Relatively colder air temperatures also lead to weaker longwave

radiative cooling. On the other hand, there is more condensation heating and stronger radiative cooling during the deficient snow cases. As a result, the meridional heat transport is strong/weak during the deficient/excessive snow cases.

The heat budget analysis indicates the lower boundary forcing induced by anomalous snow cover influences the lower to middle level atmosphere mainly by longwave radiation and condensation heating. This influence could reach the middle levels of the atmosphere, as shown in Figure 5.4

5.4 Predictability associated with snow-atmosphere coupling

Signal-to-Total Ratio (STR) is a measurement of predictability by comparing the signal to the total variability associated with the ensemble forecast. Similar to the index Ω, STR also ranges from 0 to 1 with bigger values indicating the larger predictability.

The enhancements of air temperature predictability due to prescribed snow boundary conditions represented by the difference of STR between **ModBoth** and **Control** (STR_T(**ModBoth**)-STR_T(**Control**)) are shown in Figure 5.6. The pattern of enhancement is very similar to the coupling strength (Figure 5.2). In the regions of higher values of Ω_T(**ModBoth**)-Ω_T(**Control**), the predictability differences (STR_T(**ModBoth**)-STR_T(**Control**)) are also larger. These consistencies in

predictability and coupling strength suggest the snow-atmosphere coupling can enhance the potential predictability of the ensemble forecast.

Similarly, Figure 5.7 shows the predictability enhancement in precipitation by prescribed snow boundary conditions. The enhancements are smaller than for temperature, as expected.

In this series of experiments, we forced the model with exactly same climatological SST cycle. The enhancements of potential predictability in STR with boundary snow forcing are consistent with the snow-atmosphere coupling strength as shown in the previous section, indicating this coupling contributes to the potential climate predictability.

5.5 The Gain of snow-atmosphere interaction

Figure 5.8 shows the Gain of air temperature variability due to snow-atmosphere coupling from March to June, by comparing the mean standard deviations between **Control** and **ModBoth**. Where the Gain is larger than 1, it indicates that the snow coupling or interaction will amplify the variability. Otherwise, the snow coupling will suppress the climate variability. From March to June, the Gain in the surface air temperature is larger than 1 over most of the mid-latitudes of Eurasia and the North American continent. The large Gain areas are consistent with strong snow-atmosphere coupling strength shown as Figure 5.2. There are some scatter areas, mainly located over Scandinavia, Greenland and

occasionally the eastern margins of Asia and North America, where the Gain is less than 1.

Similar patterns of Gain also can be observed at difference pressure levels (Figure not shown). Generally, the Gains decrease with height. However, the strong couplings are still evident at the 500 hPa level. This feature further supports the idea that the snow-atmosphere coupling signal propagates to the middle-levels of the atmosphere as shown on Figure 5.4.

For precipitation, the Gain due to snow-atmosphere coupling displays a complicated, irregular pattern as shown at Figure 5.9. During March and April, there are significant areas at high-latitudes where the Gains of precipitation are less than 1, indicating suppression of precipitation due to stability-snowfall feedback. However, in the low and middle-latitudes, the Gains of precipitation are more than 1, reflecting the positive evaporation-precipitation feedback due to the snowmelt hydrological effect. From May to June, the Gains in most areas are larger than 1, suggesting the snow hydrological effect is mainly to amplify the precipitation variability.

These results demonstrate contrasting impacts of snow-atmosphere coupling on temperature and precipitation. For air temperature, whether it is the albedo effect during the early ablation phase or the hydrological effect in the later stage, the coupling will amplify the temperature variability. However, the snow atmosphere coupling has a different impact on precipitation based on snowmelt timing. Before

snow melt, the albedo effect induces negative stability-snowfall feedbacks that will depress the variability. After the snow melts, the hydrologic effect induced by the evaporation-precipitation feedback will amplify the variability.

5.6 Sensitivity to SCF parameterization

We have demonstrated strong snow-atmosphere coupling by the ideal snow simulations **Control** and **ModBoth**. In any snow scheme, the SCF parameterization is critical for computing the ground albedo.

Figure 5.10 demonstrates the sensitivity of albedo effect to the snow depth that is derived from SWE. The panels 5.10.a and 5.10.b show the mean and standard deviation of snow depth (SD) within the ten ensemble members for March in experiment **Control**. The snow depths increase northward from the middle latitudes except over the high terrain such as the Tibetan plateau and Rocky Mountains. However, the standard deviations are relative larger at middle latitudes indicating that there is considerable variability over these regions. Figure 5.10.c shows the change of snow cover fraction with snow depth (*df/dh*, the slope of the parameterization curve from Figure 3.2) at the climatological mean snow depth of March. With relatively larger variability in snow depth, the snow cover fraction in the middle latitudes experience large sensitivity to the change of snow depth. Multiplied by the mean incident shortwave radiation (Figure 5.10.d), the sensitivities of snow albedo effect to the change in snow depth are demonstrated in

Figure 5.10.e. This sensitivity pattern is consistent with the snow-atmosphere coupling pattern quantified by numerical experiments shown in Figure 5.2.a.

The slope of the SCF parameterization curve *df/dh* is a key factor controlling variability of the snow albedo effect in any land model. The coupling strength computed by ideal snow simulations is strongly impacted by this key parameterization. Importing realistic SCF observed by satellite will remove this model-dependent sensitivity.

5.7 Discussion

In general, impacts of snow anomalies on the atmosphere are strong only in the unstable snow transition zone in middle latitudes, between stable snow-covered high latitude region and snow-free subtropics (Figure 5.11). Model experiments show that there are what we might call "cold spots" of snow-atmosphere coupling in these unstable snow transition zones because there exists high sensitivity of the albedo effect to the snow change and relatively large incident shortwave radiation. In the high latitudes north of the edge where snow cover retreats to Polar Regions from spring to summer, snow fractions are relative larger and less sensitive to snow depth change. There the albedo effect is mainly controlled by the weak incident solar radiation. There are no snow albedo effects in the low latitudes even though there is plenty of incident solar radiation. Only in the transition zone between the stable snow area and snow free area, where there are strong albedo changes

induced by snow variations and relatively large incident radiation, do variations in snow state have strong impacts on the atmosphere.

The Tibetan Plateau, located in the 25°-45° latitude band, demonstrates strong snow atmosphere coupling due to its high elevation. Shallow snow can persist for long periods in this elevated plateau. With strong incident solar radiation, high elevations give the Tibetan Plateau a strong albedo effect. Observational studies have found significant connections between snow anomalies over Tibet and the Asian monsoon [*Wu and Qian*, 2003a; *Xu et al.*, 2009b].

The snow–atmosphere coupling could propagate to the middle levels of atmosphere (500 hPa) although the impact decreases with height. Longwave radiation and convective heating are the main mechanisms for vertical propagation of the impact of snow anomalies.

The enhancements of potential predictability due to the snow-atmosphere coupling are very consistent in location with the strong coupling region; that implies the contribution of snow-atmosphere coupling to climate predictability is mainly local, without significant downstream effect as hypothesized by Xu et al. [2009a].

The coupling strength in March could be largely explained by the snow albedo effect. The theoretical estimate of the sensitivity of the albedo effect from observations is consistent with the numeric experiment results. However, the slope of SCF parameterization *df/dh* is a model-dependent factor to control the sensitivity of albedo effect.

The snow atmosphere coupling and interaction will increase the variability of air temperature (Gain > 1). However, the precipitation shows different features: before snow melt, the negative feedback can suppress snowfall variation; after snow melt, the snow hydrological effect with evaporation-precipitation feedback can amplify the rainfall variability.

Missing from this idealized study, however, is an estimation of the degree to which the experiment results are model dependent. In particular, the interannual variability of snow, including both SWE and SCF, is underestimated by the CLM model as analyzed in the previous chapter. These underestimations in the inter-annual variability will weaken the snow-atmosphere coupling in the model simulation. Importing realistic snow information based on satellite observations or data assimilation into the model is the next step.

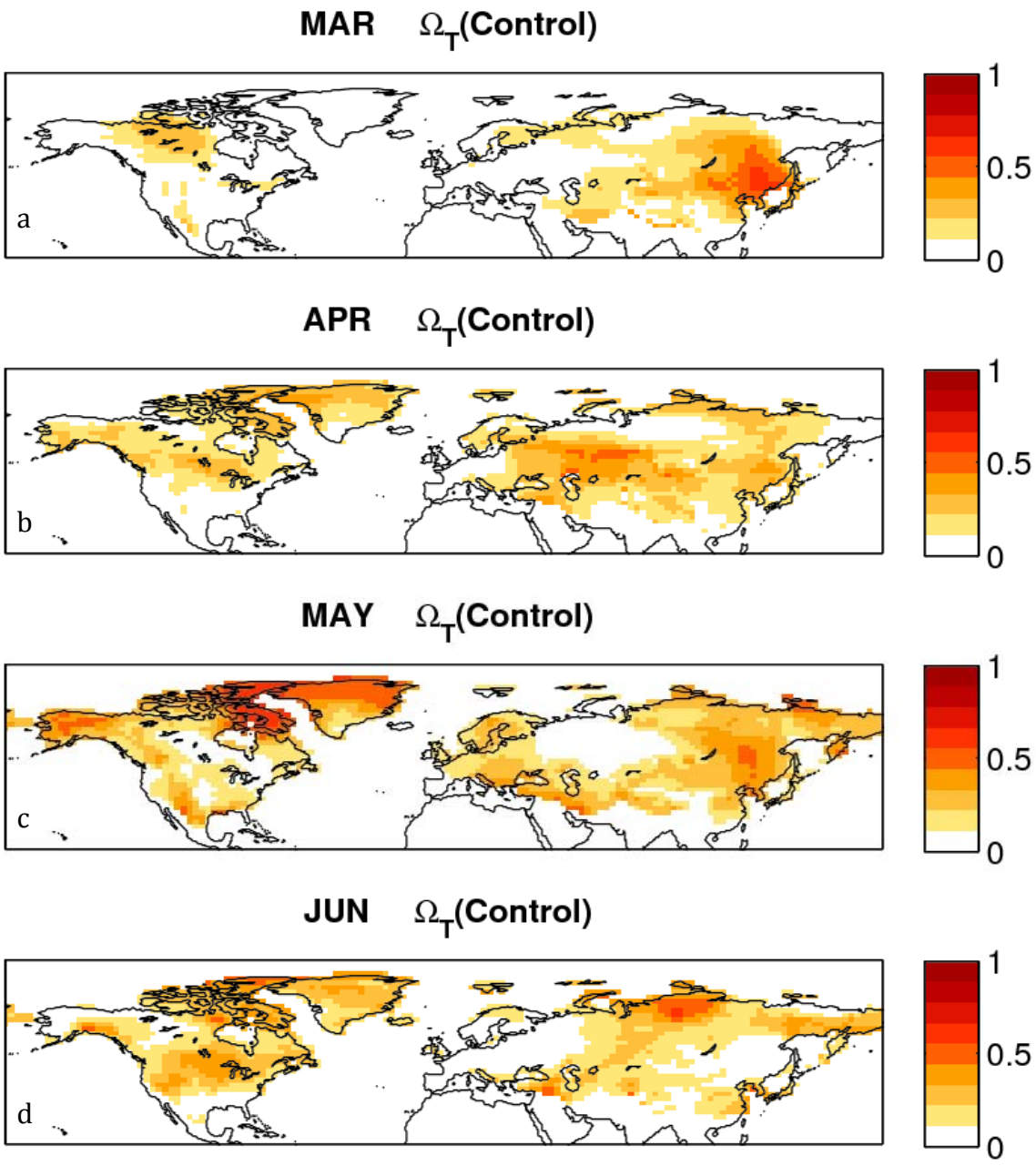

Figure 5. 1 The intra-ensemble similarity of surface air temperature time series Ω_T within the Control experiment from March to June

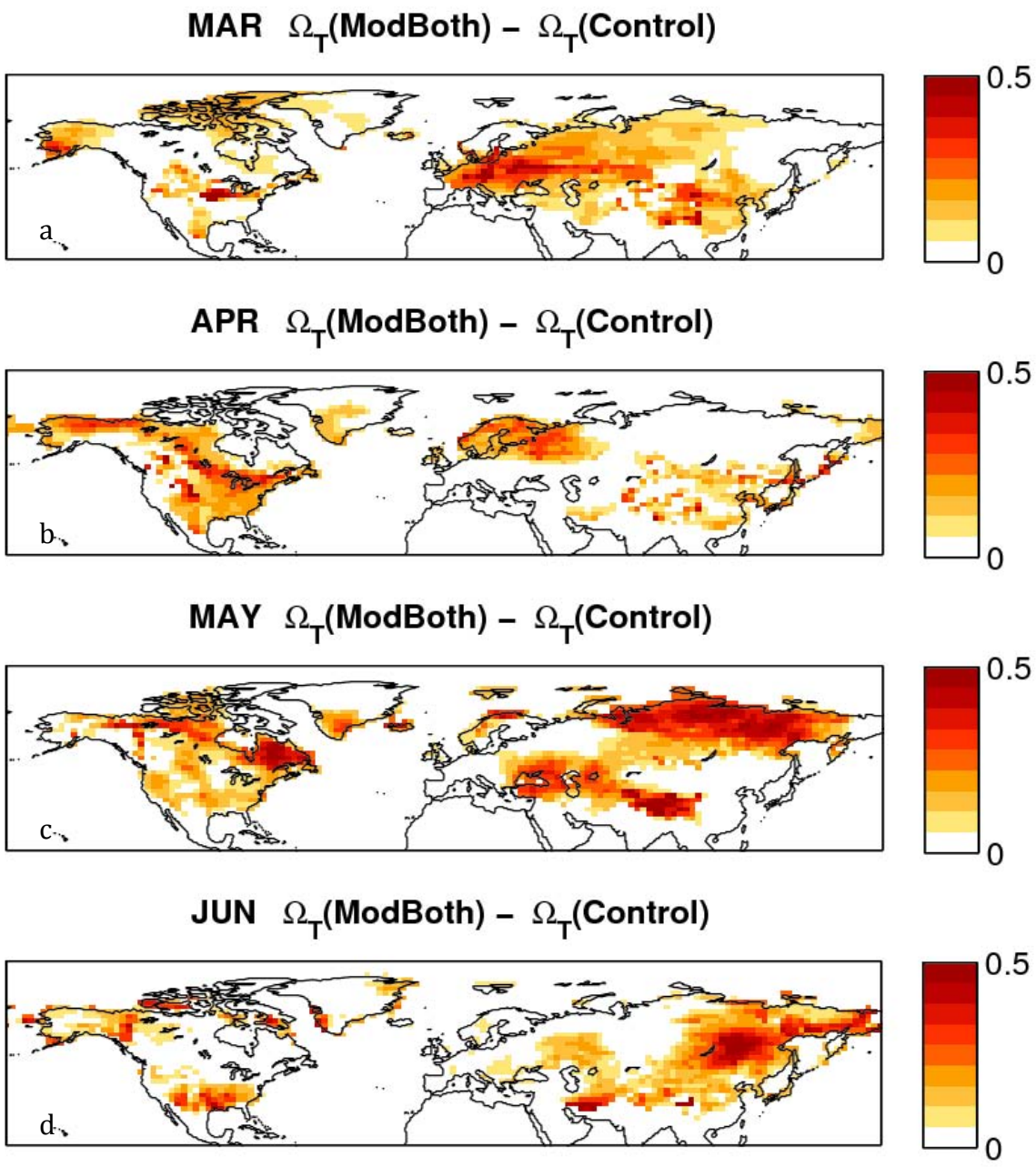

Figure 5. 2 The coupling strength of surface air temperature (represented by the change of similarity from ModBoth to Control experiments Ω(ModBoth)-Ω(Control)) from March to June.

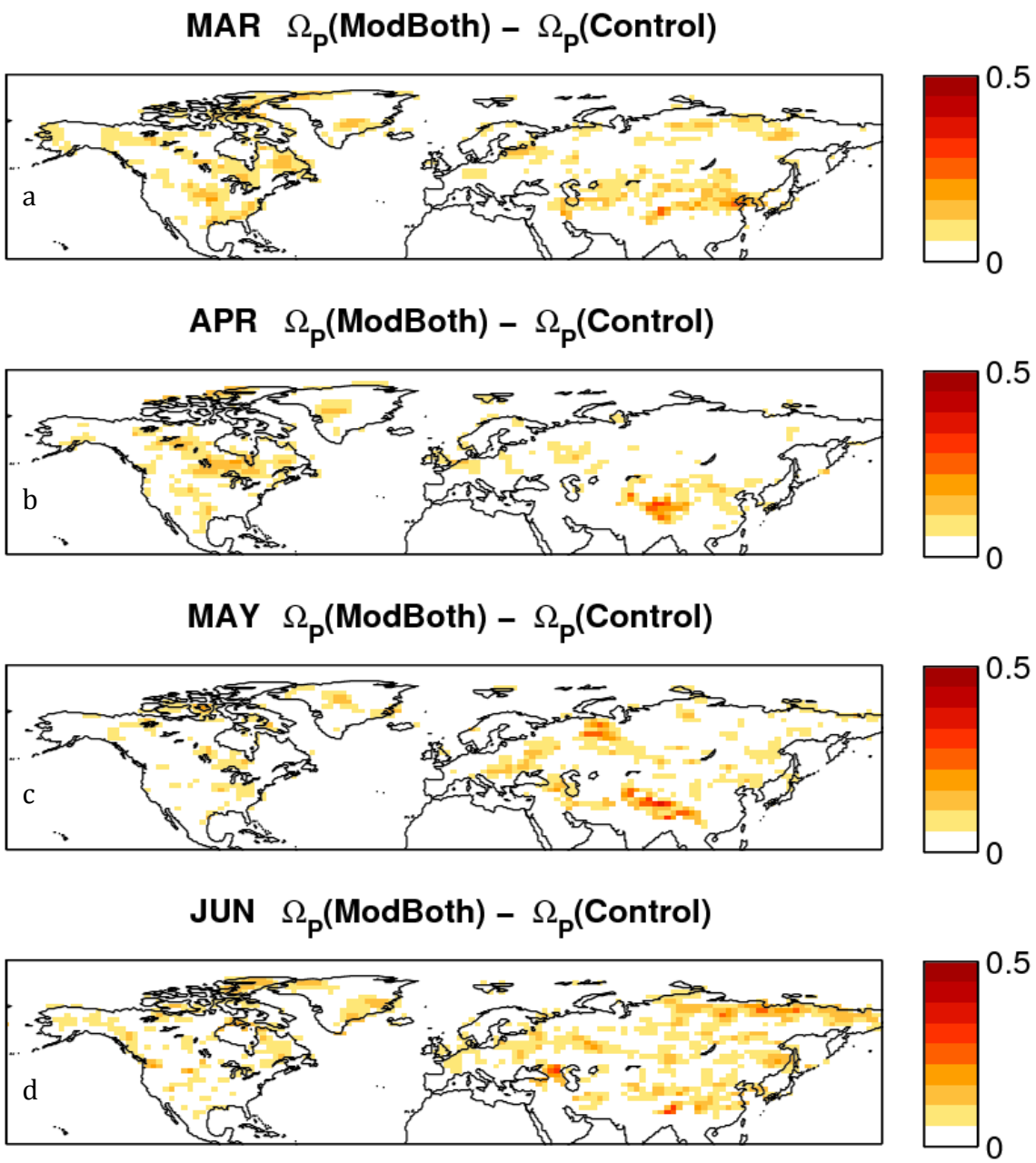

Figure 5. 3 As in Fig 5.2 for precipitation.

MAR 850hPa Ω_T(ModBoth) – Ω_T(Control)

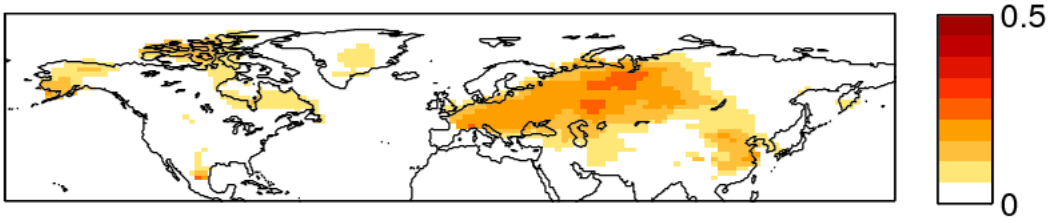

MAR 700hPa Ω_T(ModBoth) – Ω_T(Control)

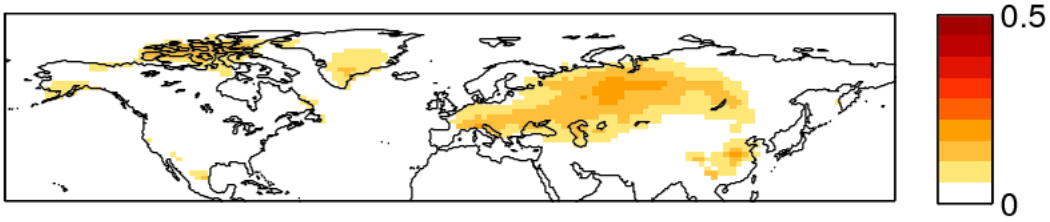

MAR 500hPa Ω_T(ModBoth) – Ω_T(Control)

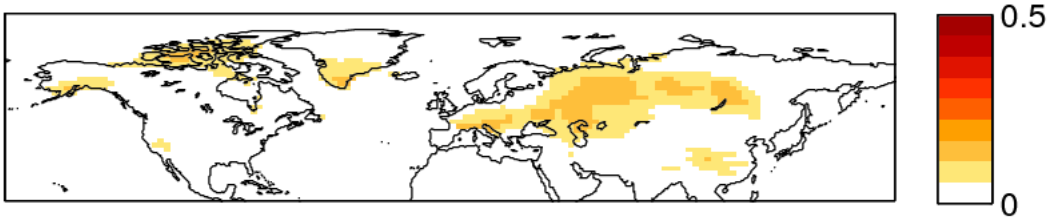

MAR Ω_{PS}(ModBoth) – Ω_{PS}(Control)

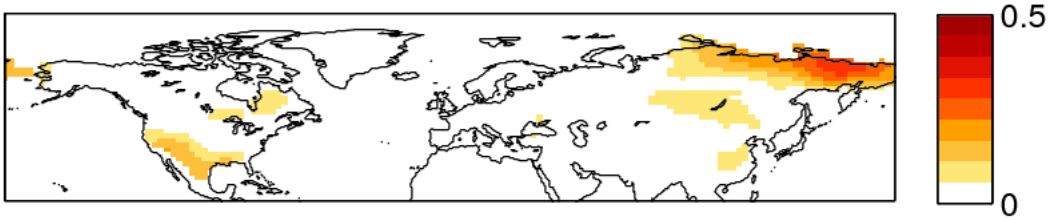

MAR Ω_{PBLH}(ModBoth) – Ω_{PBLH}(Control)

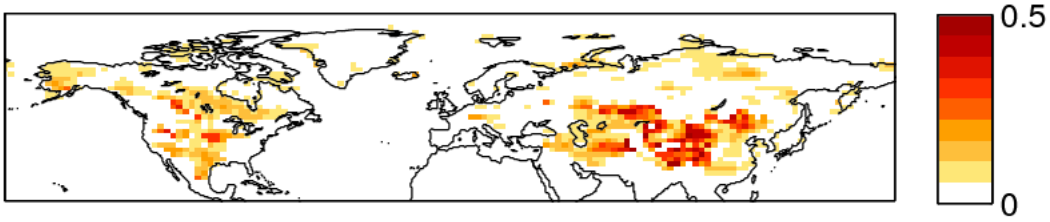

e

Figure 5. 4 The coupling strength of air temperature at 850 hPa (T850), 700hPa (T700), 500 hPa (T500), surface pressure (PS) and planetary boundary layer height (PBLH) in March.

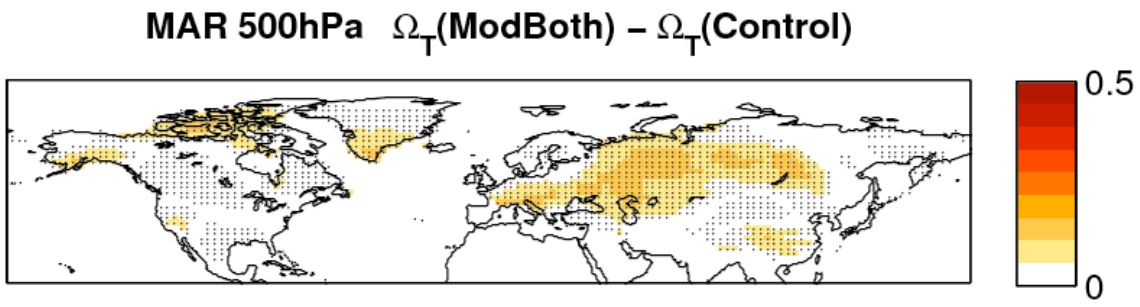

Figure 5. 5.a The significance test for the difference of the Ω between ModBoth and Control. The shading shows the difference of the Ω of 500 hPa temperature. The dots indicate the difference of Ω is significant according to the Student's t-test based on the jackknifing estimation

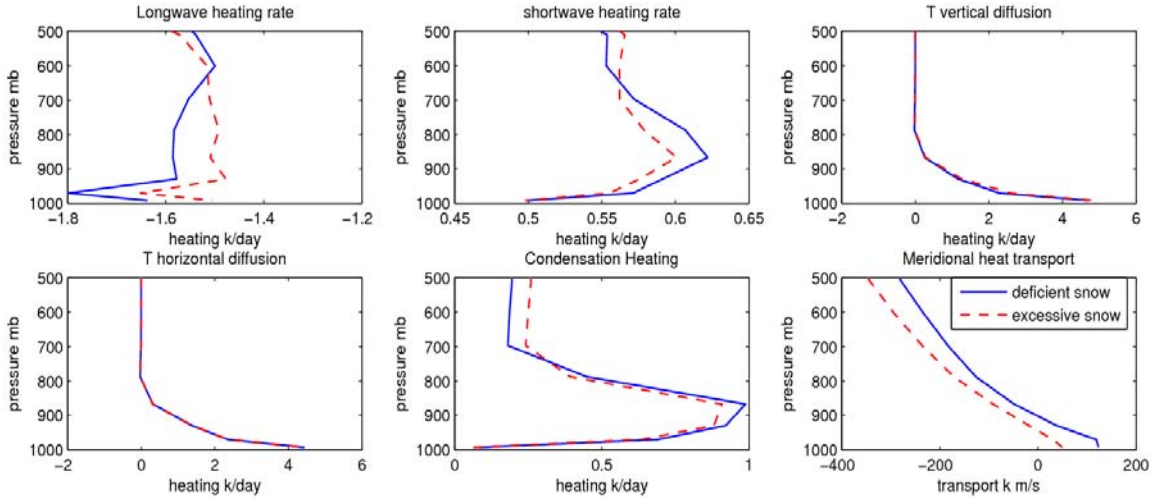

Figure 5.5.b The heat budget over the lower troposphere (500-1000 hPa) during typical deficient snow and excessive snow at middle latitudes (30-60°) during March.

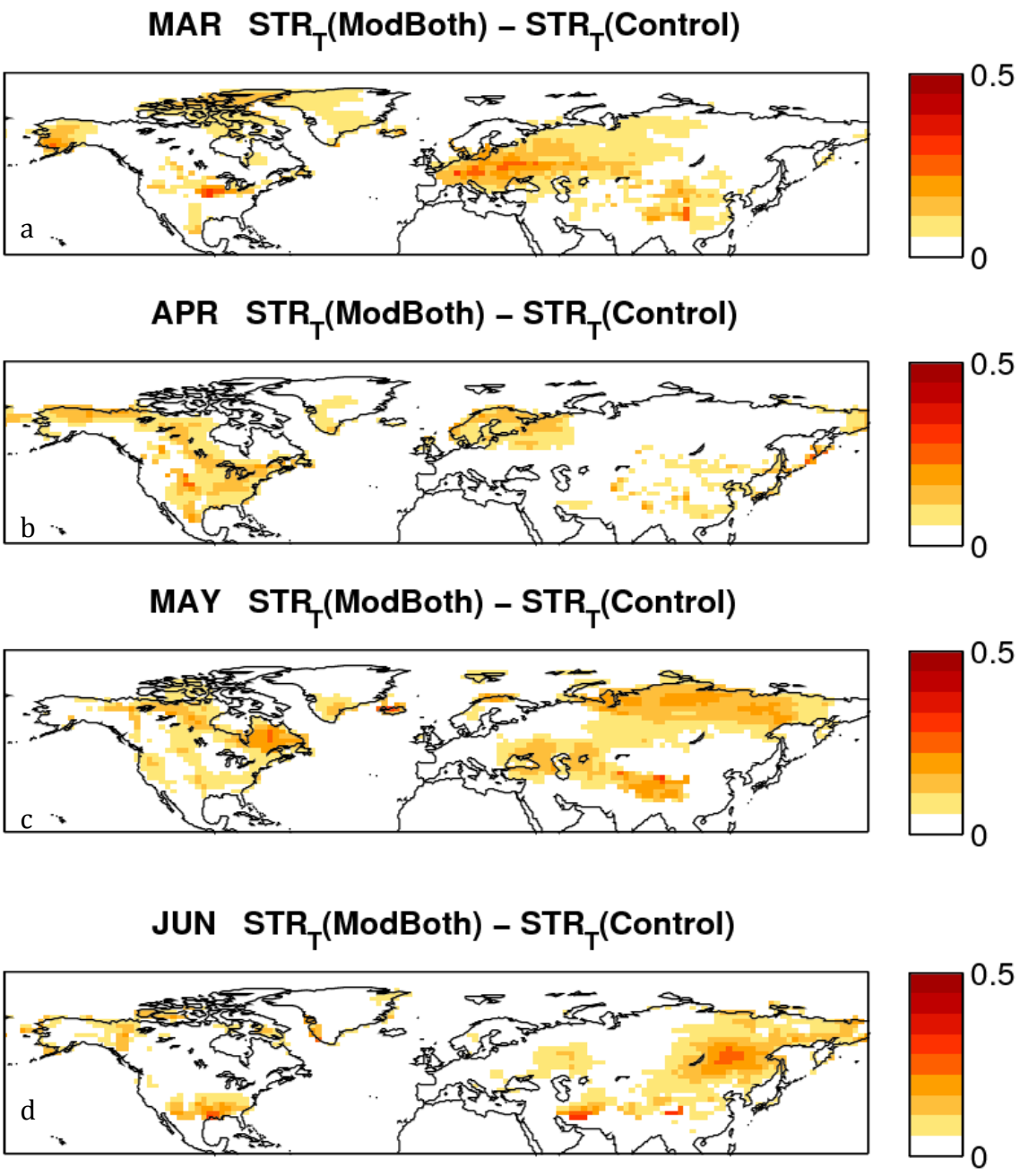

Figure 5. 6 The air temperature predictability enhanced by prescribed snow boundary conditions (the difference of Signal-to-Total-Ratio between Control and ModBoth experiment) from March to June.

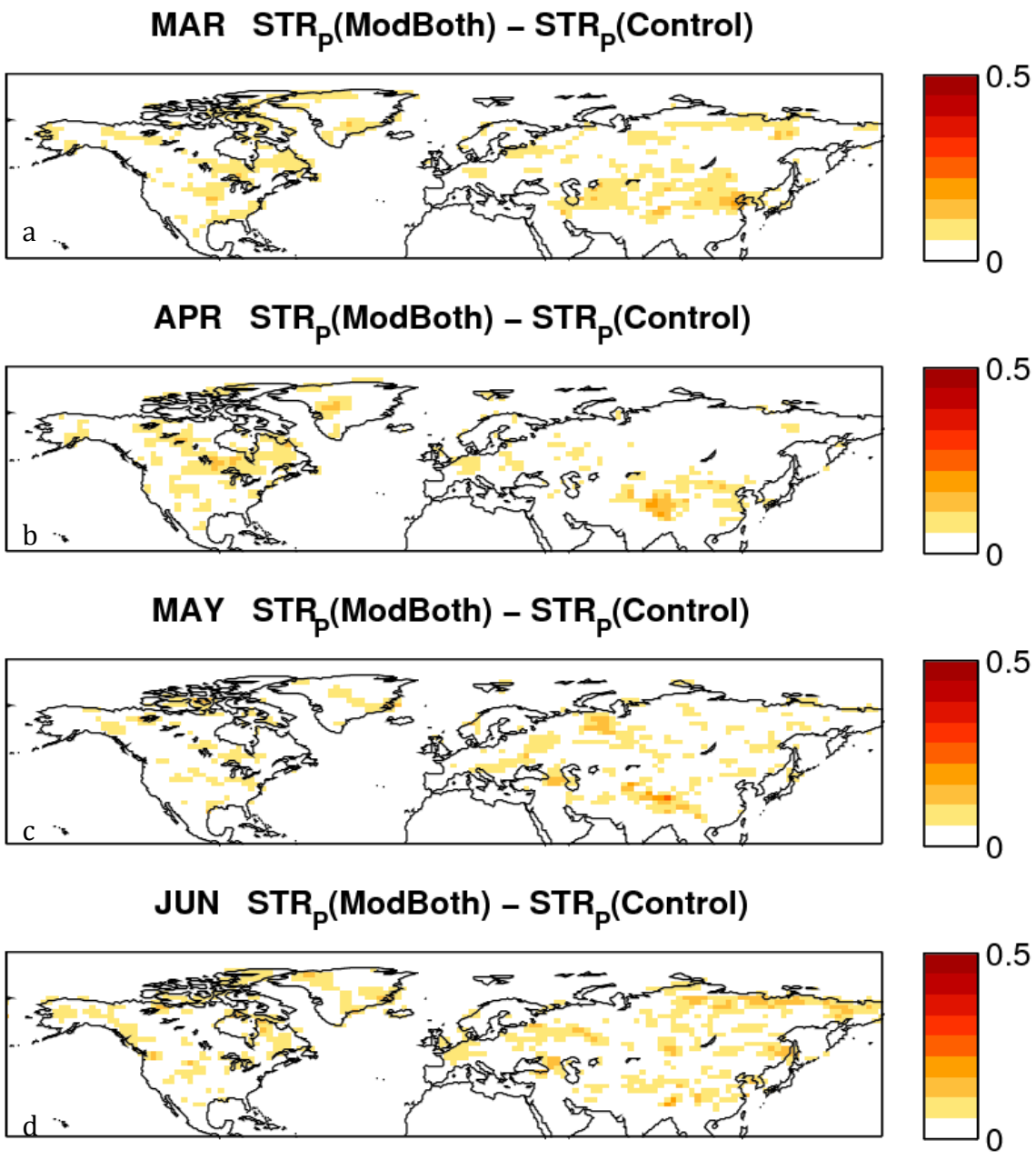

Figure 5. 7 As in Fig 5.6 for precipitation

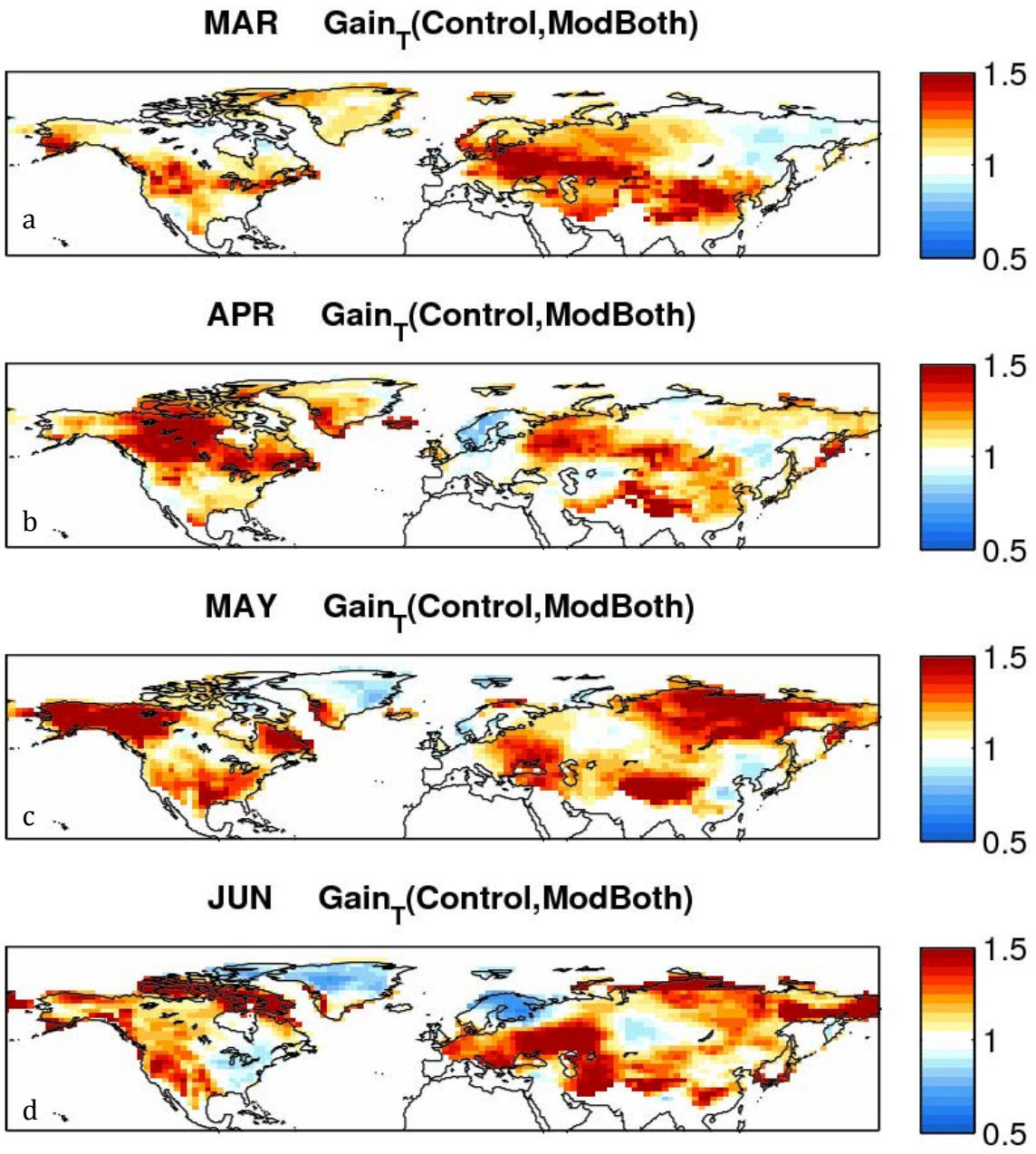

Figure 5. 8 The gain in air temperature variability due to snow-atmosphere coupling between Control and ModBoth experiment.

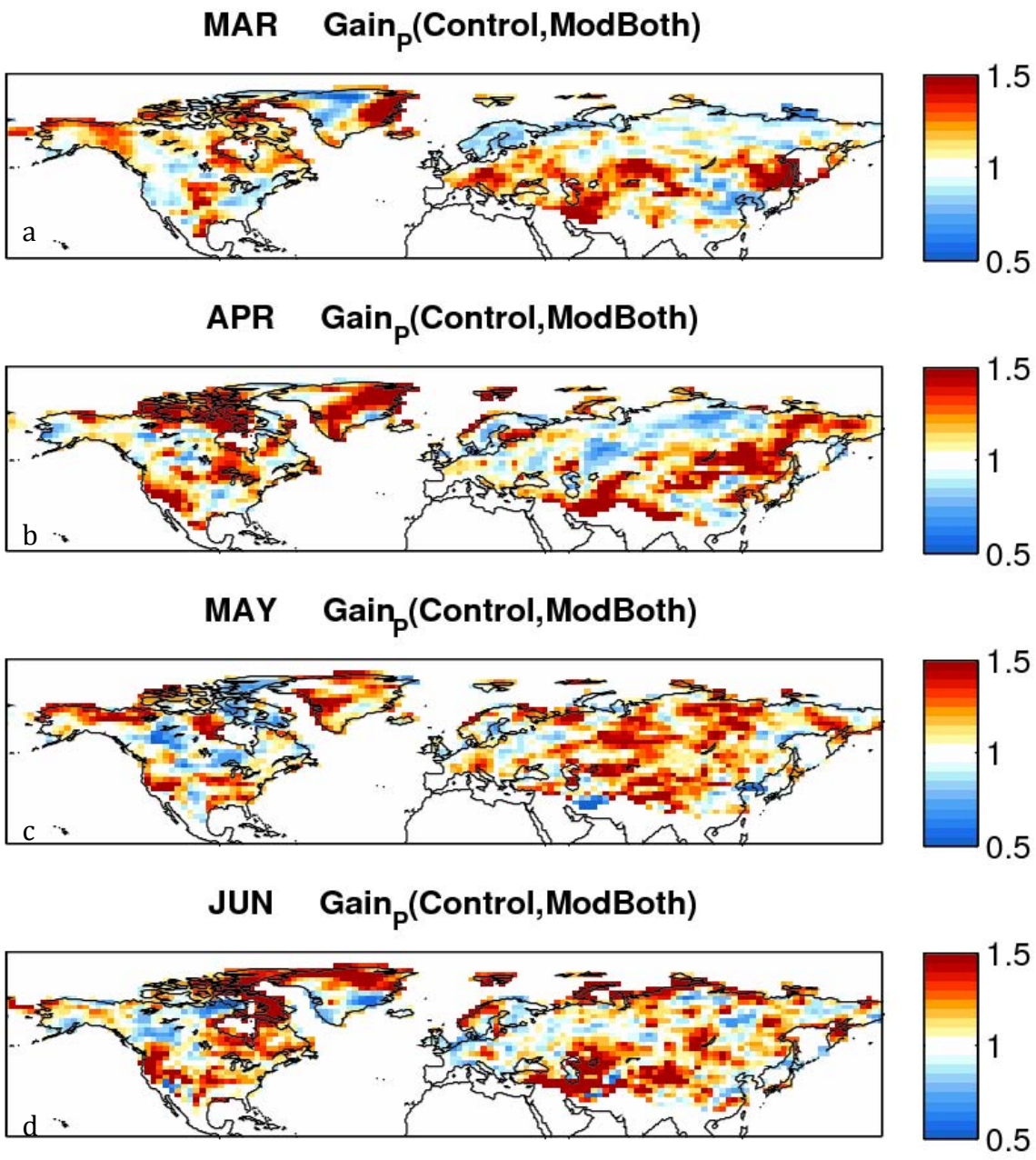

Figure 5. 9 the same as Figure 5.8, but for the precipitation.

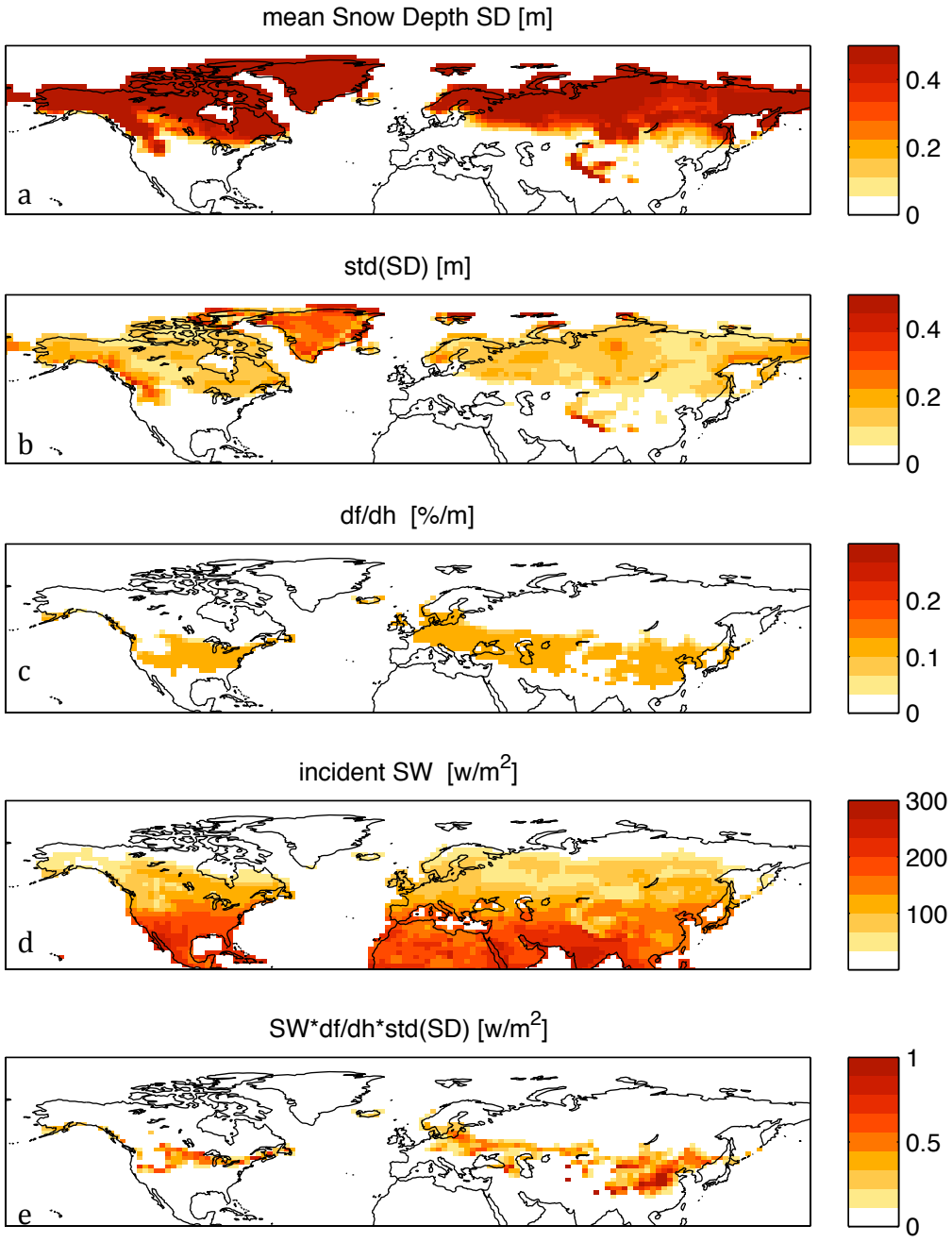

Figure 5. 10 The sensitivity of net solar radiation to the snow albedo effect at March.

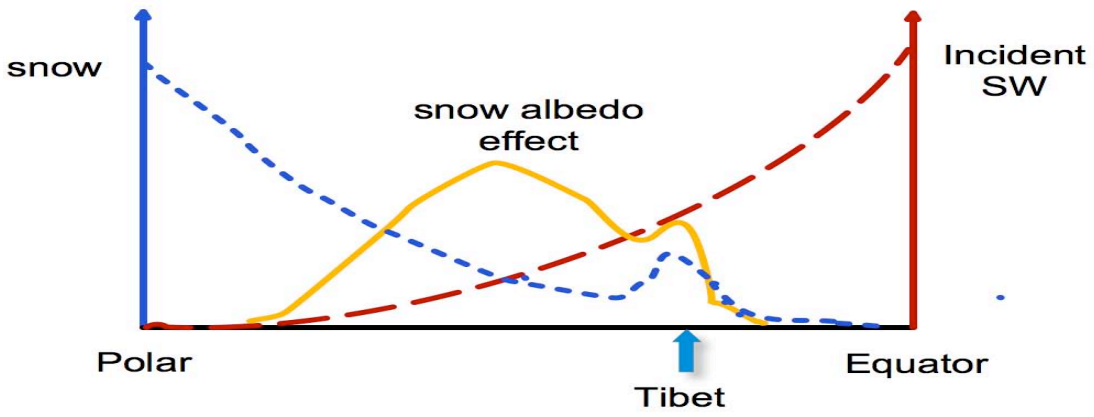

Figure 5. 11 Schematic of the snow albedo effect. The right axis is the incident solar radiation, the left axis indicate the snow depth and snow cover fraction. The maximum snow albedo effect is located at the middle latitude transition zone

CHAPTER 6. COUPLING STRENGTH AND PREDICTABLITY DUE TO SNOW ALBEDO EFFECT

6.1 RealSCF experiment

The **RealSCF** experiment is similar to the **ModBoth** experiment except the snow cover fraction is prescribed from realistic observations based on remote sensing. Each ensemble member in **RealSCF** takes the specified realistic surface SCF prescribed from MODIS remote sensing retrievals during 2000-2009. Meanwhile, the SWE at each time step is still read from the same S1_state data file as in the **ModBoth** experiment. The main purpose of the **RealSCF** experiment is to investigate how the simulation will be improved by specified realistic SCF without parameterization. Since the land surface albedo is a linear function of snow cover fraction, the snow albedo effect is largely determined by the SCF. Then any predictability enhancement of ensemble **RealSCF** compared with ensemble **ModBoth** is due to the contribution of accurate representation of the snow albedo effect.

6.1.1 CDF-matching

Comparing MODIS remote sensing and CLM land surface simulations, the satellite retrieval of SCF shows a distinct systematic bias due to errors arising from the SD-SCF parameterization in CLM (Figure 4.3). A statistical scaling approach bias correction scheme, CDF-matching, is proposed and tested to remove the possible bias in the **RealSCF** experiment. Comparing with the experiment **ModBoth**, we can analyze the impact of model bias and the benefit from observational information.

To correct the systematic difference between the MODIS retrieved and the model derived SCF, the CDF-matching approach of *Reichle and Koster* [2004] was employed by scaling MODIS SCF mean and variability to match the climatology of the CLM model. The strategy for this bias correction is to map the cumulative distribution function (CDF) of the model to the CDF of the satellite retrieval by scaling the satellite retrievals (Figure 6.1). All available MODIS observations are used for the CDF-matching during a common training period (2000-2009). Note that CDF-matching in theory can correct all moments of the distribution, but may be subject to statistical errors due to the limited sample size.

Figures 6.2 and 6.3 show the difference in mean (top) and standard derivation (bottom) of MODIS SCF minus CLM during March before and after CDF-matching. Matching of the CDF is done separately at each grid point. All biases in the climatology (monthly mean in the top panel) have been successfully removed. Comparing the interannual variability (standard derivation in bottom panel), biases

also have been greatly reduced. There are only some small differences in the standard deviations in the middle-latitudes where the snows are unstable.

6.1.2 Sub-grid heterogeneity

To prescribe the MODIS SCF for each CLM grid-point, we must specify the snow coverage at the sub-grid scale. A grid box in CLM is designed as a nested sub-grid hierarchy composed of multiple land-units, snow/soil columns and Plant Functional Types (PFT) in three sub-grid levels [*Oleson et al.*, 2004b]. In the first level, each grid cell has different land-units, which are intended to capture the spatial pattern of sub-grid heterogeneity, including glacier, lake, wetland, urban, and vegetated areas (figure 6.4). Based on the MODIS snow cover fraction, we prescribed the SCF over each land-unit based on the following assumption:

- 100% SCF over glaciers
- 0% SCF over wetlands (all snowfall immediately melts)
- 100% SCF over frozen lakes and 0% SCF over non-frozen lakes, determined by the lake surface temperature.
- 0% SCF over the urban fraction (all snowfall is immediately removed)

The remaining part of SCF in each grid-cell is ascribed to the vegetated land-unit. In this experiment, we apply the same SCF over all PFTs in the vegetated land-unit.

6.1.3 Evaluation of bias-removing

Based on the four key criteria prescribed in section 3.6, we assess the effect of bias-removal on the simulated temperature. The NCEP/NCAR reanalysis [*Kalnay*

et al., 1996] air temperature data are used to evaluate the skill before and after the CDF-matching.

Figure 6.5 shows the evaluation of the surface air temperature (T2m) of the experiment with prescribed MODIS observed SCF without CDF matching (denoted as **F**) against re-analysis 1 data (**R1**) using four different indices. In the root mean square error (RMSE) map, the errors for temperature in the Tropics are smallest and generally increase with latitude. In the high latitude regions of North America and Eurasia, the RMSE is largest, reaching 6-8 K. There are relatively large RMSEs in the major mountainous terrains, such as the Tibetan Plateau and the Rockies. In the R square map, the lower values are also located in the topical and lower-latitude regions and generally increase with latitude. In contrast, however, the higher R square indicates the better agreement of inter-annual variability between observations and simulations. This implies the simulation with prescribed snow fraction performed better in the high latitudes, especially in the regions with large annual cycle of temperature and precipitation. There is almost no correlation between observed and simulated values in the tropics even though the RMSE is lower in those regions. From the percent of bias map (PBIAS), over-predictions (PBIAS > 1) dominate over the land except a few regions with slight under-prediction (PBIAS <1). The Nash-Sutcliffe Coefficient of efficiency (NSE) in most snow regions is close to the 1, which means there is agreement between the observed and predicted values. In the tropical regions, however, the NSEs are less

than 0 indicating prescribed snow fraction simulation imparts no skill in those regions compared to a climatological forecast.

Figure 6.6 is the same as Figure 6.5, but using SCF adjusted by CDF-matching (marked as **NF** simulation). All four parameters show similar patterns and distributions as the **F** simulation. Figure 6.7 shows the difference of forecast skill between **F** and **NF** simulations. In the RMSE difference map (upper panel), positive values indicate a better simulation (smaller RMSE) by using adjusted SCF after CDF-matching (**NF** experiment). On the other hand, the negative values indicate larger RMSE (worse simulation) after CDF-matching. In the high-latitude regions of Siberia and Greenland, the RMSE is reduced after bias correction. But over most of the Eurasian continent and North America, the RMSE is slightly increased with bias correction (**NF** case). Comparing with the map of differences of SCF in CLM with MODIS (Figure 5.3), the RMSE improvements agree well with the region of larger bias. Since the RMSEs increase with latitude and maximize over high-latitude regions, the bias correction improves the simulation in these most erroneous regions. However, bias corrections do not improve the simulation in middle-latitude regions since the CDF-matching artificially adjusts the variability of snow (at daily, weekly and seasonal time scales), although the mean climatology biases are removed.

Based on the map of differences in percent of bias (PBIAS), however, the bias-correction by CDF-matching shows obvious improvements at high-latitudes,

but without significant effect at middle to lower-latitude regions. Since the CDF-matching can reduce the bias in temperature between model simulation and reanalysis data, we used MODIS SCF after CDF-matching in the **RealSCF** and **RealBoth** experiments.

6.2 Coupling strength and predictability due to snow albedo effect

As mentioned previously, the only difference between **RealSCF** and **ModBoth** is that the specified SCF is from different sources. The coupling strength and predictability differences between **ModBoth** and **RealSCF** are contributed only by the snow albedo effect.

Figure 6.8 shows the coupling strength (the difference of intra-ensemble similarity between **ModBoth** and **RealSCF** experiments) for air temperature (2m height) from March to June. During March and April, the coupling strengths are relatively weak and concentrated in the middle latitudes. Only a few patches of higher values are located in Eastern Europe, Tibet and the Great Lakes. Beginning in May, the stronger couplings move to high latitudes and altitudes, inculding Siberia and the Far East. One noteable feature is the Tibetan pleatau, displaying a strong coupling during May. There is strong coupling over the Middle East in May and June that cannot be explained by the snow albedo effect. Detailed investigation indicates those false signals may be due to commission errors in MODIS retreivals that mistake some clouds as the snow.

Simaliar to the ideal snow evolution **Control** experiment, the coupling strength of precipitation is very weak and scattered (Figure 6.9); far less robust than the air temperature response.

Figure 6.10 shows the predictability enhancement (the difference of STR of **ModBoth** and **RealSCF** experiments) for air temperature (2m height) from March to June. The distribution patterns of predictability enhancement are very similar to the coupling strength, although notably less in magnitude. The improvements in STR by prescribing realistic SCF are mainly due to the snow albedo effect.

The gains of temperature variability due to the albedo variation by snow are shown in Figure 6.11. During March, there is some small amplification in variabilities of temperature (Gain>1) at middle latitudes corresponding to the strong snow-atmosphere coupling regions. However, There are no significant gains or even decreasing variabilities (Gain< 1) in the high latitude regions. From April to June, the amplification regions move northward toward the pole. There are still significant temperature gains over Tibet and its downstream region.

The decreasing temperature variabilities at high latitudes are probably due to the high sensitivity of SCF to SD in the parameterization in **ModBoth**. In the high latitudes, snow is relatively stable and keeps SCF steady before snowmelt; however, the SCF will change via decreasing SD by gravity compaction in the model, even while the SWE remains constant. This deficiency in SCF parameterization will artificially produce some “albedo effect” noise at high latitudes. On the other hand,

the SCF obtained from MODIS is very steady at high latitudes prior to snowmelt. That will cause a decrease of air temperature variability at high latitudes.

Similarly, there are some small decreases of precipitation variability at high latitudes (figure not shown). The reason is the stable boundary layer (SBL) that is a ubiquitous feature over snow at high latitudes, due to the strong snow albedo cooling effect. It is the combined effect of the strong reflection of shortwave (visible) radiation and longwave (infrared) radiational cooling from the snow surface (high emissivity). The net loss of radiation will further cool the atmosphere from below, with low absolute humidity, increasing the stability of the boundary layer and then frequently lead to cloud free conditions. This cloud-free condition will further increase the longwave loss and reinforce the stability of boundary layer.

6.3 Snow albedo sensitivity index

In the previous analysis, we found that any variations in albedo, due to change in SCF, will only have an effect when a sufficient supply of shortwave radiation is available. We can define an index to quantify the climate forcing due to the snow albedo effect.

$$SASI = SW\downarrow * \frac{df}{dh} * \sigma(h_{sno}) * \Delta\alpha \qquad \text{for model SCF parameterization} \qquad \text{EQ. 32.}$$

$$SASI = SW\downarrow * \sigma(f_{sno}) * \Delta\alpha \qquad \text{for SCF observations} \qquad \text{EQ. 33.}$$

where $SW\downarrow$ is the average incident solar radiation for each month, $\sigma(h_{snow})$ and $\sigma(f_{snow})$ are the standard deviations of snow depth (or SWE depending on model) in the model or SCF from observations for same period. $\Delta\alpha$ is the average albedo difference of the snow surface with snow-free land surface (tunable, 0.4 in here). The *df/dh* are the slope of SD-SCF parameterization.

Figures 6.12 and 6.13 show the snow albedo sensitive index obtained from the CLM model **Control** run and MODIS SCF retrievals from March to June. The snow albedo sensitivity index map obtained form the CLM model (Figure 6.12) displays similar patterns compared to the snow-atmosphere coupling strength obtained from **Control** and **ModBoth** (Figure 5.2). The region of strong coupling strength shows reasonable movement from middle-latitudes to the polar region during the snow ablation period from March to June. However, the snow albedo sensitivity index obtained from MODIS SCF retrievals displays different patterns that agree much more with the snow atmosphere-coupling strength obtained from **RealSCF** (Figure 6.8). This simple snow albedo sensitivity index can capture major patterns of the effects of snow albedo simulated by **RealSCF** experiment. We can use this simple index based on model or observed data to get a rough insight into how strong the albedo effect is without employing a complicated land-atmosphere coupling model.

6.4 Snow albedo effect

The land surface albedo with snow is given as:

$$\alpha = (1 - f_s) * \alpha_{bg} + f_s \alpha_s = \alpha_{bg} + f_s(\alpha_s - \alpha_{bg}) \qquad \text{EQ. 34.}$$

where f_s is SCF. To simplify, we assume the background albedo α_{bg} and snow albedo α_s are constant or do not change with latitude, then the change of albedo in the meridional direction is

$$\frac{d\alpha}{dy} = \frac{df_s}{dy}(\alpha_s - \alpha_{bg}) \qquad \text{EQ. 35.}$$

The net shortwave energy input to the land surface is

$$E = (1 - \alpha)SW \qquad \text{EQ. 36.}$$

where the SW is the incident shortwave radiation. The net SW gradient in the meridional direction is:

$$\frac{dE}{dy} = -\frac{d\alpha}{dy}SW + (1 - \alpha)\frac{dSW}{dy} = -\frac{df_s}{dy}(\alpha_s - \alpha_{bg})SW + [1 - \alpha_{bg}(1 - f_s) - f_s\alpha_s]\frac{dSW}{dy}$$

EQ. 37.

Rearranging,

$$\frac{dE}{dy} = (1 - \alpha_{bg})\frac{dSW}{dy} - f_s(\alpha_s - \alpha_{bg})\frac{dSW}{dy} - \frac{df_s}{dy}(\alpha_s - \alpha_{bg})SW \qquad \text{EQ. 38.}$$

So the net SW change with latitude is composed of three components. The first component is the SW radiation change with latitude multiplied by absorption with

the background albedo. This component is the same as the land surface without snow.

$$\frac{dE}{dy} = (1 - \alpha_{bg})\frac{dSW}{dy} \qquad \text{EQ. 39.}$$

The remaining two components, both including the difference of the albedo between snow and background land $(\alpha_s - \alpha_{bg})$, contribute to the snow albedo impact on the change of meridional SW radiation input, defined as snow albedo effect (SAE).

$$SAE = -f_s(\alpha_s - \alpha_{bg})\frac{dSW}{dy} - \frac{df_s}{dy}(\alpha_s - \alpha_{bg})SW \qquad \text{EQ. 40.}$$

The first term (Term1) is the SCF f_s multiplied by meridional SW radiation change $\frac{dSW}{dy}$ and albedo difference $(\alpha_s - \alpha_{bg})$. This term indicates the SCF contribution to the SW energy input. The larger the SCF f_s, the stronger the impact on the SW energy. The sign of this term is negative, implying it always reduces the SW energy.

The second term (Term2) is the meridional gradient of SCF $\frac{df_s}{dy}$ multiplied by SW radiation and the albedo difference. This term measures the snow gradient contribution to the albedo effect. The larger the meridional gradient of SCF $\frac{df_s}{dy}$, the stronger the impact on the SW radiation. Since the meridional gradient of SCF $\frac{df_s}{dy}$ could be either positive (increase) or negative (decrease), the contribution is

depended on the sign of $\frac{df_s}{dy}$. Since the SW is rather large in value, a small change in $\frac{df_s}{dy}$ can cause a large change in the second term.

Figure 6.14 shows the zonal mean (line) and inter-annual variability (shading, shown as the range) of the first term (Term1, red) and the second term (Term2, blue) of the snow albedo effect (W/m^2/degree) based on the data from March to June. The original data for computation are obtainted from MODIS and the **Control** simulations. The magitude of Term1 in the mean are generally larger than Term2 for all months; however, the inter-annual variablity (shading) of Term1 is far less than for Term2. During March, Term1 is generally increasing in magitude with latitude and reaches a maximum at roughly 70°N. From April to June, this term decreases quickly in magitude and moves northward toward the Pole. After May, there is almost no impact by the first term south of 60°N. However, the second term is generally small in the mean but shows relative larger range (variablity). The maximum inter-annual variability moves from middle latitudes northward to high latitudes from March to June. The Tibetan Plateau near 35°N still shows large inter-annual variablity even after May. The variblity in the zonal SCF gradient $\frac{df_s}{dy}$ contributes most of the inter-annual variability for the snow albedo effect.

6.5 Discussion

Due to nonlinear interactions between snow and other hydrological processes at the land surface, it is difficult to study the albedo changes due to snow variations and their effect on energy and water balance at the lower boundary of atmosphere. Any deficiency in the snow modeling or SD-SCF parameterization will introduce large biases in ground albedo, affecting air temperature and other atmosphere states. For example, a quick reduction in SCF (such as earlier snowmelt) will lead to a subsequently lower albedo at the surface and quickly warm near surface air temperatures, affecting the vertical stability and the general circulation of the atmosphere. Prescribing realistic SCF observed from MODIS in **RealSCF** eliminates errors in the snow albedo effect associated with imperfect snow modeling and SCF parameterization. Forcing all ensemble members to the same SWE in **RealSCF** also provides an approach to isolate the snow hydrological effect. The **RealSCF** experiment provides a reasonable estimation of snow-atmosphere coupling strength and potential predictability due solely to the snow albedo effect.

Although MODIS provides the most accurate SCF monitoring currently available, it is still far from perfect. Errors of SCF across the Northern Hemisphere in the absence of cloud are roughly 8% [*Hall et al.*, 2002a]; highest in the middle-latitude forest regions. The commission of errors due to misidentification of clouds as snow adds artificial noise to the **RealSCF** simulation. On the other hand, omission errors, where the sensor misses the shallow and short-term snow, will weaken the

snow impact compared to reality. In addition, the 8-day composited snow maps (MOD10C2) used in this study lack the high frequency snow variability on shorter time scales, acting as a temporal filter to modulate the snow-atmosphere coupling.

Besides the SCF, snow albedo itself is also an important regulator of the albedo effect. Although snow albedo at small spatial scales has been well studied in terms of its dependence on spectral characteristics, snow grain size and type, and solar zenith angle (SZA), grid-point scale spectrally averaged snow albedo is much more complicated. Marshall [*Marshall and Warren*, 1986; *Marshall*, 1989] pointed out that the spectrally averaged snow albedo varies with snow grain size, snow cover depth, underlying background albedo (thin snow), solar zenith angle and impurities absorbed in the snow (such as black carbon, etc.). Among these factors, grain size is the most critical variable controlling snow albedo. However, the snow grain size is so difficult to predict or simulate that it can be only roughly parameterized by snow age and temperature history [*Anderson*, 1976]. Based on the evaluation of the snow albedo parameterization in CLM, compared with four other different weather and climate models [*Wang and Zeng*, 2010], CLM version 3 has substantially improved the snow albedo simulation by use of a two-stream scheme for radiative transfer, separating the calculation between direct beam and diffuse albedo. The improved snow albedo estimation should improve the simulation of the snow albedo effect. Furthermore, the vegetation fraction covered by intercepted snow has also been reduced, addressing the albedo overestimation over the grass.

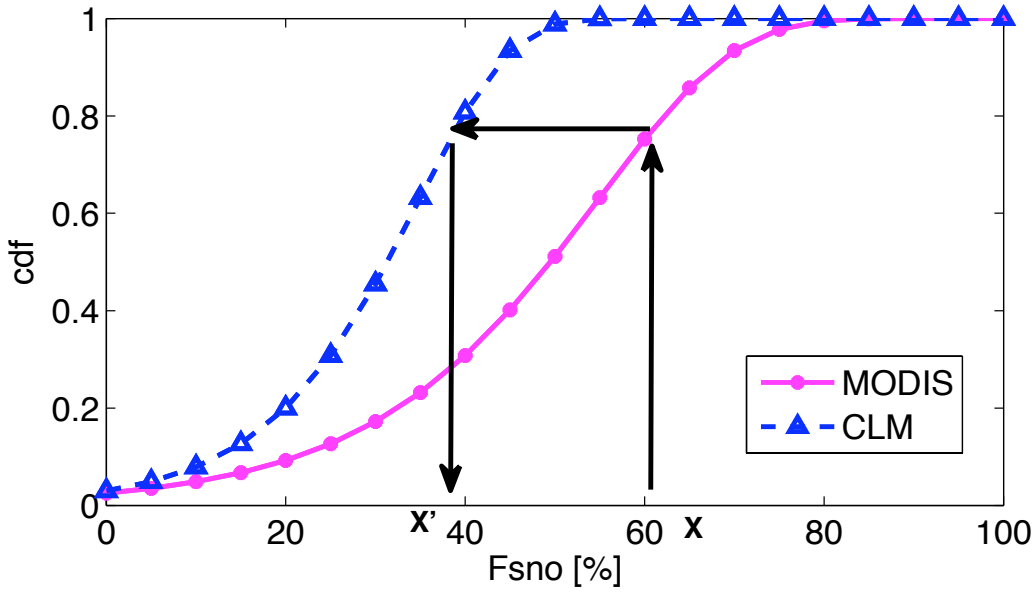

Figure 6.1 A demonstration of CDF-matching. The solid line and the triangle-dash line show the cumulative distribution function (cdf) of snow cover fraction obtained from CLM simulation and MODIS retrieval respectively during 2000-2009.

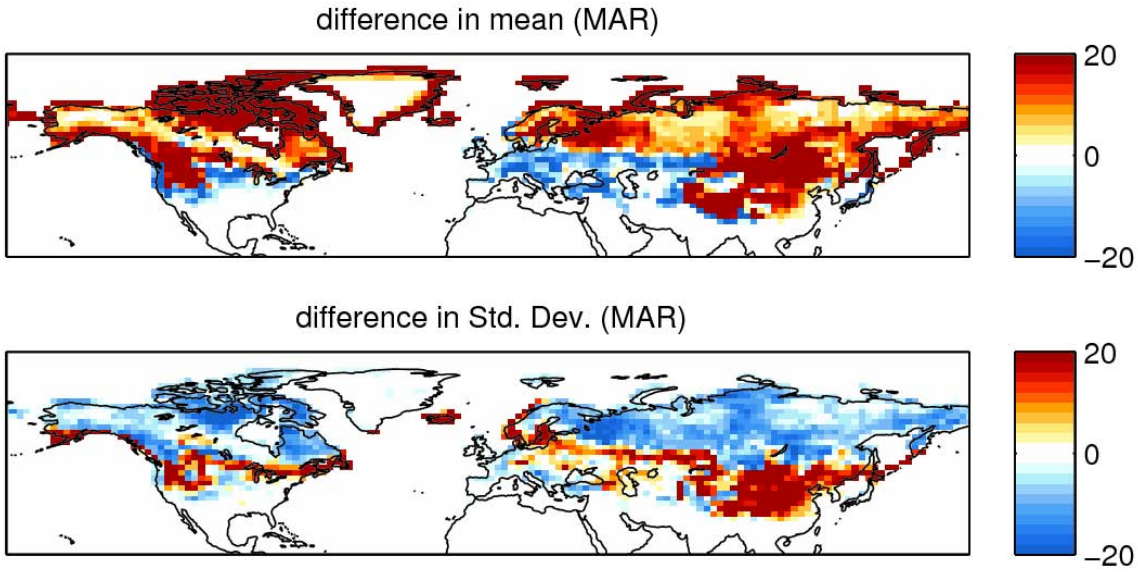

Figure 6.2 The differences of mean (top) and standard deviation (bottom) of model simulated SCF [%] minus MODIS MOD10C2 retrievals during 2000-2009 in March.

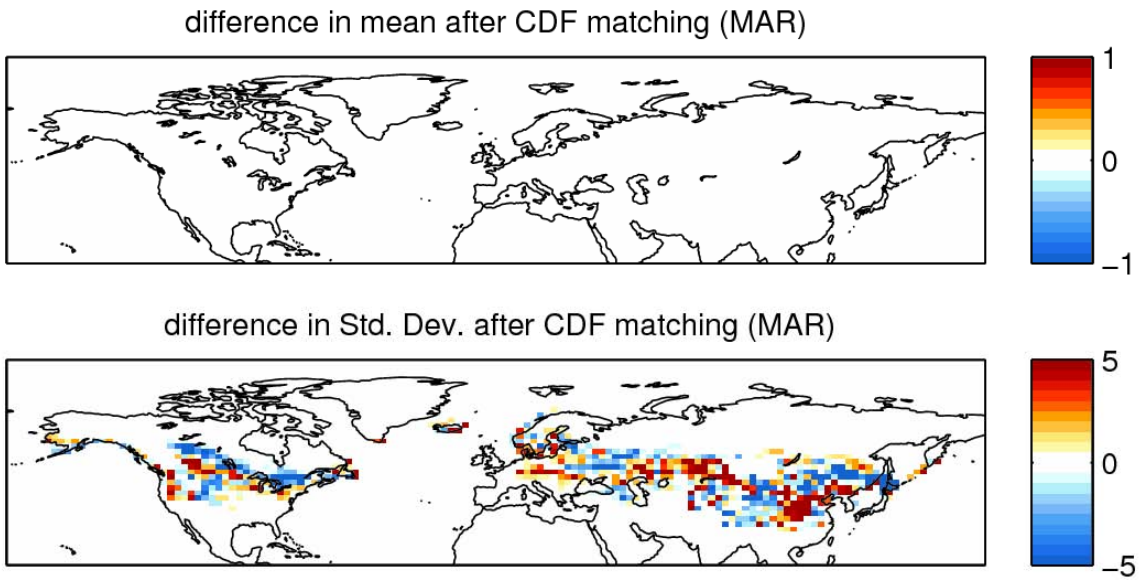

Figure 6.3 The same as Figure 6.2, except the MODIS retrievals were scaled by a CDF-matching based on 10 years of model simulations (2000-2009).

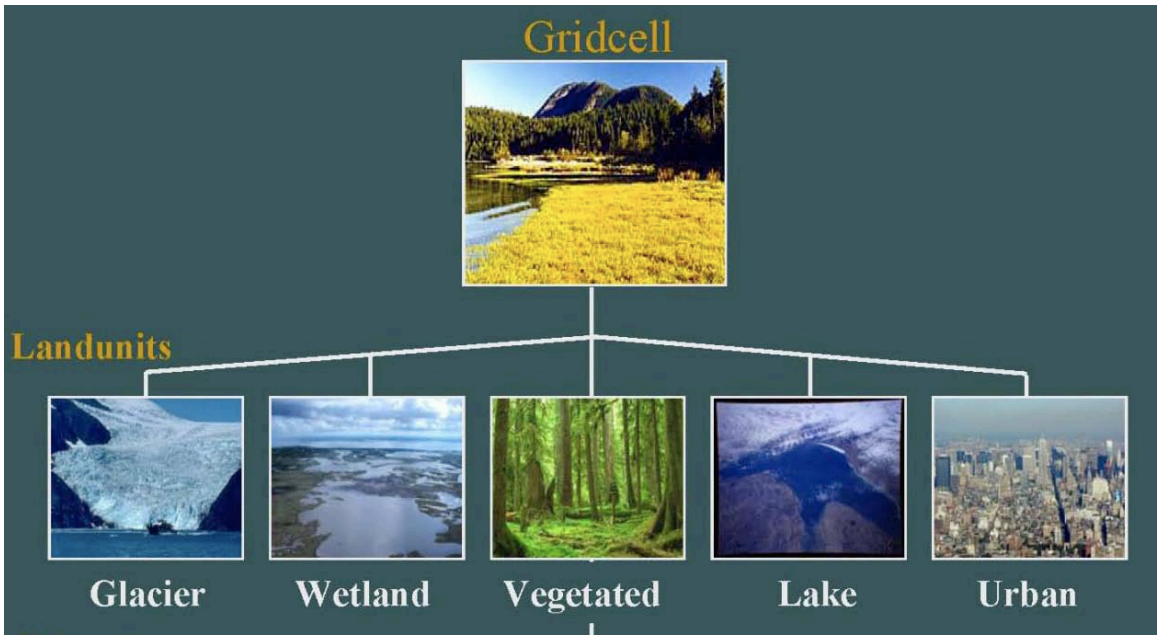

Figure 6.4 The current default configuration of the CLM sub-grid hierarchy [*Oleson et al.*, 2004c]

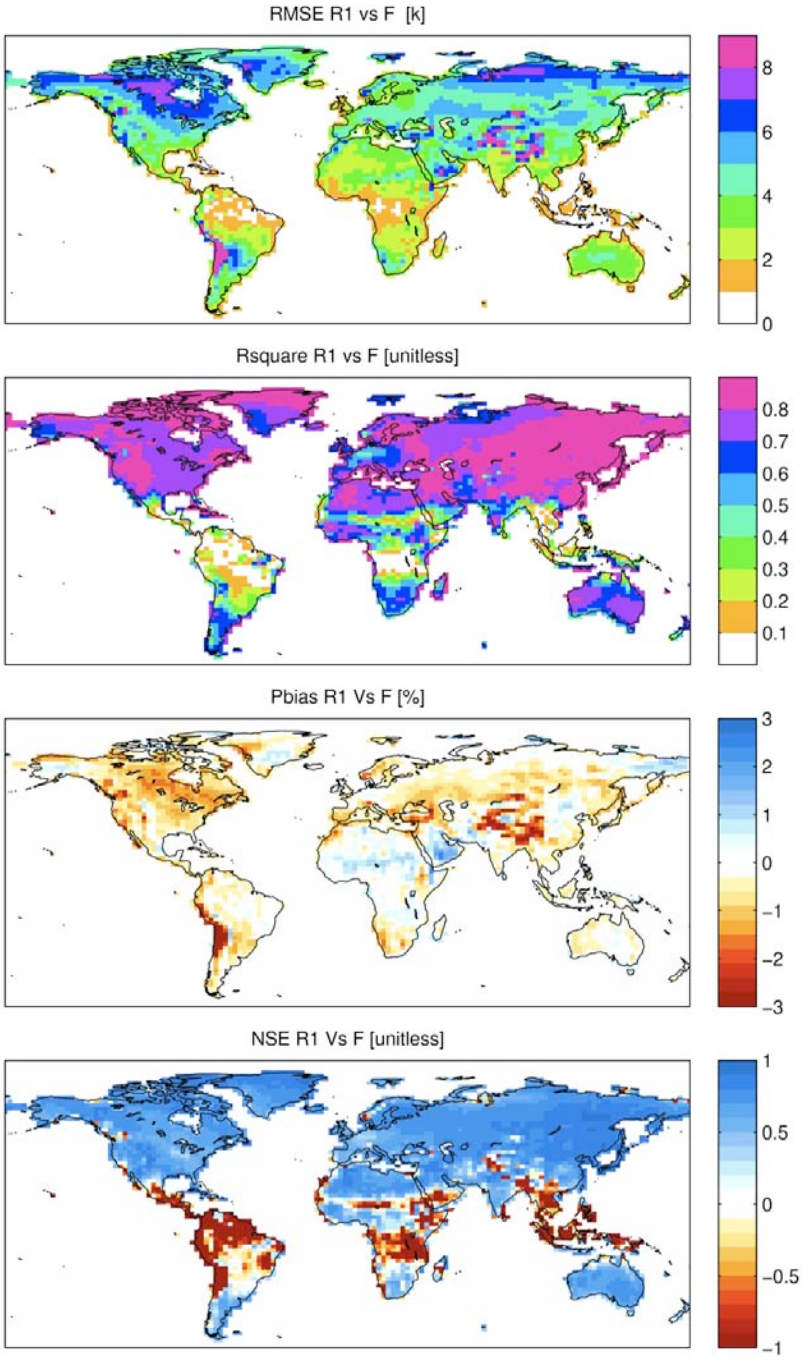

Figure 6.5 Evaluation of the surface air temperature (T2m) of F simulations (directly insert MODIS SCF without CDF-matching) against reanalysis 1 data (R1) : 1) root mean square error (RMSE); 2)the coefficient of determination (squared correlation R^2); 3) percent of bias (PBIAS) and 4) Nash-Sutcliffe Coefficient of efficiency (NSE)

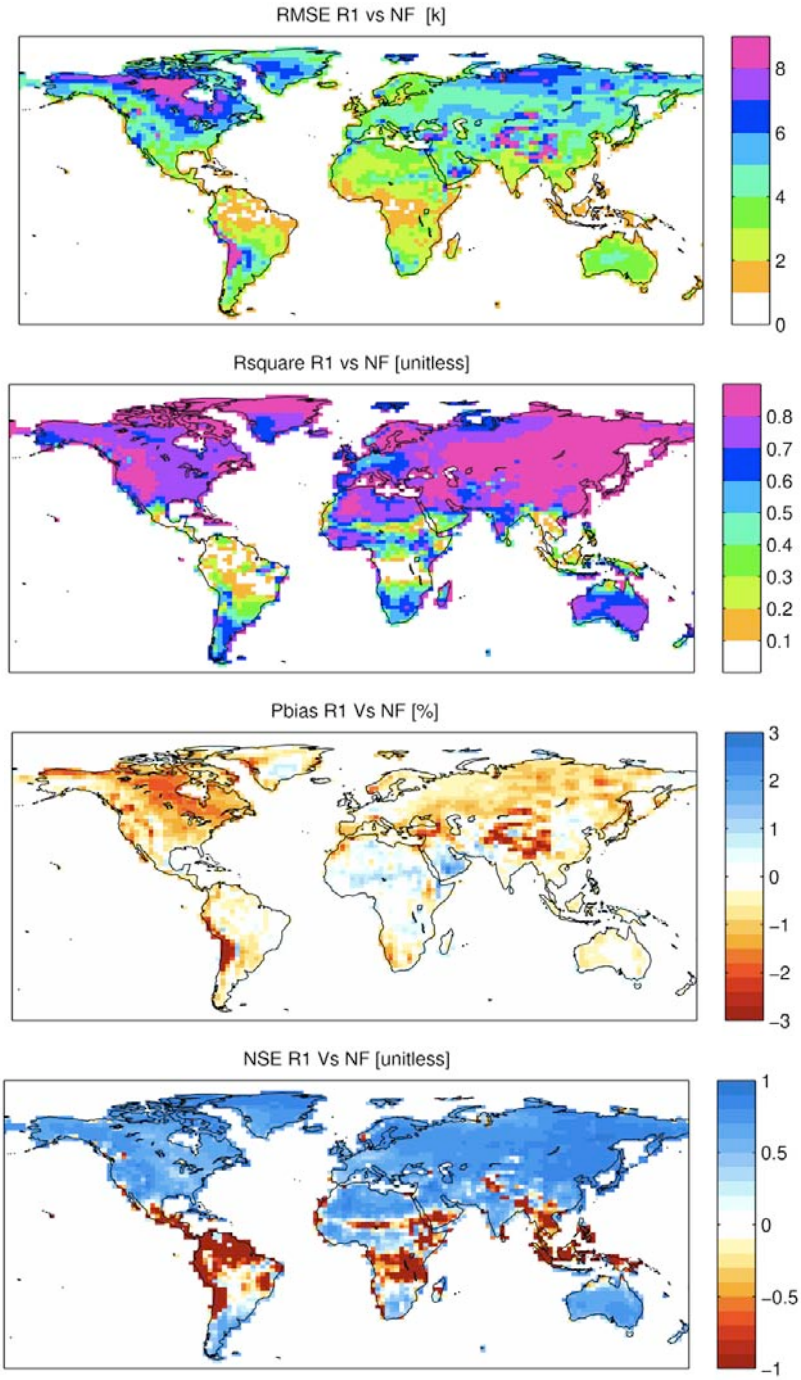

Figure 6. 6 The same as Figure 6.5, but using adjusted MODIS SCF after CDF-matching (NF simulation).

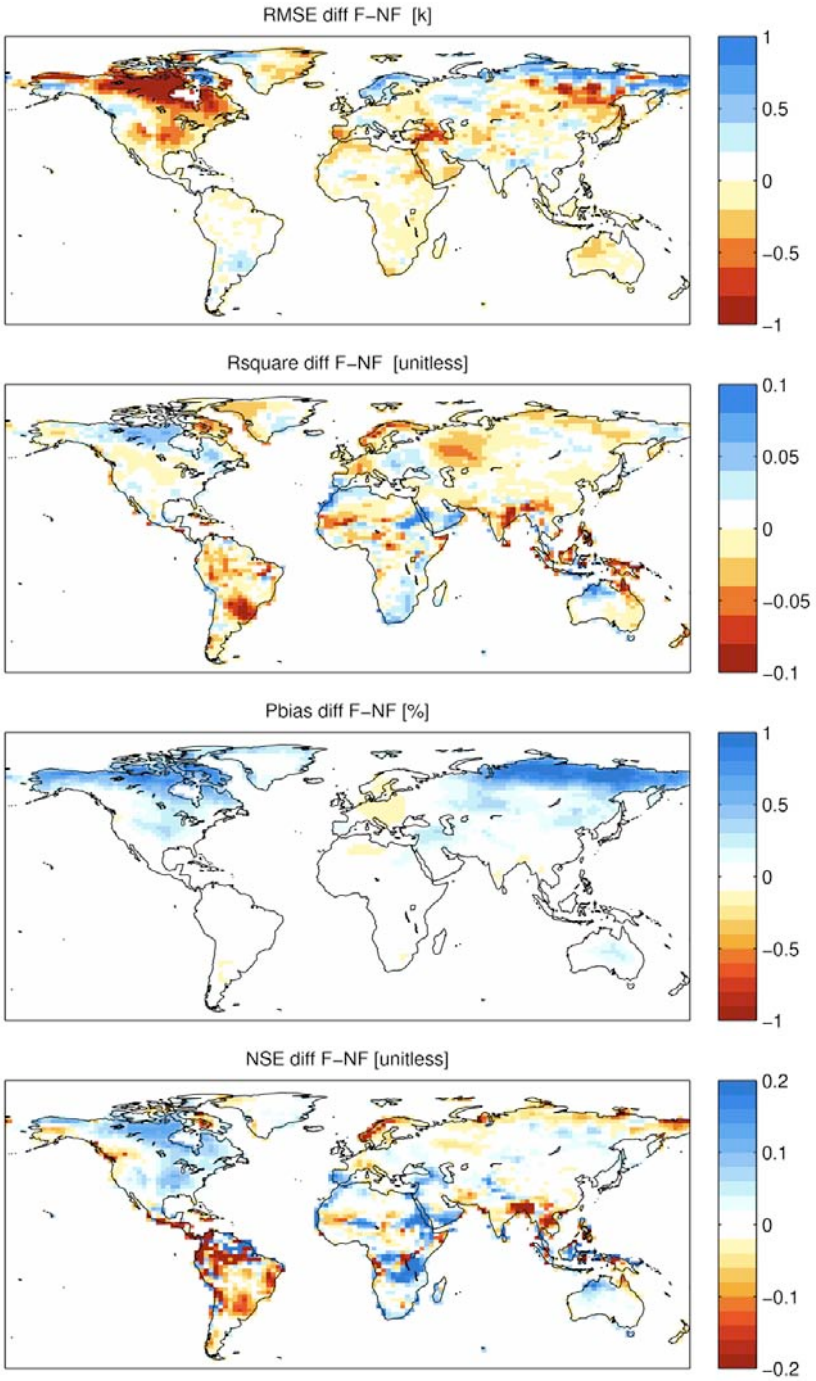

Figure 6.7 The difference of forecast skill metrics between directly insert MODIS SCF and adjusted SCF after CDF-matching.

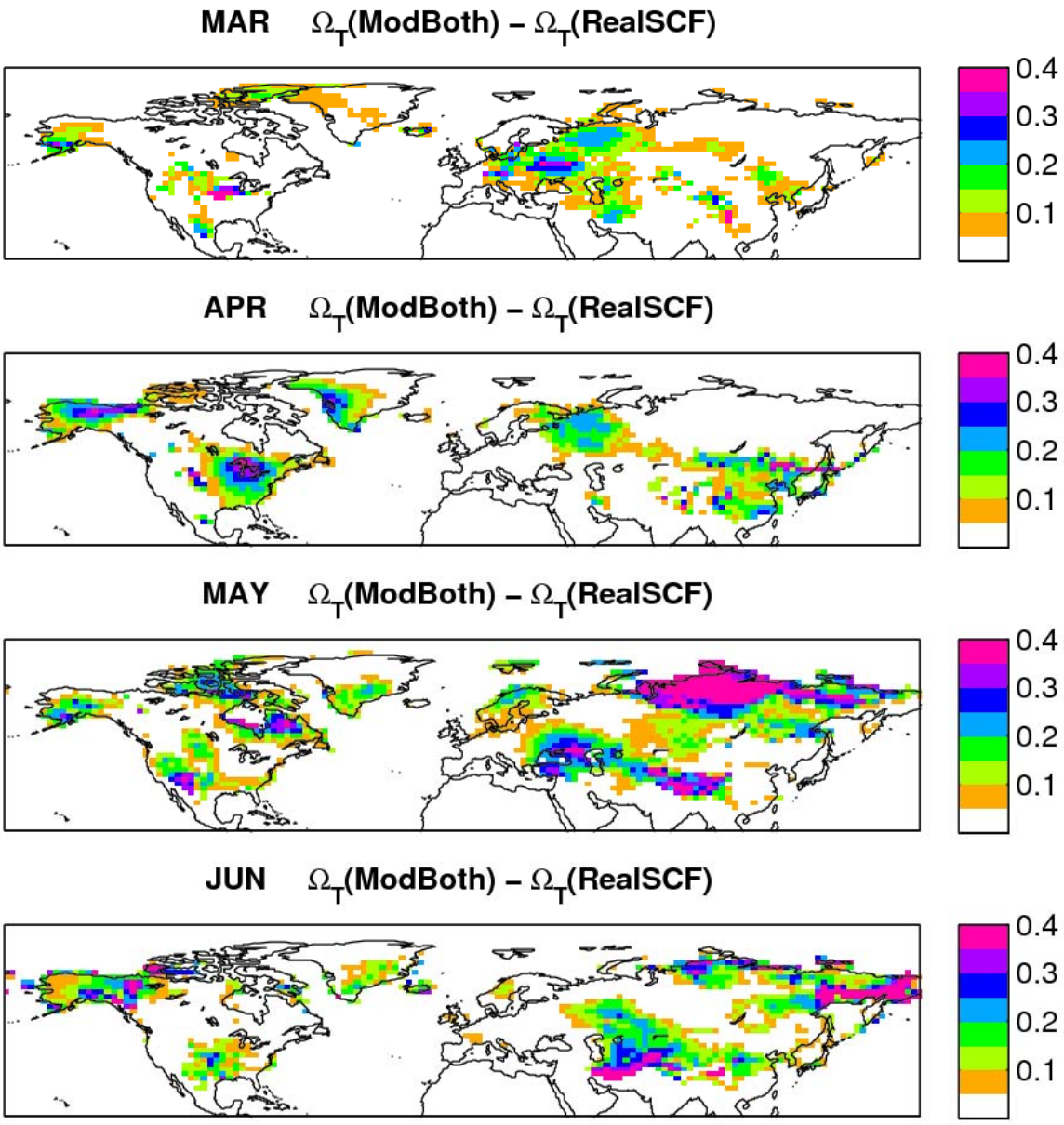

Figure 6.8 Coupling strength (the difference of similarity of **ModBoth** and **RealSCF** experiments) for air temperature (2m height) from March to June.

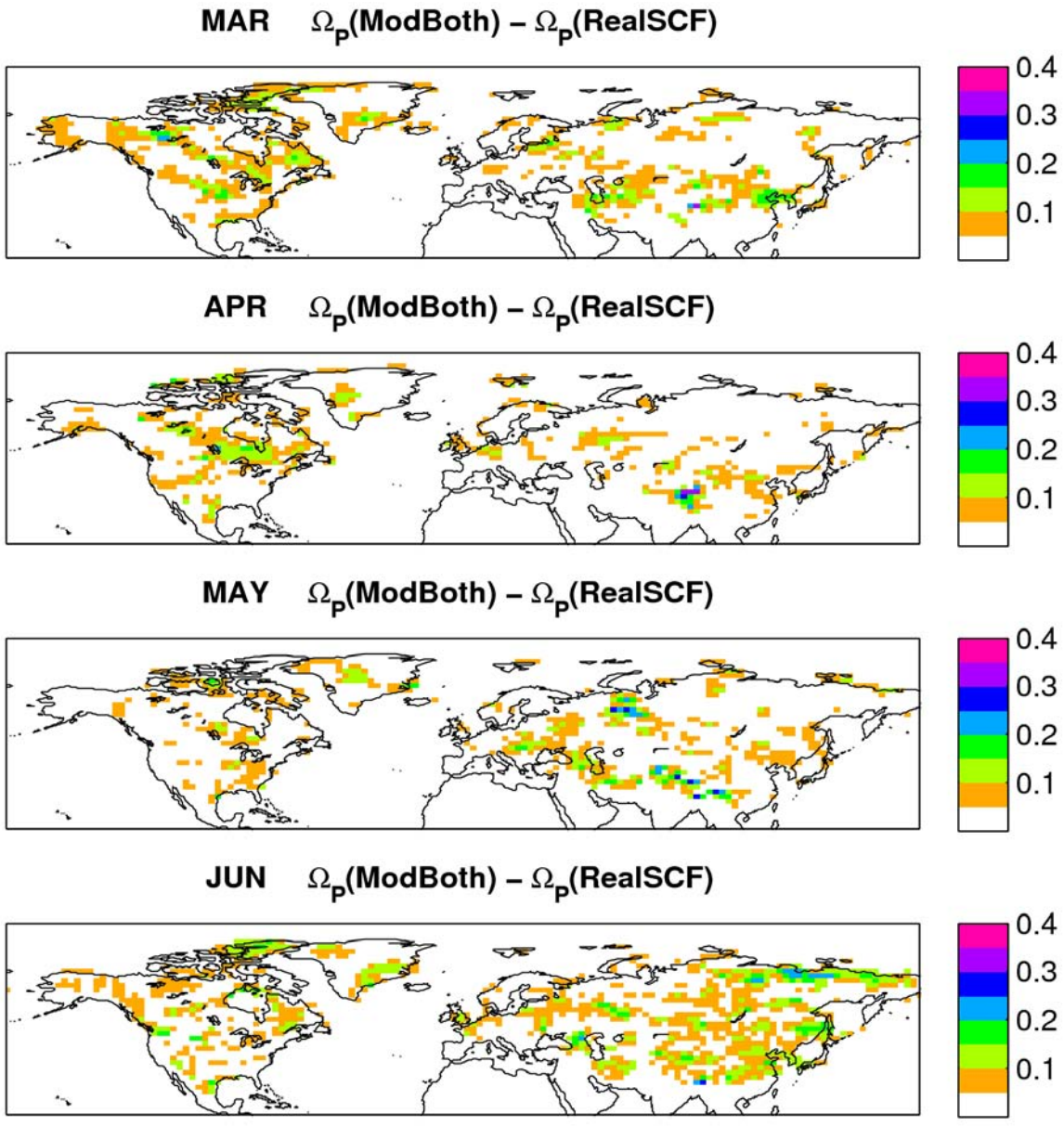

Figure 6.9 As in Figure 6.8, for precipitation.

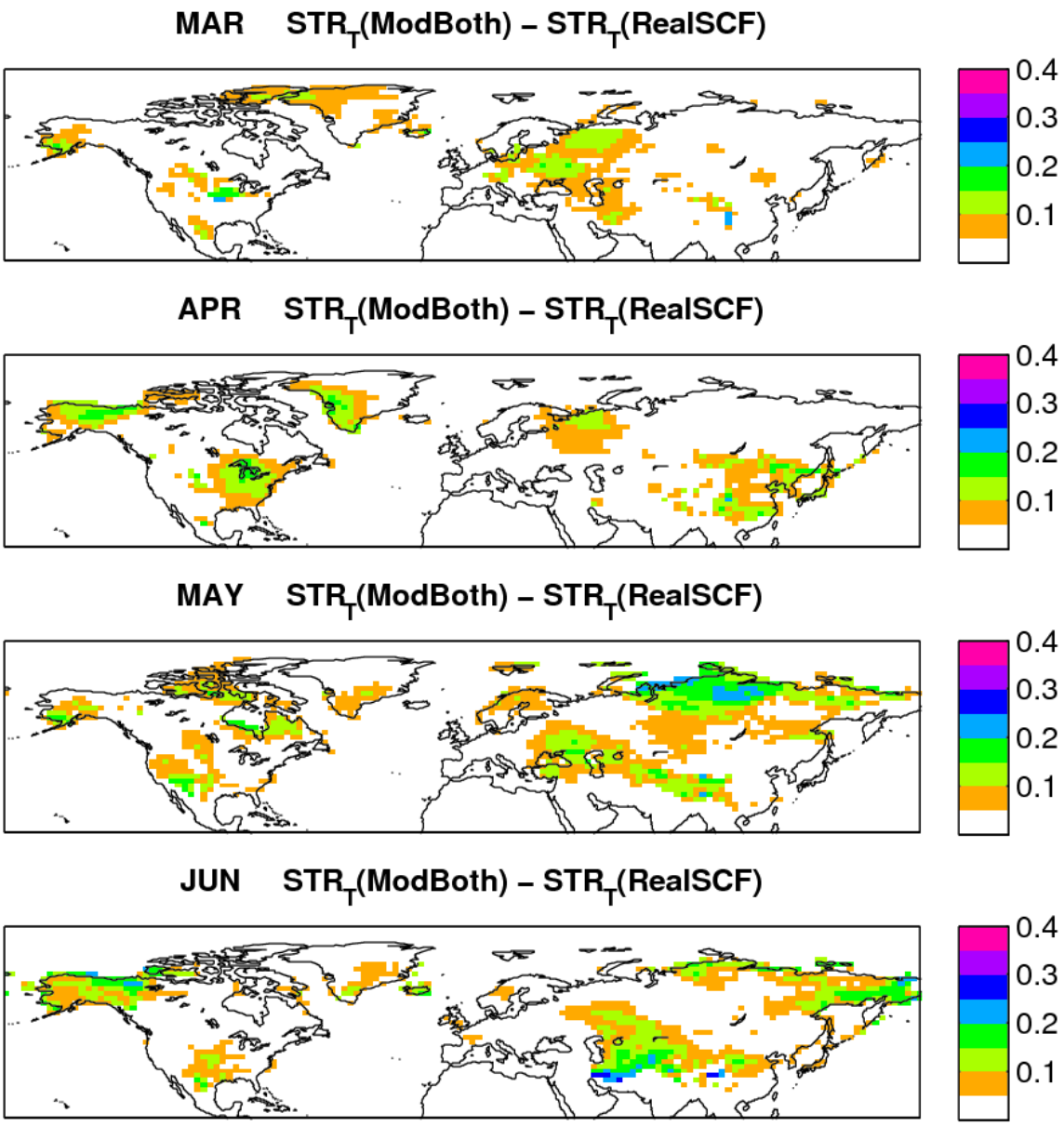

Figure 6.10 Predictability enhancement (the difference of STR of **ModBoth** and **RealSCF** experiments) for air temperature (2m height) from March to June.

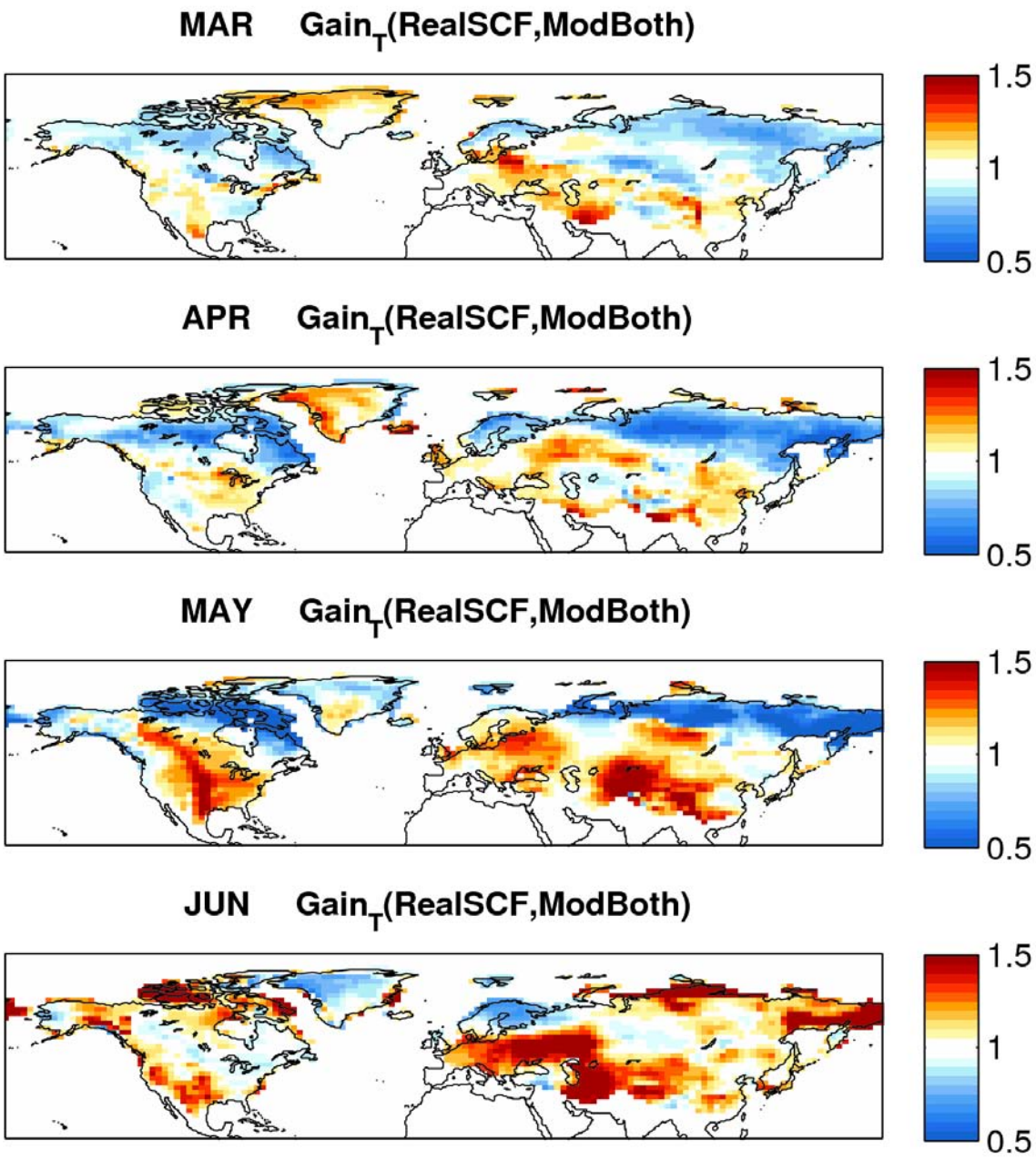

Figure 6.11 Gain index (the ratio of Standard deviation of **RealSCF** and **ModBoth** experiments) of air temperature (2m height) from March to June.

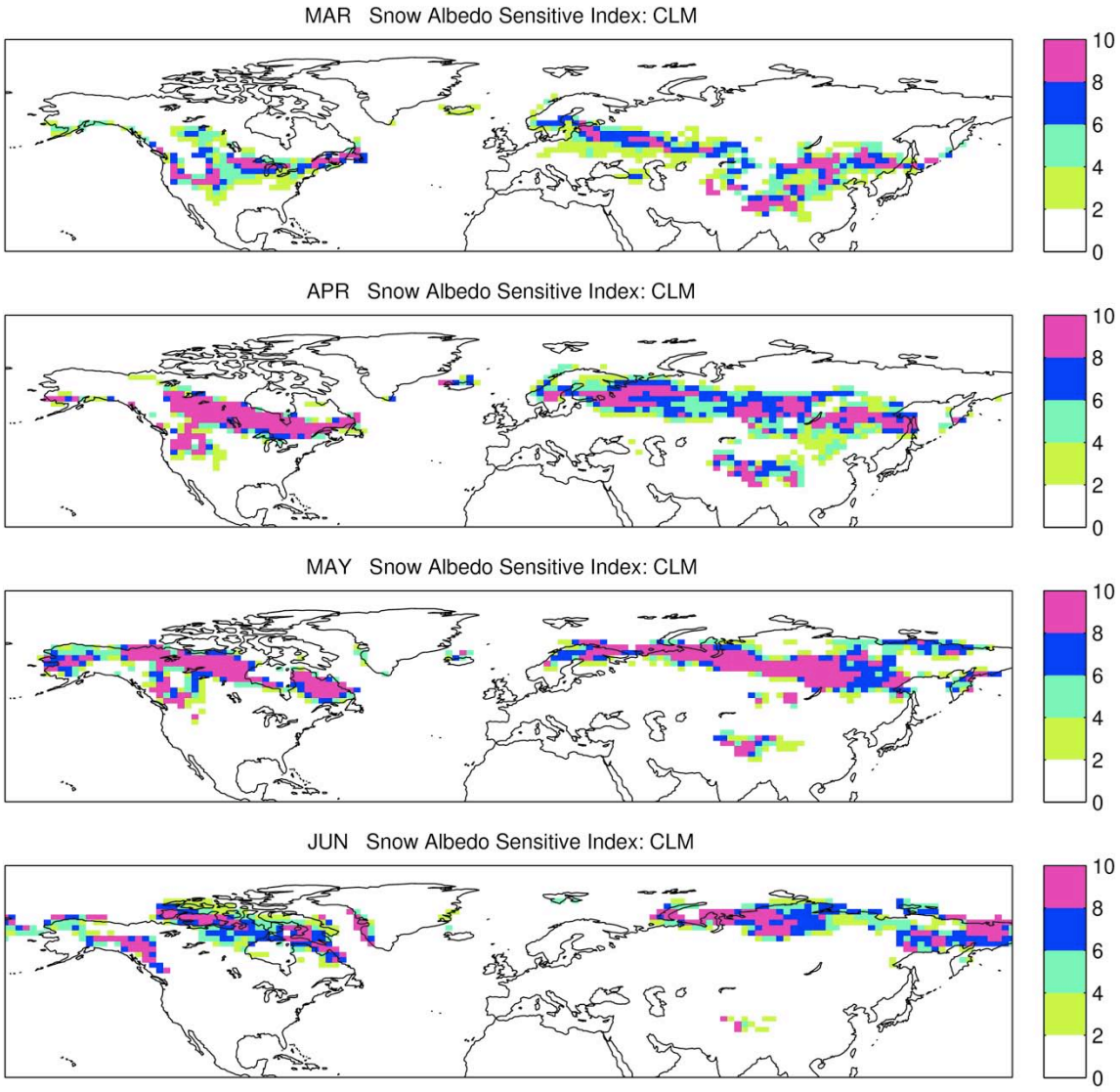

Figure 6.12 Snow albedo sensitivity index from March to June based on the CLM model.

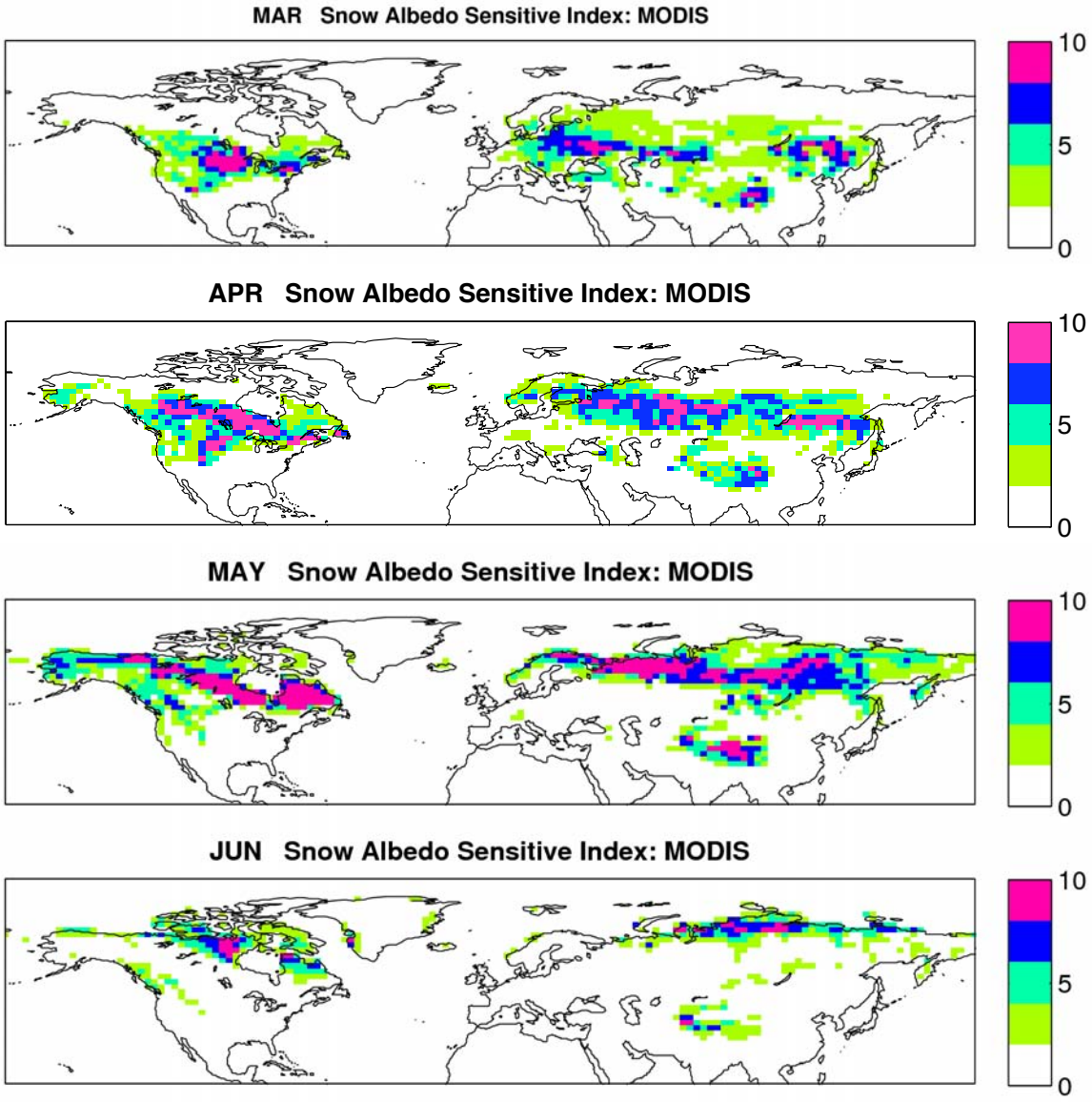

Figure 6.13 The same as Figure 6.12, but based on MODIS retrievals.

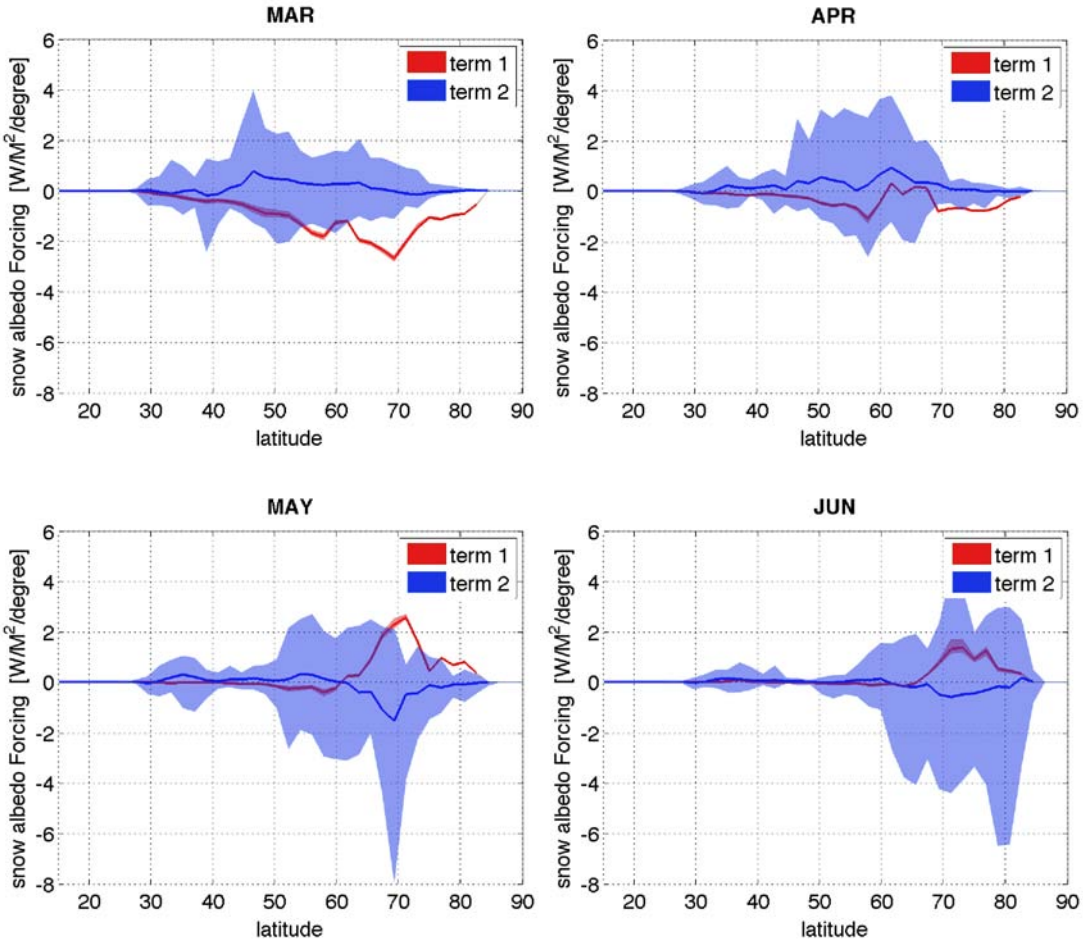

Figure 6.14 Zonal mean (line) and inter-annual variability (shading, shown as the range) of snow albedo forcing (W/m^2/degree) in first term (term1) and second term (term2) of EQ 40 from March to June. the data for computaiton obtainted from MODIS and the **Control** simulation.

CHAPTER 7. COUPLING STRENGTH AND PREDICTABILITY DUE TO SNOW HYDROLOGICAL EFFECT

7.1 RealSWE experiment

All ensemble members in **RealSWE** are prescribed by the realistic SWE obtained from GLADS during 2000-2009 but using the same SCF read from S1_state. The only difference between ensemble **RealSWE** and ensemble **ModBoth** is the SWE that is obtained from offline analysis GLDAS, which will eliminate the possible errors in the SWE simulation. In other words, the SWE depletion curve at each grid-point is precisely described by GLDAS SWE at each time step. As the most important factor to determine the potential available water for melt, infiltration and runoff, the more accurate the SWE depletion curve, the more precise in the simulation of snow hydrological processes.

Although the AMIP-style simulation still shows a relative large difference between CLM model and GLDAS reanalysis (Figure 4.4) we use the GLDAS SWE directly inserted into the Ensemble **RealSWE** experiment without any bias-correction.

Generally speaking, the impact of snow on soil moisture anomalies has two aspects: Firstly, snow cover insulates the soil from the atmosphere, decoupling the soil-atmosphere interaction during the snow-covered periods. This process prolongs the soil moisture memory throughout the snow season by preserving soil moisture anomalies and increasing the redness of the soil moisture spectrum [*Delworth and Manabe*, 1989]. Secondly, snowmelt infiltrates the underlying soil and contributes to later soil moisture anomalies. This is what we call the snow hydrological effect (SHE).

In CLM, any precipitation or dew in liquid form reaching the snow-capped surface is assigned to liquid snow capped runoff, and then directly sent to the River Transport Model (RTM) where it is routed to the ocean [*Oleson et al.*, 2004d]. The snow pack properties and soil moisture are unchanged during snow-covered season. This is a manifestation of the first aspect, decoupling the soil-atmosphere interaction.

Once snow begins to melt, the melt water infiltrates the soil triggering anomalies in soil moisture. However, there are few previous studies that focus on the SHE. Snowmelt in spring suddenly increases water infiltration until the underlying soil becomes saturated. This is a two-step process. The excess will first lead to Hortonian runoff (due to snowmelt excess over infiltration). Once the soil becomes saturated, Dunne runoff (due to saturation excess) happens and water is discharged into the river network. These processes are highly nonlinear, depending

on many localizations, parameterizations and estimations. The snowmelt and maximum soil infiltration capacity are critical parameters for studying this issue.

For the hydrological modeling of snowmelt, the maximum of SWE prior to snowmelt is a key variable to quantify how much water is available to affect soil moisture. On the other hand, the maximum soil infiltration capacity is determined from soil texture and soil moisture [*Entekhabi and Eagleson*, 1989b] which are computed based on the effective porosity and saturated fraction.

If we define the SHE to include all composited climate effects due to snowmelt in the soil and subsequent soil moisture-evaporation-precipitation feedbacks, the **RealSWE** experiment can be used to isolate the climate impact due to snowmelt by excluding the climate effect associate with snow albedo. Since atmosphere initial and boundary forcings are the same in the ensemble **RealSWE** and **ModBoth** except for SWE, in particular prescribing the same SCF, the coupling strength and predictability difference between **RealSWE** and **ModBoth** is largely contributed by the SHE.

7.2 Coupling strength and predictability due to hydrological effect

Similarly to previous chapter, the only difference between **RealSWE** and **ModBoth** is the SWE that is read from GLDAS from 2001 to 2009 and will trigger different soil moisture anomalies after the snow melts. The coupling strength and predictability differences between **ModBoth** and **RealSWE** are contributed only by the snow hydrological effect (SHE).

Figure 7.1 shows the coupling strength (the change of intra-ensemble similarity from **ModBoth** to **RealSWE** experiments) for air temperature (2m height) from March to June. During March and April, the coupling strengths are much weaker than for the albedo effect (Figure 6.1), mainly concentrated on unstable snow regions where the snow begins to melt after March 1st. The snow hydrological effect is strongest in May, especially near the Tibetan Plateau. There are large areas in both Eurasia and North America in June that show strong snow-atmosphere coupling due to the lagged hydrological effect.

Simaliar to the ideal snow evolution **Control** experiment, the coupling strength of precipitation due to SHE is very scattered and patchy as shown in Figure 7.2; However, the coupling strength increases slightly with time from March to June. This feature agrees with the general hypothesis that the hydrological effect will be delayed and will gradualy increase after snowmelt.

In terms of STR, the predicatablity enhancement due to SHE (the difference of STR between **ModBoth** and **RealSWE** experiments) for air temperature and precipitation are shown in Figure 7.3 and Figure 7.4. As expected, the patterns of predictability enhancement are very similar to the coupling strength but notably weaker in magnitude.

Similarly, the gains of temperature and precipitation variability due to the hydrological effect are shown in Figure 7.5 and Figure 7.6. Note the significant increases in the Gain of variability both in temperature and precipitation over the

strong snow-atmosphere coupling regions. During March and April, there are some obvious areas of suppression in variability of precipitation (Gain < 1) in the high-latitude regions due to negative snowfall-instability feedbacks.

7.3 Snow hydrological sensitivity index

Similarly, we can define a Snow Hydrological Sensitivity Index (SHSI) to quantitatively determine the climate forcing due to hydrological effect of snowmelt as shown in Figure 7.7. To quantify this hydrological effect, snowmelt infiltration is the key process that strongly depends on the surface infiltration-runoff parameterization. The key concept underlying this parameterization is that of fractional saturated or impermeable area which is determined by the topographic characteristics and soil moisture, including overland flow due to both saturation excess (Dunne runoff) and infiltration excess (Hortonian runoff).

Based on the parameterization of maximum infiltration capacity [*Entekhabi and Eagleson*, 1989a], we define the Snow Hydrological Sensitivity Index (SHSI) as

$$SHSI = \sigma(W_{sno}) * R_{\inf}$$

where $\sigma(W_{\text{sno}})$ is the standard deviation of SWE, and $R_{\inf}$ is the infiltration capacity that is determined by soil texture and soil moisture, which could be empirically estimated from observational data.

Figure 7.8 shows the fraction of snowmelt infiltrated into the soil from the **Control** experiment during March to June. The infiltration ratio was computed as

the water flux into the soil reported by CLM divided by the total model snowmelt. In general, the infiltration is a maximum roughly along the edge of snowmelt, but displays a sharp gradient toward stable snow regions. The sharp gradient is not only due to the decreasing snowmelt but also to the increasing of the impermeable fraction of the soil because of the prevalence of frozen ground. Multiplied by the standard deviation of SWE obtained from GLDAS (Figure 7.9) the SHSI is shown in Figure 7.10.

Comparing the SHSI (Figure 7.10) to the coupling strength (Figure 7.1 and Figure 7.3), there are similarities in pattern but some large differences in magnitude. The hydrological forcing due to snowmelt gradually decreases with snow depletion, but the coupling strengths are mostly increasing. This indicates that the snow hydrological effect will act later and increase the impact (magnitude) due to soil moisture-evaporation-precipitation feedbacks.

7.3 Comparing with GLACE results

The snow hydrological effect is essential to the soil moisture-evapotranspiration-precipitation interaction and feedback after snow has melted. Classical land-climate interaction studies provide a useful conceptual framework to explain the evapotranspiration regimes as a function of soil moisture, based on the original idea of Budyko [1961] and recently improved by Koster [2002]. Three main evapotranspiration regimes, characterized by the evaporative fraction and soil

moisture, can be defined: two soil moisture-limited regimes (dry and transitional regimes) and an energy-limited evapotranspiration regime (wet regime). In the energy-limited evapotranspiration regime, the evaporative fraction is independent of soil moisture content above a given critical soil moisture value. Below this critical value, soil moisture content provides a first-order constraint on evapotranspiration (soil moisture-limited evapotranspiration regime). Based on the wilting point, another important threshold for whether or not evapotranspiration takes place separates the soil moisture-limited regimes into the dry and transitional regimes. In the wet (above a critical high soil moisture value) and dry (below the wilting point) climate regimes, soil moisture anomalies do not greatly impact evapotranspiration variability. In the transitional regime (between wilting point and critical high value), however, soil moisture strongly constrains evapotranspiration variability and thus the resulting feedbacks to the atmosphere.

Figure 7.11 shows the land-atmosphere coupling strength $\Omega(R)$-$\Omega(W)$ estimated from the CAM model coupled to CLM 3.0 using the same method as in GLACE-I project (From Guo et al. 2006). Although this land-atmosphere coupling strength is estimated during summer (JJA), we can compare it with the coupling strength due to the snow hydrological effect during the spring transition to summer (April, May, and June). The "hotspots" of land-climate interaction (strong coupling regions of soil moisture-evapotranspiration-precipitation feedback) generally agree with the regions with strong snow hydrological effects (SHE) as shown in Figure 7.1

and Figure 7.2. SHE is basically land-climate interaction driven by available snowmelt infiltration in spring.

7.5 Discussion

In the climate model, soil hydrologic processes are strongly impacted by the heterogeneity of soil hydraulic conditions. At the top soil layer, infiltration, exfiltration and hence runoff depend on the nature of soil properties and states, including soil type, texture, permeability, slope, elevation and water content. The more accurate the representation of heterogeneous soil properties in the model, the more precise the model will be in representing SHE. However, most land models or hydrological models have focused efforts at improvement on the runoff scheme, very little attention on snowmelt infiltration.

Snowmelt infiltration is the key process to determine SHE, which is also strongly and nonlinearly dependent on the soil water content. The Hortonian component of surface runoff is the residual of snowmelt intensity over the soil infiltration, and is highly sensitive to soil moisture conditions. This infiltration will further determine whether or not the topsoil becomes saturated, thus producing the Dunne component of surface runoff. In this **RealSWE** experiment, we compare SHE by unifying the model initial soil moisture to the climatological mean. This setup effectively removes the possible impact of the soil moisture anomalies, but also removes the possible variability in infiltration due to different soil moisture conditions. How variations of soil moisture conditions impact snowmelt infiltration,

such as by initializing the soil with GSWP-2 data [*Dirmeyer et al.*, 2006], needs to be investigated in future studies.

Frozen ground or permafrost is another key factor for SHE. The presence of ice in the soil dramatically alters soil hydrological properties. If the topsoil is frozen, the surface soil is impermeable. The frozen ground prevents any infiltration of snowmelt, resulting in early and above-normal spring runoff. The CLM 3.5 model has been greatly improved recently in the frozen soil scheme and has introduced fractional permeable area [*Niu and Yang*, 2006]. Comparing with the previous frozen soil scheme where ice content is solely determined by available energy, this parameterization of hydraulic properties for frozen soil has shown superior results. Due to the complicated nonlinear interaction between atmosphere, snowmelt and underlying frozen soil, there are more uncertainties in the SHE at high-latitudes.

The **RealSWE** experiment is still far from perfect as a means to investigate SHE. Experiments with different frozen ground and soil moisture conditions need to be implemented to further study these uncertainties.

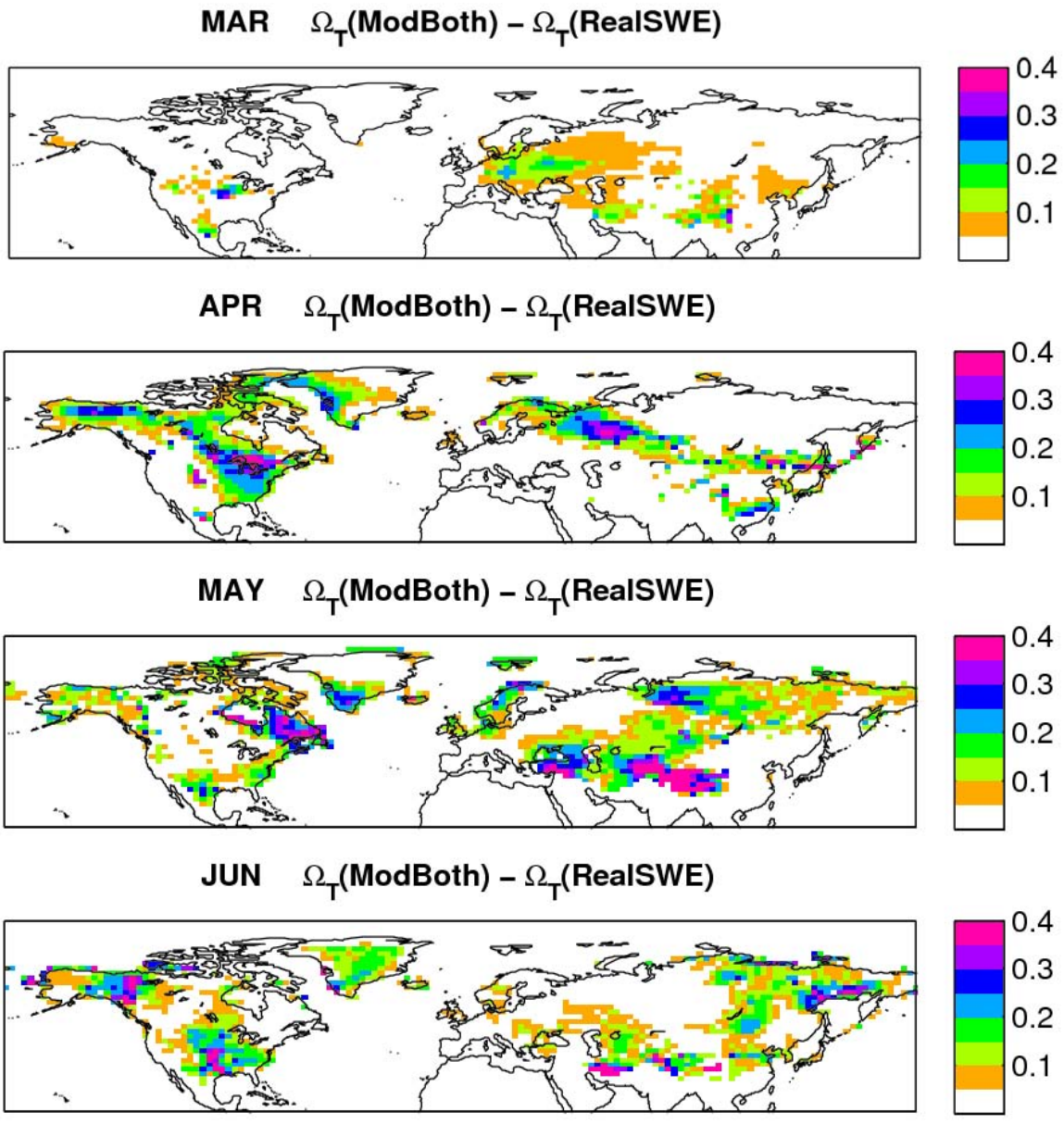

Figure 7.1 Coupling strength (the difference of intra-ensemble similarity of ModBoth and RealSWE experiments) for air temperature (2m height) from March to June.

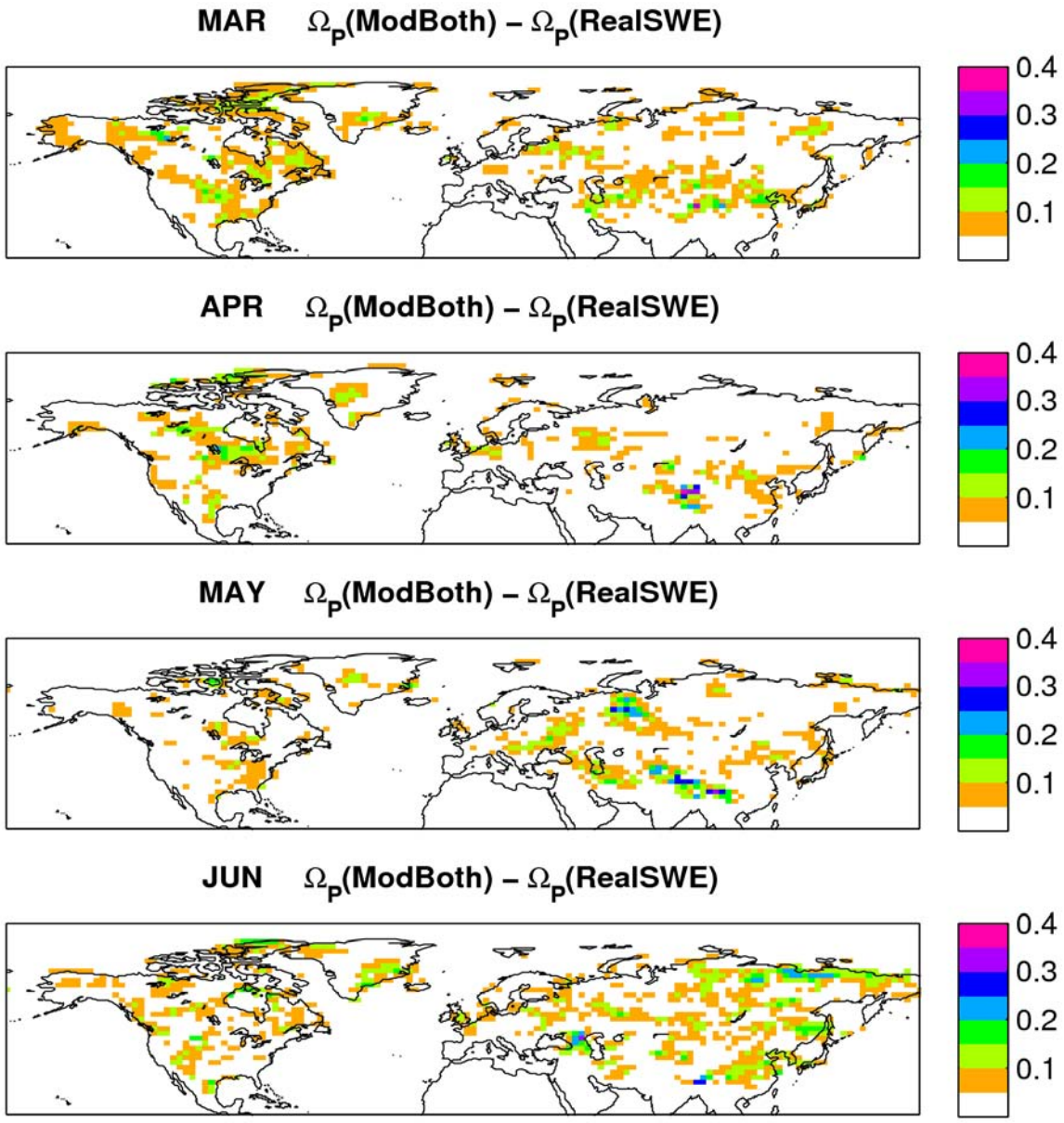

Figure 7.2 The same as Figure 7.1, but for precipitation.

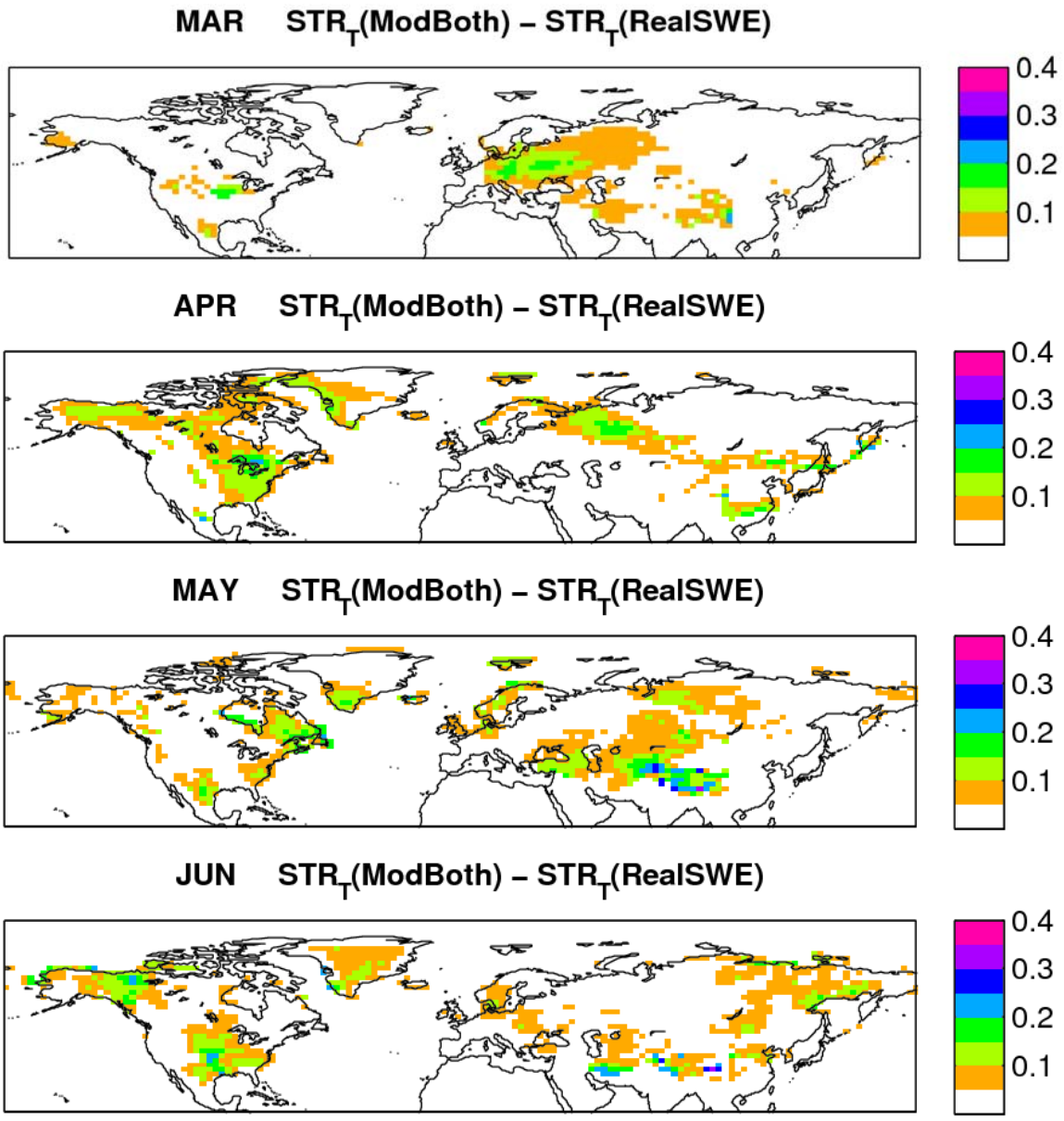

Figure 7.3 Predictability enhancement (the difference of STR of ModBoth and RealSWE experiments) for air temperature (2m height) from March to June.

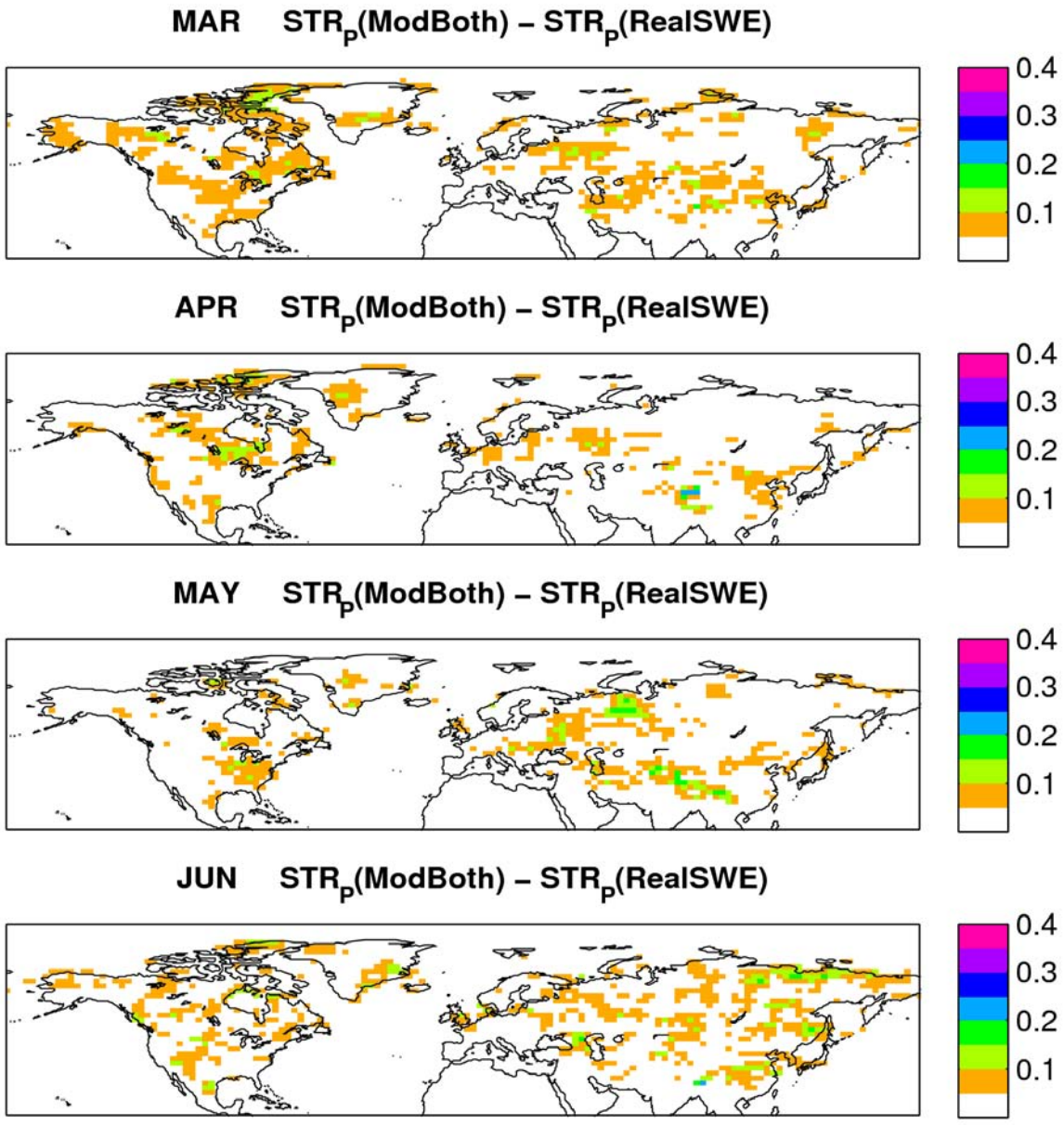

Figure 7.4 As in Figure 7.3 for precipitation.

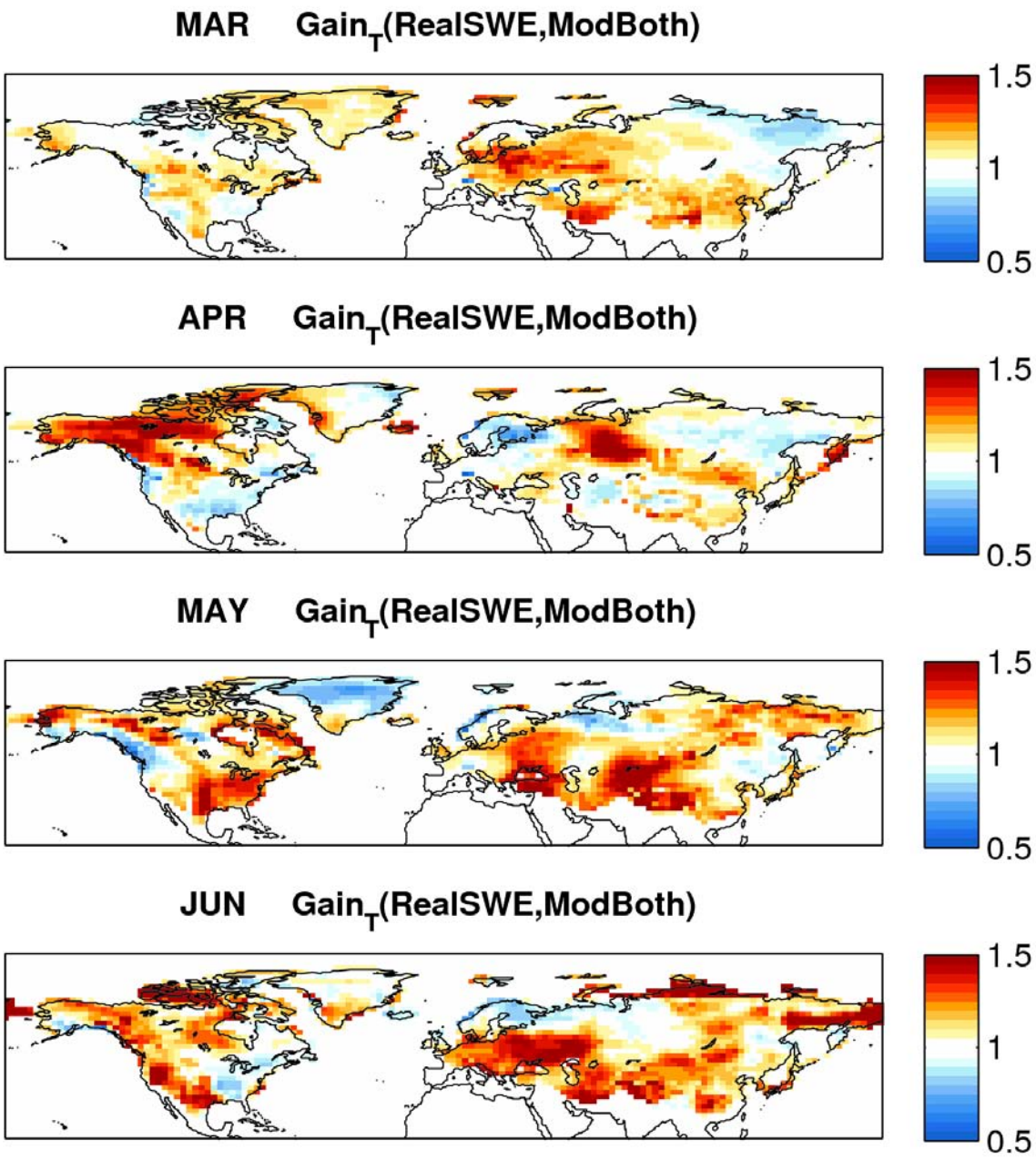

Figure 7.5 Gain index (the ratio of standard deviation of RealSWE and ModBoth experiments) for air temperature (2m height) from March to June.

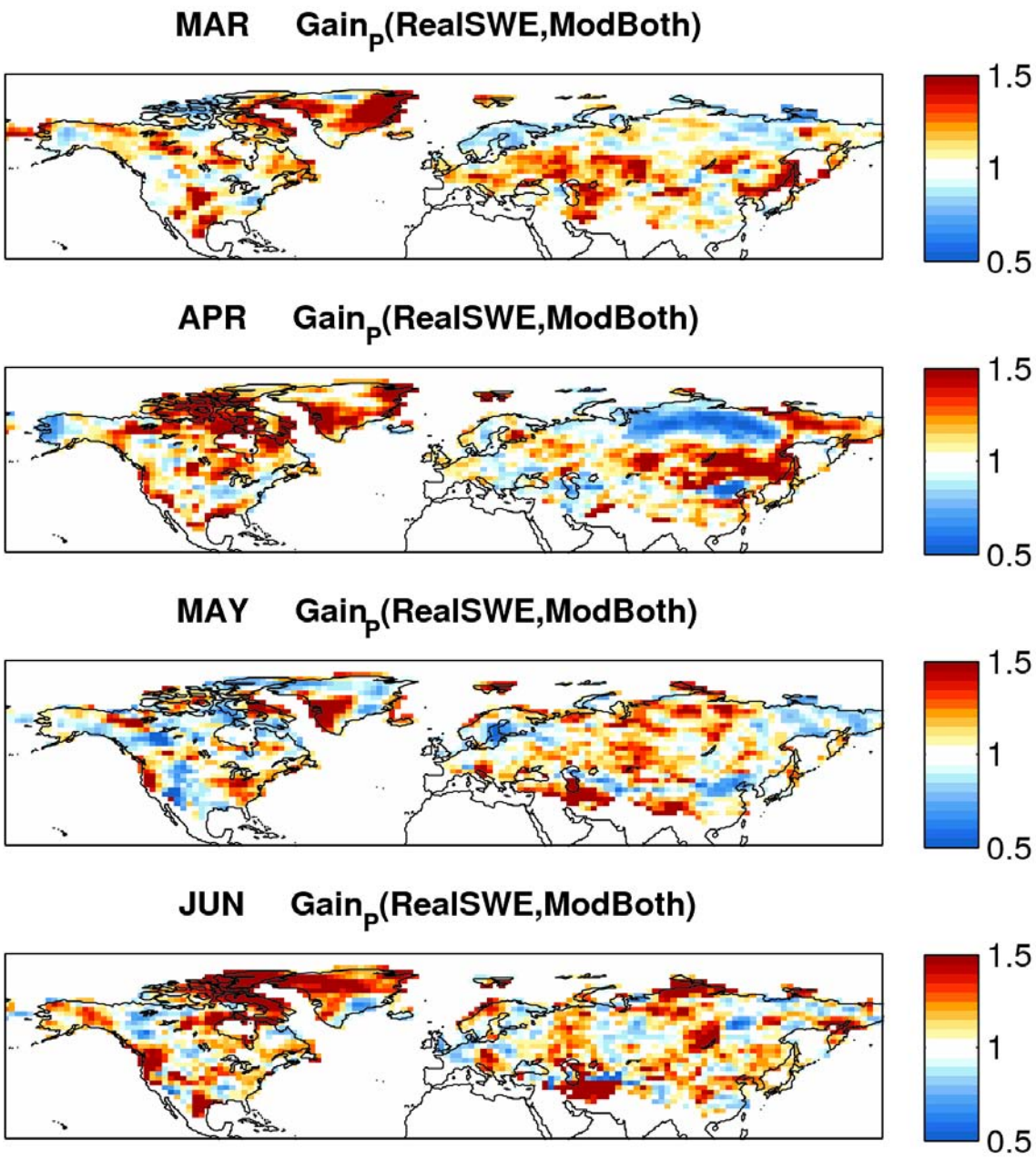

Figure 7.6 As in Fig 7.5 for precipitation.

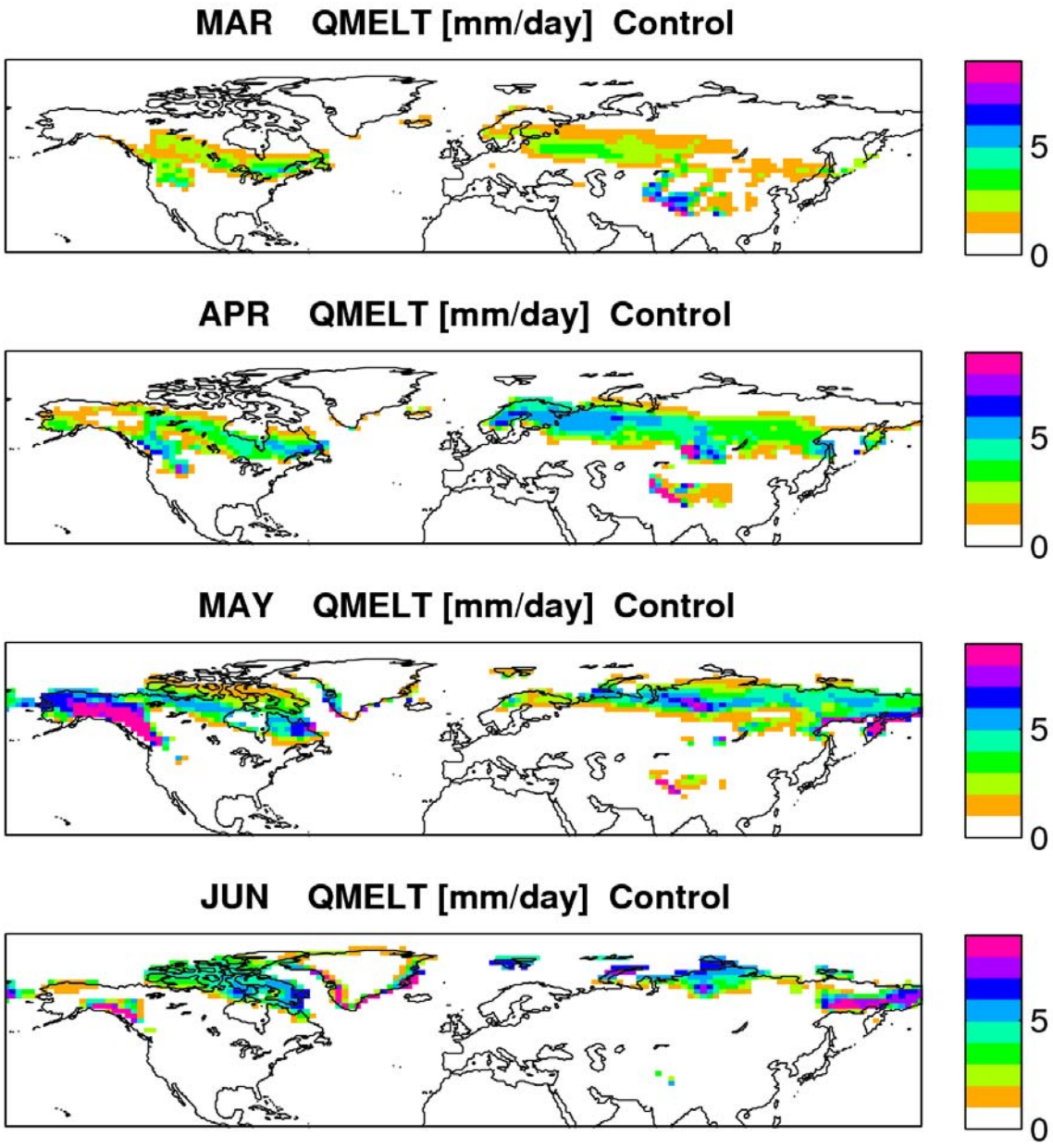

Figure 7.7 The monthly mean snowmelt (QMELT) climatology [mm/day] obtained from the Control experiment during March to June.

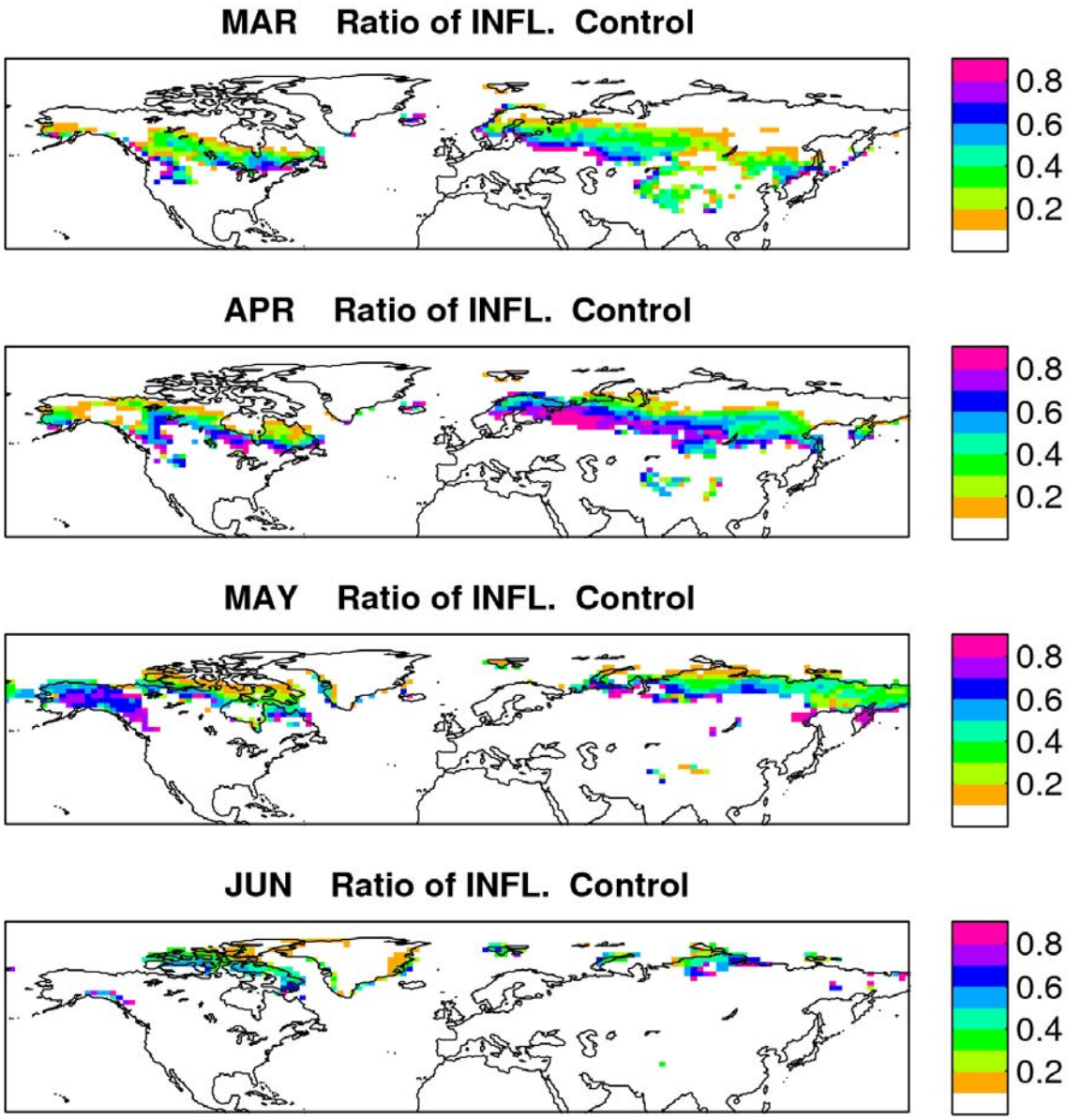

Figure 7.8 The fraction of snowmelt infiltrated into the soil obtained from the Control experiment during March to June.

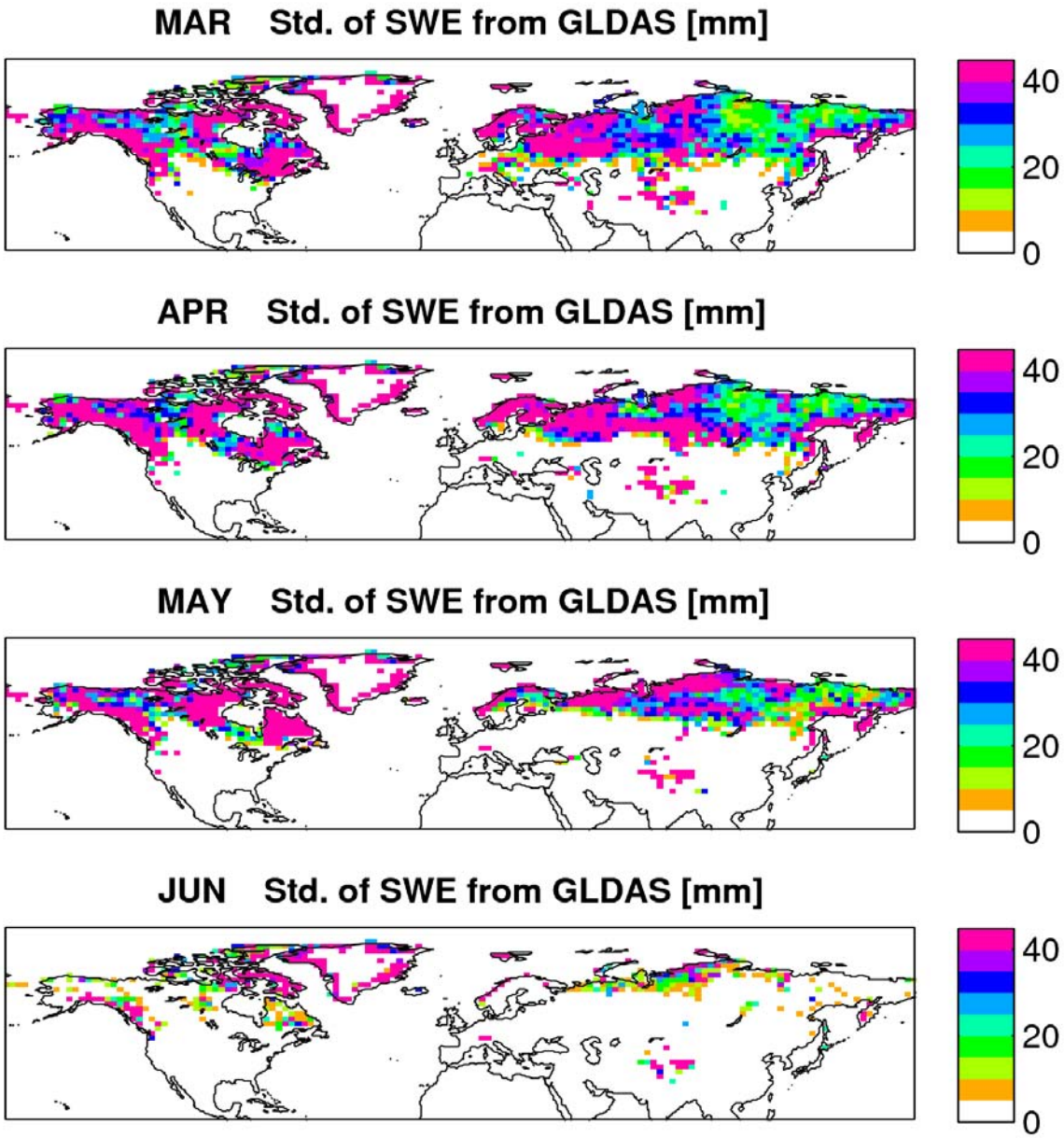

Figure 7.9 The interannual variability (standard deviation) of monthly SWE obtained from GLDAS during March to June.

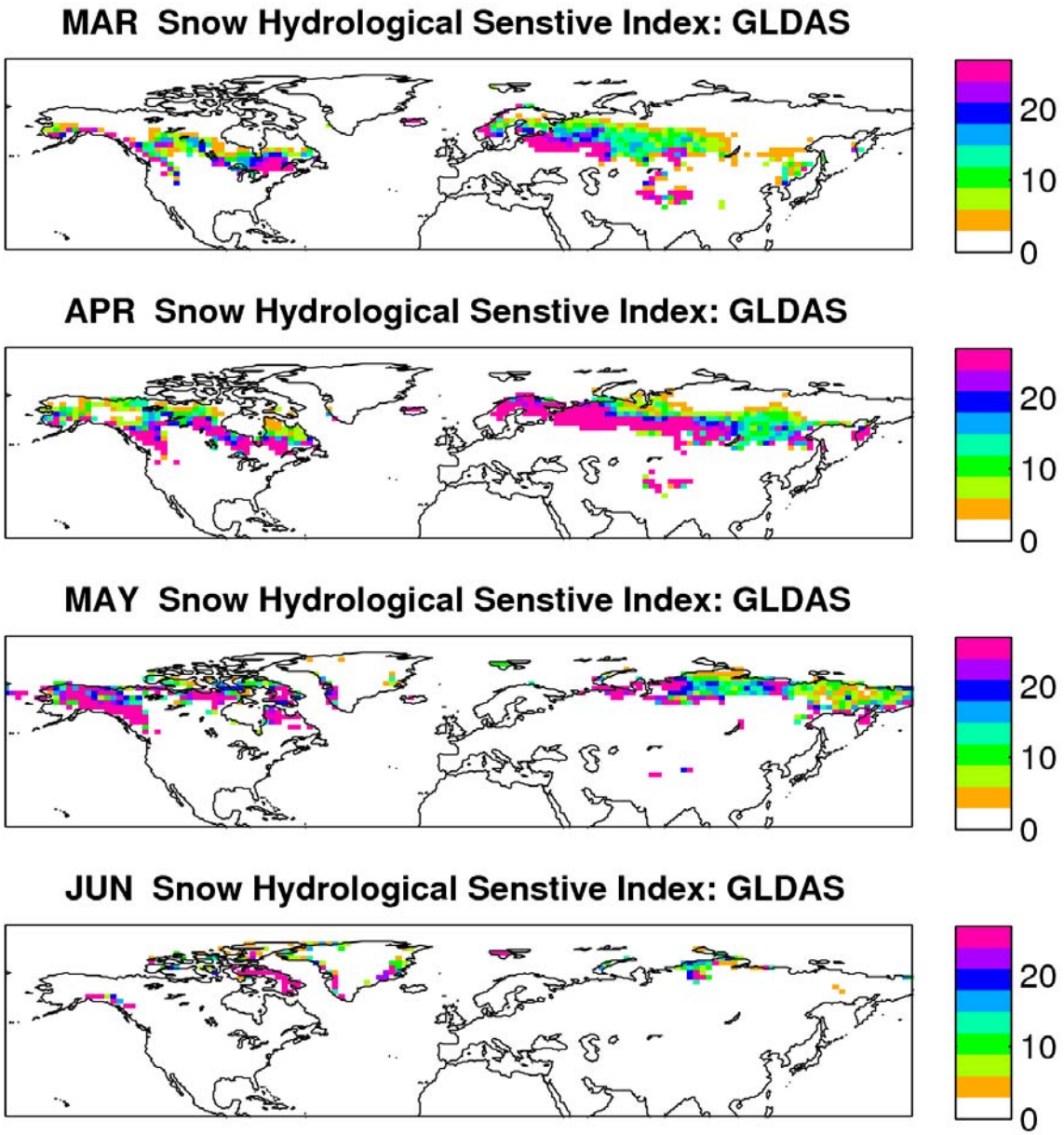

Figure 7. 10 Snow hydrological sensitivity index (SHSI) obtain from GLDAS during March to June.

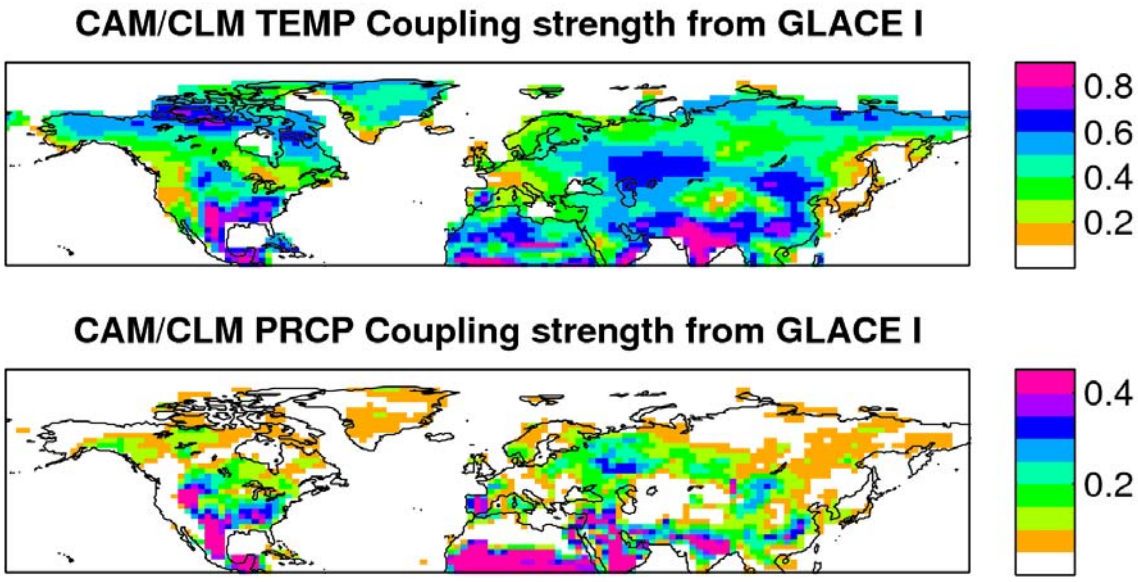

Figure 7.11 the CAM/CLM model land-atmosphere coupling strength [Ω(R)-Ω(W)] for temperature (top) and precipitation (bottom) obtained from the GLACE I experiment (From Guo et al. 2006).

CHAPTER 8. COUPLING STRENGTH AND PREDICTABILITY DUE TO REALISTIC SNOW FORCING

8.1 RealBoth experiment

As shown in Figure 4.3 and Figure 4.4, the CLM model seriously overestimates the climatological mean of SCF and SWE in coupled AMIP-style simulations, but it generally underestimates the interannual variability. The bias in the mean SCF has been corrected by CDF-matching; however, the underestimation of inter-annual variability remains and may lead to weak snow-atmosphere coupling strength. Prescribing realistic variability for both SWE and SCF is key to accurately quantifying realistic coupling strength and the contribution of snow to predictability.

In the ensemble experiment **RealBoth**, both SCF and SWE are prescribed from realistic values obtained from MODIS and the GLDAS dataset. In this sense, the ensemble **RealBoth** is similar to an observational simulation with "perfect" snow modeling. Compared with the ensemble **Control** experiment, in which the land snow scheme is fully coupled with the atmosphere**,** the ensemble **RealBoth**

experiment eliminates errors from snow modeling and provides a more realistic estimation of snow's effect on the atmosphere and predictability.

In addition, the difference between ensembles **RealSCF** and **RealBoth** provides another way to estimate the contribution due to the SWE information, which is strongly connected to the snow hydrological effect. On the other hand, the difference of ensembles **RealSWE** and **RealBoth** will isolate the improvement due to SCF and the snow albedo effect.

The **RealBoth** experiment will also provide a comprehensive survey of climate predictability and forecast skill associated with "perfect" snow boundary conditions, both in SWE and SCF, in CAM coupled with CLM. It is speculated that the increase in potential predictability associated with realistic snow information is strongly connected to snow-atmosphere coupling strength. It is essentially negligible in the lower-latitudes and Polar regions that show weak coupling; in contrast, it should be maximum in the transition zones in the middle-latitudes and high elevation regions. The increase in potential predictability for air temperature should be larger than precipitation with realistic snow boundary information.

8.2 Coupling strength and predictability due to realistic snow forcing

Figure 8.1 shows the snow-atmosphere coupling strength (the difference of intra-ensemble similarity between **ModBoth** and **RealBoth** experiments) for air temperature (2m height) from March to June. The coupling patterns are similar to

the estimations based on the model snow simulations, with only slight difference in magnitudes. Likewise, the coupling strength with precipitation (Figure 8.2) shows the same characteristics as previous estimations by model. The differences in coupling strength between realistic and model snow variability are plotted in Figure 8.3 and Figure 8.4. The positive anomalies indicate that CLM underestimates the coupling strength and negative anomalies imply overestimation, compared to realistic snow variability prescribed from MODIS and GLDAS data.

Regarding the temperature coupling strength (Figure 8.3), the CLM shows uneven bias. During March, the areas downstream of Tibet and over Eastern Europe are mainly overestimated while North America and Siberia are underestimated. During April, most regions are underestimated except for a few scattered regions. This underestimation could partially explain the sudden weakening in coupling strength in April in Figure 5.2b. Due to the biases in the snow scheme, CLM seriously underestimates the coupling strength during April. During May and June, CLM underestimates the coupling strength in regions just after snowmelt. A possible reason is underestimation of SWE that will lead to a weak snow hydrological effect.

For precipitation (Figure 8.4), the model underestimates coupling strength almost everywhere over the NH, except for a few scatter spots with negative anomalies. The possible reason is the underestimation of SWE by CLM 3.5 compared to GLDAS data (Figure 4.4). Underestimation in SWE will cause a weak snow hydrological effect and then reduce the snow-soil moisture-precipitation feedback.

Over the Tibetan Plateau, the difference of coupling strengths shows obvious negative biases, implying the overestimation of coupling strength.

Since the STR shows very similar patterns with coupling strength (Figure not shown), the differences of Signal-to-Total-Ratio for temperature and precipitation are shown in Figure 8.5 and Figure 8.6. Unsurprisingly, The CLM model shows a similar predictability difference pattern with the coupling strength as shown at previous experiment.

8.3 Second look at snow albedo effect and hydrological effect estimated by RealBoth

Like in chapters 6 and 7, the difference between ensembles **RealSCF** and **RealBoth,** where the only difference is the SWE, provides another way to estimate the contribution due to the snow hydrological effect. Based on the same principle, the difference of ensembles **RealSWE** and **RealBoth,** which vary in SCF, will isolate the improvement due to the snow albedo effect.

The temperature coupling strength computed as Ω(**RealSWE)-** Ω(**RealBoth)** shows similar characteristics with the temperature coupling strength computed as Ω(**ModBoth)-**Ω(**RealSCF),** except the magnitude is reduced (figure not shown). The major strong coupling regions are located in middle-latitudes along the intense SCF gradient (snow edge) and move northward over time with the snow edge withdraw. The Ω(**RealSCF)-**Ω(**RealBoth)** also shows reasonable estimated coupling strength

compared with Ω(**ModBoth)-**Ω(**RealSWE).** Both estimated coupling strengths are less in magnitude and more vague in the distribution of features compared to the results shown in Chapters 6 and 7, implying the original GLACE–type method provides better picture of coupling strength.

8.4 Discussion

In the **RealBoth** experiment, we investigated the atmospheric response to snow anomalies and interaction based on realistic observations of both SWE and SCF. Detail of the differences of snow-atmosphere coupling strength in air temperature at different regions is summarized in Table 8.1. Overall in the Northern Hemisphere (> 20°N), the simulation by CLM coupled with CAM slightly overestimates the coupling strength (negative difference) during spring, except during March. There are slight underestimations of snow coupling strength during March due to less snow variability simulated by CLM. In the continental average, the coupling strength over Eurasia is stronger than over North American due to the large land area at middle latitudes. The overestimation of coupling strength is most significant over the Tibetan Plateau, implying that the CLM still needs to improve its snow simulation over this complicated terrain.

As discussed in the experiment design section, there is roughly a 2% rate of inconsistencies between the SCF obtained from MODIS and SWE obtained from GLDAS, especially where SWE is equal to zero but the SCF is larger than zero, or vice

versa, during the ten-year period from 2000 to 2009. These kinds of inconsistencies happen most in middle-latitude regions where snow is unstable and not well simulated by the model, but where snow atmosphere coupling is strong. How important or significant these inconsistencies are to the results is unknown. There are no serious impacts on the high latitude regions where snow is stable and well simulated by CLM model.

In this experiment, we remove the possible ENSO effect by forcing all ensembles to same climatological SST cycle. To compare the ENSO effect to the snow boundary condition effect could reveal the relative roles of land versus ocean in local climate during the snow accumulation or ablation period. In a future study, comparing the snow contribution to forecast skill with the ocean contribution would be advantageous.

Table 8. 1 the regional means of coupling strength for temperature

	Model snow variability				Realistic snow forcing				Difference: realistic-model			
	March	April	May	June	March	April	May	June	March	April	May	June
Northern Hemisphere (>20°)	0.0899	0.0796	0.1392	0.0938	0.0918	0.0708	0.1041	0.0833	0.0019	-0.0088	-0.0351	-0.0105
Eurasia (>20°)	0.1116	0.0631	0.1549	0.1097	0.0846	0.0542	0.1027	0.0895	-0.027	-0.0089	-0.0522	-0.0202
North American (>20°)	0.0748	0.1154	0.117	0.0721	0.0458	0.1047	0.1071	0.0797	-0.029	-0.0107	-0.0099	0.0076
Middle-Lat. (40-60°)	0.123	0.0833	0.1138	0.088	0.0963	0.0906	0.1026	0.0539	-0.0267	0.0073	-0.0112	-0.0341
Tibetan Plateau (25-40°N, 70-110°E)	0.1544	0.0943	0.2063	0.1254	0.0627	0.069	0.1572	0.1146	-0.0917	-0.0253	-0.0491	-0.0108

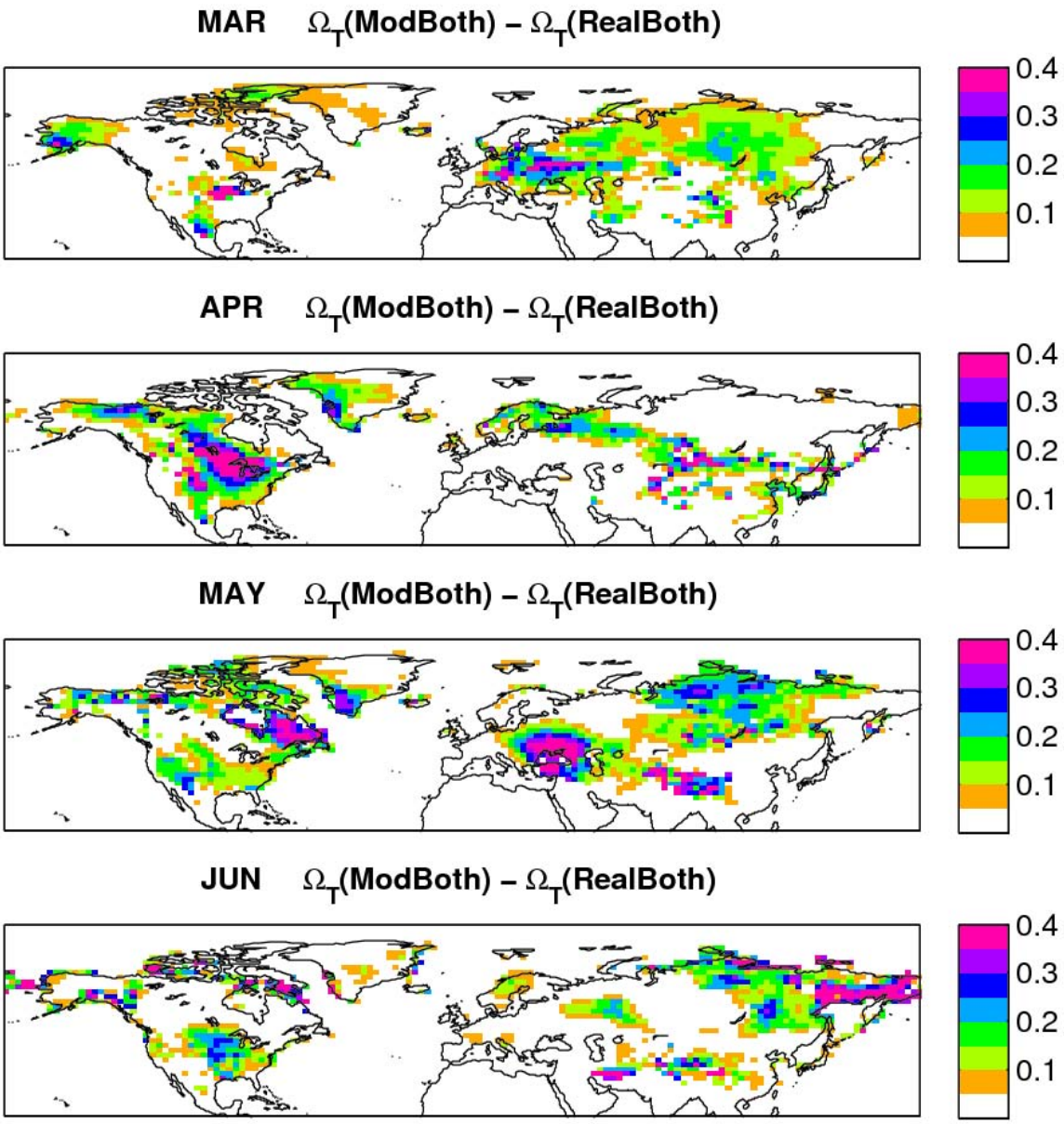

Figure 8.1 Coupling strength (the difference of intra-ensemble similarity of ModBoth and RealBoth experiments) for air temperature (2m height) from March to June.

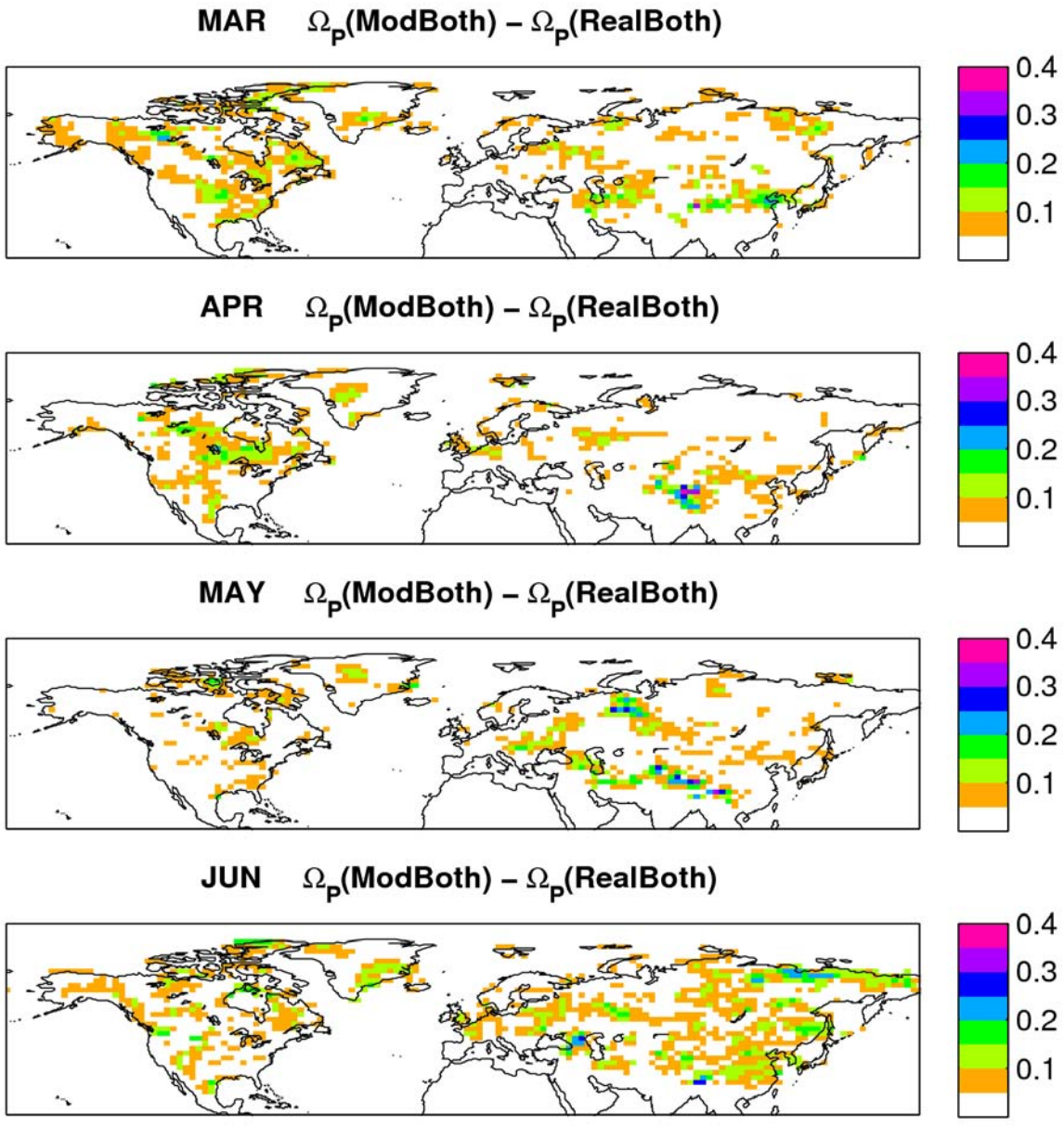

Figure 8.2 The same as Figure 8.1, but for precipitation.

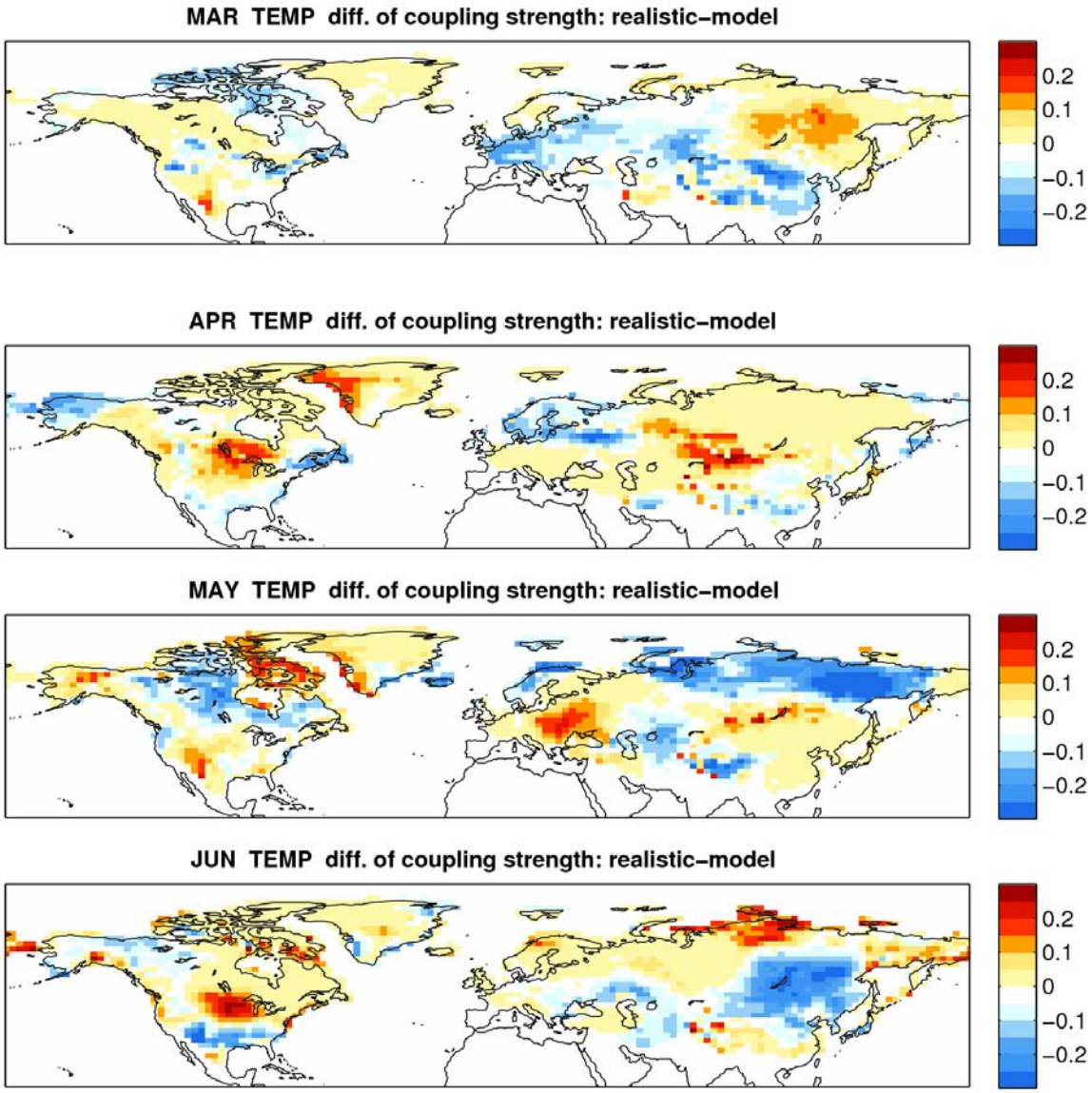

Figure 8.3 The differnce in coupling strength estimated by realistic snow forcing and model snow variability for air temperature (2m height) during March to June (the difference between Ω(ModBoth)-Ω(RealBoth) and Ω(ModBoth)-Ω(Control)) .

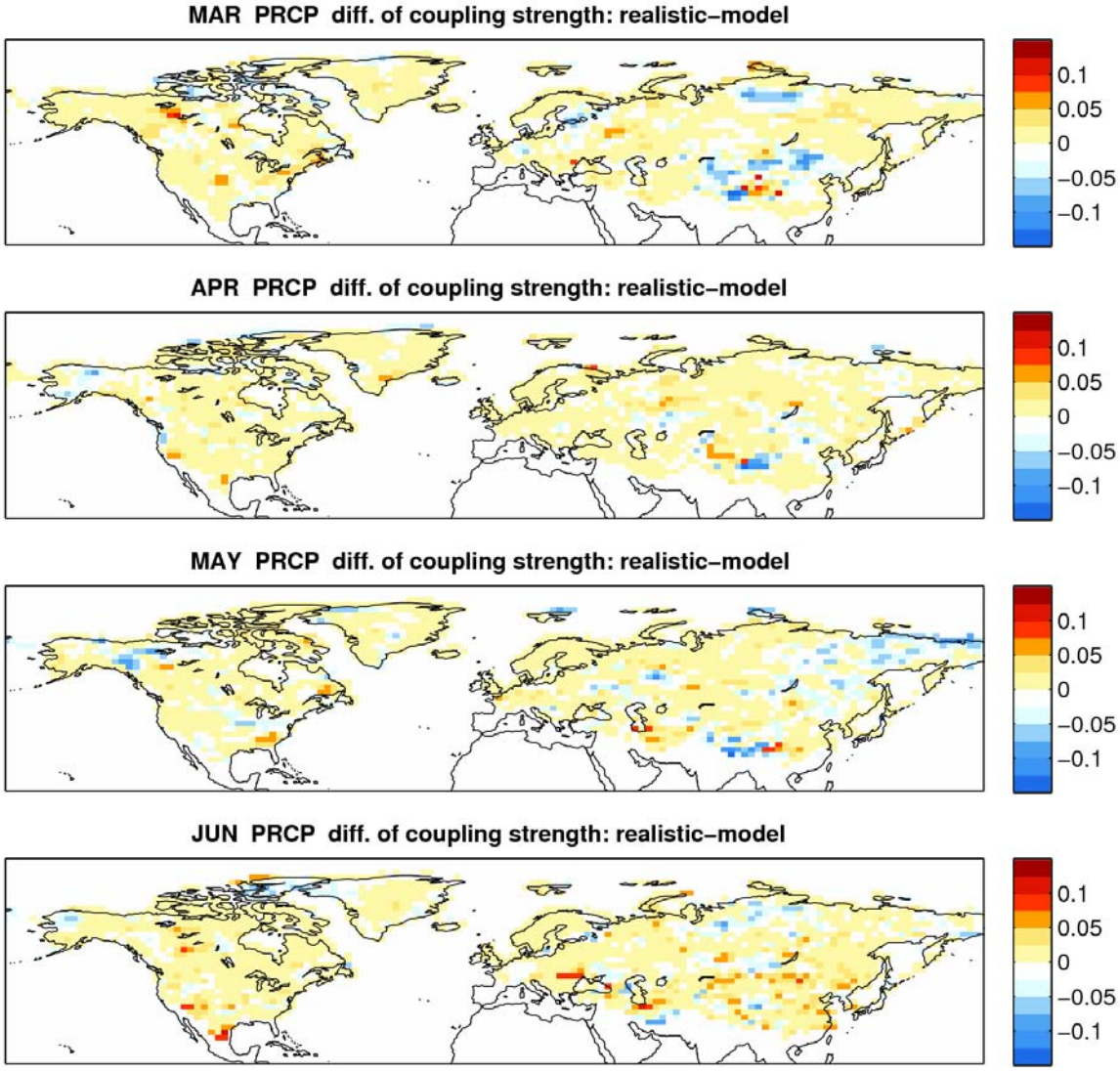

Figure 8.4 The same as Figure 8.3, but for precipitation.

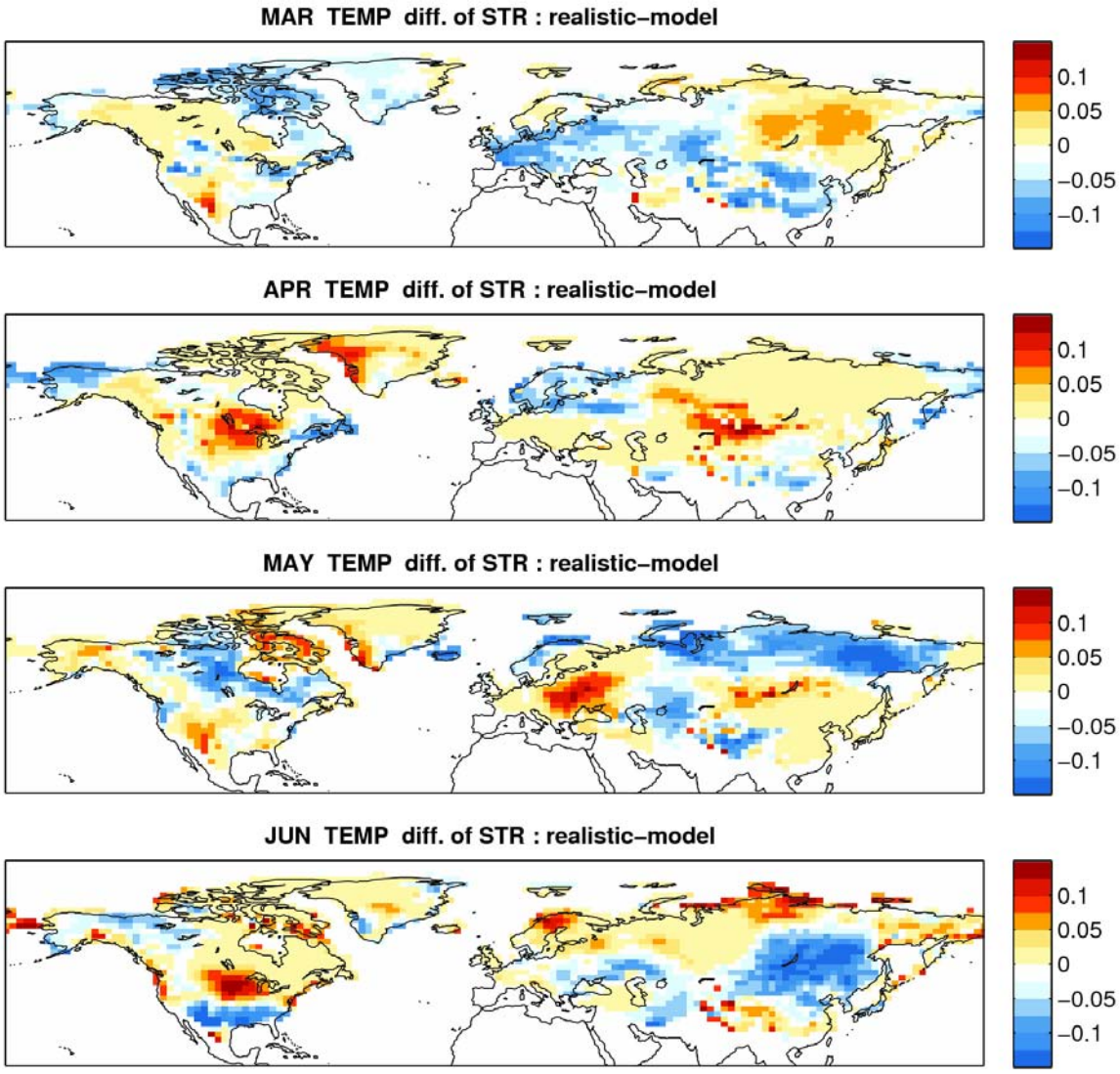

Figure 8.5 The difference of Signal-to-Total-Ratio for temperature estimated between realistic snow forcing and model predicted snow variability during March to June(the difference between STR(ModBoth)-STR(RealBoth) and STR(ModBoth)-STR(Control)).

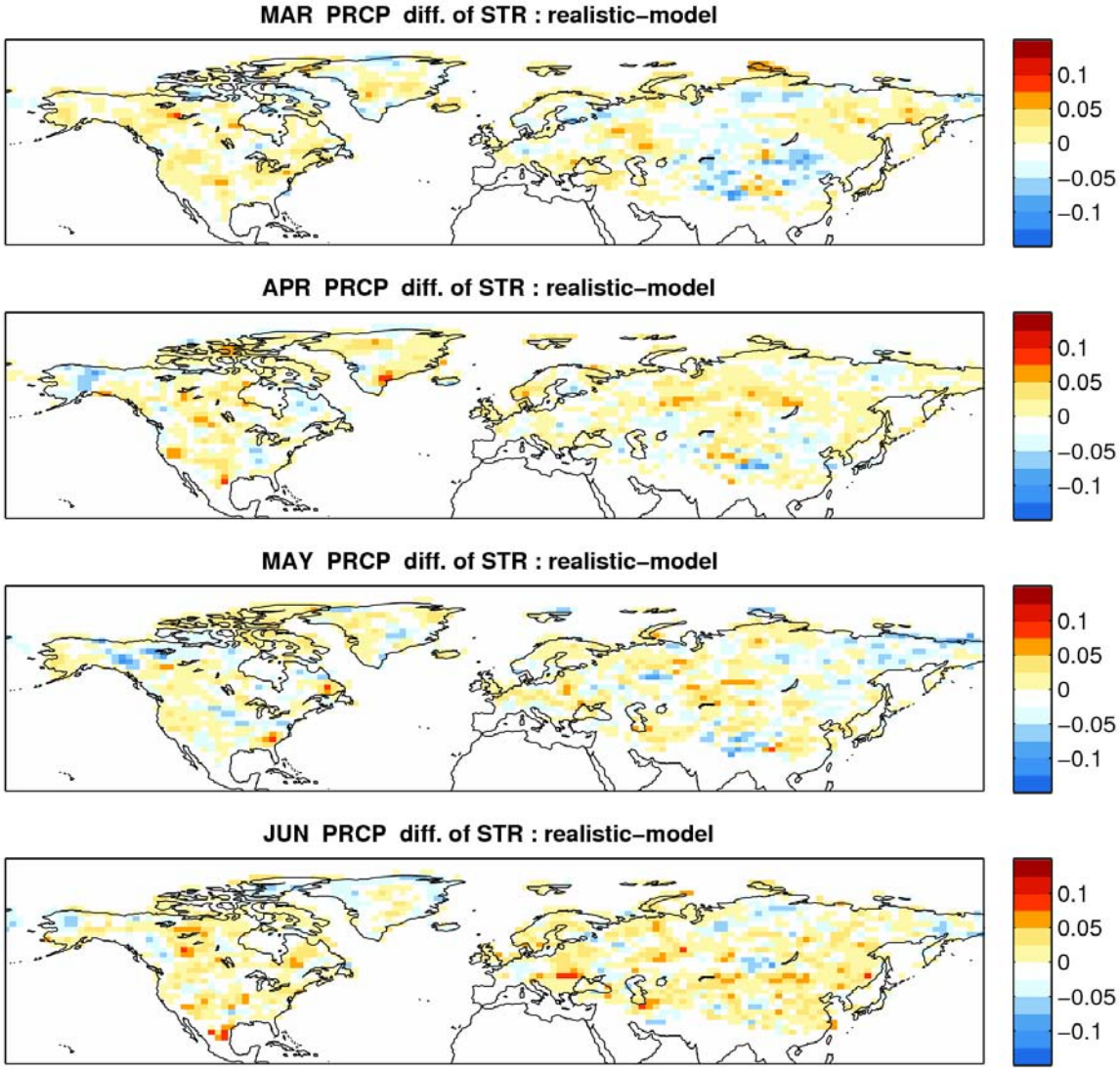

Figure 8.6 Same as the Figure 8.5, but for precipitation.

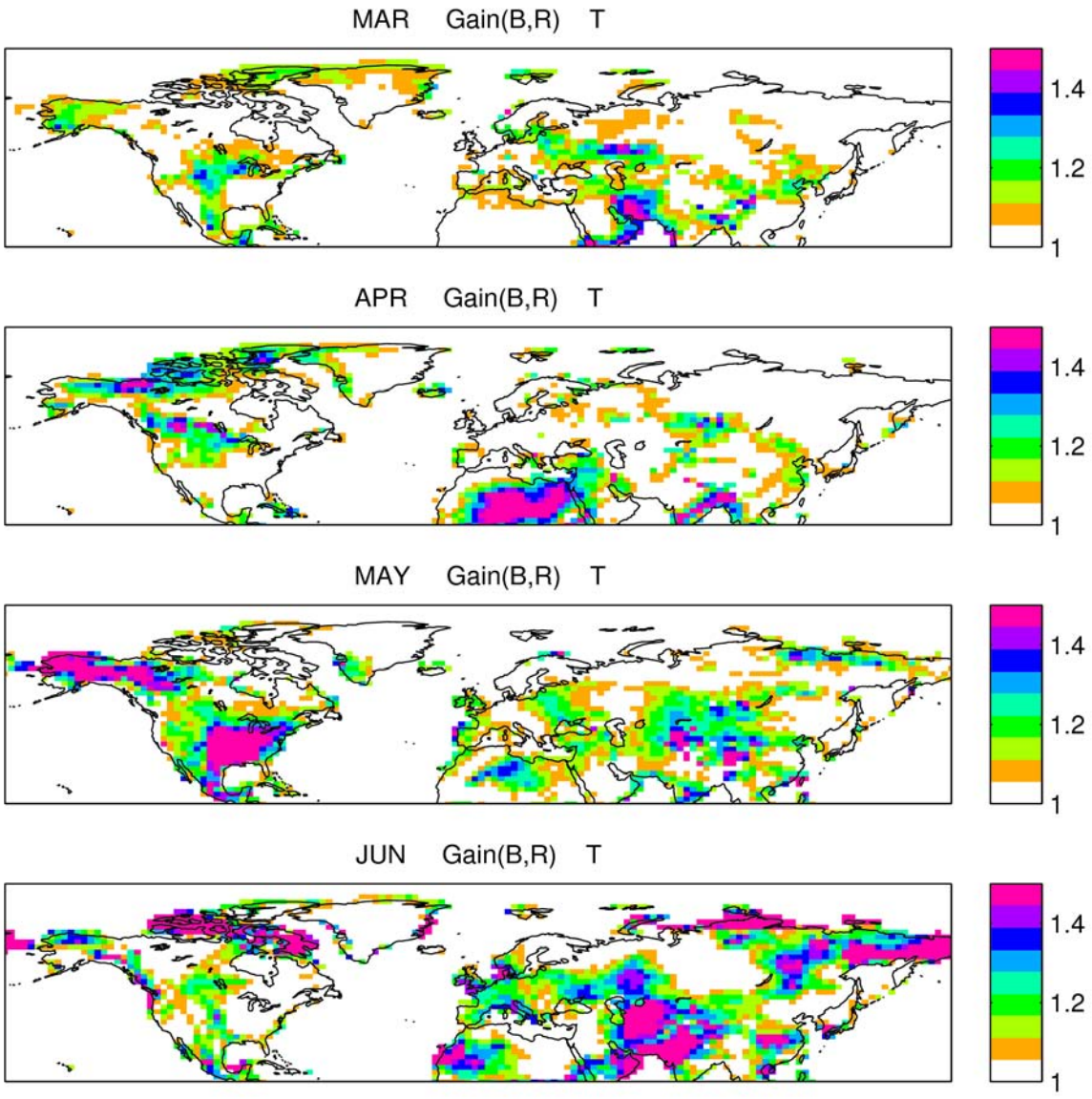

Figure 8.7 Gain index (the ratio of standard deviation of RealBoth and ModBoth experiments) for air temperature (2m height) from March to June.

CHAPTER 9. COMPARISON OF COUPLING STRENGTH BEFORE, DURING AND AFTER SNOWMELT

9.1 Three stages of snow evolution

Previous analyses are mainly organized by the calendar month. However, due to the various latitudes and elevations, different grid points show large variability in snow duration and melt timing. For example, the snow cover in the Canada will melt much late than those in the Tibetan plateau, but earlier than those in Siberia as shown at Figure 4.7 and Figure 4.8

Based on the typical SWE and SCF depletion curve (Figure 3.4), the snow cover is relatively stable with low variability in both SWE and SCF in the weeks and months before the annual snow melting. With increasing solar radiation and air temperature in spring, the snow rapidly begins to melt after a certain threshold. The snowmelt timing depends on several factors, but usually begins to accelerate at the time when SWE reduces to roughly 80% of its peak value. After the snowmelt begins, the snow quickly reduces in both the SWE and the SCF. After ablating 80% of

SWE, the depletion curve becomes flatter and as some patchy scattered snow persists in shadowed valleys.

Based on these features, we define the snowmelt begin date as the date when SWE reduces to 80% of peak value and the snowmelt end date as the date when SWE reduces to 20% of the peak. According to these two key thresholds, we can separate snow evolution into three stages: a stable persistence period before snowmelt, a rapid snowmelt period and an after snowmelt period. Figure 9.1 shows the climatological snowmelt begin date and end date obtained from GLDAS SWE depletion curves. The color scale is based on the Julian day. The snowmelt begins at the end of February at low-latitudes and generally delays with increasing latitude. The begin date and end dates are roughly parallel with latitude. The Tibetan Plateau shows a relatively later begin date and correspondingly later end date due to its high elevation. The snowmelt period, the interval between snowmelt begin and end dates, is short at middle-latitudes and increases with latitude. Almost all snow will melt after May.

Throughout this chapter, we locally define at each grid point the time periods for these three stages. This illustrates the various impacts better than using calendar months, especially in global maps. We have recomputed the coupling strength at each stage for the different experiments. Note that there are some grid points where the snowmelt is very rapid. If the snowmelt interval is less than 10

days in a grid, we artificial extend 5 days before and after for stability of the Ω calculation.

9.2 Snow albedo effect vs. hydrological effect

The snow albedo effect will directly change the energy balance of the land surface. The anomaly in albedo is a strong and fast forcing to the atmosphere. It will disappear immediately after the snows melt. On the other hand, the hydrological effect is a slow and persistent forcing to the atmosphere. Even after snow melt, the hydrological effect will still impact the atmosphere through soil moisture-evaporation-rainfall feedback. Table 9.1 summaries the differences between the snow albedo and hydrological effect.

Table 9.1 The comparison of snow albedo effect and hydrological effect

	Snow albedo effect	Snow hydrological effect
Impact	Direct	Indirect
Time scale	Instantly	Delayed (week to months)
Mechanism	Reflect more SW radiation	Soil-moisture-evaporation-precipitation feedback
Consequence	Change net energy	Change partitioning of sensible heat and latent heat

Figure 9.2 shows the temperature coupling strength due to the albedo effect before and during snowmelt. The snow and atmosphere show weak coupling before snowmelt but quite strong coupling during snowmelt. Before the snowmelt, there

are only a few regions, mainly located in Tibet, Alaska, Central and Eastern Europe, that show even weak coupling with the atmosphere. Most stable snow regions, such as Siberia and Canada, do not show substantial snow-atmosphere coupling. After the snowmelt begins, the coupling strengths are significant increased. The coupling strengths generally increase with latitude as shortwave radiation increases above critical thresholds. This implies the large variability in SCF during snowmelt will produce substantial albedo change then exert a strong forcing to the atmosphere above.

On the other hand, the infiltrated water during snowmelt also produces strong land atmosphere coupling as shown as Figure 9.3. The snow hydrological effects are stronger during snowmelt than after snowmelt. The snowmelt process requires a large amount of latent heat that maintains a relative stable low temperature. Europe also shows strong coupling strength due to the hydrological effect. The strong coupling in Siberia for the albedo effect is significantly weaker than due to the hydrological effect.

9.3 Model vs. realistic snow evaluations

Figure 9.4 shows the temperature coupling strength estimated by CLM snow evolution before, during, and after the snowmelt stage, including both the albedo effect and the hydrological effect (**Control**). Before snowmelt, the coupling strengths are generally weak. The stronger couplings are limited to the Tibetan Plateau, some middle latitudes of Europe and Center Asia. In contrast, the snow

coupling is stronger over Eurasia and North America during snowmelt. The strongest couplings happen over Europe and Siberia. The Tibet and East China regions also show relative stronger coupling. The weak coupling during snowmelt is collocated with arid regions in Central Asia. After the snowmelt, the atmosphere still shows considerable coupling due to the hydrological effect. The pattern of coupling strength is similar to the land-atmosphere coupling strength during summer shown in Figure 7.11.

On the other hand, the temperature coupling strengths estimated by realistic snow evolution (**RealBoth**) are shown at Figure 9.5. The overall structure of coupling strength estimated by realistic snow agrees well with the estimation by model-simulated snow, except the magnitudes of coupling strength are slightly less. The coupling strength in Siberia is less than for the model estimate. This implies CLM can capture well the snow-atmosphere coupling phenomena.

9.4 Zonal mean

Figure 9.6 shows the zonal mean of temperature coupling strength over NH snow regions estimated before, during and after snowmelt stage grouped by sources: model snow, realistic snow, albedo effect and hydrological effect. In all cases, the coupling strengths are strongest during the snowmelt period and weakest before the snowmelt. Generally speaking, the coupling strengths increase poleward with a maximum at around 50-65° and then sharply decrease to the north of 70°. There is a local peak of coupling strength at rough 30° corresponding to the Tibetan

Plateau. During the snowmelt period, both the albedo and hydrological effect contribute to the coupling strength. The coupling strength due to the albedo effect during snowmelt is almost triple than before snowmelt. The hydrological effect during snowmelt is generally much stronger than after melting. Note that there are few regions with stronger hydrological effect after snowmelt. Before snowmelt, the model snow evolution slightly underestimates the coupling strength compared to the realistic snow evolution. During snowmelt and after snowmelt, however, the model snow evolution overestimates coupling strength.

9.5 summary

The snowmelt process and the evolution of snow-atmosphere coupling strength can be separated into three stages: a stable stage before melt, a quick reduction stage during snowmelt and a lagged impact stage after snowmelt. Table 9.2 summarizes the means of coupling strength over NH snow regions during these three stages. Before snowmelt, the coupling strengths are weakest and the albedo effect contributes to most of the coupling strength. CLM with prognostic snow slightly underestimates the coupling strength compared to when realistic snow forcing is specified. During snowmelt, the snow-atmosphere coupling is strongest; the albedo effect contributes slight more to the coupling strength than the hydrological effect. CLM slightly overestimates coupling strength during snowmelt. After snowmelt, the hydrological effect contributes most of the coupling strength.

Compared to the albedo effect before snowmelt (0.039), the hydrological effect after snowmelt exhibits stronger coupling strength (0.080).

Separating the snowmelt phase into three stages well distinguishes the different mechanisms for snow coupling: by albedo effect, or hydrological effect or both. However, each stage is different in length based on local geographic features that may introduce some uncertainties in comparing the coupling strength. Longer period data series tend to have less similarity and shorter data series have higher Ω values in general. However, the coupling strength is defined as the difference of Ω between two experiments that are computed from the same length of data. Thus the uncertainties due to different lengths in horizontal comparison are reduced.

Table 9. 2 the mean of coupling strength over NH snow regions during three stages

	Model	Albedo effect	Hydrological effect	Realistic
Stable snow before melt	0.059	0.039	N/A	0.066
During snowmelt	0.128	0.104	0.094	0.108
After snowmelt	0.086	N/A	0.080	0.081

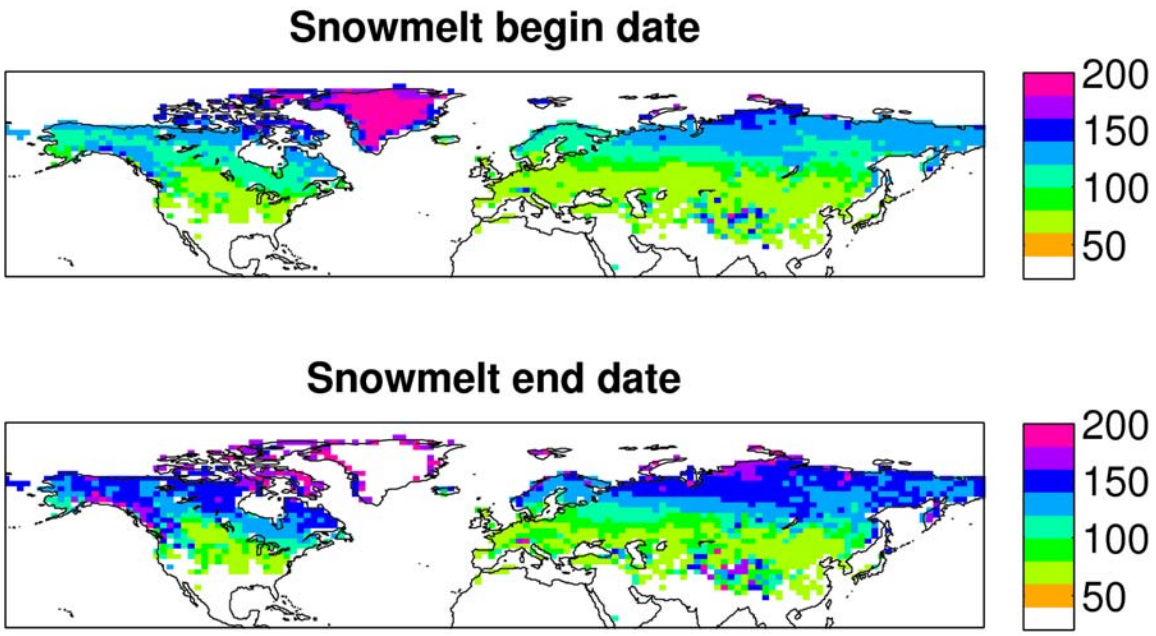

Figure 9.1 the climatological snowmelt begin date and end date based on the SWE ablation curve obtained from GLDAS. The color scales indicate the Julian day.

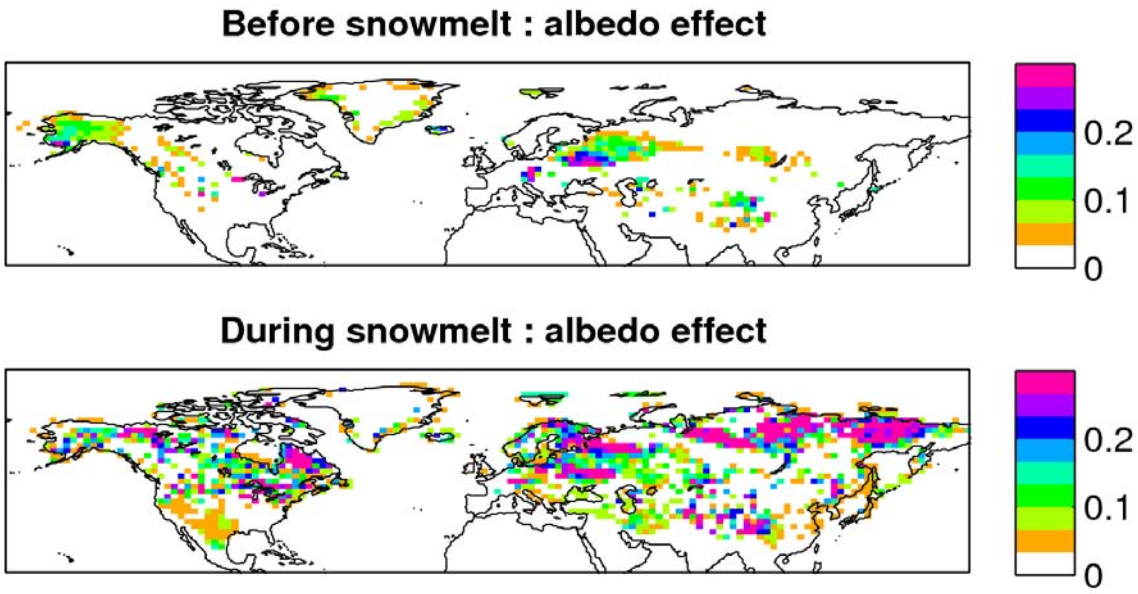

Figure 9.2 The temperature coupling strength (the difference of Ω) due to snow albedo effect before and during snowmelt stage.

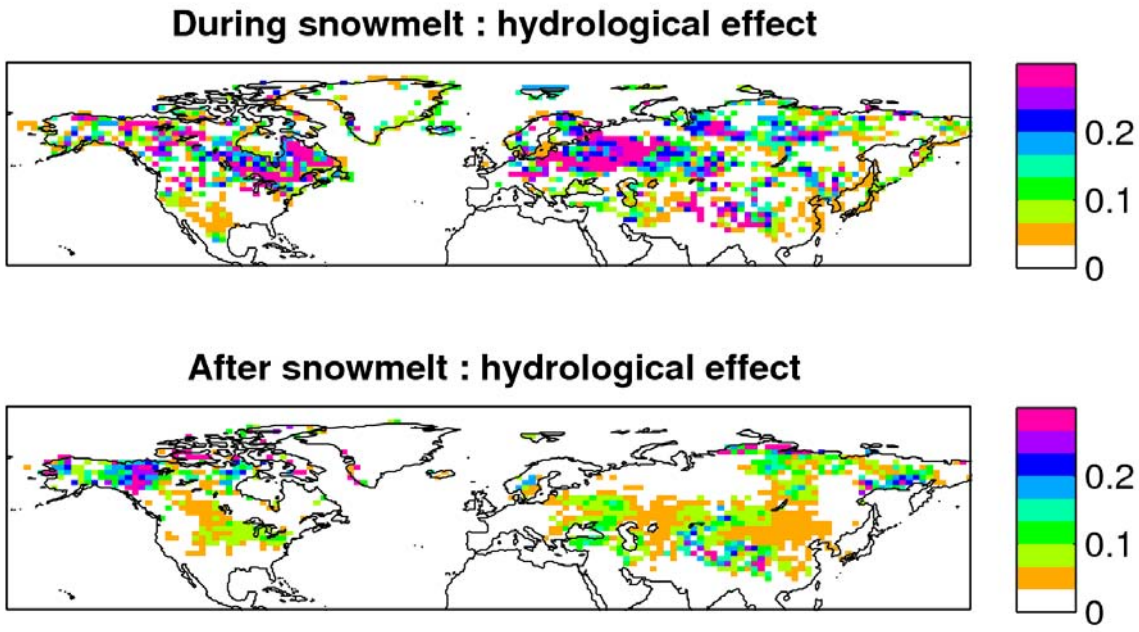

Figure 9.3 Same as the Figure 9.2, but for the snow hydrological effect at during and after snowmelt stage.

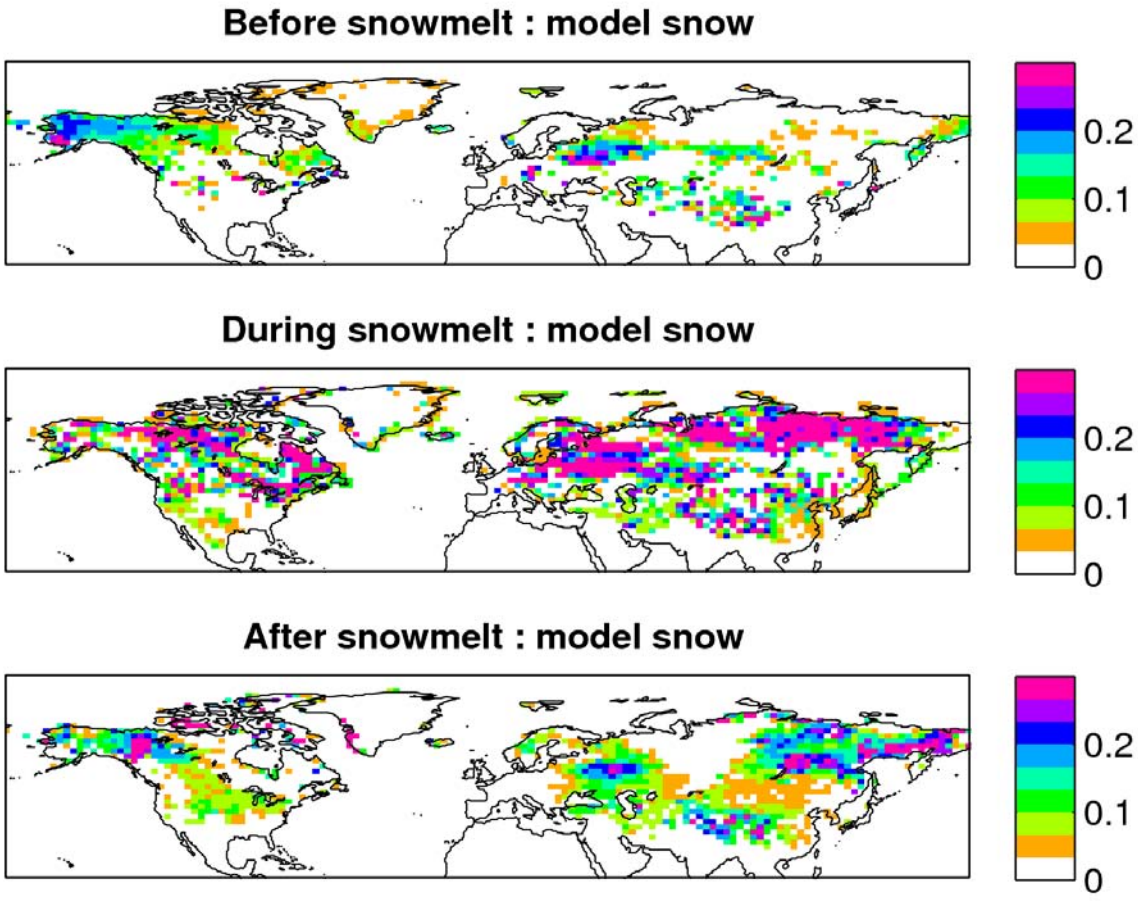

Figure 9.4 The temperature coupling strength (the difference of Ω) estimated by model snow evolution before, during, and after snowmelt stage.

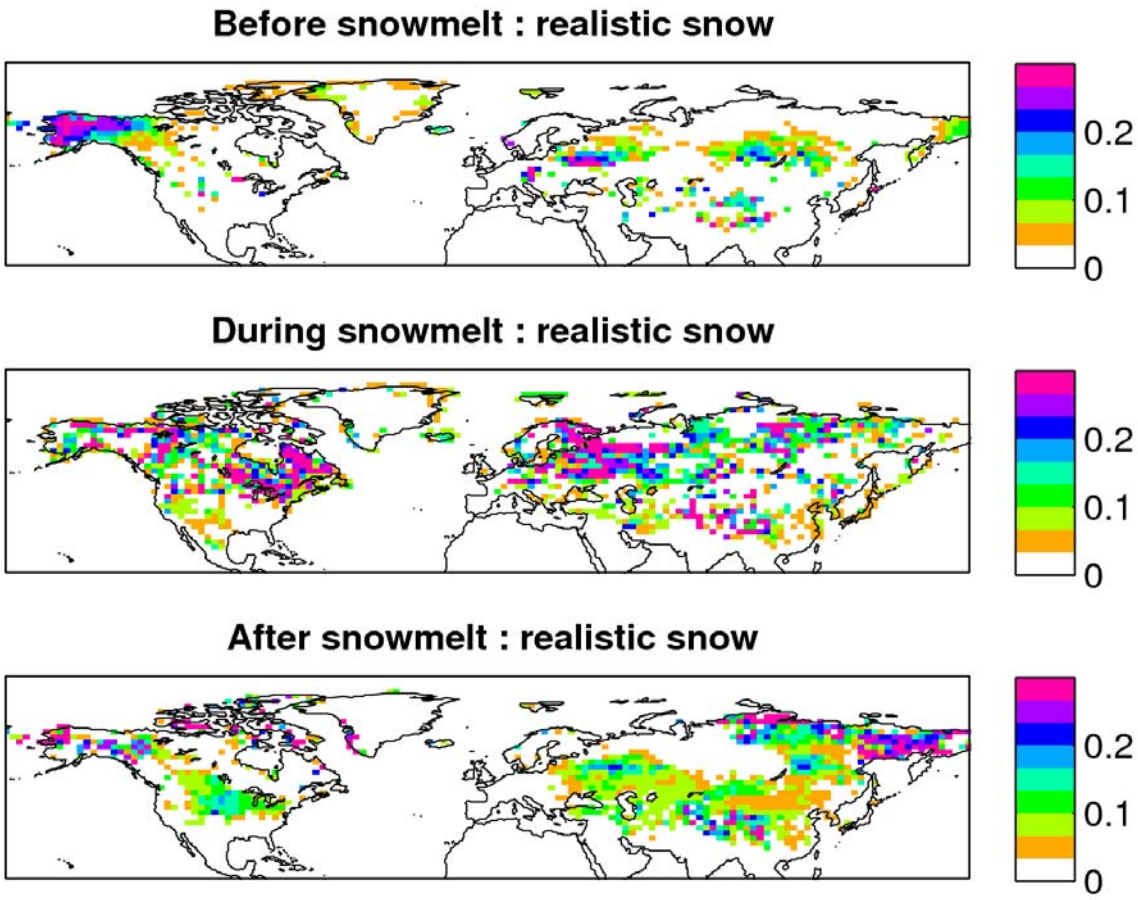

Figure 9.5 Same as the Figure 9.4, but for realistic snow evolution.

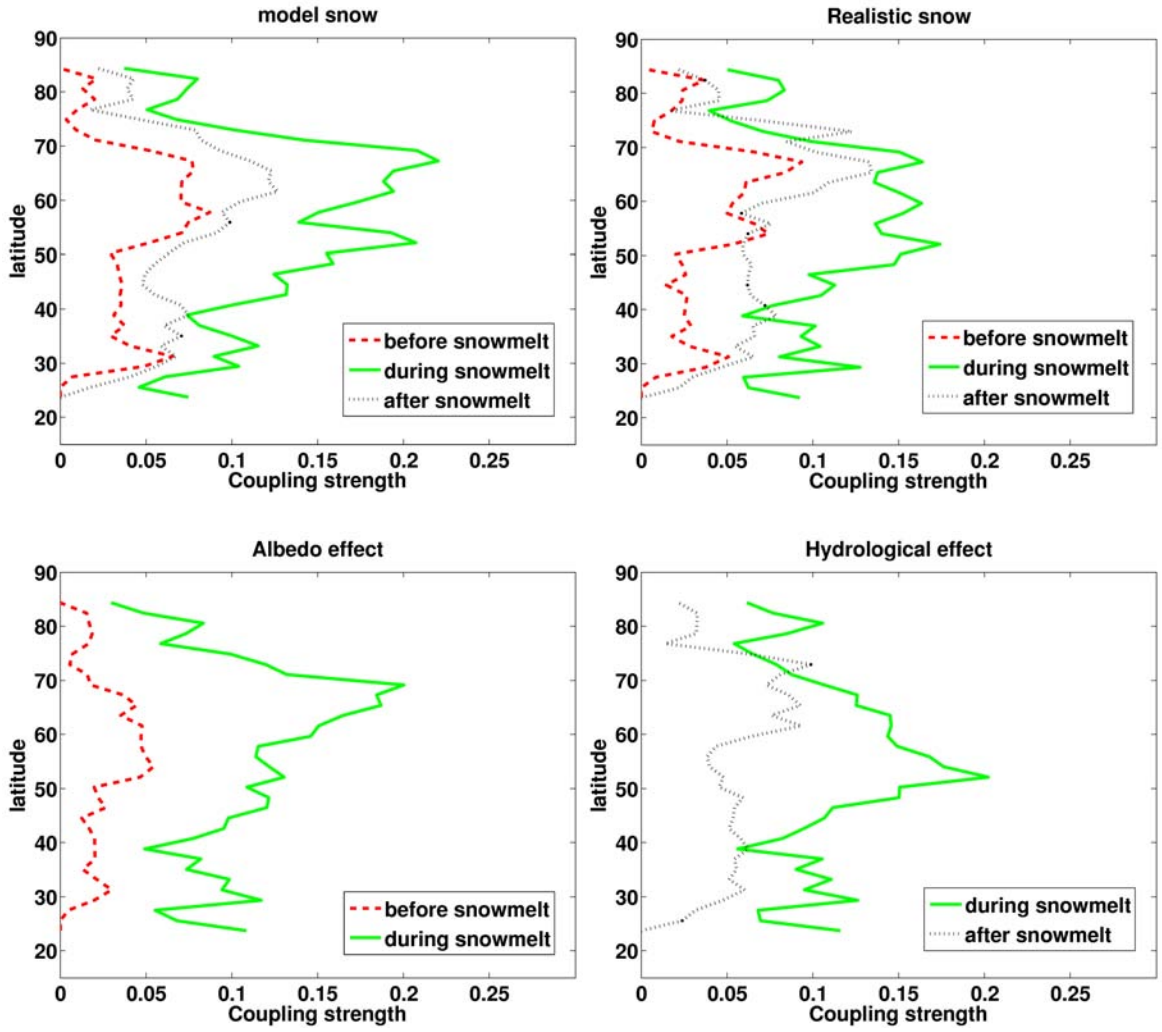

Figure 9.6 The zonal means of temperature coupling strength (the difference of Ω) for different snowmelt stages.

CHAPTER 10 THE EVALUATION OF FORECAST SKILL DUE TO SNOW-ATMOSPHERE COUPLING

10.1 Evaluation

Previous chapters have demonstrated that the potential predictability measured by STR is systematically enhanced by snow-atmosphere coupling. The spatial distribution of the enhancement of STR is almost identical with the snow-atmosphere coupling strength. **How skillful is the climate simulation with and without prescribed snow information? How much forecast skill comes from snow atmosphere coupling?** In this chapter, we determine the degree to which the model can predict climate both with and without the realistic snow boundary information. We try to reveal the geographical variation of the model's forecast skill at sub-seasonal timescales as produced by the albedo effect, the hydrological effect or both.

In each ensemble experiment, the daily time series of atmospheric states, such as temperature and precipitation, in the ten ensemble members are temporally averaged to produce 8-day means (the same as the MODIS MOD1OC2 data interval)

from 1 March to June 30th, and then evaluated against observed values during 2000-2009. Since the temperature and precipitation have relatively larger annual cycles, we evaluated the anomalies after removing the annual cycle. The key elements to evaluate the forecast skill are R squared (R^2), Root Mean Square Error (RMSE) and Nash-Sutcliffe Coefficient of Efficiency (NSE) as described in Chapter 3.

The temperature data used in this validation come from NCEP/DOE reanalysis data (R-2, [*Kanamitsu et al.*, 2002]). The precipitation was obtained from the NASA Global Precipitation Climatology Project (*GPCP*) Version 2.1 1-degree daily (1DD) dataset [*Huffman et al.*, 1997]. Both temperature and precipitation data were bi-linear interpolated onto the native 1.9x2.5 CAM grid.

10.2 R squared (R^2)

Figure 10.1 shows the difference of temperature forecast skill represented by the R squared (R^2) among various experiments (**RealSCF**, **RealSWE**, **RealBoth**) and the **RealClim** experiment. The correlations are calculated by 15 8-day periods and then averaged over the 10 years at each grid-point. Since the **RealClim** experiment removes all possible inter-annual variability of snow boundary forcing, the R squared of **RealClim** could be considered as the baseline of predictability (forecast skill) of the atmosphere model with minimal contribution from snow atmosphere coupling. The difference of R squared between **RealBoth** and **RealClim** experiments is a simple measure of how much forecast skill is due to the realistic snow cover information. Similarly, the differences R^2(**RealSCF**)-R^2(**RealClim**) and

R^2(**RealSWE**)-R^2(**RealClim**) will assess separately how much forecast skill is due to the accurate representation snow albedo effect and hydrological effect.

General speaking, the forecast skill represent by R squared over the majority of NH snow regions is increased by prescribing realistic snow information in **RealSCF**, **RealSWE**, **RealBoth** compared to the **RealClim** experiment. There are some scattered regions, mainly located in the coastal regions and upstream of snow regions, where forecast skill is degraded, although the magnitudes of the changes are small. The biggest enhancements in forecast skill are located in the centers of the mid-latitude continents where the snow-atmosphere coupling dominates climate variability.

On the other hand, the difference of R squared between the three experiments and **RealClim** for precipitation shows a much more complicated structure (Figure 10.2). As with coupling strength, the forecast skill in precipitation due to snow coupling is very patchy. Overall, the forecast skill is enhanced but with sporadic distributions.

10.3 Nash-Sutcliffe Coefficient of Efficiency (NSE)

The Nash-Sutcliffe Coefficient of Efficiency (NSE) is similar to the skill score used to quantitatively describe the accuracy of model predictions compared with climatological forecasts. The closer the model NSE is to 1, the more accurate the model is. If the NSE is below zero, it indicates the forecast does not show skill compare to a climatological forecast. Figure 10.3 shows the difference of NSE for

temperature. Compared to R squared, the overall enhancement in NSE is significantly less for all three experiments. The skill is not improved over most regions based on the albedo effect (**RealSCF**). The hydrological effect (**RealSWE**) contributes more to the enhancement in the skill score. Combining both effects, the **RealBoth** experiment shows the largest enhancement in skill score relative to a climatological forecast.

However, in the NSE skill score for precipitation (Figure 10.4), all three experiments show clear enhancement compared to **RealClim**. This indicates the snow atmosphere coupling contributes more to the precipitation forecast skill by this metric. The snow-atmosphere coupling will impact the atmospheric temperature profile, in particular the lower to middle troposphere, and thus the stability and convective development.

10.4 Root Mean Square Error (RMSE)

Root mean square error (RMSE) is another frequently used index to quantity the differences between the prediction and observations, representing a measure of precision. RMSE serves to aggregate all differences or residuals at each 8-day period into a single measure of predictive power. Unlike the previous two parameters, the lower the RMSE, the better prediction is.

Figures 10.5 and 10.6 show the difference of RMSE in temperature and precipitation simulations for the different experiments against to the baseline simulation **RealClim**. Similar to the NSE, the precipitation is improved almost

everywhere over the NH. The RMSE during MAMJ is reduced due to realistic snow variability. However, the temperature forecasts are only improved over some regions. In the center of the continents, the temperature forecast is improved due to snow-atmosphere coupling. However, there are still large areas over the NH where the temperature forecasts are not improved. The forecast improvement due to the albedo effect, i.e. RMSE(**RealSCF**)-RMSE(**RealClim**), is the weakest. The hydrological effect contributes more forecast skill than the albedo effect overall. Having both realistic SCF and SWE information in **RealBoth** provides the greatest improvement in the temperature forecast skill.

10.5 Time evolution

To reveal the time variation of snow coupling contributions to predictability, we analyze the time evolution of the spatial mean of forecast skill over the NH snow region. The NH snow regions are defined as the areas where climatological MODIS SCF is large than 1% on March 1st in the 10-year climatological map. The temperature predictions are evaluated against the reanalysis data at each 8-day period during 2000-2009, and then spatially average over specific regions, such as the whole NH snow region, Eurasian continent, North American continent, NH middle-latitudes and the Tibetan Plateau.

Figure 10.7 shows the spatial mean of Root Mean Square Error (RMSE) over the NH snow region over the NH for **Control**, **RealSCF**, **RealSWE** and **RealBoth** experiments. The **RealBoth** experiment has greatly reduced RMSE over the whole

NH snow region compared to **Control**, which lacks realistic snow information. Except for a few days around 145th-155th Julian Day, the RMSE is reduced during the snow ablation period. The biggest improvement in RMSE occurs during 100th-140th Julian Day, corresponding to the main snowmelt period, with the strongest snow-atmosphere coupling strength. In contrast, before the snowmelt stage (60-100th day) and after the snowmelt stage (140-180), the improvements are less. Before the snowmelt (60-100th Julian day), the **RealSCF** experiment is dramatically improved, but with little or no improvement for the **RealSWE** experiment. After the snowmelt (140th Julian day), the RMSE is improved most in the **RealSWE** experiment. In Figure 10.8, similar characteristics are shown for the 10-years mean of spatial correlation R^2 over the snow region NH.

Figure 10.9 plots the spatial mean of RMSE over four particular snow regions: Eurasia (the north of 20°N at Eastern Hemisphere), North America (the north of 20°N at Western Hemisphere) , NH middle-latitudes (40-60°N) and the Tibetan Plateau (25-45°N, 70-110°E). The forecast improvement from use of realistic snow information measured by RMSE is larger over the Eurasia (EA) than over North America (NA). During the snowmelt period (rough 100th – 140th Julian day) the forecast improvements in **RealSWE** and **RealBoth** are most significant over the NH middle latitudes (40-60°). The average RMSEs over the Tibetan Plateau are smallest, but they do not show obvious improvement with prescribed realistic snow information.

10.6 Discussion

Although these experiments are mainly designed to reveal the snow-atmosphere coupling strength, they also potentially provide some insight into the predictability contributed by the snow boundary forcing. In all evaluated experiments, **RealSWE**, **RealSCF** and **RealBoth**, the atmosphere initial conditions come from the same restart files of the CAM GCM. They provide atmospheric conditions that are well balanced and representative of that time, but without any realistic information. In addition, the ocean boundary conditions are prescribed from a climatological annual cycle that completely removes inter-annual SST boundary information. The only predictability source in the evaluated experiment comes from realistic snow boundary information.

In future study, the role of snow cover in climate predictability needs to be investigated further. The second Global Land-Atmosphere Coupling Experiment (GLACE-2) [*Koster et al.*, 2010] provides a prototype to further quantify the degree to which realistic land surface initialization contributes to the skill of sub-seasonal precipitation and air temperature forecasts. An objective quantification and documentation of the forecast skill enhancement (benefit) due to snow initiation across the globe would be valuable to our knowledge of snow-climate interaction. Determining how snow initialization contributes to seasonal forecast skill will improve our understanding of climate predictability.

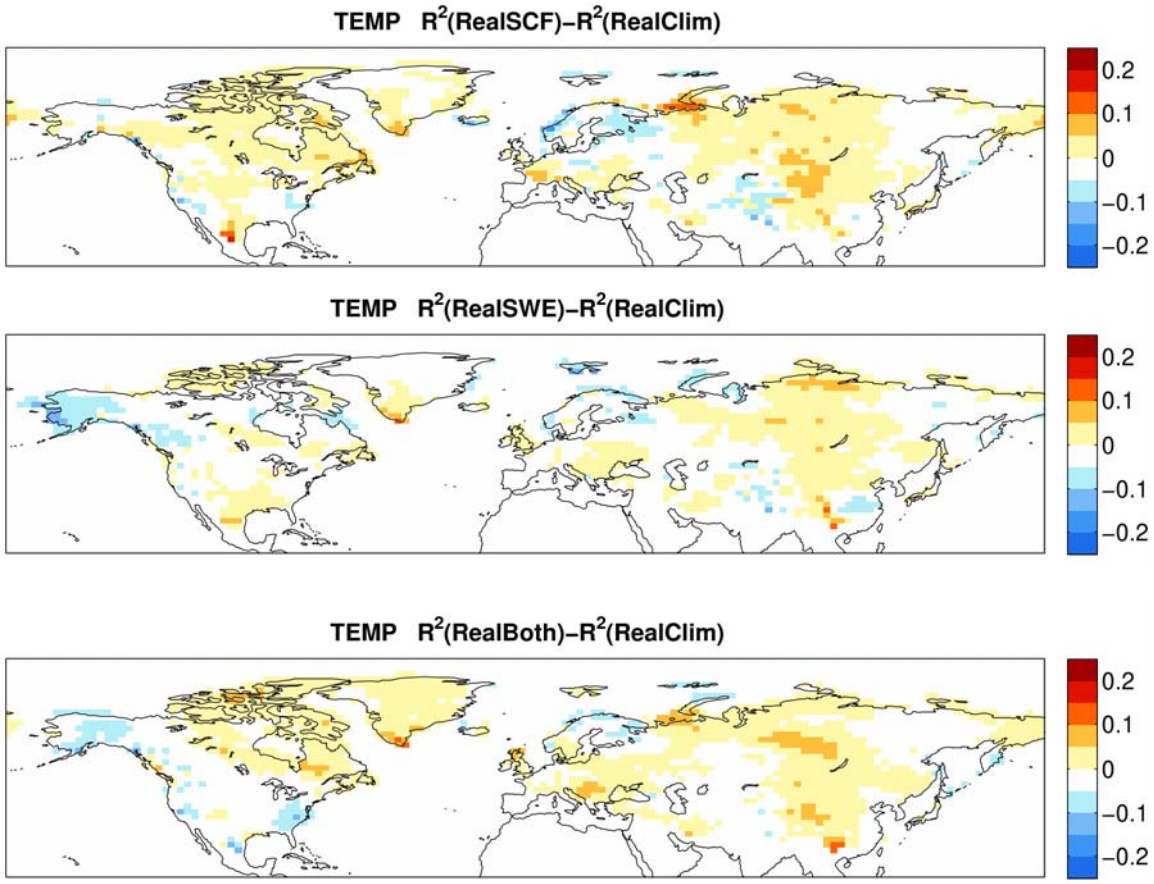

Figure 10.1 The difference of R squared (R^2) for temperature between the different experiments.

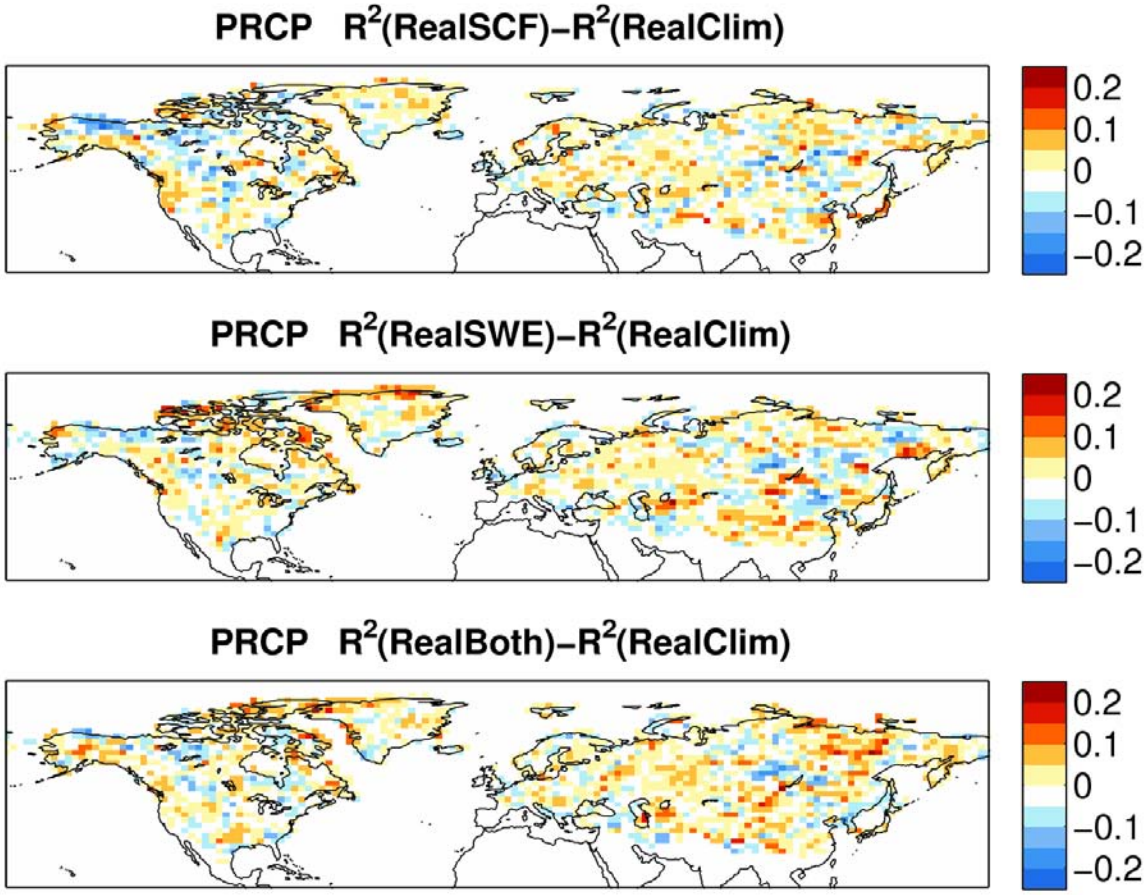

Figure 10.2 The same as Figure 10.1, but for precipitation.

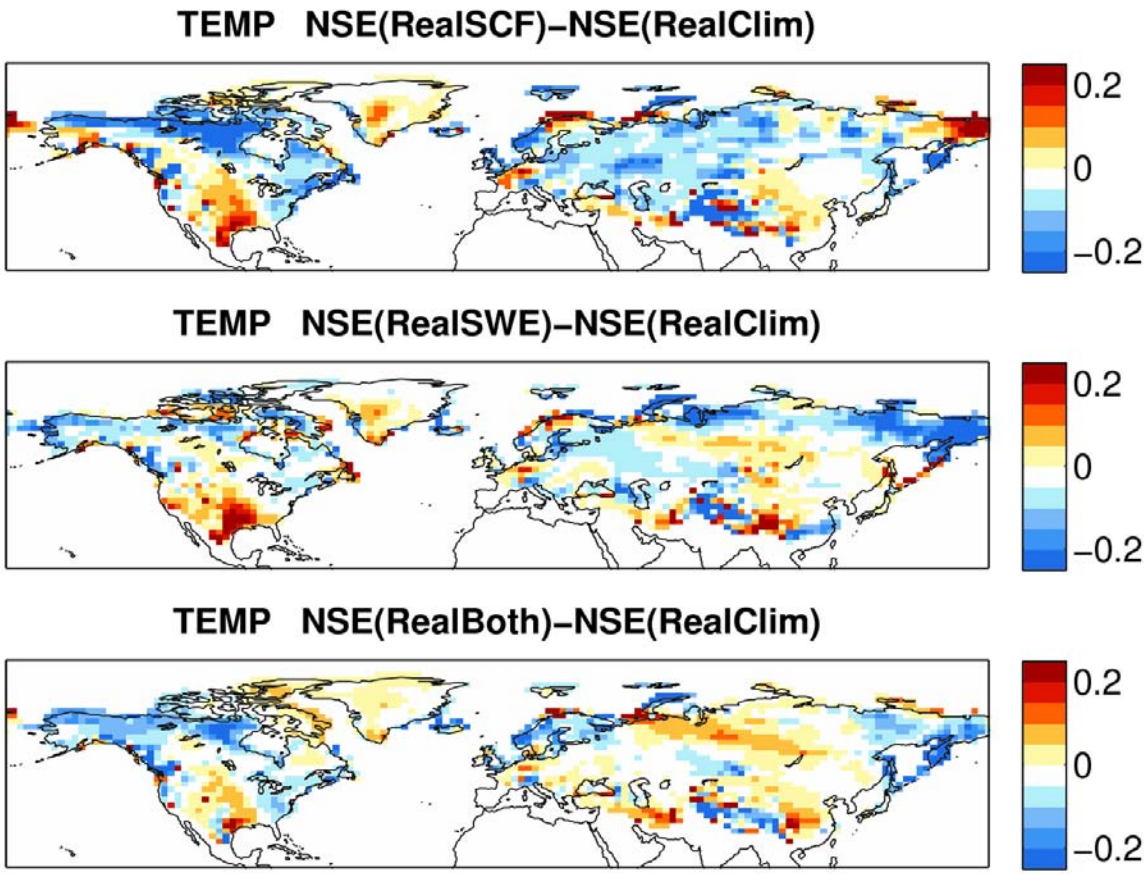

Figure 10.3 The difference of Nash-Sutcliffe Coefficient of Efficiency (NSE) for temperature among the different experiments.

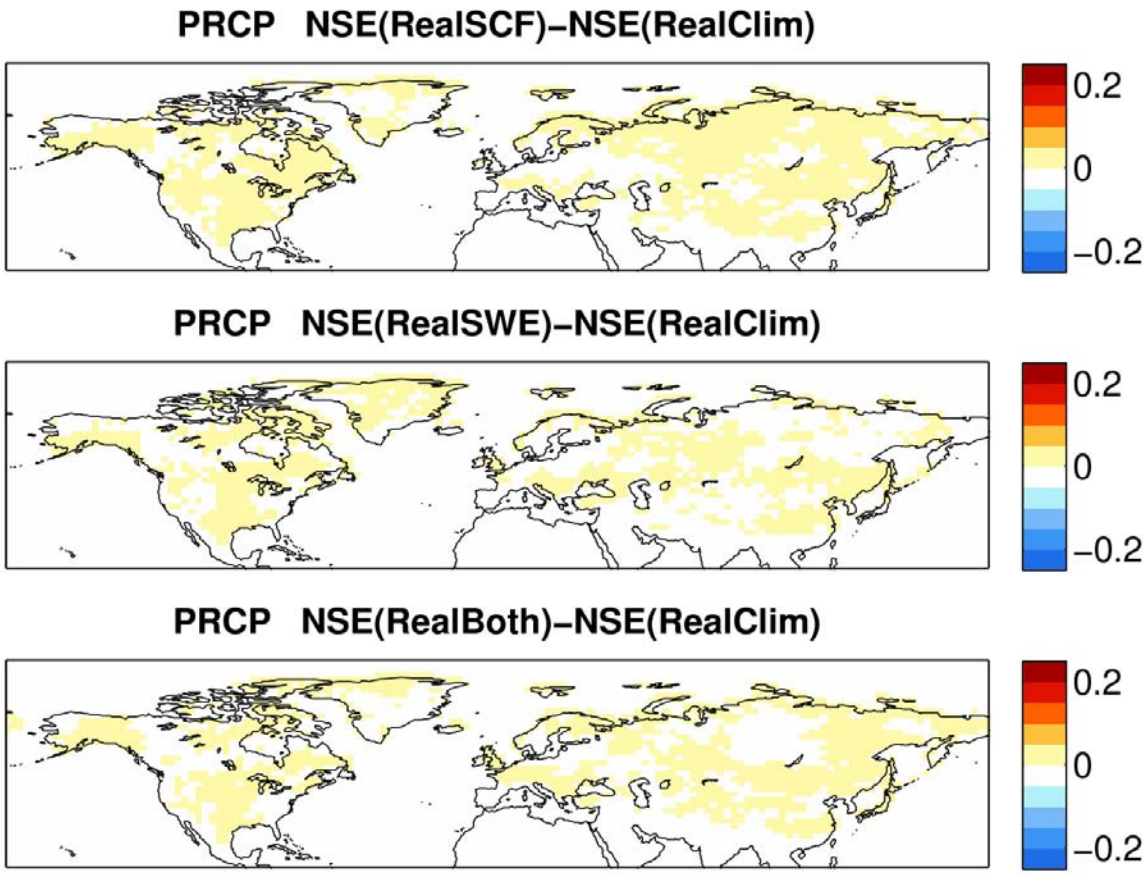

Figure 10.4 The same as Figure 10.3, but for precipitation.

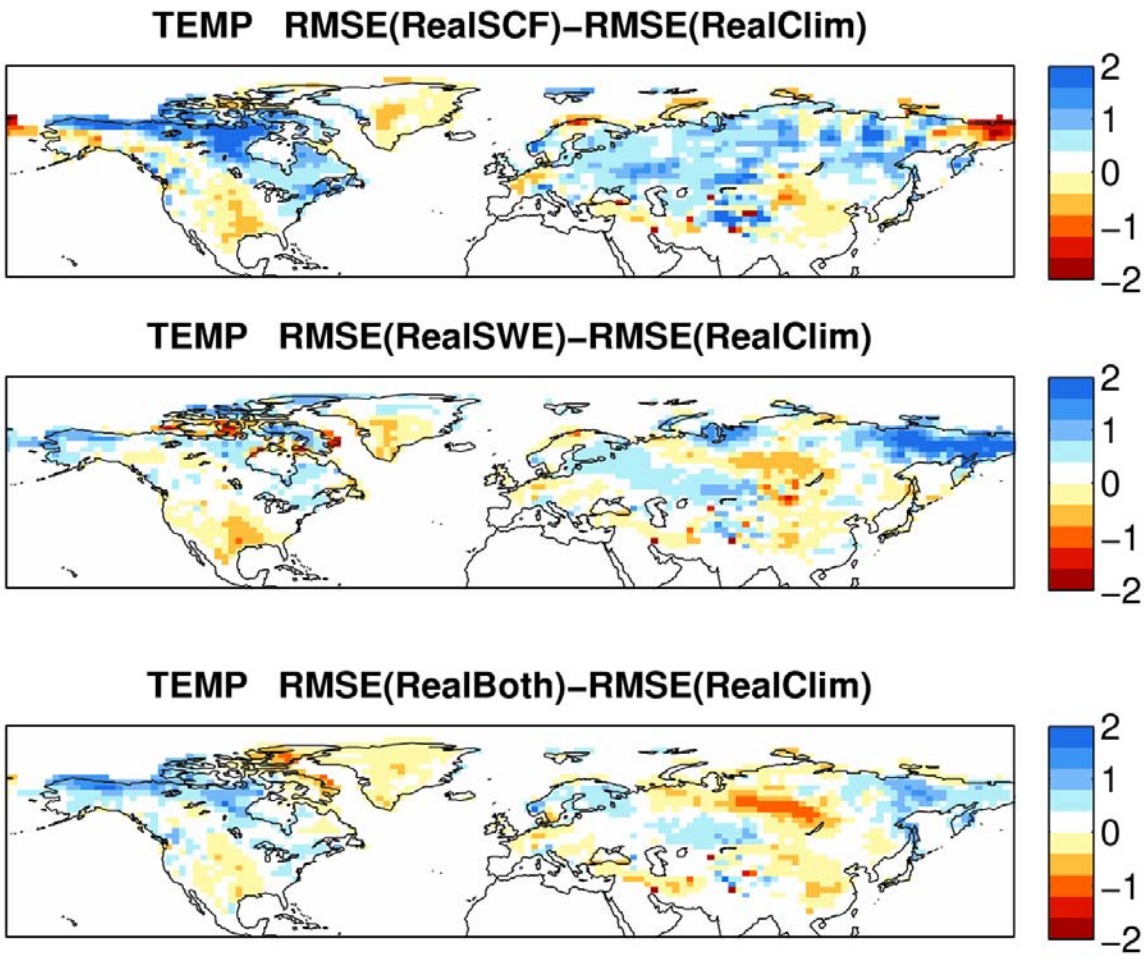

Figure 10.5 The difference of Root Mean Square Error (RMSE) in temperature among different experiments.

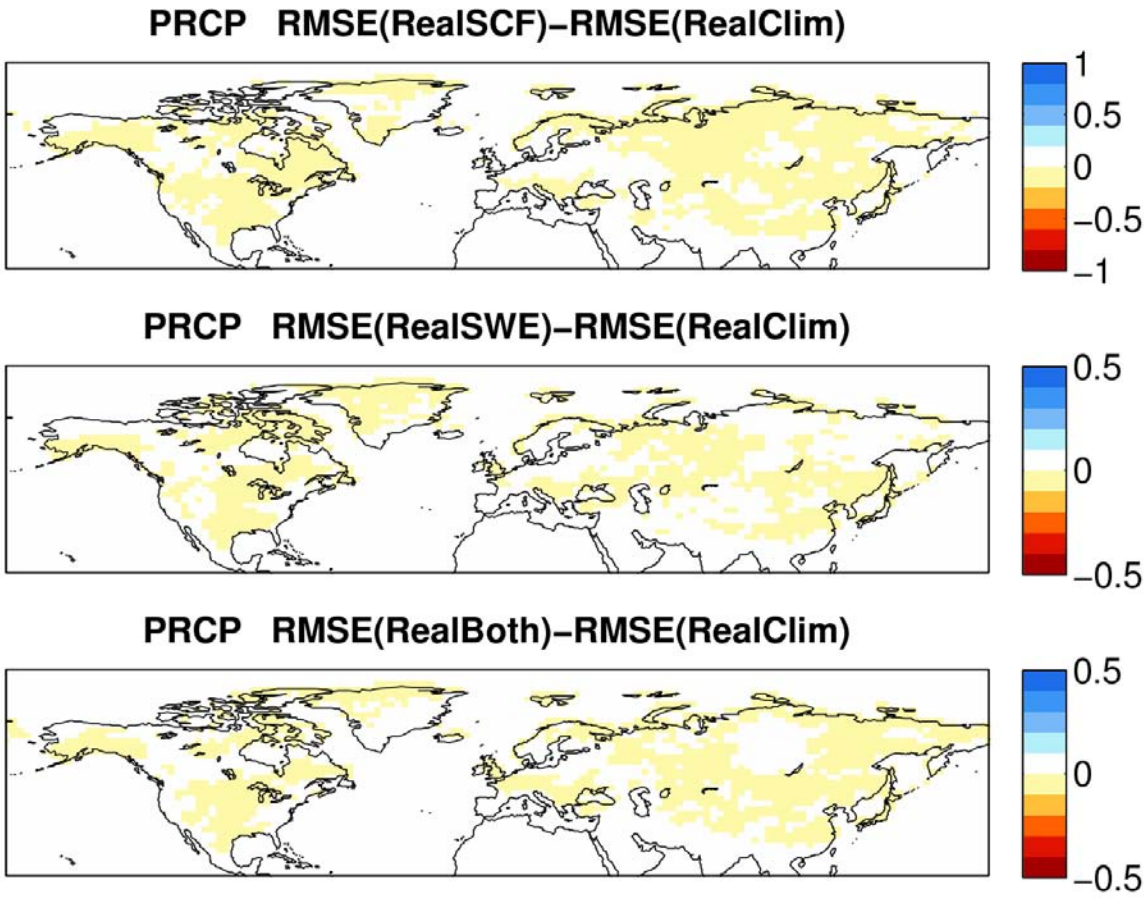

Figure 10.6 The same as Figure 10.5, but for precipitation.

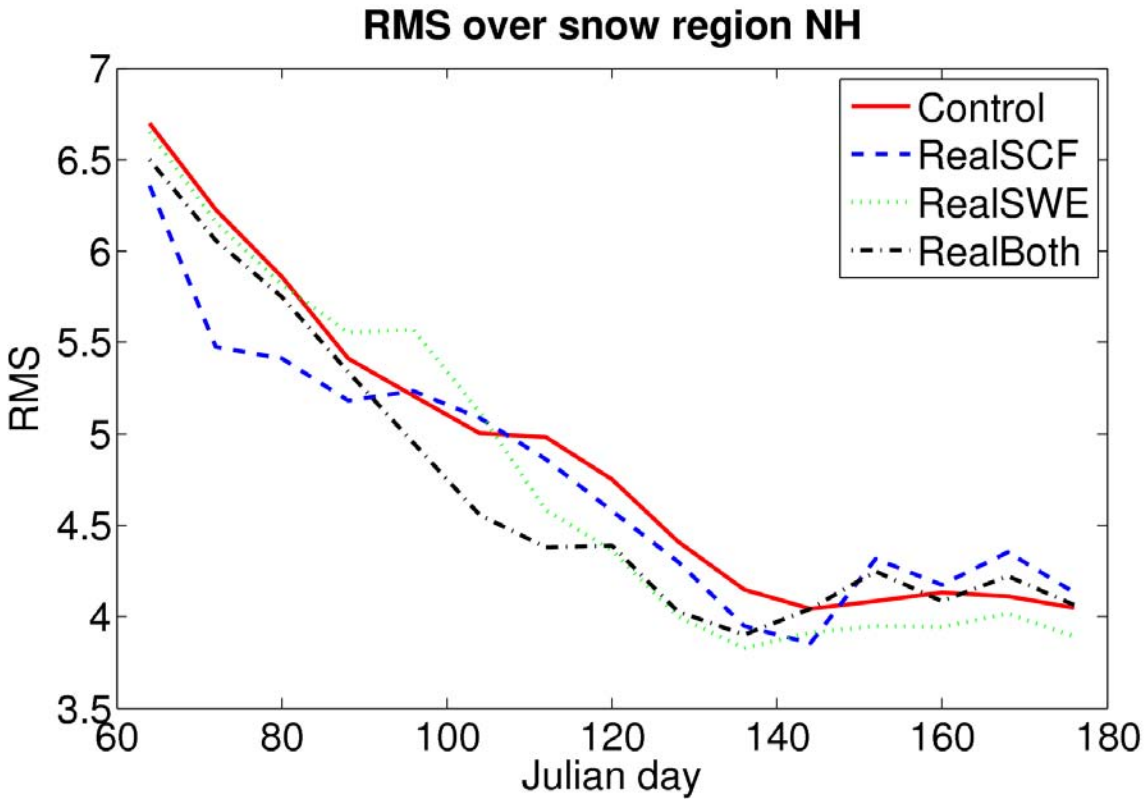

Figure 10.7 The spatial mean of Root Mean Square Error (RMS) over the snow region NH (defined by MODIS SCF > 1% at March 1st) for different experiments.

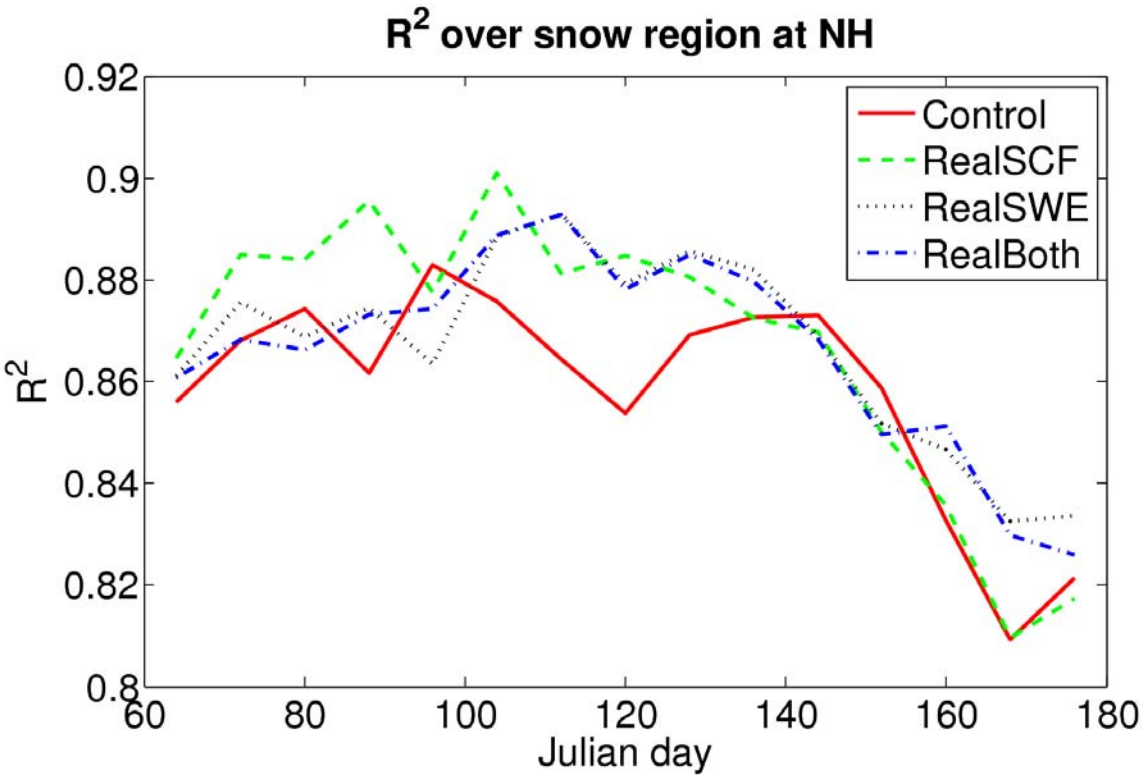

Figure 10.8 the 10-yrs mean of spatial correlation R^2 over the snow region NH (defined by MODIS SCF > 1% on March 1st) for different experiments.

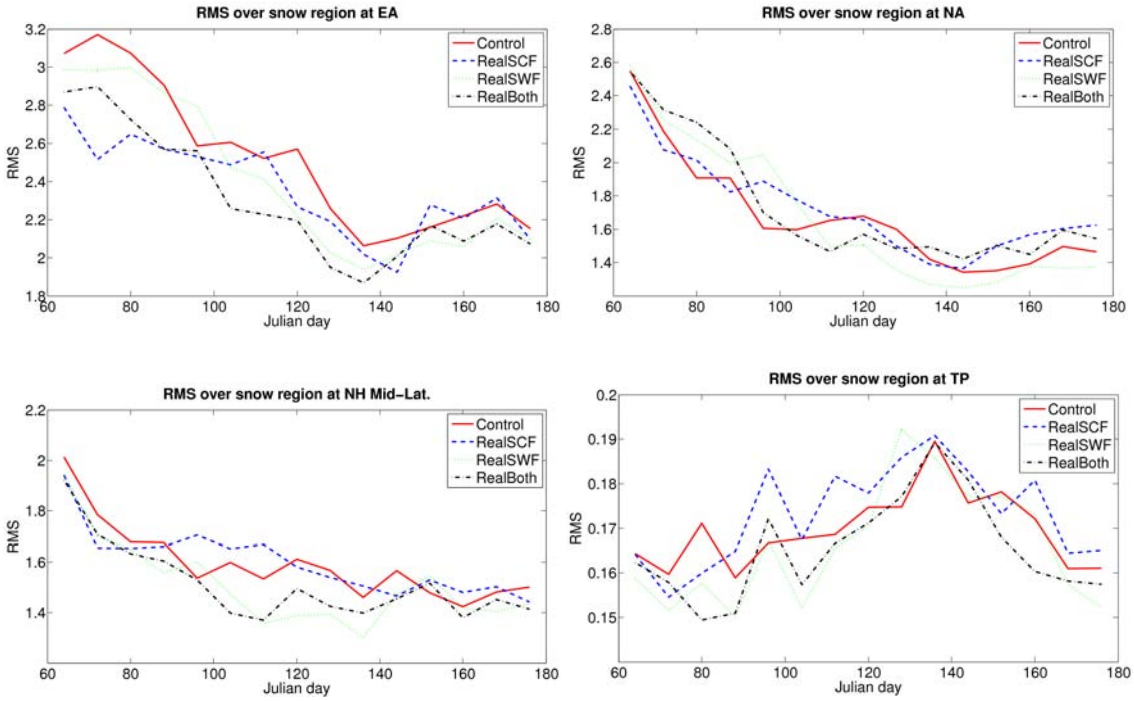

Figure 10. 9 Same as Figure 10.7, but for the four regions: Eurasia, North America, all NH middle-latitudes (40-60°) and the Tibetan Plateau.

CHAPTER 11. CONCLUSION AND DISCUSSION

In this study, a series of highly idealized numerical experiments have been designed to illustrate some key aspects of snow–atmosphere coupling behavior and its contribution to climate predictability. This series of experiments extend the GLACE experimental framework substantially, especially as follows:

- Use of imported realistic snow information (SWE and SCF) obtained by satellite or data assimilation. This approach neutralizes uncertainty within snow schemes in the land model, especially the SCF parameterization.
- Separation of snow albedo and hydrological effects in designed experiments and evaluation the snow-air coupling based on three distinct snow evolution stages.
- Effect on climate variability and predictability. Based on estimates of Gain and the STR index, the potential predictability and feedback factors associated with boundary snow information are quantified.

However, an evaluation of the model-simulated coupling behavior against observations could not be made, since the strength of coupling in the real world is difficult to measure. In reality, direct estimates of coupling strength of this type from

observations do not exist [*Koster et al.*, 2006].

Based on this modeling investigation, the key scientific questions can be addressed:

- **To what degree does the atmosphere respond to anomalies in the snow cover?**

  From spring to early summer, the snow regions over the Northern Hemisphere (NH) demonstrate significant snow-atmosphere coupling with varying degrees in different seasons and different regions. The **ModBoth** and **RealBoth** experiments revealed the spatial and temporal distribution of coupling strength during the snow depletion phase (March to June) with model simulated snow and realistic snow forcing. The maximum coupling strength appears to explain about 40% synoptic scale temperature variability.

- **Where and when does the atmosphere respond most strongly to snow anomalies?**

  The spatial and temporal distribution of coupling strength displays distinct features linked with snow distribution and evolution stage. The strongest coupling happens in the middle-latitude snow transient zone during the snowmelt stage. The snow coupling is general weak over polar (high-latitude) and low-latitude regions. There is a secondary peak of coupling strength around the Tibetan Plateau due to its high elevation and incident solar radiation. The overall coupling strength is strongest during snowmelt. After snowmelt, the

coupling strength due to the hydrological effect (soil moisture impact) is stronger than that due to the albedo effect (radiative impact) before snowmelt. A conceptual model was proposed to explain the mechanism behind the spatial distribution of coupling strength.

- **What is the relative importance of the snow direct impact (albedo effect) and indirect impact (hydrological effect)?**

  We established that the coupling originates from two mechanisms, the snow albedo effect and hydrological effect, which could be quantified separately by the **RealSCF** and **RealSWE** experiments. We can also separate two mechanisms by different snow evolution stages. Albedo effect mainly impacts before snowmelt, and hydrological effect contributes after snowmelt. The hydrological effect exerts stronger impacts than albedo effect.

- **How much would snow-albedo feedback and the hydrological effect contribute to climate predictability?**

  The potential predictably measured by Signal-To-Total-Ratio (STR) show identical pattern with coupling strength, implying the coupling contribute to potential predictability. Evaluations show that SCF mainly improves simulation before snowmelt and SWE mainly improves afterward.

This study has helped to improve our understanding of the interaction between snow cover and the atmosphere. Determining the coupling strength and seasonal forecast skill attributed to snow information has also increased our knowledge of climate predictability. These experiments would also offer a prototype for testing snow-atmosphere coupling strength that could be applied to other weather and climate models in the future.

11.1 Model uncertainty

Although CLM 3.5 has greatly improved snow modeling, which is concentrated on realistically capturing the high albedo and hydrological properties of snow cover, other important thermodynamic properties of snow cover may still not be well represented in the current CLM, including the high emissivity and low thermal conductivity of snow cover as well as processes associated with melting and runoff.

Moreover, CLM 3.5 represents spatial land surface heterogeneity by multiple separate land-units, including glacier, lake, wetland, urban, and vegetated as shown by Figure 5.5. However, snow cover often shows significant heterogeneity for mid-latitude grid-boxes with relative larger contrasts based on the surface elevation, even in the same land unit/type. This heterogeneity introduces remarkable inhomogeneities in land surface properties, such as albedo, roughness and moisture availability. Due to the non-linearity in the relationships between fluxes and

gradients, gridbox-average fluxes are not simply related to gridbox-average gradients over heterogeneous surfaces.

The coarse resolution of CAM/CLM (1.9x2.5°) in this study contributes to uncertainties over complicated terrain. Since snow cover is highly sensitive to local geographic features, such as elevation, slope, aspect and vegetation, the grid-average SWE does not well represent sub-grid snow variation although remote sensing MODIS data can provide high resolution snow monitoring as fine as 500m. Higher resolution climate models are both necessary and possible for future study of this coupling phenomenons [*Shukla et al.*, 2009]. Increasing resolution of models could reduce the uncertainty due to sub-grid heterogeneous of snow cover.

Furthermore, snow can easily submerge below vegetation, greatly changing the net albedo and roughness of the surface, but dense forest canopies retain low albedo even when snow is present. Moreover, intercepted snow on a forest canopy has a large exposed surface area for sublimation, moistening and cooling the air, whereas snow on the ground below the canopy is sheltered from wind and solar radiation so sublimation is limited and melt is delayed. CLM 3.5 computes moisture and heat fluxes separately for snow on the ground and snow held in vegetation canopies, but we cannot distinguish the effects of snow on the ground or on canopies in the design of this experiment.

Rain-on-snow events in spring [*Putkonen and Roe, 2002*] can drastically alter snow cover distribution and stream runoff, but less is known about how such events

will affect large-scale snow-atmosphere coupling strength. The CLM model still cannot well simulate rain-on-snow events. Given the predicted effects of climate change, these kind of rain-on-snow events will happen more frequently and will need to be investigated in the future.

11.2 Multi-model inter-comparison

Modeling studies, of course, are far from perfect. The potential ability of snow anomalies to affect the atmosphere in climate models could not be explicitly prescribed or parameterized, but rather be a net result of complex interactions between numerous physical process, including snow hydrology, water and energy exchange, boundary layer and convective process.

Although snow-atmosphere coupling strength can be computed from the SACE experiments, the results are strongly model-dependent, reflecting here the behavior of the CAM model. Nevertheless, an inter-model comparison could illustrate the uncertainty associated with specific models, particularly in the atmospheric boundary layer and convective processes that control the coupling. Therefore, further studies of coupling strength using multiple models are needed. A similar GLACE-type multi-model inter-comparison project is needed to further eliminate model dependence of results, to estimate the reliability or robustness of these results, and to provide the best picture of the contribution of snow-atmosphere coupling strength to climate predictability. The SACE experiment offers

a prototype for testing snow-atmosphere coupling strength that could be implemented in a multi-model inter-comparison in the future.

11.3 Future studies

To further the understanding of snow-atmosphere coupling strength, we identify several additional issues that require investigation in the future. First, the snow-atmosphere coupling needs to be quantified during the snow accumulation season from September to February, to compare with snow ablation season in this study. Second, a more complicated series of experiment with different model configurations, such as changes to the boundary layer parameterization, snow hydrological processes and convective schemes, maybe provide more insight into the mechanisms of snow-atmosphere coupling. Third, a high-resolution land model coupled to a relative coarser atmosphere could be set up to study the impact of model resolution on the coupling strength. Finally, the strength of snow-atmosphere coupling could be compared with other lower boundary processes in climate system; For example, comparing with different SST boundary conditions could establish the relative importance of land and ocean on the climate predictability.

As we have shown, snowmelt plays an essential role for the snow hydrological effect. In the high latitude regions, snowmelt will impact river runoff timing and magnitude, soil moisture anomalies and the regional hydrological cycle. Microwave sensors operating at a higher frequency such as the Ku-band (13.4 GHz) are especially sensitive to changes in snow. Although it was designed for ocean

applications, SeaWinds on the QuikSCAT satellite provides assessment of seasonal snowmelt (freeze/thaw detection) patterns. Almost ten years of data are now available, which could give insights into the spatial variability of snowmelt on circumpolar scales for future studies.

In this study, we focus on the snow-atmosphere coupling and interaction at daily to monthly time scales. The diurnal variations in the atmosphere have been filtered by use of daily mean time series. However, there exist some shorter scale coupling phenomena, such as the diurnal shortwave radiation cycle, nocturnal boundary layer (NBL) growth, etc. In the future, these shorter time-scale coupling phenomenon also need to be considered.

Global warming also seriously impacts snow cover by reducing accumulation, causing earlier spring melt and a shorter snow season. Shallow snow covers at low elevations in middle latitudes are the most sensitive to temperature increases and thus most likely to experience quick melt [*Raisanen*, 2008]. This change in snow extent and snow depth will have major implications for weather, climate and hydrological impacts. Based on the World Climate Research Programme (WCRP) Third Coupled Model Inter-comparison Project (CMIP3), Raisanen [2008] evaluated the change in snow on the warmer climate. Snow was significantly reduced at middle- latitudes but increase in the high-latitudes. The average borderline for decreasing and increasing SWE coincides with the -20° C isotherms in November-March mean temperature. In the backdrop of global warming, how snow changes

and its effect on the climate system still needs further investigation.

REFERENCES

REFERENCES

Anderson, E. A. (1976), A POINT ENERGY AND MASS BALANCE MODEL OF A SNOW COVER.

Bamzai, A. S., and J. Shukla (1999), Relation between Eurasian Snow Cover, Snow Depth, and the Indian Summer Monsoon: An Observational Study, *J. Clim.*, *12*(10), 3117-3132 %U http://dx.doi.org/3110.1175%3112F1520-0442%281999%229012%281993C283117%281993ARBESCS%281993E281992.281990.CO%281993B281992.

Bamzai, A. S., and L. Marx (2000), COLA AGCM simulation of the effect of anomalous spring snow over Eurasia on the Indian summer monsoon, *Quarterly Journal of the Royal Meteorological Society*, *126*(568), 2575-2584.

Barnett, T. P., J. C. Adam, and D. P. Lettenmaier (2005), Potential impacts of a warming climate on water availability in snow-dominated regions, *Nature*, *438*(7066), 303-309.

Barnett, T. P., L. Dumenil, U. Schlese, and E. Roeckner (1988), THE EFFECT OF EURASIAN SNOW COVER ON GLOBAL CLIMATE, *Science*, *239*(4839), 504-507.

Blanford, H. F. (1884), On the connexion of Himalayan snowfall and seasons of drought in India, in *Proc. Roy. Soc. London*, edited, pp. 3–22.

Brown, R. D. (2000), Northern Hemisphere Snow Cover Variability and Change, 1915-97, *J. Clim.*, *13*(13), 2339-2355 %U http://dx.doi.org/2310.1175%2332F1520-0442%282000%229013%282003C282339%282003ANHSCVA%282003E282002.282000.CO%282003B282002.

Brubaker, K. L., R. T. Pinker, and E. Deviatova (2005), Evaluation and Comparison of MODIS and IMS Snow-Cover Estimates for the Continental United States Using Station Data, *Journal of Hydrometeorology*, *6*(6), 1002-1017 %U http://dx.doi.org/1010.1175%1002FJHM1447.1001.

Budyko, M. I., and L. I. Zubenok (1961), The determination of evaporation from the land surface, *Izv. Akad. Nauk SSSR Ser. Geogr*, *6*, 3,Äì17.

Chang, A. T. C., and A. Rango (2000), Algorithm Theoretical Basis Document (ATBD) for the AMSR-E Snow Water Equivalent Algorithm, *NASA/GSFC, Nov*.

Chang, A. T. C., J. L. Foster, and D. K. Hall (1987), Nimbus-7 SMMR derived global snow cover parameters, *Ann. Glaciol*, *9*, 39,Äì44.

Chen, L.-T., and R. Wu (2000), Interannual and decadal variations of snow cover Qinghai-Xizang Plateau and their relationship to summer monsoon rainfall in China., *Adv Atmos Sci*, *17*, 18-30.

Chen, L. T., and Z. X. Yan (1979), Impact of the snow cover over the Tibetan Plateau in winter and spring on the atmospheric circulation and the precipitation in South China during the rainy season, *I, Water Resources and Electric Power Press, Beijing*, 185-195.

Chen, L. T., and Z. X. Yan (1981), Statistics of the impacts on early summer monsoon of the anomalous snow cover in winter and spring over the Tibetan Plateau, in *Proceedings of the Symposium of the Tibetan Plateau Meteorology*, edited, pp. 151-161.

Chen, Q.-J., B. Gao, and W.-J. Li (2000), Studies on relationships among winter snow cover over the Tibetan Plateau and droughts/floods during Meiyu season in the middle and lower reaches of the Changjiang river as well as in the atmosphere/ocean system *Acta Meteorol. Sina*, *58.* , 582–595.

Clark, M. P., and M. C. Serreze (2000), Effects of variations in east Asian snow cover on modulating atmospheric circulation over the north pacific ocean, *J. Clim.*, *13*(20), 3700-3710.

Cohen, J., and D. Rind (1991), The Effect of Snow Cover on the Climate, *J. Clim.*, *4*(7), 689-706.

Cohen, J., and D. Entekhabi (1999), Eurasian snow cover variability and Northern Hemisphere climate predictability, *GEOPHYSICAL RESEARCH LETTERS*, *26*(3), 345-348.

Cohen, J. L., and K. Saito (2003), Eurasian snow cover, more skillful in predicting U.S. winter climate than the NAO/AO?, *Geophys. Res. Lett.*, *30*(23), CLM 3-1 - CLM 3-4.

Dai, Y., et al. (2003), The Common Land Model, *Bulletin of the American Meteorological Society*, *84*(8), 1013-1023 %U http://dx.doi.org/1010.1175%1012FBAMS-1084-1018-1013.

Dash, S. K., G. P. Singh, M. S. Shekhar, and A. D. Vernekar (2005), Response of the Indian summer monsoon circulation and rainfall to seasonal snow depth anomaly over Eurasia, *Climate Dynamics*, *24*(1), 1-10.

de Goncalves, L. G. G., W. J. Shuttleworth, S. C. Chou, Y. K. Xue, P. R. Houser, D. L. Toll, J. Marengo, and M. Rodell (2006), Impact of different initial soil moisture fields on Eta model weather forecasts for South America, *Journal of Geophysical Research-Atmospheres*, *111*(D17), 14.

DelSole, T., and M. K. Tippett (2008), Predictable Components and Singular Vectors, *Journal of the Atmospheric Sciences*, *65*(5), 1666-1678 %U http://dx.doi.org/1610.1175%1662F2007JAS2401.1661.

Delworth, T., and S. Manabe (1989), THE INFLUENCE OF SOIL WETNESS ON NEAR-SURFACE ATMOSPHERIC VARIABILITY, *J. Clim.*, *2*(12), 1447-1462.

Dey, B., and B. Kumar (1983), Himalayan Winter Snow Cover Area and Summer Monsoon Rainfall over India, *Journal of Geophysical Research*, *88*.

Dickinson, R. E. (1983), Land Surface Processes and Climate-Surface Albedos and Energy Balance, *Advances in Geophysics*, *25*.

Dickson, R. R. (1984), Eurasian Snow Cover versus Indian Monsoon Rainfall,ÄîAn Extension of the Hahn-Shukla Results, *Journal of Applied Meteorology*, *23*(1), 171-173.

Dirmeyer, P. A., X. Gao, M. Zhao, Z. Guo, T. Oki, and N. Hanasaki (2006), GSWP-2: Multimodel Analysis and Implications for Our Perception of the Land Surface, *Bulletin of the American Meteorological Society*, *87*(10), 1381-1397 %U http://dx.doi.org/1310.1175%1382FBAMS-1387-1310-1381.

Dong, B., and P. J. Valdes (1998), Modelling the Asian summer monsoon rainfall and Eurasian winter/spring snow mass, *QUARTERLY JOURNAL-ROYAL METEOROLOGICAL SOCIETY*, *124*, 2567-2596.

Entekhabi, D., and P. S. Eagleson (1989a), Land Surface Hydrology Parameterization for Atmospheric General Circulation models Including Subgrid Scale Spatial Variability, *J. Clim.*, *2*(8), 816-831 %U http://dx.doi.org/810.1175%1172F1520-0442%281989%229002%281983C280816%281983ALSHPFA%281983E281982.281980.CO%281983B281982.

Entekhabi, D., and P. S. Eagleson (1989b), Land Surface Hydrology Parameterization for Atmospheric General Circulation models Including Subgrid Scale Spatial Variability, *J. Clim.*, *2*(8), 816-831.

Evensen, G., and P. J. van Leeuwen (1996), Assimilation of Geosat Altimeter Data for the Agulhas Current Using the Ensemble Kalman Filter with a Quasigeostrophic Model, *Monthly Weather Review*, *124*(1), 85-96 %U http://dx.doi.org/10.1175%1172F1520-0493%281996%229124%281993C280085%281993AAOGADF%281993E281992.281990.CO%281993B281992.

Ferranti, L., and F. Molteni (1999), Ensemble simulations of Eurasian snow-depth anomalies and their influence on the summer Asian monsoon, *Quarterly Journal of the Royal Meteorological Society*, *125*(559), 2597-2610.

Gong, G., D. Entekhabi, and J. Cohen (2002), A Large-Ensemble Model Study of the Wintertime AO,ÄìNAO and the Role of Interannual Snow Perturbations, *J. Clim.*, *15*(23), 3488-3499 %U http://dx.doi.org/3410.1175%3482F1520-0442%282002%229015%282003C283488%282003AALEMSO%282003E282002.282000.CO%282003B282002.

Gong, G., D. Entekhabi, and J. Cohen (2004a), Orographic Constraints on a Modeled Siberian Snow,ÄìTropospheric,ÄìStratospheric Teleconnection Pathway, *J. Clim.*, *17*(6), 1176-1189 %U http://dx.doi.org/1110.1175%1172F1520-0442%282004%229017%282003C281176%282003AOCOAMS%282003E282002.282000.CO%282003B282002.

Gong, G., D. Entekhabi, J. Cohen, and D. Robinson (2004b), Sensitivity of atmospheric response to modeled snow anomaly characteristics, *Journal of Geophysical Research-Atmospheres*, *109*(D6), 13.

Groisman, P. Y., T. R. Karl, R. W. Knight, and G. L. Stenchikov (1994), Changes of Snow Cover, Temperature, and Radiative Heat Balance over the Northern Hemisphere, *J. Clim.*, *7*(11), 1633-1656 %U http://dx.doi.org/1610.1175%1632F1520-0442%281994%229007%281993C281633%281993ACOSCTA%281993E281992.281990.CO%281993B281992.

Guo, Z., et al. (2006), GLACE: The Global Land-Atmosphere Coupling Experiment. Part II: Analysis, *Journal of Hydrometeorology*, *7*(4), 611-625 %U http://dx.doi.org/610.1175%1172FJHM1511.1171.

Hahn, D. G., and J. Shukla (1976), An Apparent Relationship between Eurasian Snow Cover and Indian Monsoon Rainfall, *Journal of the Atmospheric Sciences*, *33*(12), 2461-2462.

Hall, D. K., G. A. Riggs, and V. V. Salomonson (2001), Algorithm Theoretical Basis Document (ATBD) for the MODIS Snow and Sea Ice-Mapping Algorithms, *NASA GSFC, September*.

Hall, D. K., G. A. Riggs, V. V. Salomonson, N. E. DiGirolamo, and K. J. Bayr (2002a), MODIS snow-cover products, *Remote Sensing of Environment*, *83*(1), 181-194.

Hall, D. K., R. E. J. Kelly, G. A. Riggs, A. T. C. Chang, and J. L. Foster (2002b), Assessment of the relative accuracy of hemispheric-scale snow-cover maps, *Annals of Glaciology*, *34*(1), 24-30.

Huffman, G. J., R. F. Adler, P. Arkin, A. Chang, R. Ferraro, A. Gruber, J. Janowiak, A. McNab, B. Rudolf, and U. Schneider (1997), The Global Precipitation Climatology Project (GPCP) Combined Precipitation Dataset, *Bulletin of the American Meteorological Society*, *78*(1), 5-20 %U http://dx.doi.org/10.1175%1172F1520-0477%281997%229078%281993C280005%281993ATGPCPG%281993E281992.281990.CO%281993B281992.

Hurrell, J. W., J. J. Hack, D. Shea, J. M. Caron, and J. Rosinski (2008), A New Sea Surface Temperature and Sea Ice Boundary Dataset for the Community Atmosphere Model, *J. Clim.*, *21*(19), 5145-5153.

IPCC (2007), *Climate Change 2007: The scientifc basis.*, 944 pp., Cambridge University Press, Cambridge.

Kalnay, E., M. Kanamitsu, R. Kistler, W. Collins, D. Deaven, L. Gandin, M. Iredell, S. Saha, G. White, and J. Woollen (1996), The NCEP/NCAR 40-Year Reanalysis Project, *Bulletin of the American Meteorological Society*, *77*(3), 437-471.

Kanamitsu, M., W. Ebisuzaki, J. Woollen, S. K. Yang, J. J. Hnilo, M. Fiorino, and G. L. Potter (2002), NCEP–DOE AMIP-II Reanalysis (R-2), *Bulletin of the American Meteorological Society*, *83*(11), 1631-1643.

Koster, R. D., P. A. Dirmeyer, A. N. Hahmann, R. Ijpelaar, L. Tyahla, P. Cox, and M. J. Suarez (2002), Comparing the Degree of Land-Atmosphere Interaction in Four Atmospheric General Circulation Models, *Journal of Hydrometeorology*, *3*(3), 363-375 %U http://dx.doi.org/310.1175%1172F1525-7541%282002%229003%282003C280363%282003ACTDOLA%282003E282002.282000.CO%282003B282002.

Koster, R. D., M. J. Suarez, P. Liu, U. Jambor, A. Berg, M. Kistler, R. Reichle, M. Rodell, and J. Famiglietti (2004), Realistic Initialization of Land Surface States: Impacts on Subseasonal Forecast Skill, *Journal of Hydrometeorology*, *5*(6), 1049-1063.

Koster, R. D., et al. (2010), Contribution of land surface initialization to subseasonal forecast skill: First results from a multi-model experiment, *GEOPHYSICAL RESEARCH LETTERS*, *37*.

Koster, R. D., et al. (2006), GLACE: The Global Land-Atmosphere Coupling Experiment. Part I: Overview, *Journal of Hydrometeorology*, *7*(4), 590-610 %U http://dx.doi.org/510.1175%1172FJHM1510.1171.

Kripalani, R. H., and A. Kulkarni (1999), Climatology and variability of historical Soviet snow depth data: some new perspectives in snow-Indian monsoon teleconnections, *Climate Dynamics*, *15*(6), 475-489.

Li, Q., and Y. Chen (2006), Impact of anomalous snow cover over Tibetan plateau on East Asian summer monsoon climate. Journal of PLA University of Science and Technology, , *Journal of PLA University of Science and Technology*, *7*, 605-612.

Lin, S. J., and R. B. Rood (1997), An explicit flux-form semi-Lagrangian shallow-water model on the sphere, *Quarterly Journal of the Royal Meteorological Society*, *123*(544), 2477-2498.

Ma, Y. M., S. C. Kang, L. P. Zhu, B. Q. Xu, L. D. Tian, and T. D. Yao (2008), Tibetan Observation and Research Platform Atmosphere-Land Interaction over a Heterogeneous Landscape, *Bulletin of the American Meteorological Society*, *89*(10), 1487-+.

Marshall, S., and S. G. Warren (1986), Parameterization of Snow Albedo for Climate Models, *Available from the National Technical Information Service, Springfield VA 22161, as DE 86-011983. Price codes: A 12 in paper copy*.

Marshall, S. E. (1989), a Physical Parameterization of Snow Albedo for Use in Climate Models, *Thesis (PH. D.)--UNIVERSITY OF COLORADO AT BOULDER, 1989. Source: Dissertation Abstracts International*, *51*, 1716.

Nash, J. E., and J. V. Sutcliffe (1970), River flow forecasting through conceptual models. Part I: a discussion of principles. , *Journal of hydrology*, *10*, 282-290.

Niu, G. Y., and Z. L. Yang (2006), Effects of frozen soil on snowmelt runoff and soil water storage at a continental scale, *Journal of Hydrometeorology*, *7*(5), 937-952.

Niu, G. Y., and Z. L. Yang (2007), An observation-based formulation of snow cover fraction and its evaluation over large North American river basins, *Journal of Geophysical Research-Atmospheres*, *112*(D21).

Oleson, K., Y. Dai, G. Bonan, M. Bosilovich, R. Dickinson, P. Dirmeyer, F. Hoffman, P. Houser, S. Levis, and G. Y. Niu (2004a), Technical Description of the Community Land Model (CLM). Technical Note NCAR/TN-461+ STR, *National Center for Atmospheric Research*.

Oleson, K. W., Y. Dai, G. Bonan, M. Bosilovich, R. Dickinson, P. Dirmeyer, F. Hoffman, P. Houser, S. Levis, and G. Y. Niu (2004b), Technical description of the Community Land Model (CLM). NCAR Tech, edited, Note NCAR/TN-461+ STR, 174 pp.

Oleson, K. W., Y. Dai, G. Bonan, R. E. Dickinson, P. A. Dirmeyer, F. Hoffman, P. Houser, S. Levis, G. Y. Niu, and P. Thornton (2004c), Technical description of the Community Land Model (CLM). Report No. NCAR Tech. Note TN-461+ STR, *National Center for Atmospheric Research, Boulder, CO*.

Pan, M., et al. (2003), Snow process modeling in the North American Land Data Assimilation System (NLDAS): 2. Evaluation of model simulated snow water equivalent, *Journal of Geophysical Research-Atmospheres*, *108*(D22), 14.

Parthasarathy, B., and S. Yang (1995), Relationships between regional indian summer monsoon rainfall and eurasian snow cover, *Advances in Atmospheric Sciences*, *12*(2), 143-150.

Quiring, S. M., and D. B. Kluver (2009), Relationship between Winter/Spring Snowfall and Summer Precipitation in the Northern Great Plains of North America, *Journal of Hydrometeorology*, *10*(5), 1203-1217.

Raisanen, J. (2008), Warmer climate: less or more snow?, *Climate Dynamics*, *30*(2-3), 307-319.

Ramanathan, V., and G. Carmichael (2008), Global and regional climate changes due to black carbon, *Nature Geoscience*, *1*(4), 221-227.

Ramsay, B. H. (1998), The interactive multisensor snow and ice mapping system, *Hydrological Processes*, *12*(10), 1537-1546.

Rayner, N. A., P. Brohan, D. E. Parker, C. K. Folland, J. J. Kennedy, M. Vanicek, T. J. Ansell, and S. F. B. Tett (2006), Improved analyses of changes and uncertainties in sea surface temperature measured in situ sice the mid-nineteenth century: The HadSST2 dataset, *J. Clim.*, *19*(3), 446-469.

Reichle, R. H., and R. D. Koster (2004), Bias reduction in short records of satellite soil moisture, *GEOPHYSICAL RESEARCH LETTERS*, *31*(19), 4.

Riggs, G. A., and D. K. Hall (2002), Reduction of cloud obscuration in the MODIS snow data product, in *Proceedings of the 59 thEastern Snow Conference*, edited, pp. 4-6.

Robinson, D. A., K. F. Dewey, and R. R. Heim Jr (1993), Global Snow Cover Monitoring: An Update, *Bulletin of the American Meteorological Society*, *74*(9), 1689-1696.

Rodell, M., P. R. Houser, U. Jambor, J. Gottschalck, K. Mitchell, C. J. Meng, K. Arsenault, B. Cosgrove, J. Radakovich, and M. Bosilovich (2004), The Global Land Data Assimilation System, *Bulletin of the American Meteorological Society*, *85*(3), 381-394.

Saito, K., J. Cohen, and D. Entekhabi (2001), Evolution of Atmospheric Response to Early-Season Eurasian Snow Cover Anomalies, *Monthly Weather Review*, *129*(11), 2746-2760 %U http://dx.doi.org/2710.1175%2742F1520-0493%282001%229129%282003C282746%282003AEOARTE%282003E282002.282000.CO%282003B282002.

Sankar-Rao, M., K. M. Lau, and S. Yang (1996), On the relationship between Eurasian snow cover and the Asian summer monsoon, *International Journal of Climatology*, *16*(6), 605-616.

Thompson, D. W. J., J. M. Wallace, and G. C. Hegerl (2000), Annular modes in the extratropical circulation. Part II: Trends, *J. Clim.*, *13*(5), 1018-1036.

Vavrus, S. (2007), The role of terrestrial snow cover in the climate system, *Climate Dynamics*, *29*(1), 73-88.

Vernekar, A. D., J. Zhou, and J. Shukla (1995), THE EFFECT OF EURASIAN SNOW COVER ON THE INDIAN MONSOON, *J. Clim.*, *8*(2), 248-266.

Walker, G. T. (1910), Correlations in seasonal variations of weather, *Mem. India Meteor. Dept*, *21*, 22-45.

Walland, D. J., and I. Simmonds (1996), Modelled atmospheric response to changes in Northern Hemisphere snow cover, *Climate Dynamics*, *13*(1), 25-34.

Walsh, J. E., D. R. Tucek, and M. R. Peterson (1982), SEASONAL SNOW COVER AND SHORT-TERM CLIMATIC FLUCTUATIONS OVER THE UNITED-STATES, *Monthly Weather Review*, *110*(10), 1474-1485.

Walsh, J. E., W. H. Jasperson, and B. Ross (1985), Influences of Snow Cover and Soil Moisture on Monthly Air Temperature, *Monthly Weather Review*, *113*(5).

Wang, Z., and X. Zeng (2010), Evaluation of Snow Albedo in Land Models for Weather and Climate Studies, *Journal of Applied Meteorology and Climatology*, *49*(3), 363-380.

Watanabe, M., and T. Nitta (1998), Relative Impacts of Snow and Sea Surface Temperature Anomalies on an Extreme Phase in the Winter Atmospheric Circulation, *J. Clim.*, *11*(11), 2837-2857 %U http://dx.doi.org/2810.1175%2832F1520-0442%281998%229011%281993C282837%281993ARIOSAS%281993E281992.281990.CO%281993B281992.

Wiscombe, W. J., and S. G. Warren (1980), A Model for the Spectral Albedo of Snow. I: Pure Snow, *Journal of the Atmospheric Sciences*, *37*(12), 2712-2733 %U http://dx.doi.org/2710.1175%2712F1520-0469%281980%229037%281983C282712%281983AAMFTSA%281983E281982.281980.CO%281983B281982.

Wu, T., and Z. Qian (2003a), The Relation between the Tibetan Winter Snow and the Asian Sum. tiler Monsoon and Rainfall: An Obsen, ation Investiga,Äîdon, *J. Climate*, *16*, 2038-2051.

Wu, T.-W., and Z.-A. Qian (2003b), The Relation between the Tibetan Winter Snow and the Asian Summer Monsoon and Rainfall: An Observational Investigation, *J. Clim.*, *16*(12), 2038-2051 %U http://dx.doi.org/2010.1175%2032F1520-0442%282003%229016%282003C282038%282003ATRBTTW%282003E282002.282000.CO%282003B282002.

Xie, L., T. Yan, L. J. Pietrafesa, T. Karl, and X. Xu (2005), Relationship between western North Pacific typhoon activity and Tibetan Plateau winter and spring snow cover, *Geophys. Res. Lett.*, *32*(16), 1-4.

Xu, L., and Y. Li (2010), Reexamining the impact of Tibetan snow anomalies to the East Asian summer monsoon using MODIS snow retrieval, *Climate Dynamics*, *35*, 1039–1053.

Xu, L., H. Gao, and y. Li (2009a), Sensible Heating over the Tibetan Plateau Linked to the Onset of Asian Monsoon, *ATMOSPHERIC AND OCEANIC SCIENCE LETTERS*, *2*(6), 1-7.

Xu, L., H. Gao, and Y.-Q. Li (2009b), Sensible Heating over the Tibetan Plateau Linked to the Onset of Asian Monsoon, *Atmospheric and Oceanic Science Letters*, *2*(6), 350-356.

Yamada, T. J., R. D. Koster, S. Kanae, and T. Oki (2007), Estimation of predictability with a newly derived index to quantify similarity among ensemble members, *Monthly Weather Review*, *135*(7), 2674-2687.

Yang, S. (1996), ENSO-snow-monsoon associations and seasonal-interannual predictions, *International Journal of Climatology*, *16*(2), 125-134.

Zaitchik, B. F., and M. Rodell (2008), Forward-looking Assimilation of MODIS-derived Snow Covered Area into a Land Surface Model, *Journal of Hydrometeorology*, *preprint*(2008), 0000-0000 %U http://dx.doi.org/0010.1175%0002F2008JHM1042.0001.

Zhang, S., and S. Tao (2001), Influence of snow cover over the Tibetan Plateau on Asian summer monsoon. Chinese Journal of Atmospheric Sciences, *25*, 372-390.

Zhao, Z. (1999), *The Summer Rainfall in China and its Environment Field*, China Meteorological Press, Beijing.

CURRICULUM VITAE

Li Xu graduated with a Bachelor of Science in climatology from Nanjing Institute of Meteorology in 1998, which is the most important university for atmosphere science in the China. He worked 7 years as a climatologist at China National Climate Center in Beijing, where he received basic training to be a scientist. At main time, He received his Master of Science degree in Atmospheric science and environment from Peking University in 2005. He came to USA with his family and completed his second Master of Science degree in Meteorology from University of Utah in 2007, and then studied in the Climate Dynamics PhD Program at George Mason University under guide of distinguished Professor J. Shukla.